ISSN 2518-7198 (Print)
ISSN 2663-5089 (Online)

BULLETIN

OF THE KARAGANDA UNIVERSITY

PHYSICS

Series

№ 2(110)/2023

ISSN 2663-5089 (Online)
ISSN-L 2518-7198 (Print)
Индексі 74616
Индекс 74616

ҚАРАҒАНДЫ УНИВЕРСИТЕТІНІҢ ХАБАРШЫСЫ

ВЕСТНИК КАРАГАНДИНСКОГО УНИВЕРСИТЕТА

BULLETIN OF THE KARAGANDA UNIVERSITY

ФИЗИКА сериясы

Серия ФИЗИКА

PHYSICS Series

№ 2(110)/2023

Сәуір–мамыр–маусым
30 маусым 2023 ж.
Апрель–май–июнь
30 июня 2023 г.
April–May–June
June 30th, 2023

1996 жылдан бастап шығады
Издается с 1996 года
Founded in 1996

Жылына 4 рет шығады
Выходит 4 раза в год
Published 4 times a year

Қарағанды, 2023
Караганда, 2023
Karaganda, 2023

Қарағанды университетінің хабаршысы. «Физика» сериясы.
ISSN-L 2518-7198 (Print). ISSN 2663-5089 (Online).

Меншік иесі: «Академик Е.А. Бөкетов атындағы Қарағанды университеті» КЕАҚ.

Қазақстан Республикасы Ақпарат және қоғамдық даму министрлігімен тіркелген. 30.09.2020 ж. № KZ38VPY00027378 қайта есепке қою туралы куәлігі.

Басуға 29.06.2023 ж. қол қойылды. Пішімі 60×84 1/8. Қағазы офсеттік. Көлемі 12,75 б.т. Таралымы 200 дана. Бағасы келісім бойынша. Тапсырыс № 51.

«Акад. Е.А. Бөкетов ат. Қарағанды ун-ті» КЕАҚ баспасының баспаханасында басылып шықты.
100024, Қазақстан, Қарағанды қ., Университет к-сі, 28. Тел. (7212) 35-63-16. E-mail: izd_kargu@mail.ru

Адрес редакции: 100024, Казахстан, г. Караганда, ул. Университетская, 28
Тел.: +7 701 531 4758. Факс: (7212) 35–63–98.
E-mail: vestnikku@gmail.com; karabekova71@mail.ru
Сайт: physics-vestnik.ksu.kz

Вестник Карагандинского университета. Серия «Физика».
ISSN-L 2518-7198 (Print). ISSN 2663-5089 (Online).

Собственник: НАО «Карагандинский университет имени академика Е.А. Букетова».

Зарегистрирован Министерством информации и общественного развития Республики Казахстан. Свидетельство о постановке на переучет № KZ38VPY00027378 от 30.09.2020 г.

Подписано в печать 29.06.2023 г. Формат 60×84 1/8. Бумага офсетная. Объем 12,75 п.л. Тираж 200 экз. Цена договорная. Заказ № 51.

Отпечатано в типографии издательства НАО «Карагандинский университет им. акад. Е.А. Букетова». 100024, Казахстан, г. Караганда, ул. Университетская, 28. Тел.(7212) 35-63-16. E-mail:izd_kargu@mail.ru

Postal address: 28, University Str., 100024, Karaganda, Kazakhstan
Tel.: +7 701 531 4758; Fax: (7212) 35-63-98.
E-mail: vestnikku@gmail.com; karabekova71@mail.ru
Web-site: physics-vestnik.ksu.kz

Bulletin of the Karaganda University. "Physics" Series.
ISSN-L 2518-7198 (Print). ISSN 2663-5089 (Online).

Proprietary: NLC "Karagandy University of the name of academician E.A. Buketov".

Registered by the Ministry of Information and Social Development of the Republic of Kazakhstan. Rediscount certificate No. KZ38VPY00027378 dated 30.09.2020.

Signed in print 29.06.2023. Format 60×84 1/8. Offset paper. Volume 12,75 p.sh. Circulation 200 copies. Price upon request. Order № 51.

Printed in the Publishing house of NLC "Karagandy University of the name of acad. E.A. Buketov".
28, University Str., Karaganda, 100024, Kazakhstan. Tel. (7212) 35-63-16. E-mail: izd_kargu@mail.ru

МАЗМҰНЫ — СОДЕРЖАНИЕ — CONTENT

КОНДЕНСАЦИЯЛАНҒАН КҮЙДІҢ ФИЗИКАСЫ
ФИЗИКА КОНДЕНСИРОВАННОГО СОСТОЯНИЯ
PHYSICS OF THE CONDENSED MATTER

ТЕХНИКАЛЫҚ ФИЗИКА
ТЕХНИЧЕСКАЯ ФИЗИКА
TECHNICAL PHYSICS

DOI 10.31489/2023PH2/6-16

UDC 666.3.016:537.226.1

A.V. Pavlov[1], A.M. Zhilkashinova[2], S.S. Gert[3], N.M. Magazov[4*], Zh.S. Turar[5], A.B. Nabioldina[6]

[1] Ceramic plant LLP "KAZ CERAMICS", Ust-Kamenogorsk, Kazakhstan;
[2,4,5,6] S. Amanzholov East Kazakhstan University, Ust-Kamenogorsk, Kazakhstan;
[3,4] D. Serikbayev East Kazakhstan Technical University, Ust-Kamenogorsk, Kazakhstan
([*]E-mail: magazovn@gmail.com)

Study of electrophysical properties of beryllium ceramics with the addition of micro- and nanoparticles of titanium dioxide

In the present paper the research results of influence of nanoparticles TiO_2 additions in the range 0,1 — 2,0 wt. % on electrophysical properties of oxide-beryllium ceramics (BeO + TiO_2) made of micropowders are presented. The electrophysical characteristics of synthesized ceramics modified with 30 wt. % TiO_2 micro- and nanoparticles in the electric current frequency range of 100 Hz — 100 MHz were studied by the total complex resistance method (impedance). It is known that the introduction of TiO_2 addition to the BeO-ceramics after heat treatment in a reducing atmosphere is accompanied by a significant increase in electrical conductivity and the ability to absorb electromagnetic radiation in a wide range of frequencies. According to the results of the studies it was found that the addition of nanoparticles TiO_2 into the (BeO + TiO_2)-ceramics significantly reduces its static electrical resistance in comparison with the serial sample, and the specific conductivity of such ceramics significantly increases at high frequencies ~ 10^7 Hz. The addition of TiO_2 nanoparticles significantly increases the dielectric losses of the sample sintered in the temperature range 1530 — 1550 °C. The values of real and imaginary parts of dielectric permittivity of such ceramics and the tangent of the angle of dielectric loss are two times higher compared to the serial sample — BT-30 (B — beryllium, T — titanium). The obtained results are unique in their kind, due to the experiment with a rare and strategically important material — beryllium oxide and the possibility of synthesizing new nanostructures based on it.

Keywords: dielectric permittivity, conductivity, electric current frequency, impedance, nanoparticles, beryllium oxide, titanium dioxide.

Introduction

Currently, industrial progress requires electronics to continuously increase the level of power, efficiency, reliability and durability [1]. For modern devices, in particular powerful RF (radio frequency) and SHF (super high frequency) transmitters, power transistors, power converters, reliability under conditions of high currents and high temperatures is certainly a key factor [2]. Also, ceramic materials, often used to replace metals and alloys, have not only heat resistance and high strength, but also special electrophysical properties [3, 4], which contributes to their wide use in electronic engineering [5]. Such ceramics include beryllium oxide, the effective component of dielectric permittivity of which is 6.9 — 7.5, the tangent of angle of dielectric losses $tg\delta = 3 \cdot 10^{-4}$ at frequency f = 1 MHz [6]. BeO-ceramic is a material of super refractory class, which in addition to dielectric properties is characterized by high vacuum density, mechanical strength, thermal conductivity, thermal stability and heat resistance. The unique combination of physical and chemical properties of beryllium oxide (BeO) [7] determines a wide range of BeO-ceramics use in various fields of modern technology and special instrumentation [8]. High radiation resistance [9], thermal conductivity [10], dielectric strength and transparency to X-ray, ultraviolet radiation, visible IR (infrared) and SHF radiation

[11] make BeO-ceramics the most promising material for use in various devices of electronic engineering of responsible purpose [12]. Along with high thermal conductivity — 280 — 320 W/(m·K), pure BeO-ceramics have high electrical resistance (~$1 \cdot 10^{15}$ Ohm cm at 300 K) [13]. This makes it possible to use BeO-ceramics in high-power resistors, transistors and microcircuits as highly efficient dielectric substrates for creating electronic devices and resonator tubes for gas OQG (optical quantum generator) and much more. Thermal conductivity of the BeO-ceramic is comparable with that of metals and is second only to diamond. The thermal conductivity of BeO ceramics can reach values from 300 to 320 W/(m·K), which is comparable with that of chemically pure copper, which has a thermal conductivity of ~ 400 W/(m·K) [14]. The specific electrical resistance of beryllium oxide ceramic samples at room temperature is in the range from 10^{14} to 10^{15} Ohm·cm. BeO-ceramic is a transparent material for vacuum ultraviolet (VUV), X-ray and super-high frequency (SHF) radiation [15]. In turn, the presence of developed interfaces and intergranular interactions can significantly affect the physicochemical and performance characteristics of the composite ceramics based on BeO. One of such additives capable of essentially changing the conducting and other properties of the BeO-ceramics is TiO_2 [16]. It is known that the addition of TiO_2 to the BeO-ceramics after heat treatment in a reducing atmosphere is accompanied by a significant increase in electrical conductivity and the ability to absorb electromagnetic radiation in a wide range of frequencies [17]. The different ratio in the BeO-ceramics of the TiO_2 component and the degree of its reduction allow to regulate the magnitude of electromagnetic wave absorption by such ceramics. At present, the most effective material with the ability to absorb electromagnetic waves is the composition of BeO + 30 wt % TiO_2. It is experimentally established that the absorption properties of (BeO + TiO_2)-ceramics are caused by many factors and, first of all, by its electrical conductivity [18].

The results of studies on the electrophysical properties of (BeO + TiO_2)-ceramics modified by TiO_2 nanoparticles indicate the existence of electric polarization processes and specific relaxation of spatial charges that can accumulate at the boundaries of individual microcrystals. The experimentally observed increase in the conductivity of the synthesized ceramics with an increase in the electric current frequency is explained by the appearance of the current relaxation component accompanied by an increase in the dielectric losses [19, 20].There are very few scientific publications on the study of the effect of TiO_2 nanoparticles on the impedance characteristics of the mechanical mixture of BeO — TiO_2 oxides in the public domain, which may be due to the uniqueness of beryllium production, which requires specialized equipment and special safety conditions when working with powders of BeO. At present, the current production of beryllium oxide ceramics is established in the USA, China and Kazakhstan, so the analysis and updating of knowledge on the results of research on the properties of nanostructured ceramics using this strategically important material seems to be very important.

Thus, the main purpose of the present study is to establish the effect of titanium dioxide nanoparticles on the impedance characteristics of sintered ceramics of 70 wt. % BeO(μm) + TiO_2(μm) + TiO_2(nano) with the introduction of TiO_2 nanoparticles from 0.1 to 2.0 wt. %.

Materials and methods

As a standard sample of two-component ceramics the serial sample of composition BeO + 30 wt. % TiO_2 (mark BT-30) was investigated. To produce nanocomposite ceramics, an annealed beryllium oxide powder with an average crystallite size of 5 μm and a micron powder of titanium dioxide TU 6-10-727-78 with the same particle size were used. From 0.1 to 2.0 wt % of nanodispersed TiO_2 powder was added to the BeO and TiO_2 micropowders. Microphotographs of the particles of the powders used are shown in Figure 1.

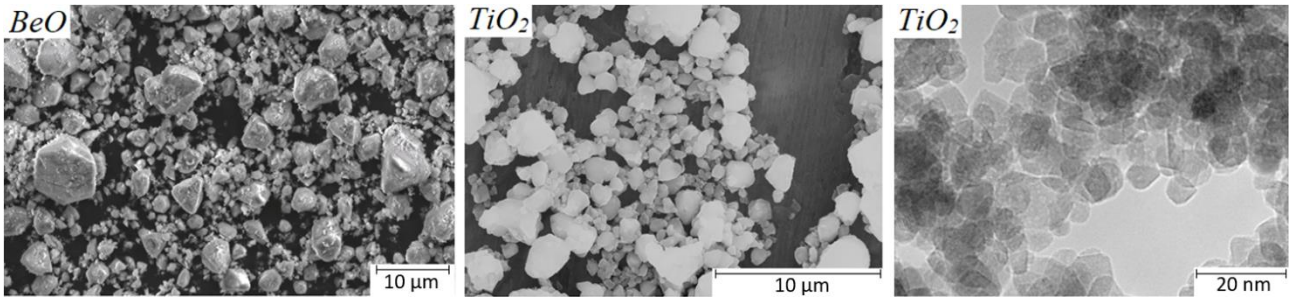

Figure 1. Electronic images of microparticles of beryllium oxide powders, titanium dioxide and nanoparticles of titanium dioxide

Then, the samples were molded by the slip casting method, burned out the bond and sintered the blank at temperatures of 1520 — 1550 ^{0}C with an interval of 10 ^{0}C. Thus, batches of ceramics based on beryllium oxide and titanium dioxide micropowders modified by TiO_2 nanoparticles were obtained with the following composition:

P.0 — BeO + 30 % $TiO_2^{\mu m}$ (BT-30 serial ceramic);
P.1 — BeO + 29,9 % $TiO_2^{\mu m}$+ 0,1 % TiO_2^{nano};
P.2 — BeO + 29,5 % $TiO_2^{\mu m}$+ 0,5 % TiO_2^{nano};
P.3 — BeO + 29,0 % $TiO_2^{\mu m}$+ 1,0 % TiO_2^{nano};
P.4 — BeO + 28,5 % $TiO_2^{\mu m}$+ 1,5 % TiO_2^{nano};
P.5 — BeO + 28,0 % $TiO_2^{\mu m}$+ 2,0 % TiO_2^{nano}.

Particular attention should be paid to the sintering process of the workpiece, which was carried out in a beryllium oxide crucible in a furnace with a graphite heater. The inner part of the crucible was lined with 0.5 mm thick molybdenum sheet, in which technological holes were provided for saturation of the billet with reducing CO gas. The crucible was covered with a beryllium cover with technological holes after the laying of workpieces. The beryllium oxide crucible was installed into the graphite rigging and covered with ballast of sintered oxide-beryllium cast, fraction not more than 10 x 10 mm. After installing graphite tooling with products in the furnace, sintering of the workpiece was carried out.

Measurements of impedance values were carried out on the AgilentE5061B spectrum analyzer designed to measure the total complex resistance (impedance) of composite samples in the frequency range of 100 Hz — 100 MHz. In this instrument model, error minimization and accurate repeatable measurement results are provided by the shielded connector. The inputs of the digital multimeter are also shielded and are optoelectronically isolated from the common case and computer interface circuits. This protection provides a high degree of input isolation, withstanding voltages up to 300 V, which is very important for reducing errors due to ground loops and common mode voltages caused by long wires and floating sources.

At least ten samples from each batch were measured in order to obtain reliable data and statistical values. If the sample had defects in the form of cracks, cavities and pores, the sample was excluded from the experiment. Some samples had relatively high electrical resistance, despite the absence of external defects, most likely there were internal defects, the measurement results of such samples were also excluded. Analysis and deciphering of the obtained data was performed using a personal computer and special software developed on the basis of Excel in the laboratory of antennas and microwave technology, created on the basis of the Department of Radio Engineering of the Institute of Engineering Physics and Radioelectronics of Siberian Federal University (Krasnoyarsk, Russia).

Results and discussion

The results of impedance spectroscopy of a serial sample (P.0) sintered at 1530 ^{0}C without the addition of nanoparticles show that such material is a conductive composite, Figure 2.

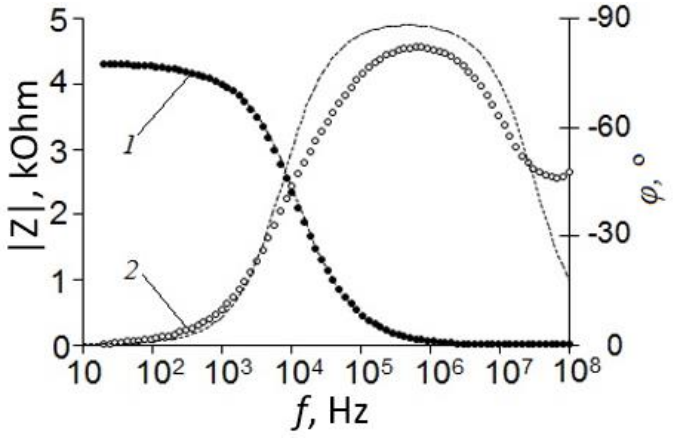

Figure 2. Frequency dependences of impedance modulus |Z| (1) (●) and φ phase angle (2) (○) for serial ceramic samples of composition BeO + 30 wt. %, T = 1530 °C

The values of impedance modulus and phase angle for the sample modified by TiO_2 nanoparticles sintered at 1550 °C are shown in Figure 2. The sample with 0.5 wt % nanoparticles (Fig. 3, a) shows the lowest resistance at low frequencies — 0.38 kOhm; at the maximum frequency of 10^8 Hz — 7.7 Ohm. The phase angle has a single peak of 50° at $5.3 \cdot 10^5$ Hz and gradually decreases with increasing frequency of electric current to -3° at the maximum frequency. When the concentration of TiO_2 nanoparticles is increased up to 1.5 wt % (Figıo 3, b), the values of electrical resistance of the sample are observed at low frequencies — 0.45 kOhm and at the maximum frequency of electric current — 8.3 Ohm. The phase angle has exactly the same one peak, which shows itself at the frequency of $4.3 \cdot 10^5$ Hz and is -56°, gradually decreasing with increasing frequency to -4° at the maximum frequency of electric current.

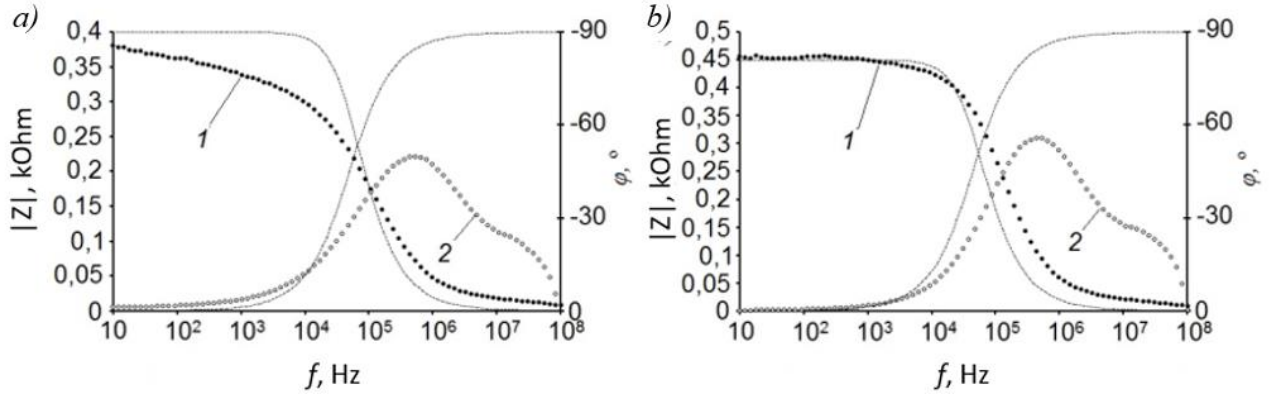

Figure 3. Typical frequency dependences of impedance modulus |Z|(1) (●) and φ phase angle (2) (○), T = 1550 °C: a) (P.2) BeO + 29,5 %$TiO_2^{\mu m}$ + 0,5 %TiO_2^{nano}; b) (P.4) BeO + 28,5 % $TiO_2^{\mu m}$ + 1,5 % TiO_2^{nano}.

The effective component of specific conductivity of serial ceramics (P.0) at low frequencies (up to 10^4 Hz) remains at the level of $2.4 \cdot 10^{-4}$ $Ohm^{-1}m^{-1}$, with further increase in frequency conductivity jumps to the value 0.15 $Ohm^{-1}m^{-1}$ (Fig. 4).

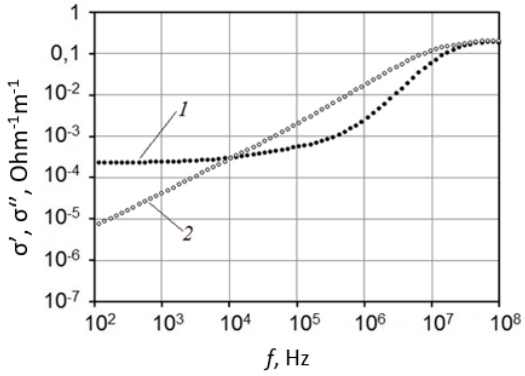

Figure 4. Frequency dependence of actual σ' (1) and imaginary σ' (2) components of specific conductivity of serial ceramics (P.0) of BeO + 30 %$TiO_2^{\mu m}$, T = 1530 °C

Here, the imaginary component of the specific conductivity increases linearly over the entire investigated frequency range, which corresponds to the real component at frequencies above $3 \cdot 10^7$ Hz.

By increasing the sintering temperature to 1550 °C (Fig. 5), the conductivity curves depending on the content of TiO_2 nanoparticles are parallel to each other in the frequency range from 10 to 10^5 Hz. The minimum conductivity value at this site is $\sigma'(1.0\ \%) = 5.5 \cdot 10^{-3}$, the maximum $\sigma'(0.1\ \%) = 4.8 \cdot 10^{-2}$ $Ohm^{-1}m^{-1}$. With increase of frequency of electric field the specific conductivity on all samples sharply increases, at the maximum frequency of 10^8 Hz conductivity curves practically coincide, here maximum value σ'(0,5 %) = 1,36 $Ohm^{-1}m^{-1}$.

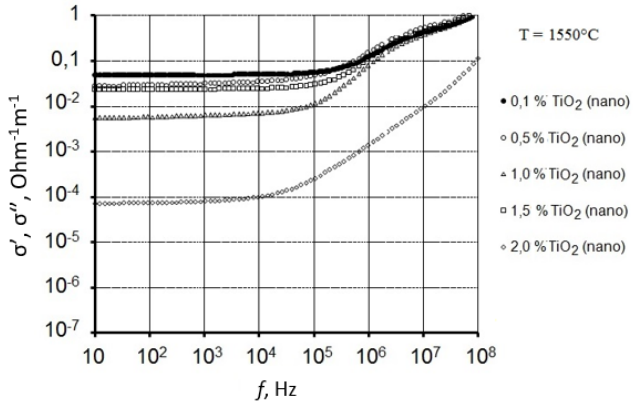

Figure 5. Frequency dependence of actual σ' component of specific conductivity as a function of TiO_2 nanoparticles content, T = 1550 °C (P.1 — P.5)

The sintering temperature, which provides stable high conductivity in the range of electric field frequencies from 10 to 10^8 Hz, is 1530 — 1550 °C. The conductivity mechanism can be explained by the fact that during sintering of ceramics the TiO_2 nanoparticles are pushed to the surface of micron granules (i.e., to the intercrystalline interlayers). Thus, the frequency dependence of the specific conductivity depending on the nanoparticle content observed in Figure 5 can be explained by the fact that the conductivity follows a random grid of interlayers between the crystals, as shown in Figure 8a. Some layers of neighboring crystals may not interact, hence the finite resistance and jumping mechanism of conductivity from one layer to another (between the layers) appear. As the concentration of titanium dioxide nanoparticles increases up to 2.0 %, they begin to adhere to each other or to titanium oxide microparticles inside the crystal and do not go into the intergranular layers, so that the material becomes a dielectric.

Figure 6 shows the curves of change in the values of the real and imaginary components of dielectric permittivity, the tangent of the angle of dielectric losses depending on the frequency of electric current in a sample of serial ceramics (P.0).

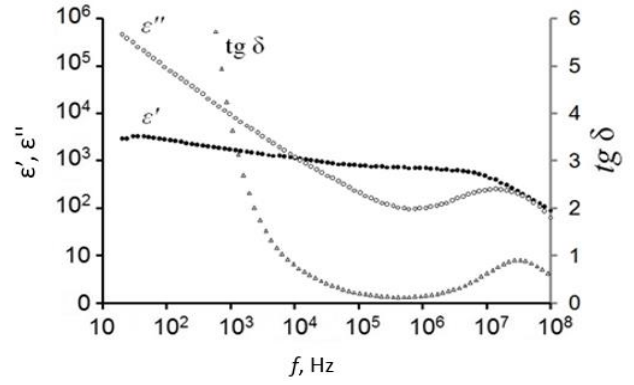

Figure 6. Variation curves of values of the actual and imaginary components of dielectric permittivity, dissipation factor for the factory sample composition: BeO + 30 % $TiO_2^{\mu m}$, T = 1530 °C (P.0)

For this sample at low frequencies both components of dielectric permittivity have anomalously high values. With increasing frequency of electric field, we observe uniform fall of values ε' and ε". For ε' after 10^7 Hz there is a sharper drop to ~ 80 at 10^8 Hz. The imaginary component ε" decreases more rapidly with increasing frequency, at $8 \cdot 10^5$ Hz there is some rise and again a drop of value ε" ~ 40 at maximum frequency.

Tangent of dielectric loss angle also has anomalously high values at low frequencies and sharply decreases with frequency increase. At frequency 10^4 Hz tgδ = 1,0, the minimum value of tgδ = 0,1 is observed at frequency $9 \cdot 10^5$ Hz, which increases with frequency and has a peak tgδ = 1,0 at frequency $5{,}5 \cdot 10^7$ Hz. At the 10^8 Hz maximum frequency tgδ = 0.63.

The maximum dielectric losses are observed in the sample of nanocomposite ceramics sintered at 1550 °C (Fig. 7).

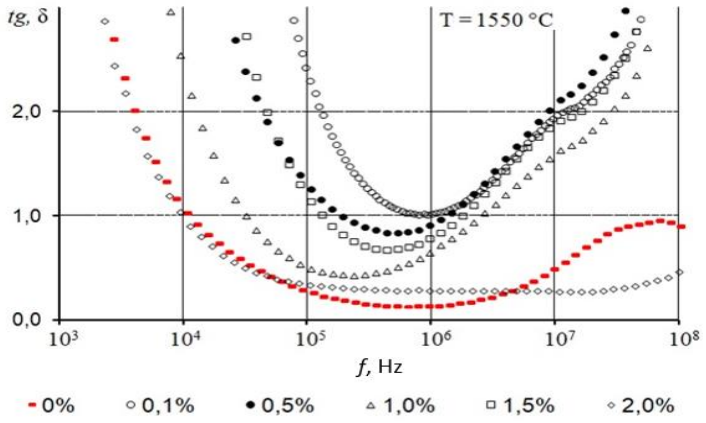

Figure 7. Frequency dependence of the dissipation factor on the content of TiO_2 nanoparticles, T = 1550 °C (P.1 — P.5)

Thus, increasing the sintering temperature of ceramics containing nanoparticles in the range (0.1-1.5) wt % leads to an increase in conductivity, dielectric permittivity, and, most importantly, the tangent of the dielectric loss angle increases.

The increase in dielectric losses observed in Figure 7 can be explained by the fact that the nanoparticles in the investigated ceramics are located on the crystal surface, where the charges can also shift to the opposite crystal boundaries, which leads to the appearance of intracluster current. Such displacement of charges can be accompanied by appearance of additional ceramic polarizability in its volume and growth of dielectric permittivity mainly in the region of low frequencies. But as the electric field frequency increases, the charges do not have time to shift to the cluster boundary, they lag behind the external field in phase, which is the cause of dielectric losses.

The mechanism of electrical conductivity of such ceramics can be explained in terms of a composite material in which the dielectric does not participate in current transfer after the p_c percolation threshold [21]. Percolation theory, from Latin percolatio is a mathematical theory that is used in physics to study processes occurring in heterogeneous media with random properties, but fixed in space and unchanged in time. Thus, it means that, under any conditions, the electrical conductivity of the filler is much higher than that of the matrix and no interfacial layers with other properties are formed in such a composite. When the concentration p of the filler increases (in our case it is TiO_2), the effective conductivity increases according to:

$$\sigma(p) = \sigma_1(p - p_c)^t, \quad (1)$$

where t is the critical conductivity index; σ_1 is the specific conductivity of the dispersed conductive phase. This formula is applicable to describe the electrical conductivity of the system after the percolation threshold $p \geq pc$. The following complementary laws of degrees can be introduced into formula (1):

$$\sigma(p_c) = \sigma_1 h^s, \text{ at } p \approx p_c; \quad (2)$$

$$\sigma(p) = \sigma_2(p_c - p)^{-q} = \sigma_1 h(p_c - p)^{-q}, \text{ at } p < p_c\ , \quad (3)$$

where s and q are critical indexes, $h = {}^{\sigma_2}/_{\sigma_1}$.

The increase in σ with increasing p by (3) is associated with a gradual increase in the size of metal clusters and the area of dielectric interlayers between neighboring clusters. Immediately in the region of pc the power laws (1) and (3) are disturbed and by (2) pass into each other. If the disperse phase is randomly distributed over the volume, then up to the percolation threshold ($p < pc$) the dielectric matrix interlayers, whose local resistance is much greater than that of the disperse phase particles, participate in charge transfer through the sample. Thus, in the region of the percolation threshold at direct current, dielectric interlayers have the most significant effect on the electrical characteristics of the entire composite.

On alternating current, in addition to the resistance of the matrix interlayers, it is necessary to take into account the capacitances of the "capacitors" formed by the particles (cluster sites) of the electrically conducting phase and the dielectric matrix interlayers.

A schematic representation of such a composite, up to the percolation threshold is shown in Figure 8, a.

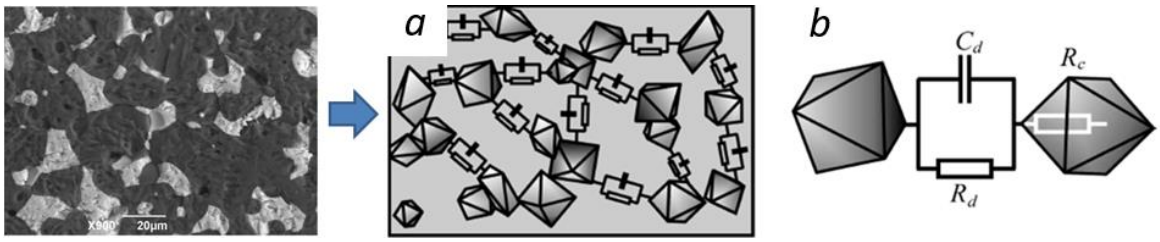

Figure 8. Schematic representation of the composite material structure [21] (in the inset on the left is an electronic image of the microstructure of a ceramic sample of composition P.3): a) up to the flow threshold; b) equivalent substitution scheme

Figure 8, a shows the resistive-capacitive coupling between the clusters and the particles of the electrically conducting phase by parallel RC circuits.

In composites at $p < p_c$ the infinite cluster is not formed and the equivalent circuit of Figure 8 b must contain two resistors connected in series. The first resistor corresponds to the resistance *Rc* of clusters and particles of the electrically conductive phase. The second resistor takes into account the resistance of dielectric matrix interlayers *Rd*, and the resistor *Rd* is shunted by a capacitor *Cd*, the capacity of which corresponds to the capacitance of matrix interlayers.

To analyze the resistive-capacitive properties of the studied substances and to understand the electrophysical processes occurring in them, we used the method of constructing suitable electrical circuits impedance of which agrees with the experiment. For these samples of ceramics using a special program *EISA-analizer* the most suitable equivalent circuits were selected, which are shown in Figure 9 a, b.

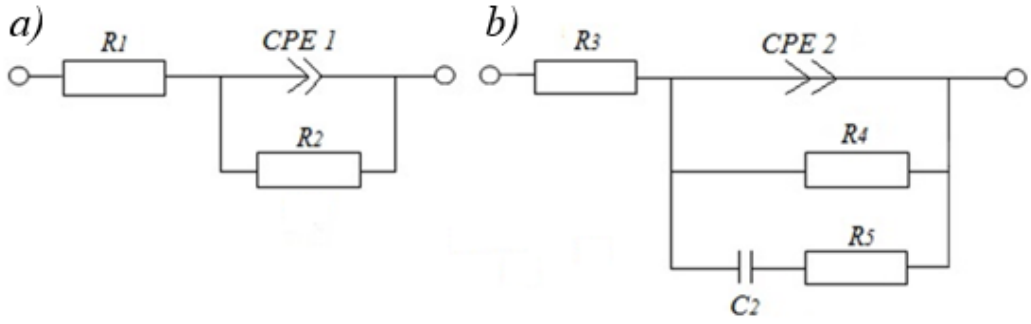

a — sample of composition P.1; b — sample of composition P.0
Figure 9. Equivalent schemes for samples

As can be seen, both circuits contain the usual radio engineering elements R-resistance and C-capacitance. In these circuits there is a linearly dependent parameter, an artificial constant phase element (CPE), which to some extent reflects the electrical properties of a variety of structurally heterogeneous materials. The impedance (Z_{CPE}) of this element is written in the following form:

$$Z_{CPE} = \frac{1}{A(i\omega)^n} = \frac{1}{A\omega^n}\left[\cos\left(\eta\frac{\pi}{2}\right) - i\sin\left(\eta\frac{\pi}{2}\right)\right] \quad (4)$$

where *A* is the numerical multiplier, ω is the circular frequency, *i* is the imaginary unit, and η is the exponent determining the nature of the impedance frequency dependence ($-1 \le \eta \le 1$). The *CPE* element has

both a real and imaginary component. For integer values of η = 1, 0, -1 the *CPE* element degenerates to the usual *C, R, L* elements. Fractional values of the index of degree η < 1 formally characterize the cluster structure of the material.

The simplest electrical circuit for TiO_2 nano-added ceramics Figure 9a contains only three elements: resistance R_1 = 2.9 Ohm, R_2 = 827 Ohm and element CPE_1 with numerical multiplier $A_0 = 5.32 \cdot 10^{-9}$ and exponent close to unity η = 0.92. The smaller number of resistances in the circuit for the nanophase sample, explains the increase in specific conductivity and dielectric losses with increasing frequency of electric current. It can be noted that the resistance R_2 almost coincides in magnitude with the low-frequency impedance of this ceramic |Z| = 830 Ohm and naturally simulates the static resistance of ceramics. Resistance R_1 = 2.9 Ohm in the region of radio frequencies remains virtually unnoticed, but with increasing frequency, when the impedance of the sample decreases, this resistance makes a tangible contribution to the formation of the impedance spectrum. In particular, it is this resistance in the region of high and possibly ultra high frequencies leads to the observed in the impedance spectrum reduction of the phase of the AC current flowing through the sample. The results of numerical approximation of the experimentally measured impedance spectrum of these ceramics with the equivalent circuit are shown in Figure 10a with solid lines. As can be seen the coincidence of the calculation with the experiment is quite satisfactory.

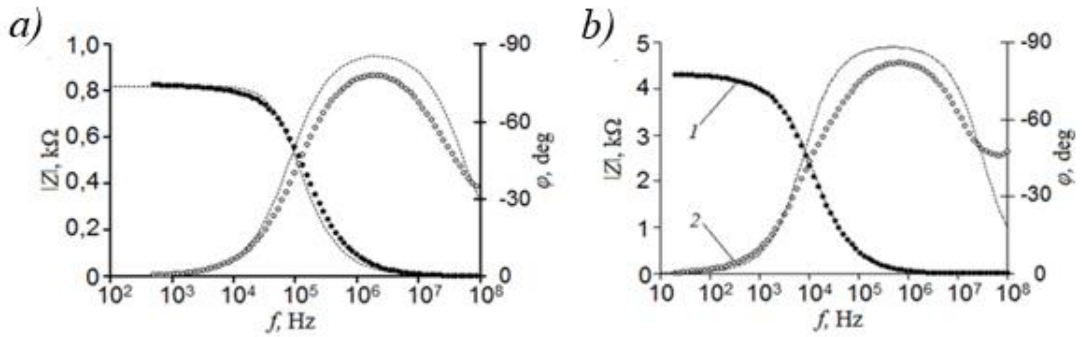

a — sample of composition P.1; b — sample of composition P.0.

Figure 10. Frequency dependences of the impedance modulus Z (1) and phase angle φ (2) (white markers). The results of numerical approximation using the equivalent scheme are shown by solid lines.

For a sample of ceramics with micropowder TiO_2, the frequency dependence of impedance is shown in Figure 10b, and the equivalent circuit is shown in Figure 9 b. As can be seen this scheme is more complex and in addition to the element CPE_2 contains two parallel circuits one of which consists of a resistance $R_4 = 4300$ *Ohm* simulating the static resistance of ceramics. The second circuit is formed by series elements $C_2 = 2{,}9 \cdot 10^{-8}$ *F* and *R5 = 4 Ohm* which form impedance characteristics in the middle frequencies. The CPE_2 element has a numerical multiplier $A_0 = 2.9 \cdot 10^{-8}$ and power factor n = 0.72. This power factor means that the CPE_2 element can be treated as a frequency-dependent capacitance and simultaneously as a frequency-dependent resistance. Resistor R_3, as for the previous sample, serves to simulate high-frequency electrical losses. To simulate impedance in the decimeter and centimeter wavelength range it may be necessary to introduce additional elements. Thus, the different ratio in the ceramic of TiO_2 nanoparticles and the degree of its reduction allow to significantly reduce the static impedance, thereby improving the conductivity and regulating the magnitude of electromagnetic radiation absorption by such ceramics.

Conclusion

Analyzing the experimental results obtained in the work, we can make the following conclusions:

– It is established that the introduction of nanoparticles TiO_2 in an amount (0.5 — 1.5) wt. % in the composition of (BeO + TiO_2)-ceramics significantly reduces its static electrical resistance in comparison with the serial sample. So at high frequencies, ~ 10^7 Hz, resistance decreases three times (from 0.024 to 0.008 kOhm), with the introduction of nano-particles (0.5 — 1.5) mass % and sintering temperature of ceramics 1530 — 1550 °C. The sample made of micropowders at the same frequency has an electrical resistance of 0.036 kOhm.

– It is established that the specific conductivity of ceramics modified by TiO_2 nanoparticles (0.5 — 1.5) mass % at high frequencies ~ 10^7 Hz increases from 0.3 to 1.4 $Ohm^{-1}m^{-1}$ in samples obtained in the tempera-

ture range of sintering ceramics 1530 — 1550 °C. The conductivity of the sample made of micropowders at the same frequency is 0.68 $Ohm^{-1}m^{-1}$. The increase in sintering temperature is associated with the formation of new phases.

– The addition of nanoparticles TiO_2 (0,5 — 1,5) wt. %, in composition of (BeO + TiO_2)-ceramics essentially increases dielectric losses of the sample sintered in the interval of temperatures 1530 — 1550 °C. Values of real and imaginary components of dielectric permittivity of such ceramics $\varepsilon' = 58$ — 120, $\varepsilon'' = 52$ — 314. For the sample made of micropowders at the same frequency $\varepsilon' = 60$, $\varepsilon'' = 40$. The tangent angle of dielectric losses in nanocomposite ceramics is twice as high.

– It is shown that the ceramic samples have electrical conductivity, which increases in proportion to the angular frequency with a fractional index of degree. This allowed us to identify the conductivity of the sample with microparticles as a jump-type conductivity. In the sample with TiO_2 nanoparticles the conductivity dispersion is not detected, and the observed in the experiment non-monotone growth of conductivity with increasing frequency is explained by the appearance of the current relaxation component accompanied by an increase in dielectric losses.

Acknowledgments

This research was funded by the Science Committee of the Ministry of Education and Science of the Republic of Kazakhstan (Grant No. AP09058686).

References

1 Бухарин Е.Н. Объемные поглотители СВЧ-энергии в конструкциях современных электровакуумных СВЧ-приборов и измерительных устройств / Е.Н. Бухарин, Е.Н. Ильина // Радиотехника. — 2014. — Т. 15. — № 11. — С. 57–64.

2 Lu G. Dielectric and microwave absorption properties of KNN/Al2O3 composite ceramics / G.Lu, Z. Wancheng, L.Fa, Z. Dongmei, W. Jie // Ceramics International. — 2017. — V. 43. — Is. 15. — P. 12731-12735.

3 Belyaev B.A. Study of electrophysical properties of cation-substitution ceramic of barium hexa-aluminate by impedance spectroscopy / B.A. Belyaev, N.A. Drokin, V.A. Poluboyarinov // FTT. — 2018. — Vol. 60(2). — P. 266-275.

4 Kiiko V.S. Ceramics Based on Beryllium Oxide: Preparation, Physicochemical Properties, and Application / V.S. Kiiko, Yu.N. Makurin, A.L. Ivanovskii // UrO RAN, Ekaterinburg. — 2006.

5 Дрокин Н.А. Электрофизические свойства керамики БТ–30 / Н.А. Дрокин, В.С. Кийко, А.В. Павлов, А.И. Малкин // Новые огнеупоры. — 2020. — № 6. — С. 56–63.

6 Щербина А. Изделия из керамики на основе оксида алюминия, нитрида алюминия и оксида бериллия производства АО «Тестприбор» ООО «Медиа КиТ», Санкт-Петербург / А. Щербина, Л. Федорович // Силовая электроника. — 2019. — № 4. — С. 68–70.

7 Беляев Р.А. Окись бериллия / Р.А. Беляев // Атомиздат. — 1980. — С. 221.

8 Вайспапир В.Я. Бериллиевая керамика для современных областей техники / В.Я. Вайспапир, В.С. Кийко // Вестн. воздушно-космической обороны. — 2018. — № 1 (17). — С. 59–69.

9 Zdorovets V. Study of change in beryllium oxide strength properties as a result of irradiation with heavy ions / V. Zdorovets, A.L. Kozlovskiy, D.B. Borgekov, D.I. Shlimas // Eurasian Journal of Physics and Functional Materials. — 2021. — Vol. 5(3). — P. 192-199.

10 Akishin G.P. Thermal conductivity of beryllium oxide ceramic / G.P. Akishin, S.K. Turnaev, V.Ya. Vaispapir, M.A. Gorbunova, Yu.N. Makurin, V.S. Kiiko, A.L. Ivanovskii. // Refractories and Industrial Ceramics. — 2009. — Vol. 5050. — P. 465-468.

11 Kiiko V.S. Fabrication, physicochemical properties, and transmission of microwave radiation by BeO-based ceramics / V.S. Kiiko, S.N. Shabunin, Yu.N. Makurin // Ogneup. Tekh. Keram. — 2004. — No. 10. — P. 8-17.

12 Kiiko V.S. Transparent beryllia ceramics for laser technology and ionizing radiation dosimetry / V.S. Kiiko // Refractories and Industrial Ceramics. — 2004. — Vol. 45, No 4. — P. 266-272.

13 Акишин Г.П. Свойства оксидной бериллиевой керамики / Г.П. Акишин, С.К. Турнаев, В.Я. Вайспапир [и др.] // Новые огнеупоры. — 2010. — № 10. — С. 42–47.

14 Кийко В.С. Теплопроводность и перспективы применения BeO-керамики в электронной технике / В.С. Кийко, В.Я. Вайспапир // Стекло и керамика. — 2014. — № 11. — С. 12–16.

15 Ивановский А.Л. Электронная структура и свойства оксида бериллия / А.Л. Ивановский, И.Р. Шеин, Ю.Н. Макурин, В.С. Кийко, М.А. Горбунова // Неорганические материалы. — 2009. — Т. 45, № 3. — С. 263–275.

16 Drokin N.A. BT-30 ceramic electrophysical properties / N.A. Drokin, V.S. Kiiko, A.V. Pavlov, A.I. Malkin // Refractories and Industrial Ceramics. — 2020. — Vol. 61, No. 3. — P. 341-348.

17 Лепешев А.А. Особенности получения и исследование электрофизических характеристик (BeO+TiO_2)-керамики методом импедансной спектроскопии // А.А. Лепешев, А.В. Павлов, Н.А. Дрокин, А.И. Малкин, В.С. Кийко // Новые огнеупоры. — 2019. — № 6. — С. 55–63.

18 Кийко В.С. Керамика на основе оксида бериллия: получение, физико-химические свойства и применение //В.С. Кийко, Ю.Н. Макурин, А.Л. Ивановский // Екатеринбург: УрО РАН, 2006. — С. 440.

19 Кийко В.С. Микроструктура и электропроводность композиционной (BeO+TiO_2)-керамики // В.С. Кийко, М.А.Горбунова, Ю.Н. Макурин // Новые огнеупоры. — 2007. — № 11. — С. 68–74.

20 Кийко В.С. Влияние добавок диоксида титана на физико-химические и люминесцентные свойства бериллиевой керамики / В.С. Кийко // Неорганические материалы. — 1994. — Т. 30, № 5. — С. 688–693.

21 Поклонский Н.А. Основы импедансной спектроскопии композитов: курс лекций / Н.А. Поклонский, Н.И. Горбачук. — Минск: Белорус. гос. ун-т, 2005. — С. 83–90.

А.В. Павлов, А.М. Жилкашинова, С.С. Герт, Н.М. Магазов, Ж.С. Тұрар, А.Б. Набиолдина

Титан диоксиді микро және нанобөлшектері қосылған бериллий керамикасының электрофизикалық қасиеттерін зерттеу

Мақалада микроұнтақтардан жасалған оксид-бериллий керамикасының (BeO + TiO_2) электрофизикалық қасиеттеріне 0,1-2,0 масс% аралығындағы TiO_2 наноөлшемді бөлшектердің қоспаларының әсерін зерттеу нәтижелері келтірілген. Толық кешенді кедергі (импеданс) әдісімен 30 масс% мөлшерінде TiO_2 микро және нанобөлшектерімен модификацияланған синтезделген керамиканың 100 Гц — 100 МГц электр тогының жиілік диапазонында электрофизикалық сипаттамалары зерттелді. Тотықсыздану атмосферасында термиялық өңдеуден кейін TiO_2 қоспасын BeO-керамикаға енгізу электр өткізгіштігінің айтарлықтай жоғарылауымен және жиіліктің кең диапазонында электромагниттік сәулеленуді сіңіру қабілетімен бірге жүретіні белгілі. Зерттеу нәтижелері бойынша TiO_2 нанобөлшектерінің (BeO + TiO_2)-керамикасына енгізу оның статикалық электр кедергісін сериялық үлгімен салыстырғанда едәуір төмендететіні анықталды, ал мұндай керамиканың нақты өткізгіштігі ~ 10^7 Гц жоғары жиілікте айтарлықтай артады. TiO_2 нанобөлшектерін енгізу 1530—1550 °С температура аралығында агломерацияланған үлгінің диэлектрлік шығынын едәуір арттырады. Мұндай керамиканың диэлектрлік өткізгіштігінің нақты және жорамал компоненттерінің мәні және диэлектрлік жоғалту бұрышының тангенсі БТ-30 (Б-бериллий, Т-титан) сериялық үлгімен салыстырғанда екі есе жоғары. Зерттеу нәтижелері сирек кездесетін және стратегиялық маңызды материалмен — бериллий оксидімен және оның негізінде жаңа нанокұрылымдарды синтездеу мүмкіндігімен эксперименттеуге байланысты болып табылады.

Кілт сөздер: диэлектрлік өткізгіштік, өткізгіштік, электр тогының жиілігі, кедергі, нанобөлшектер, бериллий оксиді, титан диоксиді.

А.В. Павлов, А.М. Жилкашинова, С.С. Герт, Н.М. Магазов, Ж.С. Тұрар, А.Б. Набиолдина

Исследование электрофизических свойств бериллиевой керамики с добавкой микро- и наночастиц диоксида титана

В статье представлены результаты исследования влияния добавок наноразмерных частиц TiO_2 в интервале 0,1–2,0 масс. % на электрофизические свойства оксидно-бериллиевой керамики состава (BeO+TiO_2), изготовленной из микропорошков. Методом полного комплексного сопротивления (импеданса) исследованы электрофизические характеристики синтезированной керамики, модифицированной микро- и наночастицами TiO_2 в количестве 30 масс. % в диапазоне частот электрического тока 100 Гц–100 МГц. Известно, что введение в BeO-керамику добавки TiO_2 после термообработки в восстановительной атмосфере сопровождается значительным увеличением электропроводности и способностью поглощать электромагнитное излучение в широком диапазоне частот. По результатам исследований установлено, что введение в состав (BeO+TiO_2)-керамики наночастиц TiO_2 значительно снижает ее статическое электросопротивление по сравнению с серийным образцом, а удельная проводимость такой керамики значительно возрастает на высоких частотах ~ 10^7 Гц. Добавка наночастиц TiO_2 существенно увеличивает диэлектрические потери образца, спеченного в интервале температур 1530–1550 °С. Значения действительной и мнимой компоненты диэлектрической проницаемости такой керамики и тангенс угла диэлектрических потерь выше в два раза в сравнении с серийным образцом БТ–30 (Б — бериллий, Т — титан). Полученные результаты исследований являются уникальными в своем роде, что обусловлено экспериментом с редким и стратегически важным материалом — оксидом бериллия и возможностью синтеза новых наноструктур на его основе.

Ключевые слова: диэлектрическая проницаемость, проводимость, частота электрического тока, импеданс, наночастицы, оксид бериллия, диоксид титана.

References

1 Bukharin, E.N., & Ilina, E.N. (2014). Obemnye poglotiteli SVCh-energii v konstruktsiiakh sovremennykh elektrovakuumnykh SVCh-priborov i izmeritelnykh ustroistv [Volumetric absorbers of microwave energy in the designs of modern electrovacuum microwave devices and measuring devices]. *Radiotekhnika – Radio engineering* 15(11), 57–64 [in Russian].

2 Lu, G., Wancheng, Z., Fa, L., Dongmei, Z., & Jie, W. (2017). Dielectric and microwave absorption properties of KNN/Al2O3 composite ceramics. *Ceramics International*, *43*(15), 12731-12735.

3 Belyaev, B.A. Drokin, N.A., & Poluboyarinov, V.A. (2018). Study of electrophysical properties of cation-substitution ceramic of barium hexa-aluminate by impedance spectroscopy. *FTT*, *60*(2), 266-275.

4 Kiiko, V.S. Makurin, Yu.N., Ivanovskii, A.L. (2006). Ceramics Based on Beryllium Oxide: Preparation, Physicochemical Properties, and Application. *UrO RAN*, Ekaterinburg.

5 Drokin, N.A., Kiiko, V.S., Pavlov, A.V., & Malkin, A.I. (2020). Elektrofizicheskie svoistva keramiki BT–30 [Electrophysical properties of BT-30 ceramics]. *Novye ogneupory — New refractories*, *6*, 56–63 [in Russian].

6 Sherbina, A. & Fedorovich, L. (2019). Izdeliia iz keramiki na osnove oksida aliuminiia, nitrida aliuminiia i oksida berilliia proizvodstva AO «Testpribor» [Ceramic products based on aluminum oxide, aluminum nitride and beryllium oxide produced by "Testpribor" JSC]. LLC «Media KiT». *Silovaia elektronika — Power electronics*, *4*, 68-70. Saint Petersburg [in Russian].

7 Belyaev, R.A. (1980). Okis berilliia [Beryllium oxide]. *Atomizdat*, 221 [in Russian].

8 Vaispapir, V.Ya. & Kiiko, V.S. (2018). Berillievaia keramika dlia sovremennykh oblastei tekhniki [Beryllium ceramics for modern engineering fields]. *Vestnik vozdushno-kosmicheskoi oborony — Bulletin of aerospace defense*, *1*(17), 59–69 [in Russian].

9 Zdorovets, V., Kozlovskiy, A.L., Borgekov, D.B., & Shlimas, D.I. (2021). Study of change in beryllium oxide strength properties as a result of irradiation with heavy ions. *Eurasian Journal of Physics and Functional Materials*, *5*(3), 192-199.

10 Akishin, G.P., Turnaev, S.K., Vaispapir, V.Ya., Gorbunova, M.A., Makurin, Yu.N., Kiiko, V.S., & Ivanovskii, A.L. (2009). Thermal conductivity of beryllium oxide ceramic. *Refractories and Industrial Ceramics*, *5050*, 465-468.

11 Kiiko, V.S., Shabunin, S.N., & Makurin, Yu.N. (2004). Fabrication, physicochemical properties, and transmission of microwave radiation by BeO-based ceramics. *Ogneup. Tekh. Keram*, *10*, 8-17.

12 Kiiko, V.S. (2004). Transparent beryllia ceramics for laser technology and ionizing radiation dosimetry. *Refractories and Industrial Ceramics*, *45*(4), 266-272.

13 Akishin, G.P., Turnaev, S.K., & Vaispapir, V.Ya. (2010). Svoistva oksidnoi berillievoi keramiki [Properties of oxide beryllium ceramics]. *Novye ogneupory — New refractories*, *10*, 42–47 [in Russian].

14 Kiiko, V.S., & Vaispapir, V.Ya. (2014). Teploprovodnost i perspektivy primeneniia BeO-keramiki v elektronnoi tekhnike [Thermal conductivity and prospects of application of BeO-ceramics in electronic engineering]. *Steklo i keramika — Glass and ceramics*, *11*, 12–16 [in Russian].

15 Ivanovskii A.L., Shein, I.R., Makurin, Yu.N., Kiiko, V.S., & Gorbunova, M.A. (2009). Elektronnaia struktura i svoistva oksida berilliia [Electronic structure and properties of beryllium oxide]. *Neorganicheskie materialy — Inorganic materials*, *45*(3), 263–275 [in Russian].

16 Drokin, N.A., Kiiko, V.S., Pavlov, A.V., & Malkin, A.I. (2020). BT-30 ceramic electrophysical properties. *Refractories and Industrial Ceramics*, *61*(3), 341-348.

17 Lepeshev, A.A., Pavlov, A.V., Drokin, N.A., Malkin, A.I., & Kiiko, V.S. (2019). Osobennosti polucheniia i issledovanie elektrofizicheskikh kharakteristik (BeO+TiO_2)-keramiki metodom impedansnoi spektroskopii [Peculiarities of obtaining and investigation of electrophysical characteristics of (BeO + TiO_2)-ceramics by impedance spectroscopy]. *Novye ogneupory — New refractories*, *6*, 55–63 [in Russian].

18 Kiiko, V.S., Makurin, Yu.N., & Ivanovskii, A.L. (2006). Keramika na osnove oksida berilliia: poluchenie, fiziko-khimicheskie svoistva i primenenie [Ceramics based on beryllium oxide: preparation, physical and chemical properties and application]. *Ekaterinburg: UrO RAN*, 440 [in Russian].

19 Kiiko, V.S., Gorbunova, M.A., & Makurin, Yu.N. (2007). Mikrostruktura i elektroprovodnost kompozitsionnoi (BeO+TiO_2)-keramiki [Microstructure and electrical conductivity of composite (BeO + TiO_2)-ceramics]. *Novye ogneupory — New refractories*, *11*, 68–74 [in Russian].

20 Kiiko, V.S. (1994). Vliianie dobavok dioksida titana na fiziko-khimicheskie i liuminestsentnye svoistva berillievoi keramiki [Influence of additives of titanium dioxide on physico-chemical and luminescent properties of beryllium ceramics]. *Neorganicheskie materialy — Inorganic Materials*, *5*, 30, 688–693 [in Russian].

21 Poklonskii, N.A., & Gorbachuk, N.I. (2005). Osnovy impedansnoi spektroskopii kompozitov: kurs lektsii [Fundamentals of impedance spectroscopy of composites: a course of lectures]. *Minsk: Belorusskii gosudarstvennyi universitet*, 83–90 [in Russian].

DOI 10.31489/2023PH2/17-24

UDC: 535.215; 539.23; 535.3; 535.3; 538.9

G.I. Omarbekova[1*], A.K. Aimukhanov[2], B.R. Ilyassov[3], A.M. Alexeev[4] A.K. Zeinidenov[5], A.M. Zhakanova[6]

[1,2,5,6] Karaganda University of the name of academician E. A. Buketov, Karaganda, Kazakhstan;
[3] Astana IT University, Astana, Kazakhstan;
[4] Kazan Federal University, Kazan, Russia
([*]E-mail:gulnur_130983@mail.ru)

Effect of the thickness and surface interface of In_2O_3 films on the transport and recombination of charges in a polymer solar cell

Indium oxide films were obtained by spin coating from a solution of indium nitrate in ethylene glycol followed by annealing at 300 °C. The influence of the thickness and surface interface of In_2O_3 films on the optical and photo-electrophysical properties of a polymer solar cell has been studied. It is shown that the surface roughness of the film gradually decreases with a decrease in the thickness of the film to 60 nm, and a further decrease in the thickness of the films leads to its increase. The absorption spectra of the films were measured. The values of the optical band gap width are determined. It was found that with a decrease in the thickness of the films, the width of the forbidden zone (Eg) also decreases. It was found that the parameters of the current-voltage characteristics (VAC) and electrophysical measurements also depend on the thickness and interface of the surface of the In_2O_3 films. It was found that with an In_2O_3 film thickness equal to 60 nm, a maximum efficiency value of 3.42 % is observed, at the same time, electrons in the photoactive layer have a maximum charge carrier lifetime and a low recombination rate.

Keywords: In_2O_3 films, polymer solar cell, current-voltage characteristics, impedance spectra.

Introduction

The conversion of solar energy into electrical energy is one of the ways that in the near future can provide a rapidly growing demand for clean energy. Among the currently existing various photovoltaic converters, organic solar cells are of great interest among various international scientific groups [1-3]. In an organic solar cell, to minimize charge recombination at both interfaces and increase the efficiency of charge extraction, a photoactive layer is placed between the electron transfer layer (ETL) and the hole transfer layer (HTL). The ETL layer in OSC plays an important role in performance. The ETL layer can not only affect the efficiency of electron extraction and charge recombination, but also has an effect on the morphology of the photoactive layer. The ETL layer based on metal oxides has attracted huge attention due to its high transparency in the visible spectral region [4, 5].

Among the known metal oxides, indium oxide (In_2O_3) is the most commonly used for organic solar cells. Indium oxide (In_2O_3) is a transparent semiconductor that has a wide band gap of ~ 3.7 eV, high transparency for visible light and chemical stability [6, 7]. In_2O_3 films are produced by various physical and chemical methods. The most common method is sol gel technology, which is characterized by versatility, cheapness and simplicity. However, there are almost no studies on the effect of the technology of obtaining on the effectiveness of OSC.

This paper presents the results of a study of the technology for obtaining an ETL layer based on In_2O_3 on the effectiveness of an OSC with an inverted structure.

Experimental

To obtain indium oxide films on the FTO surface (the FTO substrates were successively washed with ultrasound in detergent, deionized water and ethanol, then dried in air), a solution was prepared in accordance with the procedure described in our other work [8]. To obtain In_2O_3 films, the resulting solution was applied to the FTO surface by spin-coating (SPIN150i model, Semiconductor Production System) at rotational speeds of 1500 — 5000 rpm. After that, the films were annealed in an air atmosphere at a temperature of 300 °C for an hour and gradually cooled to room temperature.

To obtain organic solar cells, a photoactive layer was applied to the surface of the In_2O_3 film by the method shown in article [9], then an HTL layer of PEDOT: PSS (d~30 nm) was applied to the surface by

spin-coating (3000 rpm) and by thermal deposition at the CY-1700x-spc-2 installation (Zhengzhou CY Scientific Instruments Co., Ltd) sprayed a current-removing electrode (Ag, d~120 nm).

Morphological and topological studies of the surface were carried out using the atomic force microscope (AFM) JSPM-5400 (JEOL, Japan). A special modular scanning probe microscopy data analysis program (Win SPMII Data-Processing Software) was used to process the images obtained on the AFM. Optical absorption spectra are recorded in the range of 200-800 nm using the AvaSpec-ULS2048CL-EVO spectrophotometer (Avantes). The impedance spectra were measured using a potentiostat-galvanostat P45X in the impedance mode. The VAC of photosensitive cells was determined by the Sol3A Class AAA Solar Simulators (Newport) with PVIV-1A I-V Test Station device.

Results and Discussion

The thickness of the In_2O_3 layer was determined by SEM images of the transverse cleavage of the film. Figure 1 shows SEM images of the transverse cleavage of the studied films. The average thickness of the In_2O_3 films depends on the rotation speed of the substrate on the centrifuge. With an increase in the speed of rotation of the substrate, a decrease in the thickness of the film is observed (Figure 1).

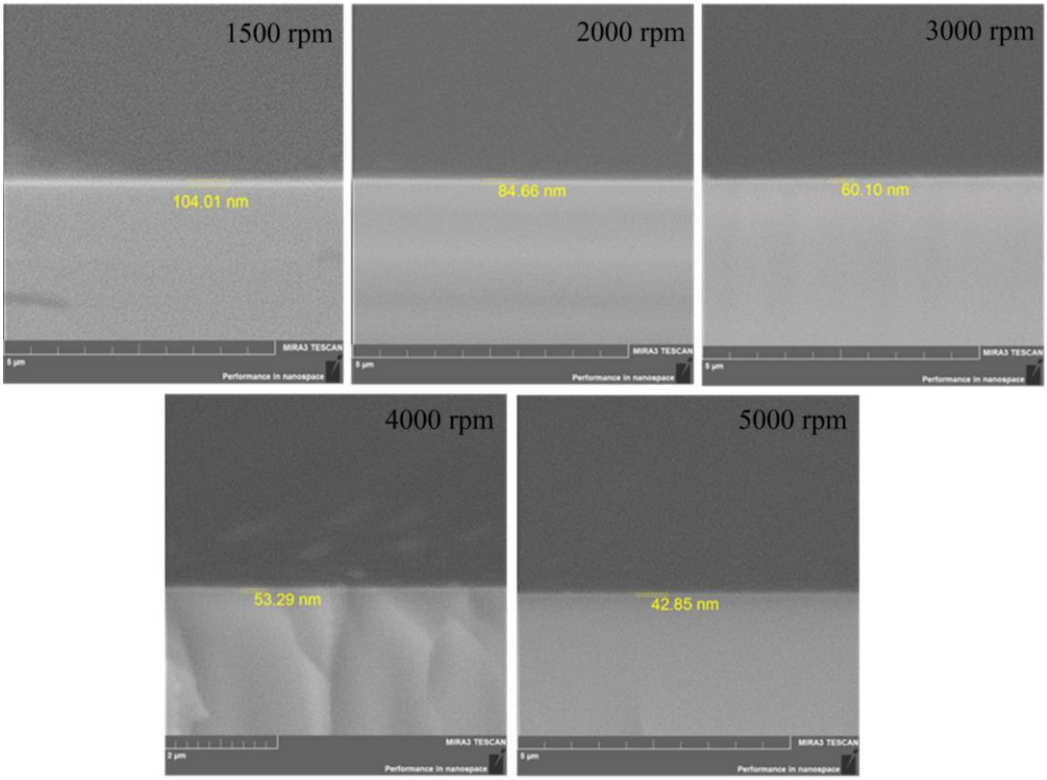

Figure 1. SEM images of transverse cleavage of In_2O_3 films.

Figure 2 shows AFM images of the surface of the studied In_2O_3 films obtained by centrifugation. It can be seen from the AFM data that the thickness of the film affects the morphology of the surface of the In_2O_3 films. The surface roughness of the films is determined by the formula:

$$R_q = \sqrt{\frac{1}{N}\sum_{j=1}^{N} r_j^2}.$$

Where, R_q represents the root-mean-square roughness, i.e. the average value of the measured height deviations taken within the length of the estimate and the measurement from the median line. According to the AFM data, it can be seen that the surface roughness of the studied In_2O_3 films has a non-unambiguous dependence on the thickness.

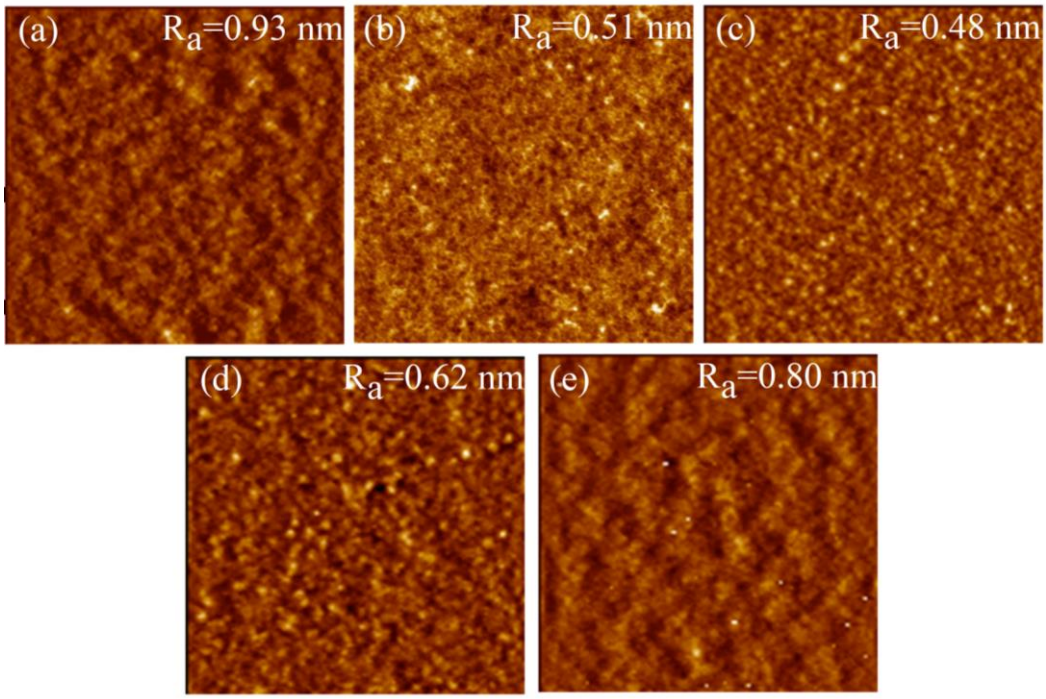

a) 1500 rpm; b) 2000 rpm; c) 3000 rpm; d) 4000 rpm; e) 5000 rpm.
Figure 2. Images of the morphology of the surface of In_2O_3 films

Thus, the roughness of the films decreases to 0.48 nm with a decrease in the film thickness to 60 ± 5 nm. However, a further decrease in the thickness of the films leads to an increase in the roughness of the In_2O_3 films. The dependence of the roughness of In_2O_3 films on the thickness is shown in Figure 3.

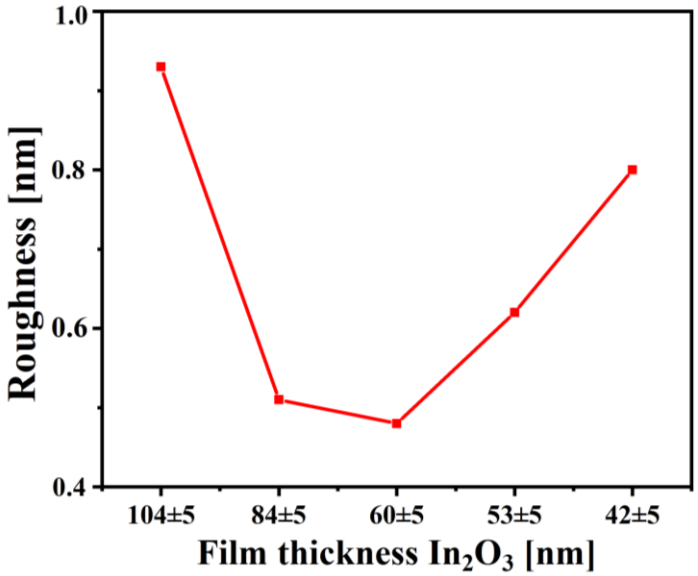

Figure 3. Dependence of the roughness of In_2O_3 films on the thickness

It is known that the morphology of the surface of thin films during growth is determined by two parameters: energy and kinetic. The energy factor is determined by the excess surface energy of the growing film, and the kinetic factor is determined by the diffusion mobility of the atoms of the deposited substance, which depends on temperature. The ratio of these parameters determines the roughness of the deposited film [10]. The observed ambiguous dependence of roughness on the thickness of the In_2O_3 film is related to the dependence of the boiling point and viscosity of the rasterizer used for the preparation of films.

Absorption spectra were measured to determine the effect of film thickness on optical characteristics (Fig. 4). The parameters of the absorption spectra of In_2O_3 films at different thicknesses are given in Table 1. The absorption spectrum is typical of the absorption spectrum of wide-band semiconductors such as TiO2, ZnO, SnO2, etc. The edge of the fundamental absorption band falls at 212 nm, which corresponds to the optical transition of the In_2O_3 band gap. Measurement of absorption spectra showed that the absorption of films decreases with a simultaneous decrease in thickness (Fig. 4). At the same time, the thickness of the films does not affect the shape of the absorption spectrum [11].

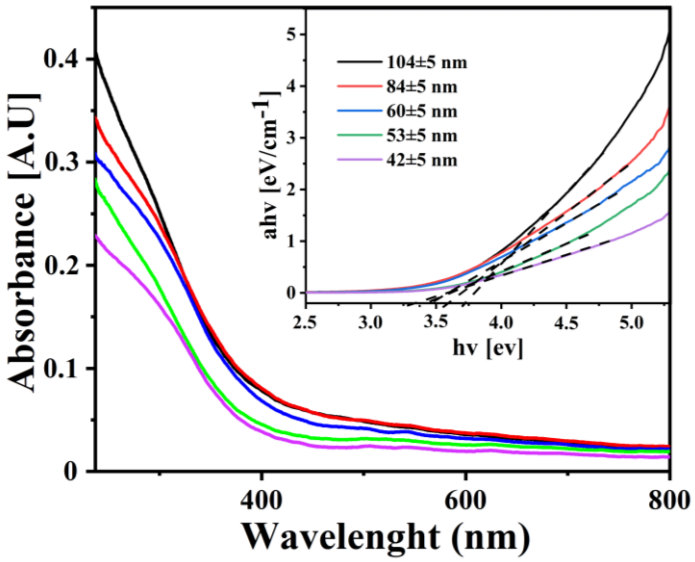

Figure 4. Optical characteristics of In_2O_3 films

The optical band gap width of In_2O_3 films was estimated by the Tauc ratio [12]. The change in the width of the Eg band gap depending on the thickness of the In_2O_3 films is shown in Figure 4. The 104 nm thick film has the highest band gap of 3.71 eV, with a decrease in the thickness of the films, the width of the Eg band gap also decreases to 3.34 eV (Table 1). The observed decrease in the optical width of the band gap with a decrease in thickness is due to the presence of surface defects in the film, the concentration of which increases with a decrease in thickness.

Table 1

Parameters of optical absorption spectra of In_2O_3 films

№	Film thickness In_2O_3, nm	D, A.U.	Bandgap, eV
1	104±5	0.40	3.71
2	84±5	0.33	3.59
3	60±5	0.30	3.44
4	53±5	0.27	3.40
5	42±5	0.22	3.34

To determine the effect of the thickness of In_2O_3 films on the transport and recombination of charges in a polymer solar cell, an In_2O_3/P3HT: ICMA/PEDOT: PSS/Ag cell was assembled. Upon photoexcitation of the photoactive OSC layer, an electron-hole pair is formed, which then decays into free electrons and holes at the interface In_2O_3/ P3HT: ICMA and P3HT: ICMA/PEDOT: PSS. The electrons are injected into the ETL layer In_2O_3, and the hole into the HTL layer PEDOT: PSS.

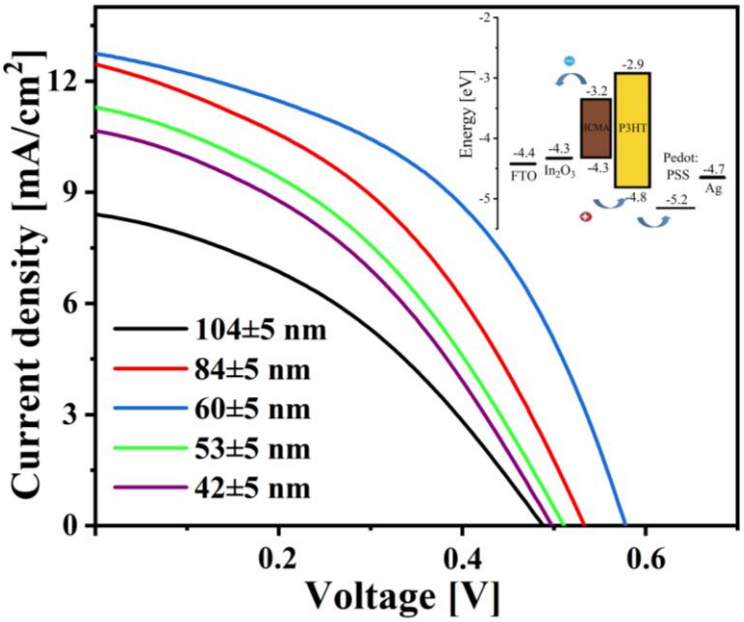

Figure 5. Current-voltage characteristic of a polymer solar cells In_2O_3/P3HT: ICMA/ PEDOT: PSS/Ag

The current-voltage characteristics of solar cells at different values of In_2O_3 thickness are shown in Figure 5. Table 2 shows the photovoltaic parameters of the OSCs. As can be seen from Figure 5 and Table 2, the VAC parameters depend on the thickness of the In_2O_3 films. Thus, when the thickness of the In_2O_3 film decreases to 60 nm, the efficiency of OSCs increases to 3.42 %. However, further reduction of the film thickness to 42 nm leads to a decrease in the values of current, FF, voltage and efficiency of OSCs.

Table 2

Parameters of the VAC solar cells

Film thickness In_2O_3, nm	V_{oc} (V)	J_{sc}(mA/cm^2)	V_{max}(V)	J_{max}(mA/cm^2)	FF	PCE %
104±5	0.49	8.38	0.3	5.25	0.38	1.58
84±5	0.53	12.41	0.34	7.91	0.41	2.69
60±5	0.58	12.74	0.39	8.78	0.46	3.42
53±5	0.51	11.25	0.32	7.04	0.39	2.25
42±5	0.5	10.67	0.31	6.68	0.39	2.07

The observed changes in the VAC are due to the effect of the surface interface of indium oxide films with a decrease in thickness on the transfer of charge carriers to OSCs. For a detailed study of the detailed study of this issue, the impedance spectra of OSCs were measured. The impedance spectra of solar cells In_2O_3/P3HT: ICMA/PEDOT: PSS/Ag are shown in Figure 6. The equivalent electrical circuit is characterized by impedance spectra, shown in the inset of Figure 6, where R_w is the resistance of the film In_2O_3, R_{rec} C describes the boundary of the photoactive layer/ In_2O_3. A decrease in the thickness of In_2O_3 contributes to the rapid transfer of electrons to the cathode (FTO), but it also contributes to an increase in the recombination of injected electrons at the boundary with the photoactive layer, which affects the photoelectric characteristics of OSCs.

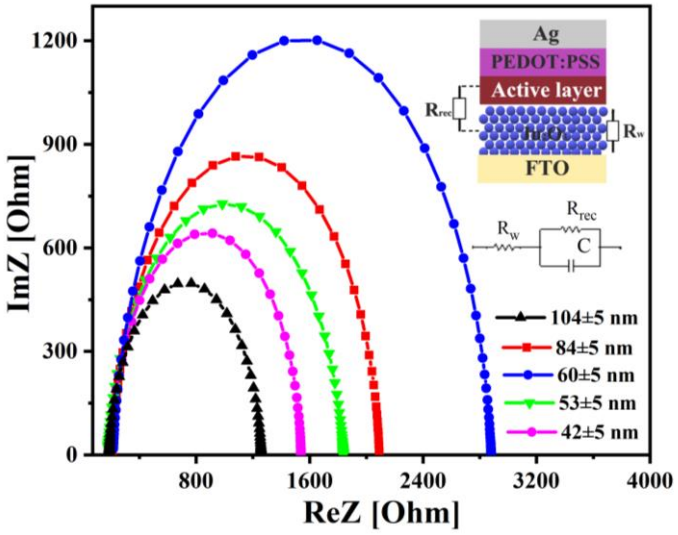

Figure 6. Equivalent electrical circuit and impedance spectra of cells

Table 3 shows the values of the film parameters, where k_{eff} and τ_{eff} are the recombination index characterizing the recombination rate and the effective lifetime of charge carriers in In_2O_3.

Table 3

The value of electrophysical parameters of films

Film thickness In_2O_3, nm	R_w, (Ом)	R_{rec}, (Ом)	C, (Ф) $*10^{-8}$	τ_{eff}, (мс)	k_{eff}, (c^{-1})
104±5	174.39	1093	3.3751	0.6	1666
84±5	133.3	1982.7	6.8205	1.3	769
60±5	117.81	2681.7	2.3751	1.7	588
53±5	145.88	1694.3	4.047	1.1	909
42±5	159.22	1362.8	1.2928	0.9	1111

It can be seen from the table that with a decrease in the thickness of the films, the resistance R_w also decreases, this improves the transport of injected electrons to the FTO. At the same time, a decrease in the thickness of In_2O_3 leads to an increase in the recombination resistance, which leads to a decrease in the recombination of injected electrons. The lifetime of the charge carriers τ_{eff} increases and the recombination efficiency k_{eff} decreases. However, a further decrease in the film thickness d ≤60 nm leads to an increase in the resistance R_w, and to a decrease in the resistance R_{rec}, which indicates an increase in recombination processes. The observed changes in the electrophysical characteristics of the OSCs are associated with a decrease in the thickness of the In_2O_3 films are associated with a change in the interference. Thus, the results of impedance spectroscopy correlate with AFM microscopy data and VAC data.

Conclusion

This paper presents the results of the influence of the thickness and surface interface of In_2O_3 films on the optical and photo-electrophysical properties of a polymer solar cell. It was found that with a decrease in the film thickness to 60 ± 5 nm, the roughness of the films decreases to 0.48 nm, and a further decrease in the thickness of the films leads to an increase in the roughness of the In_2O_3 films. It is shown that the optical width of the band gap also decreases to 3.34 eV with a decrease in the thickness of the films. The decrease in the optical width of the band gap is explained by the presence of surface defects in the film, the concentration of which increases with decreasing thickness. It is shown that the parameters of the VAC depend on the thickness of the In_2O_3 films. It is established that with the thickness of In_2O_3 films equal to 60 nm, the highest parameters of the VAC and efficiency of the polymer solar cell are observed. The nonlin-

ear dependence of electric transport characteristics on the thickness and surface interface of In_2O_3 films is established.

References

1 Che X. High fabrication yield organic tandem photovoltaics combining vacuum- and solution-processed subcells with 15 % efficiency / X. Che, Y. Li, Y. Qu, S.R. Forrest // Nature Energy. — 2018. — Vol. 3. — P. 422–427. https://doi.org/10.1038/s41560-018-0134-z1.

2 Zhang S. Over 14 % Efficiency in Polymer Solar Cells Enabled by a Chlorinated Polymer Donor / S. Zhang, Y. Qin, J. Zhu, J. Hou // Advanced Materials. — 2018. — Vol. 30. — P. 1800868. https://doi.org/10.1002/adma.201800868.

3 Li S. Wide Band Gap Polymer with a Deep Highest Occupied Molecular Orbital Level Enables 14.2 % Efficiency in Polymer Solar Cells / S. Li, L. Ye, W. Zhao, H. Yan, B. Yang, D. Liu, W. Li, H. Ade, J.A. Hou // Journal of the American Chemical Society. — 2018. — Vol. 140 — Issue 23. — P. 7159–7167. https://doi.org/10.1021/jacs.8b02695.

4 Yang G. Recent progress in electron transport layers for efficient perovskite solar cells / G. Yang, H. Tao, P. Qin, W. Ke, G. Fang // Journal of Materials Chemistry A. — 2016 — Vol. 4. — P. 3970-3990. https://doi.org/10.1039/C5TA09011C.

5 Aimukhanov A.K. The impact of SnO2 photoelectrode's thickness on photovoltaic properties of the solar cell FTO: SnO2: PTB7-TH: ITIC/Mo/Ag / A.K. Aimukhanov, T.E. Seisembekova, A.K. Zeinidenov, D.S. Kambar // Bulletin of the University of Karaganda-Physics. — 2022. — No. 2 — Issue 106. — P. 86–91. https://doi.org/10.31489/2022PH2/86-91.

6 Kraini M. Properties of In_2O_3 films obtained by thermal oxidation of, sprayed In2S3 / M. Kraini, N. Bouguila, I. Halidou, A. Timoumi, S. Alaya // Mat SciSemiconProc. — 2013. — Vol. 16. — P. 1388–1396. https://doi.org/10.1016/j.mssp.2013.04.021.

7 Savarimuthu E. Synthesis and materials properties of transparent conducting In_2O_3 films prepared by sol-gel-spin coating technique / E. Savarimuthu, K.C. Lalithambika, A. Moses Ezhil Raj, L.C. Nehru, S. Ramamurthy // J PhysChem Solids. — 2007. — Vol. 68. — P. 1380–1389. https://doi.org/10.1016/j.jpcs.2007.02.038.

8 Omarbekova G.I. The role of surface defects in the charge transport in organic solar cells based on oxidized indium thin films / G.I. Omarbekova, A.K. Aimukhanov, B.R. Ilyassov, D.T. Valiev, A.K. Zeinidenov, V.V. Kudryashov // Surfaces and Interfaces. — 2022. — Vol. 31. — P. 102026. https://doi.org/10.1016/j.surfin.2022.102026.

9 Seisembekova T.E. Competitive charge transport processes in inverted polymer solar cells based on ZnO thin films / T.E. Seisembekova, A.K. Aimukhanov, A.K. Zeinidenov, B.R. Ilyassov // Applied Physics A. — 2022. — Vol. 128. — P. 407. https://doi.org/10.1007/s00339-022-05560-7.

10 Панин А.В. О природе шероховатости поверхности тонких диэлектрических пленок / А.В. Панин, А.Р. Шугуров, Л.Н. Пучкарева // Физическая мезомеханика. — 2000. — № 3. — С. 53–60.

11 Ismail R.A. Preparation of colloidal In_2O_3 nanoparticles using nanosecond laser ablation in water / R.A. Ismail // Micro & Nano Letters. — 2011. — Vol. 6. — P. 951–954. https://doi.org/10.1049/mnl.2011.0459.

12 Ma Q. Atomic-Layer-Deposition of Indium Oxide Nano-films for Thin-Film Transistors / Q. Ma, H.-M. Zheng // Nanoscale Research Letters. — 2018. — Vol. 13. — P. 1. https://doi.org/10.1186/s11671-017-2414-0.

Г.И. Омарбекова, А.К. Аймуханов, Б.Р. Ильясов, А.М. Алексеев, А.К. Зейниденов, А.М. Жаканова

Полимерлі күн элементіндегі зарядтардың тасымалдануы мен рекомбинациясына In_2O_3 қабыршақтарының қалыңдығы және беттік интерфейсінің әсері

Индий оксидінің қабыршақтары этиленгликольдегі индий нитратының ерітіндісінен *spin coating* әдісімен, содан кейін оны 300 °С күйдіру арқылы алынды. Полимерлі күн элементінің оптикалық және фото электрофизикалық қасиеттеріне In_2O_3 қабыршақтарының қалыңдығы мен беткі интерфейсінің әсері туралы зерттеулер жүргізілді. Қабыршақ бетінің кедір-бұдырлығы қабыршақ қалыңдығы 60 нм-ге дейін жұқарғанда біртіндеп азаятыны, ал қабыршақ қалыңдығының одан әрі жұқарғанда қайта өсе бастайтыны көрсетілді. Қабыршақтардың жұтылу спектрлеріне өлшеу жүргізілді. Тыйым салынған аймақтың оптикалық енінің мәндері анықталды. Қабыршақтардың қалыңдығы жұқарған кезде тыйым салынған аймақтың оптикалық (Eg) ені де азаятыны айқындалды. Вольтамперлік сипаттамалардың (ВАС) және электрофизикалық өлшемдердің параметрлерінің In_2O_3 қабыршақтарының қалыңдығы мен беткі интерфейсіне де тәуелді екендігі белгілі болды. In_2O_3 қабыршақтарының қалыңдығы 60 нм-ге тең болған кезде тиімділіктің максималды мәні 3,42 % болатындығы, сонымен қатар фотобелсенді қабаттағы электрондар заряд тасымалдаушылардың максималды өмір сүру ұзақтығына және рекомбинацияның төмен жылдамдығына ие болатындығы анықталды.

Кілт сөздер: In_2O_3 қабыршақтары, полимерлі күн элементі, вольтамперлік сипаттамалары, импеданс спектрлері.

Г.И. Омарбекова, А.К. Аймуханов, Б.Р. Ильясов, А.М. Алексеев, А.К. Зейниденов, А.М. Жаканова

Влияние толщины и поверхностного интерфейса пленок In_2O_3 на транспорт и рекомбинацию зарядов в полимерном солнечном элементе

Пленки оксида индия были получены методом *spin coating* из раствора нитрата индия в этиленгликоле с последующим отжигом при 300 °С. Проведены исследования влияния толщины и поверхностного интерфейса пленок In_2O_3 на оптические и фотоэлектрофизические свойства полимерного солнечного элемента. Показано, что шероховатость поверхности пленки постепенно уменьшается со снижением толщины пленки до 60 нм, а дальнейшее уменьшение толщины пленок приводит к ее возрастанию. Проведены измерения спектров поглощения пленок. Определены значения оптической ширины запрещенной зоны. Установлено, что при снижении толщины пленок ширина запрещенной зоны (Eg) также уменьшается. Было установлено, что параметры вольтамперных характеристик и электрофизических измерений также зависят от толщины и интерфейса поверхности пленок In_2O_3. Доказано, что при толщине пленки In_2O_3, равной 60 нм, наблюдается максимальное значение КПД 3,42 %, в то же время электроны в фотоактивном слое имеют максимальное время жизни носителей заряда и низкую скорость рекомбинации.

Ключевые слова: пленки In_2O_3, полимерный солнечный элемент, вольтамперные характеристики, спектры импеданса.

References

1 Che X., Li, Y., Qu, Y., & Forrest, S.R. (2018). High fabrication yield organic tandem photovoltaics combining vacuum- and solution-processed subcells with 15 % efficiency. *Nature Energy, 3,* 422–427. https://doi.org/10.1038/s41560-018-0134-z1.

2 Zhang S., Qin Y., Zhu J., & Hou, J. (2018). Over 14 % Efficiency in Polymer Solar Cells Enabled by a Chlorinated Polymer Donor. *Advanced Materials*, *30*, 1800868. https://doi.org/10.1002/adma.201800868.

3 Li, S., Ye, L., Zhao, W., Yan, H., Yang, B., Liu, D., Li, W., Ade, H., & Hou, J.A. (2018). Wide Band Gap Polymer with a Deep Highest Occupied Molecular Orbital Level Enables 14.2 % Efficiency in Polymer Solar Cells. *Journal of the American Chemical Society*, *140*(23), 7159–7167. https://doi.org/10.1021/jacs.8b02695.

4 Yang, G., Tao, H., Qin, P., Ke, W., & Fang, G. (2016). Recent progress in electron transport layers for efficient perovskite solar cells. *Journal of Materials Chemistry A*, 4, 3970-3990. https://doi.org/10.1039/C5TA09011C.

5 Aimukhanov, A.K., Seisembekova, T.E., Zeinidenov, A.K., & Kambar, D.S. (2022). The impact of SnO2 photoelectrode's thickness on photovoltaic properties of the solar cell FTO: SnO2: PTB7-TH: ITIC/Mo/Ag. *Bulletin of the University of Karaganda-Physics*, *2*(106), 86–91. https://doi.org/10.31489/2022PH2/86-91.

6 Kraini, M., Bouguila, N., Halidou, I., Timoumi, A., & Alaya, S. (2013). Properties of In_2O_3 films obtained by thermal oxidation of, sprayed In2S3. *Mat SciSemiconProc,* 16, 1388–1396. https://doi.org/10.1016/j.mssp.2013.04.021.

7 Savarimuthu, E., Lalithambika, K.C., Moses Ezhil Raj, A., Nehru, L.C., & Ramamurthy, S. (2007). Synthesis and materials properties of transparent conducting In_2O_3 films prepared by sol-gel-spin coating technique. *J PhysChem Solids*, *68,* 1380–1389. https://doi.org/10.1016/j.jpcs.2007.02.038.

8 Omarbekova, G.I., Aimukhanov, A.K., Ilyassov, B.R., Valiev, D.T., Zeinidenov, A.K., & Kudryashov, V.V. (2022). The role of surface defects in the charge transport in organic solar cells based on oxidized indium thin films. *Surfaces and Interfaces*, *31*, 102026. https://doi.org/10.1016/j.surfin.2022.102026.

9 Seisembekova, T.E., Aimukhanov, A.K., Zeinidenov, A.K., & Ilyassov, B.R. (2022). Competitive charge transport processes in inverted polymer solar cells based on ZnO thin films. *Applied Physics A*, 128, P.407. https://doi.org/10.1007/s00339-022-05560-7.

10 Panin, A.V., Shugurov, A.R., & Pushkareva, L.N. (2000). O prirode sherokhovatosti poverkhnosti tonkikh dielectricheskikh plenok [On the nature of surface roughness of thin dielectric films]. *Fizicheskaia mezomekhanika — Physical mesomechanics*, *3*, 53–60 [in Russian].

11 Ismail, R.A. (2011). Preparation of colloidal In_2O_3 nanoparticles using nanosecond laser ablation in water. *Micro & Nano Letters*, *6*, 951–954. https://doi.org/10.1049/mnl.2011.0459.

12 Ma, Q., & Zheng, H.-M. (2018). Atomic-Layer-Deposition of Indium Oxide Nano-films for Thin-Film Transistors. *Nanoscale Research Letters*, *13,* 1. https://doi.org/10.1186/s11671-017-2414-0.

DOI 10.31489/2023PH2/25-33

UDC 621.794

Zh.B. Sagdoldina[1], D.R. Baizhan[2*], B.K. Rakhadilov[3], D.B. Buitkenov[4], N.E. Berdimuratov[5], M.S. Zhaparova[6]

[1,2,4,5,6]Sarsen Amanzholov East Kazakhstan University, 30 Gvardeiskoi Divisii St. 34, 070020, Ust-Kamenogorsk, Kazakhstan;
[1,2]Shakarim University, Glinka St. 20 "a", 071412, Kazakhstan;
[3]Plasma Science LLP, 37 Serikbaev St., 070010, Kazakhstan
([*]E-mail: daryn.baizhan@mail.ru)

Microstructure and mechanical properties of HA/Ti composite coatings applied by detonation spraying

This work presents the results of experimental studies of the structure and mechano-tribological properties of composite coatings based on hydroxyapatite (HA) and titanium in different ratios (wt. %): 30HA-70Ti, 50HA-50Ti, 70HA-30Ti. Composite coatings with a thickness of 40-50 μm were applied to a substrate made of Grade 2 titanium by detonation spraying. Microstructures and phase compositions of as-sprayed coatings were analyzed by scanning electron microscopy and X-ray diffraction. The deposition mechanism of HA-Ti composite coatings was also examined. The results of the study showed that during detonation powder spraying from a mixture of HA-Ti, porous coatings are formed, consisting of the phases of hydroxyapatite $Ca_{10}(PO_4)_6(OH)_2$, tricalcium phosphate, titanium, and titanium oxide. It was found that with a decrease in the content of hydroxyapatite in the composite, there is a decrease in the relative content of B-type carbonate ions in the structure, as well as a decrease in the content of the mineral phase as a whole. Composite coating 30HA-70Ti wt. % is the closest in structure to stoichiometric crystalline HA (Ca/P = 1.67). At ratios of coatings 50HA-50Ti wt. %, an increase by 1.5-2 times in wear resistance is observed.

Keywords: hydroxyapatite, titanium, detonation spraying, coating, microstructures and phase composition, mechanical properties.

Introduction

With the development of new concepts in the technology, production and application of implants for the bioengineering of bone tissue, the requirements for the functional, strength and aesthetic parameters of orthopedic structures have increased significantly [1]. First, this refers to the task of creating biocoatings, which are close to the structure of human bone tissue [2]. In order to stimulate the structure of natural bone, in recent years, the synthesis of hydroxyapatite $Ca_{10}(PO_4)_6(OH)_2$ has attracted considerable attention [3, 4]. Bioactive coatings based on hydroxyapatite and calcium phosphates are promising due to their biocompatibility and compositional proximity to bone tissue [5]. Hydroxyapatite (HA) provides ideal biocompatibility by actively stimulating osteogenesis and bone regeneration. However, HA coatings exhibit poor tribological properties, such as a strong tendency to adhesion, high and unstable coefficients of friction, and low resistance to wear during fretting. Therefore, it is also interesting to modify and progress the properties of the HA coating by including a metal in it [6]. HA/metal composite coatings are characterized by high mechanical and tribological properties [7]. Detonation technologies can be used to obtain HA/metal composite coatings [8]. The detonation gas spraying method has good prospects for the use in medicine, primarily due to the identity of the phase composition of the initial material and the formed coating. In this regard, the aim of this research is to study the effect of the ratio of the components on the structural-phase states, hardness and wear resistance of HA/metal composite coatings obtained by detonation spraying.

Experimental

To obtain coatings, CCDS2000 detonation complex was used, having a system of electromagnetic gas valves that regulate the supply of fuel and oxygen, and control the purging of the system (Fig. 1). An acetylene-oxygen mixture, which is the most demanded fuel for detonation spraying of powder materials, was used as a fuel gas. The deposition was carried out at the O_2/C_2H_2 ratio of 1.856. The volume of filling the barrel with a mixture is of acetylene-oxygen 50 %. Nitrogen was used as a carrier gas. The distance between the treated surface of the sample and the detonation barrel was 70 mm; the diameter of the straight barrel was 20 mm [9]. Commercially pure Grade 2 titanium (99.5 %) was used as a substrate. Before spraying, Grade 2 plates with dimensions of 30×30×3 mm were ground and polished, after which they were subjected to sand-

blasting. Sandblasting was carried out on the detonation unit using corundum powders with grain sizes of 0.5-1.3 mm with a volume of filling the barrel with an acetylene-oxygen mixture of 30 %. For spraying coatings, a mixture of titanium powders (grain size 10-12 microns) and HA (grain size 0.5-0.6 microns) were used in the ratios of 30/70, 50/50 and 70/30 (wt. %). Mechanical activation treatment was used to obtain a composite powder consisting of HA-Ti [10]. Mechanical activation of HA-Ti mixtures was carried out in a planetary ball mill PULVERISETTE 6 at a frequency of 380 rpm. The mechanical activation time was 60 s.

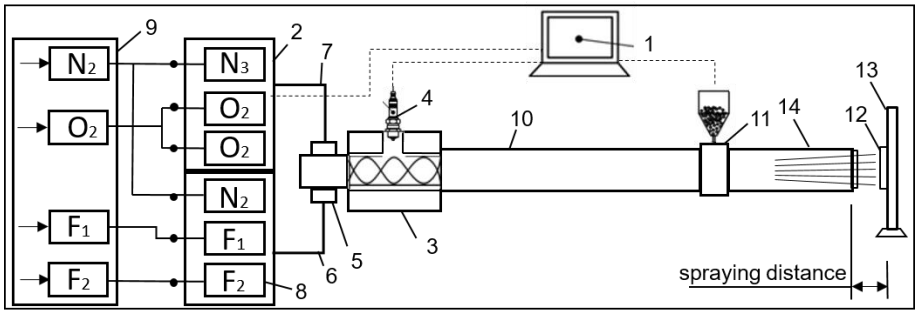

Figure 1. Scheme of the detonation complex CCDS2000: 1 — control computer, 2 — gas distributor, 3 — mixing-ignition chamber, 4 — spark plug, 5 — barrel valve, 6 — fuel line, 7 — oxygen line, 8 — gas valves, 9 — gas supply unit, 10 — part of the trunk, 11 — powder dispenser, 12 — sample; 13 — manipulator, 14 — muzzle.

The study of surface morphology was carried out by scanning electron microscopy (SEM) using backscattered electrons (BSE) on JSM-6390LV scanning electron microscope. The structure of the obtained samples was studied using Raman spectroscopy on AFM-Raman Solver Spectrum, NT-MDT spectrometer. To excite vibrational modes, a blue laser with a wavelength of 473 nm and a maximum laser power of 35 mW was used with a ×100 objective with a spot size of $2 \cdot 10^{-6}$ m. The obtained spectra were processed by the Savitsky-Golay method [11] using a second-order polynomial. The error in recording the spectra was 4 cm^{-1}. The phase composition of the samples was studied by X-ray diffraction analysis on X'PertPro diffractometer using CuKα-radiation. The study was carried out in the following modes: voltage across the tube was U = 40 kV; tube current was I = 30 mA; exposure time was 1 s; shooting step was 0.02º. The measurement of the tribological characteristics of the coatings was carried out in the sliding friction mode according to the "ball-disk" scheme on Anton Paar TRB3 tribometer. The sample rotation speed was 2 cm/s, the load was 5 N; a ball made of 100Cr6 steel with a diameter of 6 mm was used as a counterbody. Nanoindentation was carried out on NanoScan-4D nanohardness meter. In accordance with GOST R 8.748-2011. Using the Berkovich indenter, 10 injections were made at a load of 100 mN. Young's modulus and hardness were determined by the method of Oliver and Pharr [12].

Results and Discussion

Figures 2-4 show diffraction patterns of the composite powder in different ratios of 30HA-70Ti, 50HA-50Ti, 70HA-30Ti (wt. %) and coatings obtained by detonation spraying. X-ray phase analysis showed that composite HA/Ti powder consists of two phases: HA and titanium. The diffractogram of composite 50HA/50Ti, 70HA/30Ti (wt. %) coatings (Fig. 3-4) is characterized by the appearance of peaks of the α-$Ca_3(PO_4)_2$ (tricalcium phosphate) phase, while the main phase component of the coating retains the HA phase [$Ca_{10}(PO_4)_6(OH)_2$]. However, in the diffraction pattern of coatings (Fig. 2b) with a powder composition of 30HA/70Ti the phase of tricalcium phosphate (α-$Ca_3(PO_4)_2$) was not detected. $Ca_3(PO_4)_2$ has a narrow mechanical strength compared to cortical bone, which limits its use in areas subject to low mechanical stress. However, when interacting with the environment, the body is completely replaced by biological tissues [13]. In addition, after detonation spraying of composite 50HA-50Ti and 70HA-30Ti coatings, intense phases of titanium oxide TiO were found (Fig. 3b, Fig. 4b). Titanium oxide is not considered a disadvantage in the biocompatibility of the implant, while the growth of the titanium oxide layer can improve adhesion to the bone tissue [14, 15]. The change in the phase composition of calcium phosphate coatings during detonation spraying is explained by high reactivity of titanium with respect to any substances at high temperatures [16].

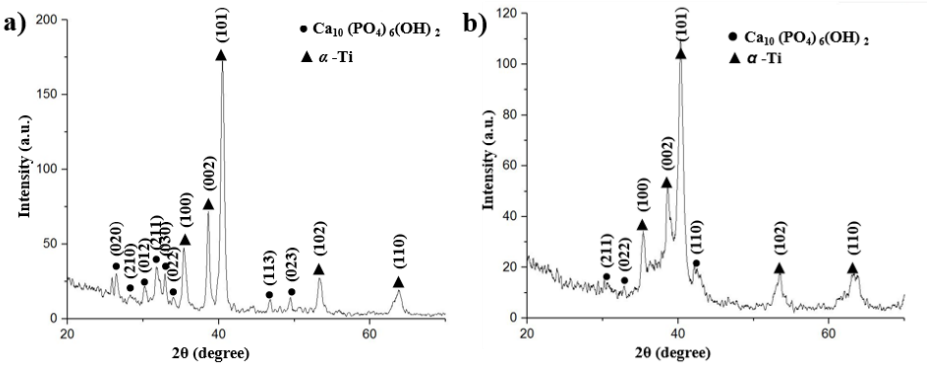

Figure 2. Diffraction patterns of the composite powder (a) and coating of 30HA-70Ti (wt. %), obtained by detonation spraying (b).

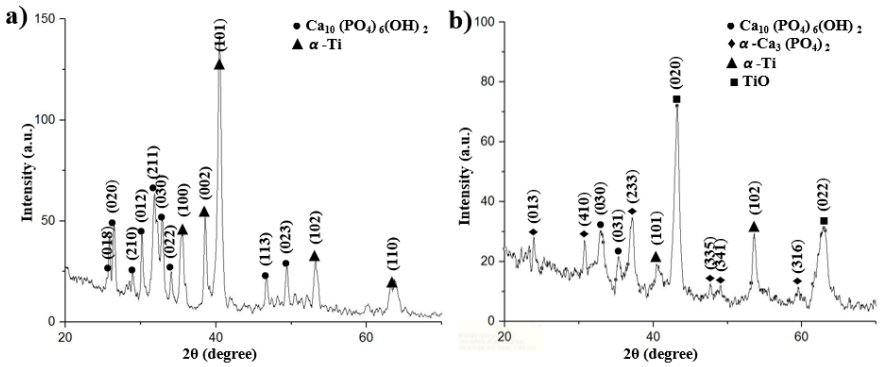

Figure 3. Diffraction patterns of composite powder (a) and coating of 50HA-50Ti (wt. %), obtained by detonation spraying (b).

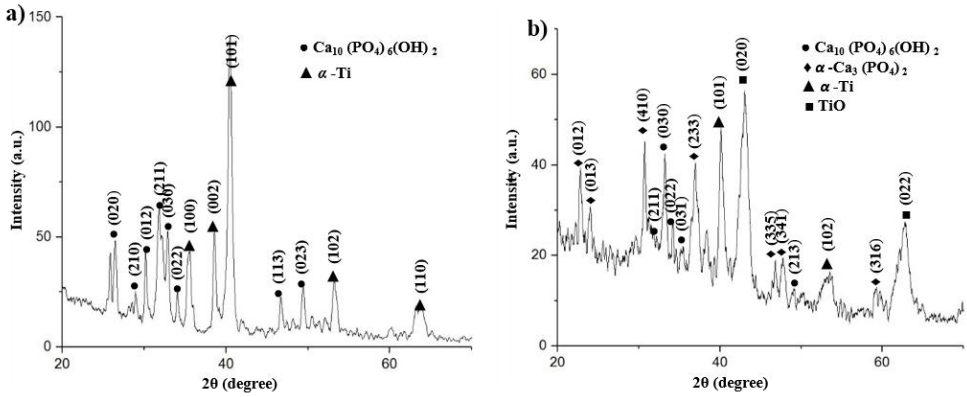

Figure 4. Diffraction patterns of (a) composite powder and coating of 70HA-30Ti (wt. %) obtained by detonation spraying (b).

To assess the microstructure of the surface of the composite coatings, the samples were analyzed by SEM. Figure 5 a-c shows SEM images and elemental analysis of composite 30HA-70Ti, 50HA-50Ti, 70HA-30Ti (wt. %) coatings. The morphology of the composite coatings (Fig. 5) showed the formation of a layered porous structure, which, in turn, promotes the effective growth of bone tissue into the pores of the implant. In the obtained coatings, pores are observed, which are formed when the coating particles melt. The formation of a porous structure and a pronounced relief is a feature of detonation technology, which can contribute to the widespread use of detonation coatings in medical implants.

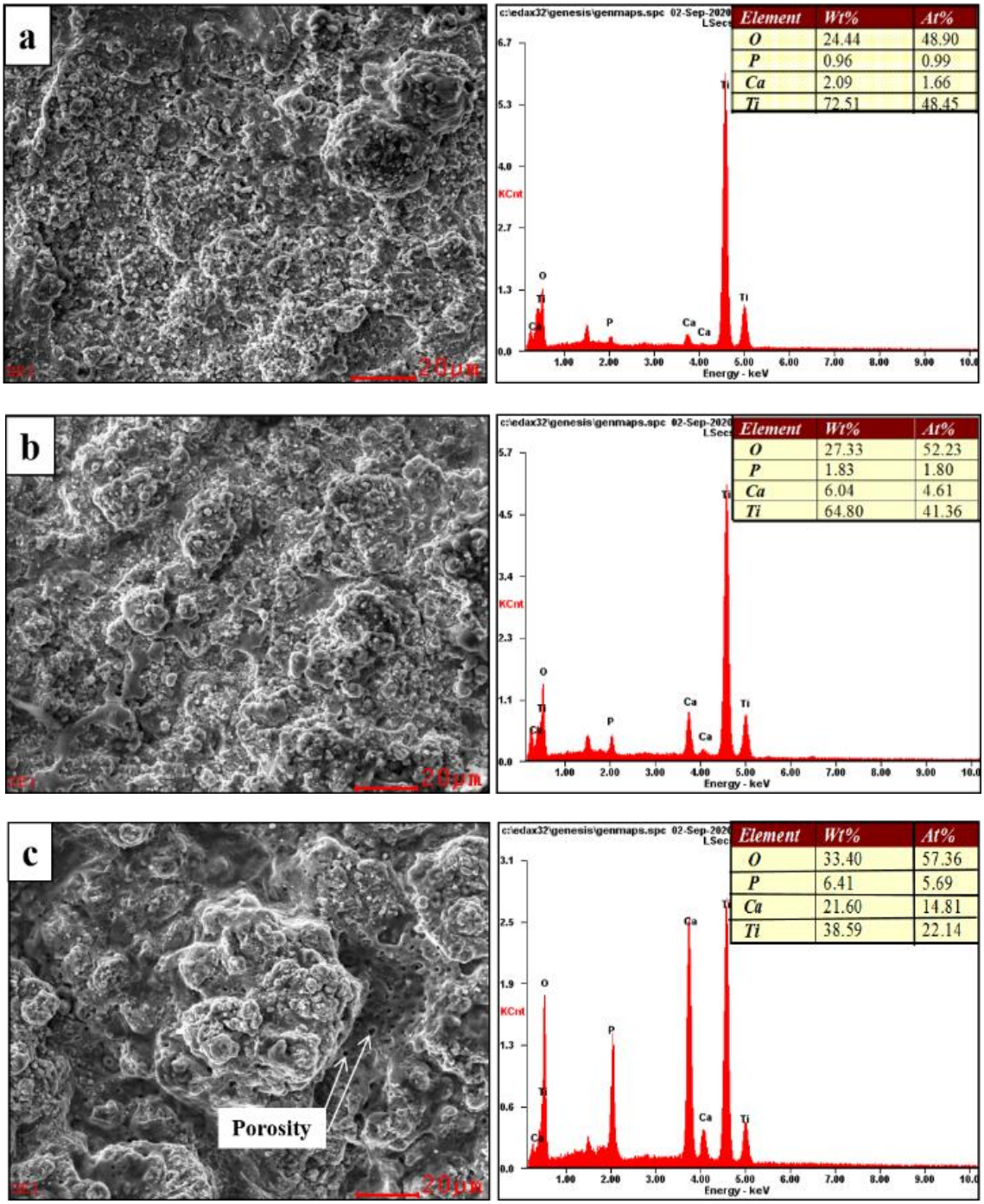

Figure 5. SEM image and EDS analysis of composite coatings (wt. %): 30HA-70Ti (a), 50HA-50Ti (b), 70HA-30Ti (c).

Figure 5 also shows the energy dispersive X-ray spectra of the coatings. Analysis of the elemental composition did not reveal the presence of other elements, except for the basic composition of the substrate and composite powder. According to the obtained results of the elemental analysis of composite coatings, it can be argued that detonation spraying does not cause a change in the chemical composition of the coating, and this factor is of decisive importance for the biocompatibility and preservation of the service life of the coating. The Ca/P ratio in coatings is one of the main parameters determining bioactivity. Elemental analysis allows comparing the concentrations of elements that make up composite coatings and calculate the Ca/P ratio. The atomic ratio of Ca/P in composite coatings ranges from 1.67-2.6. Table 1 shows the Ca/P atomic ratio for each group of composite coatings with a different content of hydroxyapatite. The atomic Ca/P ratio in composite coatings (30HA-70Ti) is 1.67; this result proves the possibility of obtaining a bioactive composition by detonation spraying.

Table 1.

Atomic Ca/P ratio in composite coatings with different content of hydroxyapatite (wt. %):

Coatings	Ca/P
30HA-70Ti	1.67
50HA-50Ti	2.56
70HA-30Ti	2.60

Figure 6 shows the Raman spectra of composite 30HA-70Ti, 50HA-50Ti, 70HA-30Ti coatings obtained by detonation spraying. The most noticeable intense band observed at 961 cm^{-1} for all groups indicates that HA is the main phase component of the coatings. This band belongs to the P-O symmetric extension mode (ν_1) of the PO_4 group and is the most characteristic band of carbonized apatites. The sharpness of this band confirms the good crystallinity of the HA coating [17]. Similarly, the bands associated with the antisymmetric stretching mode (ν_3) of PO_4 groups show a shift from 1045 cm^{-1} to the shoulder at 1033 cm^{-1} (Table 2) [18]. With a decrease in HA-substitution (Fig. 6 c), the main apatite band at 961 cm^{-1} demonstrates a broadening and a decrease in intensity, which indicates a decrease in the crystallinity of the formed mineral phase. In addition, it should be emphasized that this change in the carbonate content in the coatings is closely related to associated with changes in the growth morphology and size of crystallites, which occur with a change in temperature — higher atomic disorder corresponding to smaller crystal sizes (on a nanometer scale), the lattice becomes more and more ordered with increasing temperature.

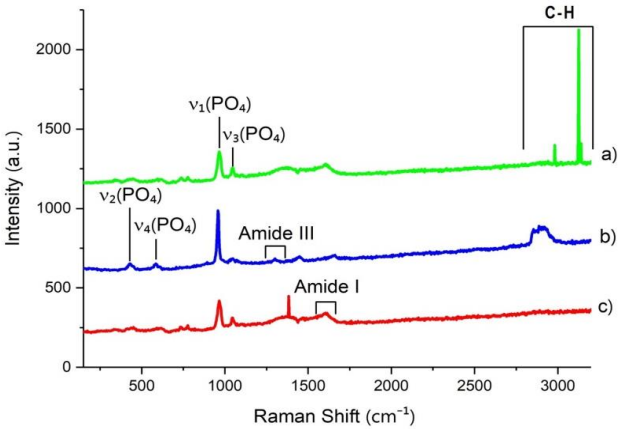

Figure 6. Raman spectra of composite coatings with different content of hydroxyapatite (wt. %): 70HA-30Ti (a); 50HA-50Ti (b); 30HA-70Ti (c).

The region of peaks at 2880-3070 cm^{-1}, as a rule, is correlated with vibrations of C — H bonds (2880–2935, 3070 cm^{-1}). Thus, according to the Raman spectroscop data, the structural features of the composite coatings have been revealed with a decrease in the content of hydroxyapatite, a decrease in the relative content of B-type carbonate ions in the structure of hydroxapatite is observed, as well as a decrease in the content of the mineral phase in general.

Table 2.

Results with different frequencies of the corresponding lines

Raman shift (cm^{-1})	Assignment
423	PO_4^{3-} ν_2(P-O deformation)
585	PO_4^{3-} ν_4 (P-O deformation)
950-965	PO_4^{3-} ν_1 (P-O deformation)
1030-1045	PO^{3-} ν_3 (P-O asymmetric valence)
1245-1270	Amide Ⅰ Ⅱ, C-N-H valence
1665-1675	Amide Ⅰ, C-C-H valence
2880-2935, 3070	C-H vibrations

Hardness and elastic modulus are the main parameters determining the plasticity, an important characteristic of the material for practical application. Figure 7 shows the data on nanoindentation obtained on transverse thin sections of the coatings.

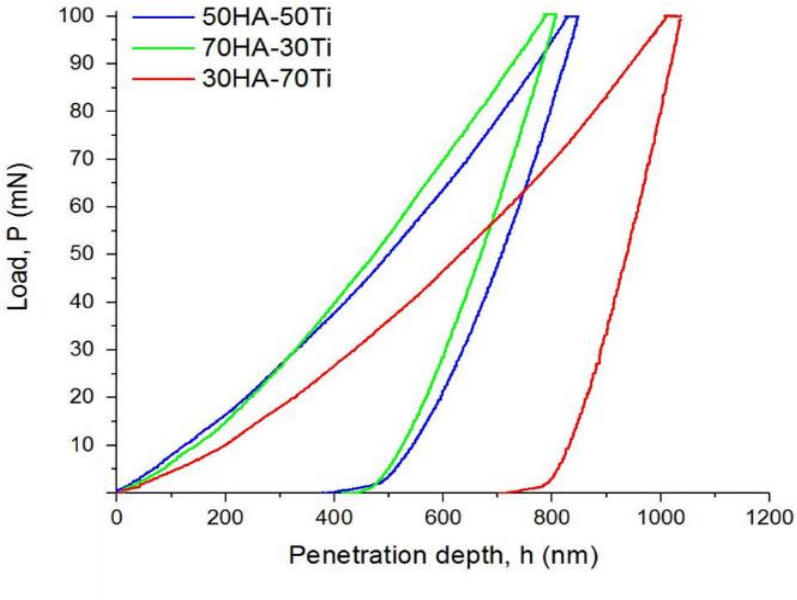

Figure 7. Curves of loading and unloading of composite coatings with different content of hydroxyapatite (wt. %).

To assess the resistance of a material to elastic deformation of fracture, the value of the ratio of hardness to Young's modulus H/E, also called the plasticity index of the material, was used [18]. In addition, to assess the mechanical properties of materials, the H^3/E^2 parameter was used, which describes the resistance to plastic deformation [19]. It was found that the plasticity of the HA-Ti coating increases with an increase in the HA concentration. High values of H/E and H^3/E^2 are indicators of high wear resistance, therefore, composite coatings with a composition of 70HA-30Ti, formed on Grade 2 titanium by detonation spraying, exhibit high performance properties of abrasive wear. The values of hardness, modulus of elasticity, elastic deformation of destruction (H/E) and resistance to plastic deformation (H^3/E^2) of composite coatings are given in Table 3.

Table 3.

Hardness and elasticity modulus of composite coatings with different content of hydroxyapatite

Sample	H, GPa	E, GPa	H/E	H^3/E^2
30HA-70Ti	4.65±0.8	154.4±7	0.03	$4.22 \cdot 10^{-3}$
50HA-50Ti	7.5±0.9	129.3±8.8	0.05	$25.23 \cdot 10^{-3}$
70HA-30Ti	8.3±1.1	135.5±5.5	0.06	$31.14 \cdot 10^{-3}$

Figure 8 shows micrographs of the surface and the results of measuring the roughness of composite coatings with different contents of hydroxyapatite (wt. %): 30HA-70Ti; 50HA-50Ti; 70HA-30Ti. The surface of all coatings has a heterogeneous structure with pores, typical layered, wavy arrangement of structural components. The surface roughness of the composite coatings was measured by the Ra parameter using a profilometer 130 on a 7 mm section on the sample surface. From the data obtained, the roughness of the composite coatings varies from 5.79 to 8.61 μm with a change in the HA in the composite. Comparison of these dependences allows concluding that coatings obtained at low concentrations of HA in the composite have reduced values of the roughness parameter Ra, and as the concentration of HA in the composite increases, the roughness of the coatings increases. Composite coatings obtained by detonation spraying have a developed surface, which will serve as their improved fusion with bone tissue.

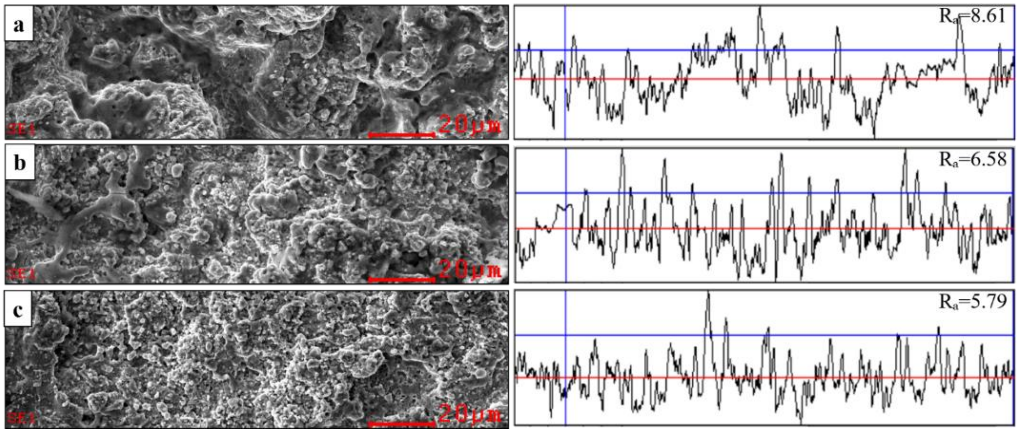

Figure 8 Micrographs and roughness of composite coatings with different content of hydroxyapatite (wt. %): 70HA-30Ti (a); 50HA-50Ti (b); 30HA-70Ti (c).

To determine the wear resistance of the coatings, tribological tests were carried out according to the "ball-disk" scheme. The coefficient of friction of HA-Ti composite coatings with different content of hydroxyapatite is shown in Figure 9. The coefficient of friction of composite 30HA-70Ti coating was 0.510. An increase in the HA content to 70 wt. % leads to an increase in the coefficient of friction and the rate of wear of coatings. According to the obtained results of tribological testing of detonation 50HA-50Ti coating, low values of the friction coefficient of 0.352 and high wear resistance under sliding friction conditions were observed.

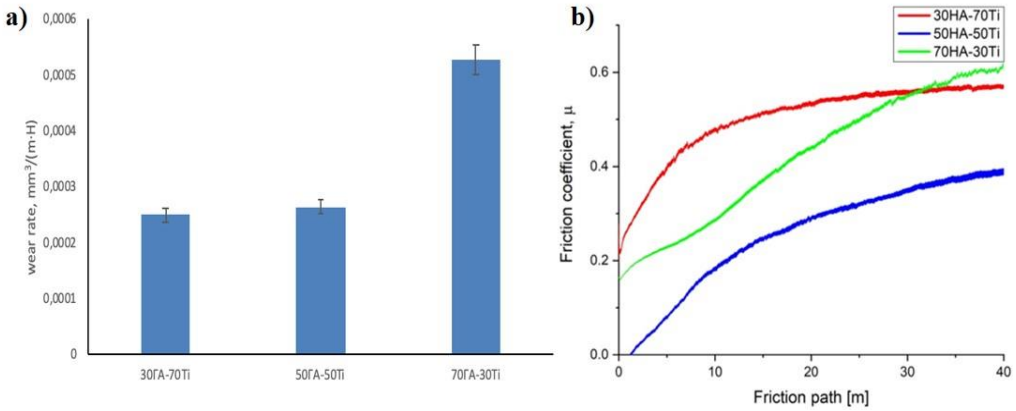

Figure 9. Intensity of wear (a) and coefficient of friction (b) of HA-Ti coatings (wt. %)

The study of the microstructure of the cross-section of the composite 50HA-50Ti coating showed the formation of a layered-porous structure with a thickness of 40-50 microns (Fig. 10 a). Elemental analysis data obtained from the coating layer correspond to the initial composition of the composite powder (Fig. 10 b).

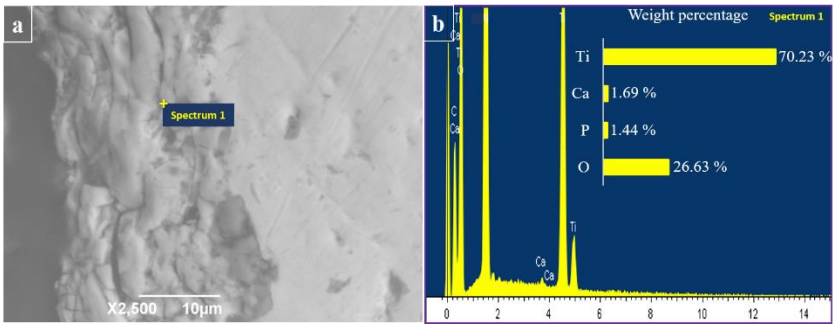

Figure 10. SEM image of a cross-section (a) and elemental analysis (b) of the composite 50HA-50Ti coating

Conclusion

Crystalline composite coatings with a thickness of 40-50 μm were obtained by the method of detonation spraying of 30HA-70Ti; 50HA-50Ti; 70HA-30Ti composites on the surface of Grade 2 titanium. Composite HA-Ti coatings have a layered porous structure. The results of X-ray phase analysis of detonation 50HA-50Ti and 70HA-30Ti coatings showed the formation of α-$Ca_3(PO_4)_2$ and TiO. Composite 30HA-70Ti coating is the closest in structure to stoichiometric crystalline HA (Ca/P = 1.67). According to the results of Raman spectroscopy, the following structural features of the composite coating were revealed: with a decrease in the HA content, a decrease in the relative content of B-type carbonate ions in the structure of hydroxyapatite is observed, as well as a decrease in the content of the mineral phase in general. Based on the phase analysis and mechanical properties, the optimal content of the Ti additive was 50 wt. % for HA-Ti composite coatings sprayed with the CCDS2000 detonation complex used in experimental conditions.

Acknowledgment

This research was funded by the Science Committee of the Ministry of Education and Science of the Republic of Kazakhstan (Grant No. AP13068485).

References

1 Corpe, R.S., Young, T.R., Steflik, D.E., Whitehead, R.Y., Wilson, M.D., & Jaramillo, C. (2000). Correlative experimental animal and human clinical retrieval evaluations of hydroxyapatite (HA)-coated and non-coated implants in orthopaedics and dentistry. *Journal of Critical Reviews in Biomedical Engineering. Prefac*, *28*, 395–398.

2 Cattini, A., Bellucci, D., Sola, A., Pawłowski, L., & Cannillo, V. (2013). Suspension plasma spraying of optimized functionally graded coatings of bioactive glass/hydroxyapatite. *Surface Coatings. Technology*, *236*, 118-126.

3 Rakhadilov, B.K., Baizhan, D.R., Sagdoldina, Zh.B., & Torebek, K. (2022). Research of regimes of applying coats by the method of plasma electrolytic oxidation on Ti-6Al-4V. *Bulletin of the university of Karaganda-Physics*, *1*, 99–106.

4 Prosolov, K.A., Lastovka, V.V., Belyavskaya, O.A., Lychagin, D.V., Schmidt, J., & Sharkeev, Y.P. (2020). Tailoring the Surface Morphology and the Crystallinity State of Cu- and Zn-Substituted Hydroxyapatites on Ti and Mg-Based Alloys. *Materials*, *13* (19), 4449.

5 Rakhadilov, B., & Baizhan, D. (2021). Creation of Bioceramic Coatings on the Surface of Ti-6Al-4V Alloy by Plasma Electrolytic Oxidation Followed by Gas Detonation Spraying. *Coatings*, 11.

6 Vadiraj, A., & Kamaraj, M. (2007). Effect of surface treatments on fretting fatigue damage of biomedical titanium alloys. *Tribology International*, *40* (1). 82-88.

7 Dong, Z.L., Khor, K.A., Quek, C.H., White, T.J., & Cheang, P. (2003). TEM and STEM analysis on heat-treated and in vitro plasma-sprayed hydroxyapatite/Ti-6Al-4V composite coatings. *Biomaterials*, *24*(1), 97-105.

8 Kang, A.S. (2020). Wear performance of hydroxyapatite coatings deposited on AISI 304L using detonation gun spray. *Materials Today: Proceedings*, *32*(3), 304-310.

9 Ulianitsky, Yu.V., Dudina, D.V., Shtertser, A.A., & Smurov, I. (2019). Computer-Controlled Detonation Spraying: Flexible Control of the Coating Chemistry and Microstructure. *Metals*, *9(12)*, 1244.

10 Sagdoldina, Z., Rakhadilov, B., Skakov, M., & Stepanova, O. (2019). Structural evolution of ceramic coatings by mechanical alloying. *Materials testing*, *61*, 304–308.

11 Savitzky, A. (1964). Smoothing and Differentiation of Data by Simplified Least Squares Procedures. *Analytical Chemistry*, *36*(8), 1627-1639.

12 Oliver, W.C., & Pharr, G.M. (1992). An improved technique for determining hardness and elastic modulus using load and displacement sensing indentation experiments. *Journal of Materials Research*, *7(6)*, 1564-1583.

13 Fidancevska, E. (2007). Fabrication and characterization of porous bioceramic composites based on hydroxyapatite and titania. *Materials Chemistry and Physics*, *103(1)*, 95-100.

14 Yonggang, Y., Wolke, J.G.C., Yubao, L., & Jansen, J.A., The influence of discharge power and heat treatment on calcium phosphate coatings prepared by RF magnetron sputtering deposition, *Journal of Materials Science: Materials in Medicine*, *18*, 1061-1069.

15 Baizhan, D.R., Rakhadilov, B.K., Zhurerova, L.G., & Torebek, K. (2022). Preparation of bio-ceramic composite coatings on Ti6Al4V titanium alloy by gas-detonation spraying. *Bulletin of the university of Karaganda-Physics*, *1*, 89–98.

16 Rakhadilov, B., Kakimzhanov, D., Baizhan, D., Muslimanova, G., Pazylbek, S., & Zhurerova L. (2021). Comparative Study of Structures and Properties of Detonation Coatings with alpha-Al_2O_3 and gamma-Al_2O_3 Main Phases. *Coatings*, 11.

17 Timchenko, E.V., Timchenko, P.E., Taskina, L.A., Volova, L.T., Miljakova, M.N., & Maksimenko, N.A. (2015). Using Raman spectroscopy to estimate the demineralization of bone transplants during preparation. *J. Opt. Technol*, *82* (3), 153-157.

18 Leyland, A., & Matthews, A. (2000). On the significance of the *H*/*E* ratio in wear control: a nanocomposite coating approach to optimised tribological behavior. *Wear*, *246* (1-2), 1-11.

19 Maksakova, O.V., Pogrebnjak, A.D., Yerbolatova, G., Beresnev, V.M., Kupchishin, A.I., & Baymoldanova, L.S. (2019). Triple sandwich design of multilayered (CrN/ZrN)/(Cr/Zr) hard coating with nanoscale architecture: microstructure and composition. *Materials Research Express, 6* (10).

Ж.Б. Сағдолдина, Д.Р. Байжан, Б.К. Рахадилов, Д.Б. Буйткенов,
Н.Е. Бердімуратов, М.С. Жапарова

Детонациялық бүрку әдісімен алынған HA/Ti композициялық жабындардың микроқұрылымы және механикалық қасиеттері

Мақалада гидроксиапатит (ГА) және әртүрлі қатынастарда (мас. %): 30ГА-70Ti, 50ГА-50Ti, 70ГА-30Ti титан негізіндегі композициялық жабындардың құрылымы мен механикалық-трибологиялық қасиеттерінің нәтижелері келтірілген. Қалыңдығы 40-50 мкм композиттік жабындар детонациялық бүрку әдісімен ВТ1-0 (Grade 2) титаннан жасалған субстратқа алынды. Жабындардың микроқұрылымы мен фазалық құрамы сканерлеуші электронды микроскопия және рентгендік дифракция әдістерімен талданды. HA-Ti композиттік жабындарының бүрку механизмі де зерттелді. Зерттеу нәтижелері ГА-Ti қоспасынан ұнтақты детонациялық бүрку кезінде $Ca_{10}(PO_4)_6(OH)_2$ гидроксиапатит фазаларынан, трикальций фосфатынан, титаннан және титан оксидінен тұратын кеуекті жабындар түзілетінін көрсетті. Композиттегі гидроксиапатит мөлшері азайған кезде құрылымдағы В типті карбонат иондарының салыстырмалы құрамы төмендейтіні, сондай-ақ жалпы минералды фазаның азаюы анықталды. 30HA-70Ti мас.% композициялық жабын құрылымы бойынша стехиометриялық кристалды HA-ға ең жақын (Ca/P = 1.67). 50 HA-50 Ti жабындарының арақатынасында тозуға төзімділіктің 1,5-2 есе артуы байқалады.

Кілт сөздер: гидроксиапатит, титан, детонациялық бүрку, жабын, микроқұрылымы және фазалық құрамы, механикалық қасиеттері.

Ж.Б. Сағдолдина, Д.Р. Байжан, Б.К. Рахадилов, Д.Б. Буйткенов,
Н.Е. Бердімуратов, М.С. Жапарова

Микроструктура и механические свойства композиционных покрытий HA/Ti, нанесенных методом детонационного напыления

В статье представлены результаты экспериментальных исследований структуры и механотрибологических свойств композиционных покрытий на основе гидроксиапатита (ГА) и титана в разных соотношениях (масс. %): 30ГА–70Ti, 50ГА–50Ti, 70ГА–30Ti. Композиционные покрытия толщиной 40–50 мкм были нанесены на подложку из титана марки ВТ–0 (Grade 2) методом детонационного напыления. Микроструктуру и фазовый состав напыленных покрытий анализировали методами сканирующей электронной микроскопии и рентгеновской дифракции. Также был исследован механизм напыления композитных покрытий HA–Ti. Результаты исследования показали, что при детонационном напылении порошка из смеси ГА–Ti формируются пористые покрытия, состоящие из фаз гидроксиапатита $Ca_{10}(PO_4)_6(OH)_2$, трикальцийфосфата, титана и оксида титана. Было обнаружено, что при уменьшении содержания гидроксиапатита в композите наблюдается снижение относительного содержания карбонат-ионов В-типа в структуре, а также уменьшение содержания минеральной фазы в целом. Композиционное покрытие 30ГА–70 Ti масс. %, наиболее близко по структуре к стехиометрическому кристаллическому ГА (Ca/P=1,67). При соотношениях покрытий 50ГА–50Ti масс. % наблюдается увеличение износостойкости в 1,5–2 раза.

Ключевые слова: гидроксиапатит, титан, детонационное напыление, покрытие, микроструктуры и фазовый состав, механические свойства.

DOI 10.31489/2023PH2/34-45

UDC 539.215.9

D.B. Tolubayeva[1], L.V. Gritsenko[2*], Y.Y. Kedruk[3], K.K. Mustafina[4], M.B. Aitzhanov[5], Kh.A. Abdullin[6]

[1]Karaganda Industrial University, Republic Ave. 30, Temirtau, Kazakhstan;
[2,3,4]Satbayev University, Satpayev str., 22, Almaty, Kazakhstan;
[2,5,6]National nanotechnology laboratory of open type at al-Farabi Kazakh National University, al-Farabi ave., 71, Almaty, Kazakhstan
([*]E-mail: gritsenko_lv@mail.ru)

Influence of zinc oxide morphology on its photocatalytic properties

The rapid development of industry, in addition to the positive impact, has led to environmental problems. The release of polluting waste containing substances such as dyes, pesticides, heavy metals and pharmaceutical waste leads to contamination of water reservoirs, that has a negative impact on humans and aquatic organisms. In this regard, the development of an inexpensive, effective, environmentally friendly method of waste water treatment from organic pollutants is an urgent research priority. Zinc oxide (ZnO) is one of the most active semiconductor photocatalysts. In this paper, the influence of the morphology of nanostructured zinc oxide synthesized by effective methods on photocatalytic properties with respect to the rhodamine-B dye (RhB) was investigated, and the influence of the length-to-thickness ratio (aspect ratio AR) of ZnO samples on its structural and optical properties was studied. The results of the study showed that an increase in the annealing temperature of zinc acetate in the atmosphere leads to an increase in the size of zinc oxide crystallites, while an increase in the concentration of alkali in the growth solution (synthesis of ZnO by chemical deposition from 0.4 M to 0.7 M) makes it possible to synthesize thinner extended 2D plates. It is shown that an increase in the AR value of the synthesized samples makes it possible to increase their photocatalytic activity.

Keywords: chemical deposition, zinc oxide, calcination, optical and structural properties, photocatalyst, rhodamine-B.

Introduction

In recent years, the production and use of dyes has increased dramatically, for example, azo dyes, reactive, solvent and sulfur dyes are widely used in the textile, food, adhesive, cosmetic, construction, paint, cellulose, glass and ceramic industries [1, 2]. The release of organic dyes into the environment is a source of harmful pollution of the ecosystem [3].

These organic pollutants have high chemical stability and low biodegradability, which complicates the search for an appropriate method for the purification of wastewater and water reservoirs [4]. There are many different technologies that are used for wastewater disinfection, including such as electrodialysis [5], membrane filtration [6], precipitation [7], adsorption [8], electrochemical reduction [9] and electrodeionization [10]. But traditional chemical, physical and biological processes of wastewater treatment containing dyes have such disadvantages as high cost, high energy consumption and the formation of secondary pollutants during the treatment process [4].

However, the process of photocatalysis, as an advanced oxidation technology, attracts highest attention of researchers to the decomposition of organic dyes [11, 12]. Such processes are based on light amplification of highly reactive hydroxyl radicals generation, which oxidize organic substance in solution and completely convert it into water, CO_2 and harmless inorganic compounds.

During the photocatalysis reaction, electrons and holes are generated under the action of ultraviolet or visible light falling on the surface of semiconductors, which act as charge carriers. Heterogeneous semiconductor photocatalysts such as ZnO, ZnS, and TiO_2 are of particular interest to researchers [13-16]. Among the presented semiconductor compounds, zinc oxide attracts special attention as a photocatalyst due to the environmental friendliness of its production, optical properties, low cost synthesis, photosensitivity and high thermal stability [17-19].

One of the advantages of ZnO as a photocatalyst is the high mobility of electrons (200-300 $cm^2 \cdot B^{-1} \cdot s^{-1}$), which contributes to greater photodegradation efficiency of pollutants due to rapid electron transfer. Furthermore, the rate of recombination of photogenerated electron-hole (e^- / h^+) pairs is also large. It decreases their availability to the oxidation-reduction reactions with the surrounding material and increases the dissi-

pated energy as heat [13]. Zinc oxide, possessing a wide band gap (3.37 eV) and a high exciton binding energy (60 meV), can absorb most of the UV spectrum, effectively oxidizing and decomposing harmful organic substances in wastewater [20].

Zinc oxide, used as an effective photocatalyst for the decomposition of persistent organic pollutants, must have a high specific surface area to allow the diffusion of active particles and electron transfer. Previous studies of the photocatalytic activity of ZnO have shown high efficiency in the decomposition of dyes [21-23].

Traditionally, ZnO nanoparticles (NPs) are synthesized by various physicochemical methods, but many of these methods have such disadvantages as high cost, the need for high temperature, high pressure, specialized equipment, the use of toxic and environmentally hazardous chemicals, which leads to high energy consumption and the formation of a large amount of waste that is dangerous to the environment [24].

This innovative research used effective, one-step, environmentally friendly and inexpensive synthesis methods of ZnO nanoparticles. These methods make it possible to control the size and shape of nanoparticles, which is useful for improving their chemical, physical, and photocatalytic properties. The close relationship between the morphology and properties of ZnO nanoparticles provides a wide range of its scientific and practical applications [25-29].

Experimental

In this work, the synthesis of ZnO nanoparticles was carried out by two environmentally friendly methods: direct thermal decomposition route [30, 31] and chemical deposition from solution [22].

Direct calcination was performed at cheap zinc acetate salt $(CH_3COO)_2Zn\times2H_2O$ annealing in a muffle furnace in the atmosphere at temperatures of 400 °C and 700 °C. The annealing duration was 10 hours. During annealing zinc acetate salt was placed in a ceramic crucible covered with a ceramic lid. At the same time, the mass of the obtained ZnO NPs sample was (1/4-1/3) of the initial mass of zinc acetate. According to [32], the main weight loss occurs due to the combustion of acetone ($(CH_3)_2CO$) and carbon dioxide (CO_2) in the precursor. The sample # 1 (annealing at 700 °C for 10 hours) and sample # 2 (annealing at 400 °C for 10 hours) were synthesized by this method.

During low-temperature chemical deposition of ZnO, the growth solution contained zinc acetate dihydrate $(CH_3COO)_2Zn\times2H_2O$ and sodium hydroxide NaOH, dissolved in distilled water. The concentration of zinc acetate ($ZnAc_2$) was 0.1 M. Initially, salt and alkali were dissolved in water separately for 30 minutes. For the formation of zinc oxide nanoparticles (ZnO NPs) sodium hydroxide solution at room temperature was added dropwise into a beaker with a solution of zinc acetate. Then the entire solution was thoroughly stirred on a magnetic stirrer for 15 minutes. The synthesis of ZnO samples was carried out at room temperature at all stages. The resulting precipitate was washed with distilled water, separated by centrifugation, and then dried in an oven at 100 °C for 12 hours. The synthesized ZnO powders were finished annealing in a muffle furnace at 450 °C for an hour. The alkali concentration during the synthesis of the sample # 3 was 0.4 M, and for the sample # 4 it was 0.7 M NaOH.

Morphology (FESEM), X-ray diffraction analysis (XRD), optical properties and photocatalytic activity were studied for all synthesized ZnO NPs samples.

Results and Discussion

The morphology of synthesized samples was studied by Quanta 200i 3D scanning electron microscope (FEI Company). Figure 1 shows the morphology of synthesized ZnO nanoparticles. An electron microscopy analysis showed that at zinc acetate calcination at 400 °C and 700 °C, ZnO grows in the form of rods, the geometric parameters of which increase with longer annealing of $ZnAc_2$ (Fig. 1 a, b). The thermal decomposition route at 400 °C allows to obtain more thin long ZnO rods (Fig. 1 b) then at 700 °C (Fig. 1 a). The method of chemical deposition from a solution with 0.4M and 0.7M an alkali concentration in the growth solution makes it possible to synthesize ZnO in the form of thin 2D plates (Fig. 1 c, d). Commercial ZnO NPs (sample # 5, Sigma-Aldrich, USA) with high purity 99,999 % have an irregular rectangular form (Fig. 1e).

The physicochemical characteristics of all ZnO samples are presented in Table 1. Table 1 shows that ZnO NPs sample # 2, synthesized in the form of rods, and sample # 3, synthesized by chemical deposition from solution, possessed by highest aspect ratio.

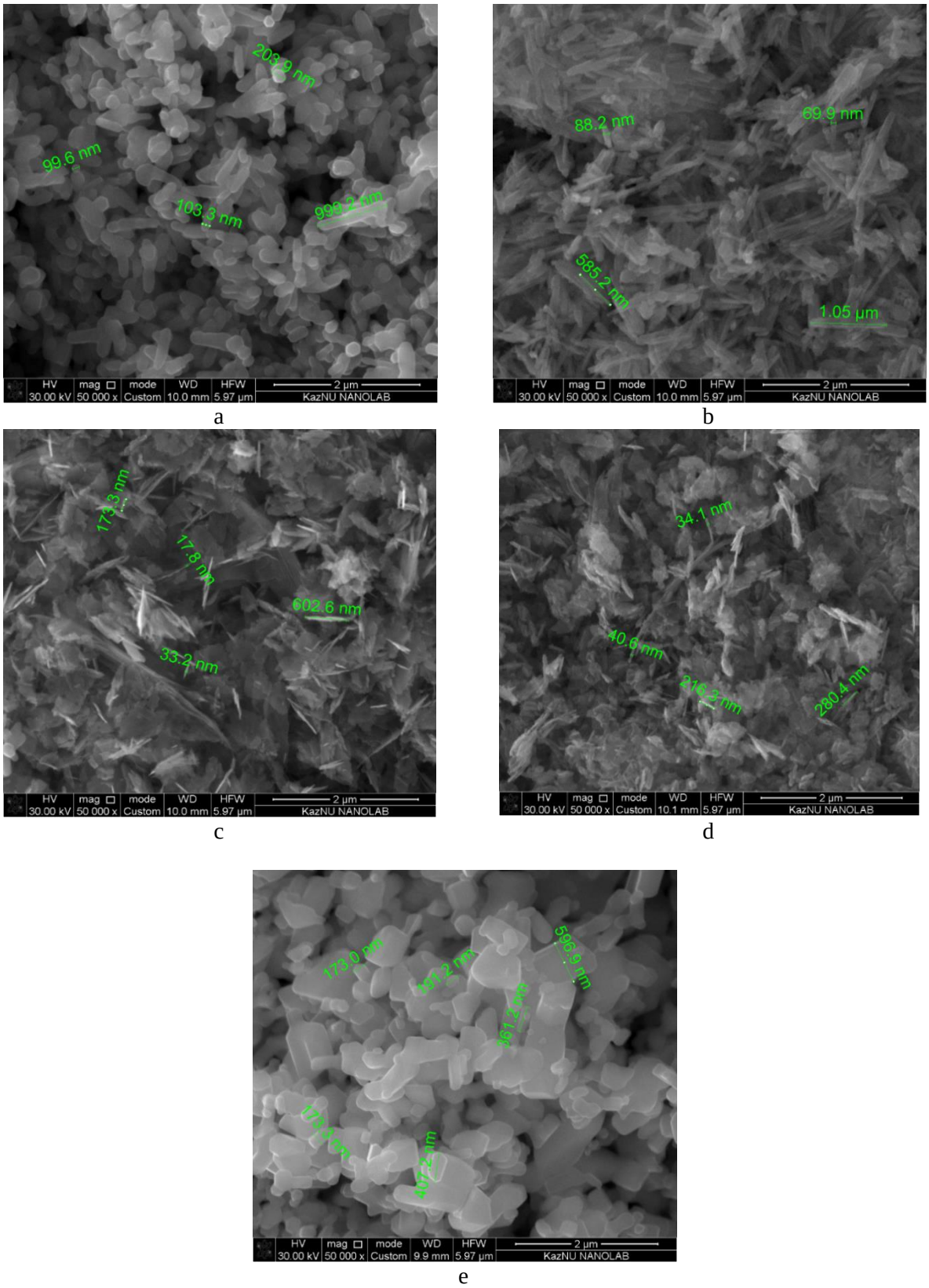

Figure 1. FESEM images of ZnO samples: a — # 1, b — # 2, c — # 3, d — # 4, e — # 5

Table 1

Physicochemical characteristics of ZnO samples

Sample	FESEM		Aspect ratio, l/d	Cell parameters, Å	
	Thickness d, nm	Length l, nm		a	c
# 1	140±20	670±50	4.8	3.243	5.197
# 2	70±20	900±50	12.9	3.245	5.200
# 3	25±5	520±5	20.8	3.253	5.209
# 4	33±5	270±5	8.2	3.251	5.208
# 5	170±20	390±50	2.3	3.251	5.208

The structural properties of the all ZnO samples were studied by X-ray diffraction analysis. X-ray diffraction measurements were performed under the same conditions for all samples on an X-ray diffractometer X'pert MPD PRO (PANalitical) (Fig. 2). The XRD peaks have been labelled according to the reference spectra (JCPDS Card No. 80-0075) of ZnO wurtzite structure with P63mc space group. We see that the (101) reflex is more intensive among all the others observed diffraction peaks that demonstrates a good crystalline quality of all considered samples. All ZnO samples show a slight difference in the intensity and width of the diffraction peaks, therefore the half-width of X-ray reflections (100), (002), and (101) was considered in more particular (Table 2).

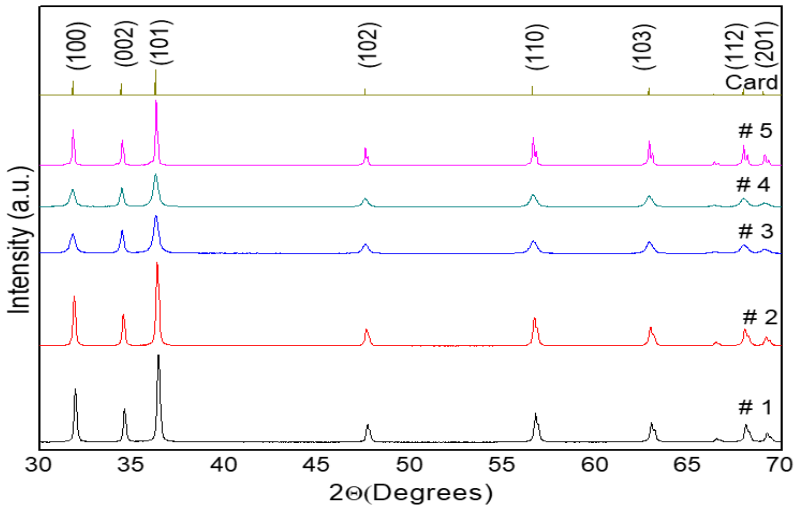

Figure 2. X-ray diffraction of ZnO samples

The results of the study showed that an increasing of the annealing temperature of zinc acetate in the atmosphere leads to an increasing in the size of zinc oxide crystallites along the (002) and (101) directions. It is noted that an increase in the concentration of alkali in the growth solution from 0.4 M to 0.7 M during the ZnO synthesis by chemical deposition makes it possible to obtain thinner extended 2D plates.

Table 2

Half-width of X-ray reflections of ZnO samples

Sample		FWHM	
	(100)	(200)	(101)
# 1	0,18	0,16	0,19
# 2	0,18	0,19	0,20
# 3	0,34	0,20	0,34
# 4	0,31	0,22	0,32
# 5	0,14	0,16	0,16

The ZnO crystallites sizes (d) were estimated based on the XRD analysis for the most intense peak (101) by employing the Scherrer's formula,

$$d = k\lambda / \beta \cos \theta, \qquad (1)$$

here k=0.89 is a dimensionless coefficient (Scherrer's constant), λ = 1.54 Å is the wavelength of CuKa radiation, θ is the diffraction angle, and β is the half-width of X-ray reflections in radians. The obtained results are consistent with the data of electron microscopy (Table 1).

The optical absorption spectra were measured by a double-beam UV / Vis Lambda 35 spectrophotometer (PerkinElmer). Figure 3 shows the absorption spectra in the UV-visible region of all considered ZnO samples. All samples are transparent in the visible spectrum and absorb light in the UV range. The maximum absorption is observed at a wavelength of 375 nm, that is corresponds to ~ 3,31 eV optical band gap according to Tauc's extrapolation [33].

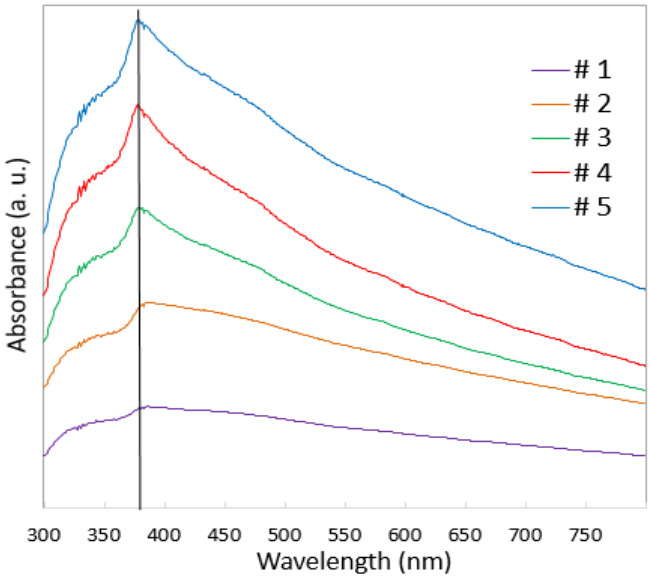

Figure 3. Absorbance spectra of synthesized ZnO samples

Photocatalysis is a change in the rate of chemical reactions under the action of catalytic substances that are activated at light irradiation, and participate in the reaction, but they are not included in the final products. Measurement of the photocatalytic activity of all synthesized ZnO NPs samples was carried out while observing the decomposition of the test substance, the dye rhodamine-B ($C_{28}H_{31}ClN_2O_3$, IMP, OAS "Reactive", Russia). Photocatalytic decomposition usually includes photoexcitation, charge separation and migration, and surface redox reactions [34]. Figure 4 is a schematic diagram illustrated the photocatalytic mechanism of dye decomposition in the presence of ZnO.

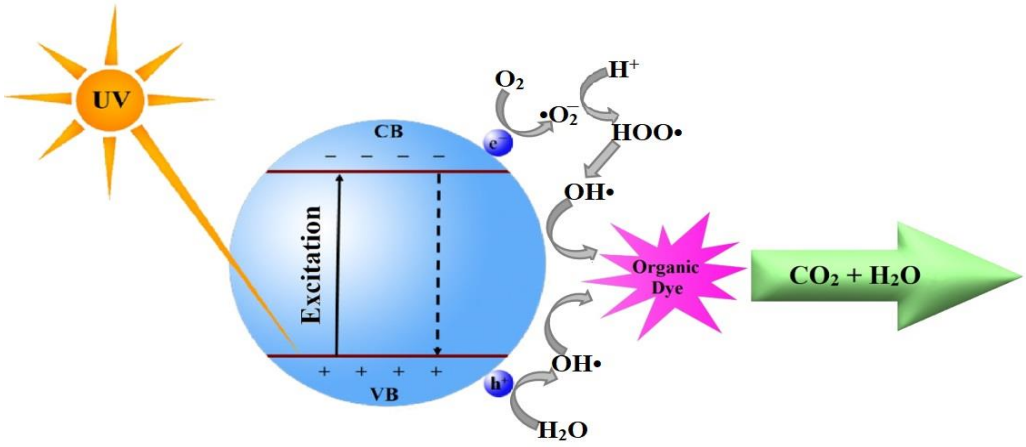

Figure 4. Scheme of the RhB decomposition mechanism on the ZnO NPs surface

Under UV light illuminated, an electron (e^-) from the ZnO valence band passes into the conduction band, and a hole (h^+) is formed in the valence band. The formed e^- (h^+) reacts with a water molecule (atmospheric oxygen), because of which hydroxyl radicals OH• and superoxide anions $•O_2^-$ are formed, and at the same time protonation gives HOO• radicals. The radicals are oxidized, leading to the production of intermediate compounds. The intermediate compounds eventually destroy the organic dye, forming CO_2 and H_2O as shown in Figure 4, while the following reactions are possible [35, 36]:

$$ZnO + h\nu \rightarrow ZnO_{CB}(e^-) + ZnO_{VB}(h^+),$$
$$ZnO_{VB}(h^+) + H_2O \rightarrow ZnO + H^+ + OH•,$$
$$ZnO_{VB}(h^+) + OH^- \rightarrow ZnO + OH•,$$
$$•O_2^- + H^+ \rightarrow HOO•,$$
$$HO_2• + HO_2• \rightarrow H_2O_2 + O_2,$$
$$ZnO_{CB}(e^-) + H_2O_2 \rightarrow OH• + OH^-, \quad (2)$$
$$H_2O_2 + •O_2^- \rightarrow OH• + OH^- + O_2,$$
$$H_2O_2 + h\nu \rightarrow 2OH•,$$
$$\text{Organic pollutants} + OH• \rightarrow \text{Intermediates},$$
$$\text{Intermediates} \rightarrow CO_2 + H_2O.$$

An aqueous dye solution, containing 0.08 mg RhB in 500g of distilled water was used at the investigation of the photocatalytic activity of the synthesized and commercial ZnO NPs under ultraviolet radiation. 9 mg of the ZnO sample was added to this solution. The prepared solution was treated in an ultrasonic bath for 30 min, followed by stirring on a magnetic stirrer at room temperature. A mercury arc lamp (LEH Germany UL Q 14 4P SE) with a power of 14 W, which was placed in a flask with a prepared dye solution, was used for ultraviolet illumination.

It was noted that with an increase in the exposure time, the absorption intensity of RhB gradually decreases in the presence of ZnO NPs, which indicates a decrease in the concentration of the RhB dye. The comparative concentration of RhB dye decreases with increasing exposure time, while for all the presented samples, RhB dye significantly decomposes on the ZnO NPs surface under the influence of UV illumination in the first 30 minutes of exposure and almost completely disappears after 150 minutes. Figure 5 is a photo of initial RhB solution and after each subsequent 30 minutes of UV exposure in the presence of a sample # 3.

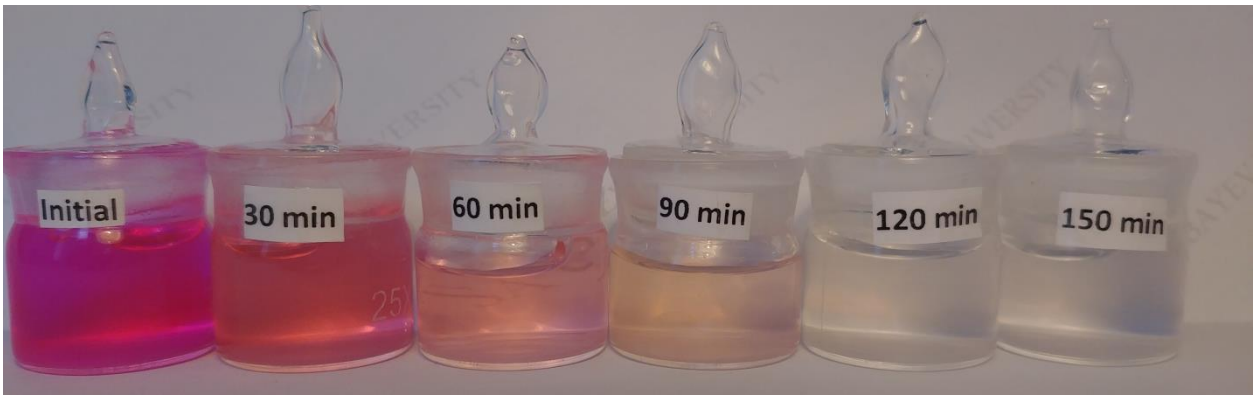

Figure 5. Photo of RhB solution in the presence of # 3 after each 30 min of UV exposure

In order to perform a quantitative analysis of the photocatalytic activity of all synthesized samples of ZnO NPs, the ratio $R = C / C_0$ was calculated as a function of the time of UV illumination (Fig. 6). In this ratio, C is the dye concentration after irradiation with UV radiation at the maximum intensity, C_0 is the initial concentration of the RhB dye.

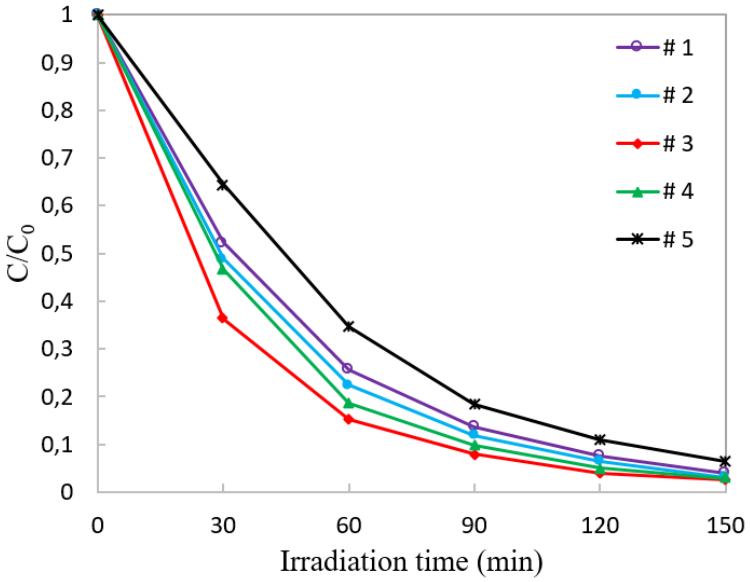

Figure 6. Photodegradation curves of RhB solution by using ZnO NPs as catalysts under irradiation with UV light

The Langmuir — Hinshelwood kinetic model was used to estimate the photodegradation rate k of ZnO NPs [36, 37]:

$$\ln (C_0 / C) = kt, \quad (3)$$

hence

$$k = \frac{lnR}{-t} = \frac{ln\,(C_0 / C)}{t}. \quad (4)$$

The dependence of $\ln(C_0/C)$ as a function of the UV illumination time is shown in Figure 7. The values of both the minimum k_{min}, maximum k_{max}, and the average degradation rate k_{av} of the dye in the presence of ZnO photocatalysts, calculated after each 30 minutes, are shown in Table 2. Based on the ratio R* = 100 (1 — R), the percentage of the decomposed RhB dye in an aqueous solution for 2.5 hours of exposure in the presence of considered ZnO samples was calculated.

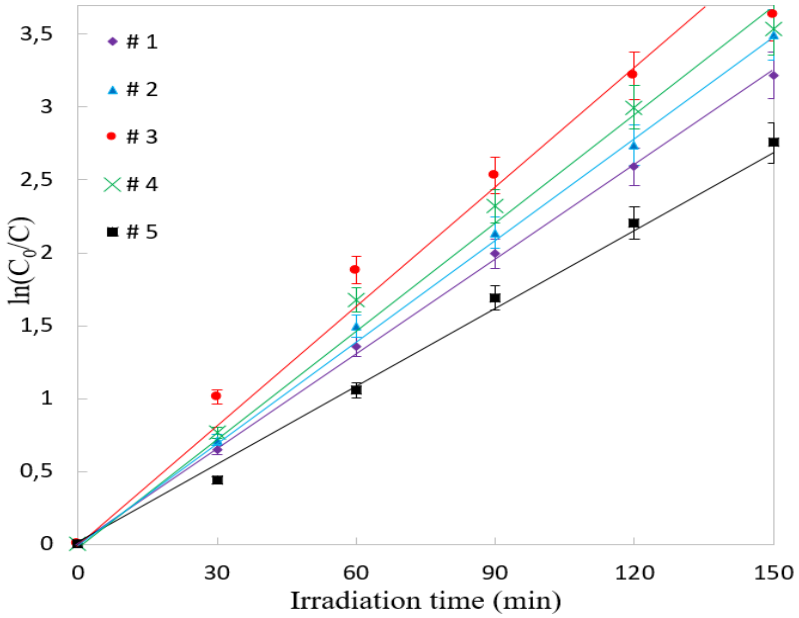

Figure 7. Plots of $\ln(C_0/C)$ as function of UV light irradiation time for the degradation of RhB dye in the presence of ZnO samples as photocatalyst

Figures 6 and 7 show that all studied samples have high photocatalytic activity. It was noted that the highest activity corresponds to samples # 3 that has the highest AR of considered ZnO samples (Table 1). Others ZnO samples demonstrate a slightly less photoactivity. The smallest photoactivity has commercial ZnO sample #5 with smallest AR.

Table 3

Photocatalytic efficiency of ZnO samples

Sample	R^* after 150 min, %	k, min^{-1}		k_{av}, min^{-1}	k_{av}, hr^{-1}
		min	max		
# 1	95.9888	0.0214	0.0226	0.0219	1.3131
# 2	96.9607	0.0228	0.0249	0.0237	1.4241
# 3	97.3601	0.0242	0.0337	0.0289	1.7312
# 4	97.0830	0.0236	0.0280	0.0256	1.5331
# 5	93.6376	0.0146	0.0188	0.0176	1.0534

As follows from Figure 7 and Table 3, in the presence of all considered ZnO samples, a high rate of RhB decomposition in an aqueous solution under UV radiation is observed. The average degradation rate of the dye varies from 0.0176 min^{-1} (for the commercial ZnO sample) to 0.0289 min^{-1} (for the sample # 3). It was noted that ~ (94 — 97) % of the initial dye concentration in the aqueous solution decomposes after 150 minutes of exposure in the presence of these samples. The highest percentage of RhB decomposition corresponds to the sample # 3 (~ 97.4 %) with k_{max} = 0.0337 min^{-1}, synthesized at room temperature by a low-cost chemical deposition from a water grow solution with 0.4M NaOH.

Conclusions

The effect of the morphology of ZnO NPs samples synthesized by simple, low-cost, environmentally friendly synthesis methods: direct thermal decomposition route and chemical deposition, on their optical and photocatalytic properties with respect to the degradation of the rhodamine-B dye in an aqueous solution under the action of UV radiation was studied. It is shown that during thermal decomposition of zinc acetate in the atmosphere at 400 °C and 700 °C for 10 hours, ZnO particles are formed in the form of rods of different diameters. The used parameters of chemical deposition from solution at an alkali concentration of NaOH in the growth solution of 0.4 and 0.7 M make it possible to grow ZnO in the form of thin 2D plates. The results of X-ray diffraction, analysis of the half-width of X-ray reflections, as well as consistent with them scanning electron microscopy data of synthesized ZnO samples showed that the determining factor for photocatalytic activity is the value of the AR parameter. Thus, an increase in the aspect ratio of ZnO NPs makes it possible to obtain more photocatalytically active ZnO samples. All studied samples demonstrate high photocatalytic activity. Within 2.5 hours of UV exposure in the presence of these samples ~ (94 — 97) % of the initial concentration of dye in the aqueous solution decomposes. The highest percentage of RhB decomposition corresponds to the sample # 3 synthesized at room temperature by a low-cost chemical deposition from a solution with 0.4 M NaOH in the growth solution. This sample has the highest value of the AR parameter. In the presence of all the considered samples of ZnO NPs, a high rate of degradation of the RhB dye in an aqueous solution under the influence of UV radiation is noted (0.0176 min^{-1} — 0.0289 min^{-1}). Hence, all considered methods used for the synthesis of ZnO NPs with the indicated parameters make it possible to obtain highly active photocatalysts for the decomposition of organic dyes under UV radiation. These methods are economical, easy to implement, do not require complex expensive equipment, and are appropriate for large-scale production.

References

1 Nyankson E. Synthesis of TiO_2–Ag_3PO_4 photocatalyst material with high adsorption capacity and photocatalytic activity: application in the removal of dyes and pesticides / E. Nyankson, J.K. Efavi, B. Agyei-Tuffour, G. Manu // RSC Adv. — 2021. — 11. — P. 17032.

2 Qi K. Review on the improvement of the photocatalytic and antibacterial activities of ZnO / K. Qi, B. Cheng, J. Yu, W. Ho // J. Alloys Compd. — 2017. — 727. — P. 792–820.

3 Sousa J.C.G. A review on environmental monitoring of water organic pollutants identified by EU guidelines / J.C.G. Sousa, A.R. Ribeiro, M.O. Barbosa, M.F.R. Pereira, A.M.T. Silva // Journal of Hazardous Materials. — 2018. — Vol. 344. — P. 146-162.

4 Ren G. Recent Advances of Photocatalytic Application in Water Treatment: A Review / G. Ren, H. Han, Y. Wang, S. Liu, J. Zhao, X. Meng, Z. Li // *Nanomaterials.* — 2021. — 11. — P. 1804.

5 Zazouli M.A. Removal of precursors and disinfection by-products (DBPs) by membrane filtration from water: A review / M.A. Zazouli, L.R. Kalankesh // J. Environ. Health Sci. Eng. — 2017. — 15. — P. 25.

6 Zularisam A.W. Behaviours of natural organic matter in membrane filtration for surface water treatment-a review / A.W. Zularisam, A.F. Ismail, R. Salim // Desalination. — 2006. — 194. — P. 211–231.

7 Azimi A. Removal of heavy metals from industrial wastewaters: A review / A. Azimi, A. Azari, M. Rezakazemi, M. Ansarpour // ChemBioEng Rev. — 2017. — 4. — P. 37–59.

8 Yagub M.T. Dye and its removal from aqueous solution by adsorption: A review / M.T. Yagub, T.K. Sen, S. Afroze, H.M. Ang // Adv. Colloid Interface Sci. — 2014. — 209. — P. 172–184.

9 Mousset E. A review of electrochemical reduction processes to treat oxidized contaminants in water / E. Mousset, K. Doudrick // Curr. Opin. Electrochem. — 2020. — 22. — P. 221–227.

10 Arar Ö. Various applications of electrodeionization (EDI) method for water treatment-A short review / Ö. Arar, Ü. Yüksel, N. Kabay, M. Yüksel // Desalination. — 2014. — 342. — P. 16–22.

11 Markhabayeva Aiymkul. Effect of synthesis method parameters on the photocatalytic activity of tungsten oxide nanoplates / Aiymkul Markhabayeva, Khabibulla Abdullin, Zhanar Kalkozova, Shyryn Nurbolat, Nurxat Nuraje // AIP Advances. — 2021. — 11. — 095220.

12 Prikhodko O.Yu. Photocatalytic activity of liquid-phase exfoliated gallium selenide flakes / O.Yu. Prikhodko, M.B. Aitzhanov, N.R. Gusseinov, Zh.K. Kalkozova, K.K. Dikhanbaev, A.A. Markhabayeva, M.M. Myrzabekova, R.R. Nemkayeva, Ye.S. Mukhametkarimov // Chalcogenide Letters. — 2021. — 18. — P. 777-781.

13 Hyeonhan L. Efficient photocatalytic degradation of dyes using photo-deposited Ag nanoparticles on ZnO structures: simple morphological control of ZnO / L. Hyeonhan, M. Yusuf, S. Song, S. Park, K.H. Park // RSC Adv. — 2021. — 11. — P. 8709-8717.

14 Abdullin Kh.A. Electrical, Optical, and Photoluminescence Properties of ZnO Films Subjected to Thermal Annealing and Treatment in Hydrogen Plasma / Kh.A. Abdullin, M.T. Gabdullin, L.V. Gritsenko, D.V. Ismailov, Zh.K. Kalkozova, S.E. Kumekov, Zh.O. Mukash, A.Yu. Sazonov, E.I. Terukov // J. Semiconductors. — 2016. — No. 50(8). — P. 1010-1014.

15 Katal R. A review on the synthesis of the various types of anatase TiO2 facets and their applications for Photocatalysis / R. Katal, S. Masudy-Panah, M. Tanhaei, M.H. Farahani, H. Jiangyong // Chem. Eng. J. — 2020. — 384. — P. 123384.

16 Kedruk Y.Y. Investigation of the Properties of Zinc Oxide by the Method of impedance spectroscopy. / Y.Y. Kedruk, A.A. Bobkov, L.V. Gritsenko, V.A. Moshnikov // Glass Physics and Chemistry. — 2022. — 48 (2). — P. 123–129.

17 Adawiya J.H. A review of Pure and Doped ZnO Nanostructure Production and its Optical Properties Using Pulsed Laser Deposition Technique / J.H. Adawiya, A.J. Allaa, A.A. Ghalib // Journal of Physics: Conference Series. — 2021. — 1795. — 012015.

18 Ramírez A.E. Significantly enhancement of sunlight photocatalytic performance of ZnO by doping with transition metal oxides / A.E. Ramírez, M. Montero-Muñoz, L.L. López, J.E. Ramos-Ibarra, J.A.H. Coaquira, B. Heinrichs, C.A. Páez // Scientific Reports. — 2021. — 11. — 2804.

19 EL-Dafrawy Sh.M. Synthesis, photocatalytic and antidiabetic properties of ZnO/ PVA nanoparticles / Sh.M. EL-Dafrawy, M. Tarek, S. Samra, Sh.M. Hassan // Scientific Reports. — 2021. — 11. — 11404.

20 Blažeka D. Photodegradation of Methylene Blue and Rhodamine B Using Laser-Synthesized ZnO Nanoparticles / D. Blažeka, J. Car, N. Klobučar, A. Jurov, J. Zavašnik, A. Jagodar, E. Kovačević, N. Krstulović // Materials. — 2020. — 13. — 4357.

21 Alberti S. Experimental and Physico-Chemical Comparison of ZnO Nanoparticles' Activity for Photocatalytic Applications in Wastewater Treatment / S. Alberti, I. Basciu, M. Vocciante, M. Ferretti // Catalysts. — 2021. — 11. — 678.

22 Kedruk Y.Y. Facile Low-Cost Synthesis of Highly Photocatalitycally Active Zinc Oxide Powders / Y.Y. Kedruk, G.A. Baigarinova, L.V. Gritsenko, G. Cicero, Kh.A. Abdullin // Frontiers in Materials. — 2022. — 9. — 1-11.

23 Guaraldo T.T. Photocatalytic ZnO Foams for Micropollutant Degradation / T.T. Guaraldo, J. Wenk, D. Mattia // *Adv. Sustainable Syst.* — 2021. — 5. — 2000208.

24 Al-Kordy H.M.H. Statistical optimization of experimental parameters for extracellular synthesis of zinc oxide nanoparticles by a novel haloalaliphilic Alkalibacillus sp. W7. / H.M.H. Al-Kordy, S.A. Sabry, M.E.M. Mabrouk // Sci. Rep. — 2021. — 11. — 10924.

25 Balakumaran M.D. Mycosynthesis of silver and gold nanoparticles: optimization, characterization and antimicrobial activity against human pathogens / M.D. Balakumaran, R. Ramachandran, P. Balashanmugam, D.J. Mukeshkumar, P.T. Kalaichelvan // Microbiol. Res. — 2016. — 182. — 8–20.

26 Wibowo A. ZnO nanostructured materials for emerging solar cell applications / A. Wibowo, M.A. Marsudi, M.I. Amal, M.B. Ananda, R. Stephanie, H. Ardy, L.J. Diguna // RSC Advances. — 2020. — 10. — — 42838-42859.

27 Kang Y. Review of ZnO-based nanomaterials in gas sensors / Y. Kang, F. Yu, L. Zhang, W. Wang, L. Chen, Y. Li // *Solid State Ionics*. — 2021. — 360. —115544.

28 Zakria M. Highly Luminescent MgZnO/ZnO Multiple Quantum Wells for Photonics Devices. ACS Appl / M. Zakria, T.T. Huynh, F.C.C. Ling, S.C. Su, M.R. Phillips, C. Ton-That // Nano Mater. — 2019. — 2. — 2574–2579.

29 Rahman, F. (2019). Zinc oxide light-emitting diodes: a review / F. Rahman // Optical Engineering. — 2019. — 58(1). — 1010901.

30 Maraeva E.V. Creating a virtual device for processing the results of sorption measurements in the study of zinc oxide nanorods / E.V. Maraeva, N.V. Permiakov, Y.Y. Kedruk, L.V. Gritsenko, Kh.A. Abdullin // Chimica Techno Acta. — 2020. — 7 (4). — 154-158.

31 Уалиханов Р.Е. Фотокаталитические свойства наноструктурированного оксида цинка / Р.Е. Уалиханов, Е.Ю. Кедрук, Л.В. Гриценко, Дж. Чичеро, Х.А. Абдуллин // Вестн. Казах. нац. исслед. техн. ун-та. — 2019. — № 3 (133). — С. 542–548.

32 Labuayai S. Synthesis and optical properties of nanocrystalline ZnO powders prepared by a direct thermal decomposition route / S. Labuayai, V. Promarak, S. Maensiri // Appl Phys A. — 2009. — 94. — 755–761.

33 Rusdi R. Preparation and band gap energies of ZnO nanotubes, nanorods and spherical nanostructures / R. Rusdi, A.A. Rahman, N.S. Mohamed, N. Kamarudin, N. Kamarulzaman // Powder Technol. — 2011. — 210 (1). — 8–22.

34 Azfar A.K. Comparative study on photocatalytic activity of transition metals (Ag and Ni)-doped ZnO nanomaterials synthesized via sol–gel method / A.K. Azfar, M.F. Kasim, I.M. Lokman, H.A. Rafaie, M.S. Mastuli // R. Soc. open sci. — 2020. — 7. — 191590.

35 Onga Ch.B. A review of ZnO nanoparticles as solar photocatalysts: Synthesis, mechanisms and applications / Ch.B. Onga, L.Y. Ngb, A.W. Mohammad // Renewable and Sustainable Energy Reviews. — 2018. — 81. — 536–551.

36 Mauro A.D. ZnO for application in photocatalysis: From thin films to nanostructures / A.D. Mauro, M.E. Fragalà, V. Privitera, G. Impellizzeri // Materials Science in Semiconductor Processing. — 2017. — 69. — 44–51.

37 Godin R. Understanding the visible-light photocatalytic activity of GaN: ZnO solid solution: the role of $Rh_{2-y}Cr_yO_3$ cocatalyst and charge carrier lifetimes over tens of seconds / R. Godin, T. Hisatomi, K. Domen, J.R. Durran // Chem. Sci. — 2018. — 9. — 7546–7555.

Д.Б. Толубаева, Л.В. Гриценко, Е.Ю. Кедрук, К.К. Мустафина,
М.Б. Айтжанов, Х.А. Абдуллин

Мырыш оксиді морфологиясының оның фотокаталитикалық қасиеттеріне әсері

Өнеркәсіптің қарқынды дамуы оң әсерін тигізумен қатар экологиялық мәселелерді де тудырды. Құрамында бояғыштар, пестицидтер, ауыр металдар және фармацевтикалық қалдықтар сияқты заттары бар ластаушы қалдықтардың шығарылуы судың ластануына әкеліп соғады, бұл адамдар мен су организмдеріне кері әсерін тигізеді. Осыған байланысты ағынды суларды органикалық ластаушы заттардан тазартудың арзан, тиімді, экологиялық таза әдісін жасау ғылыми зерттеулердің өзекті міндеті болып табылады. Мырыш оксиді (ZnO) — ең белсенді жартылай өткізгіш фотокатализаторлардың бірі. Мақалада тиімді әдістермен синтезделген наноқұрылымды мырыш оксидінің морфологиясының родамин-В (RhB) бояғышына қатысты фотокаталитикалық қасиеттерге, сондай-ақ ZnO үлгілерінің ұзындық пен қалыңдық (Ar) қатынасының оның құрылымдық және оптикалық қасиеттеріне әсері зерттелген. Зерттеу нәтижелері атмосферадағы мырыш ацетатының күйдіру температурасының жоғарылауы мырыш оксиді кристаллиттерінің мөлшерінің ұлғаюына әкелетінін және өсу ерітіндісіндегі сілтілік концентрациясының жоғарылауы (ZnO химиялық ыдырау әдісімен 0,4 М-ден 0,7 М-ге дейін синтезделуі) жұқа, ұзартылған 2D пластиналарды алуға мүмкіндік беретінін көрсетті. Синтезделген үлгілердің AR мәнін арттыру олардың фотокаталитикалық белсенділігін арттыруға мүмкіндік беретіні анықталған.

Кілт сөздер: химиялық тұндыру, мырыш оксиді, термиялық ыдырау, оптикалық және құрылымдық қасиеттері, фотокатализатор, родамин-В.

Д.Б. Толубаева, Л.В. Гриценко, Е.Ю. Кедрук, К.К. Мустафина, М.Б. Айтжанов,
Х.А. Абдуллин

Влияние морфологии оксида цинка на его фотокаталитические свойства

Бурное развитие промышленности, помимо положительного влияния, привело к экологическим проблемам. Выброс загрязняющих отходов, содержащих такие вещества, как красители, пестициды, тяжелые металлы и фармацевтические отходы, приводит к загрязнению водоемов, что оказывает негативное воздействие на человека и водные организмы. В связи с этим разработка недорогого, эффективного, экологически чистого способа очистки сточных вод от органических загрязнителей является актуальной задачей научных исследований. Оксид цинка (ZnO) является одним из наиболее активных полупроводниковых фотокатализаторов. В статье исследовано влияние морфологии наноструктури-

рованного оксида цинка, синтезированного эффективными методами, на фотокаталитические свойства по отношению к красителю родамина-B (RhB), а также изучено влияние соотношения длины к толщине (AR) образцов ZnO на его структурные и оптические свойства. Результаты исследования показали, что повышение температуры отжига ацетата цинка в атмосфере приводит к увеличению размеров кристаллитов оксида цинка, а увеличение концентрации щелочи в ростовом растворе (синтез ZnO методом химического осаждения от 0,4M до 0,7M) позволяет получать более тонкие протяженные 2D пластины. Доказано, что увеличение значения AR синтезированных образцов позволяет повышать их фотокаталическую активность.

Ключевые слова: химическое осаждение, оксид цинка, термическое разложение, оптические и структурные свойства, фотокатализатор, родамин-B.

References

1 Nyankson, E., Efavi, J.K., Agyei-Tuffour, B., & Manu, G. (2021). Synthesis of TiO_2–Ag_3PO_4 photocatalyst material with high adsorption capacity and photocatalytic activity: application in the removal of dyes and pesticides. *RSC Adv*., *11*, 17032.

2 Qi, K., Cheng, B., Yu, J., & Ho, W. (2017). Review on the improvement of the photocatalytic and antibacterial activities of ZnO. *J. Alloys Compd.*, *727*, 792–820.

3 Sousa, J.C.G., Ribeiro, A.R., Barbosa, M.O., M. Pereira, F.R., & Silva, A.M.T. (2018). A review on environmental monitoring of water organic pollutants identified by EU guidelines. *Journal of Hazardous Materials, Vol. 344*, 146-162.

4 Ren, G., Han, H., Wang, Y., Liu, S., Zhao, J., Meng, X., & Li, Z. (2021). Recent Advances of Photocatalytic Application in Water Treatment: A Review. *Nanomaterials, 11*, 1804.

5 Zazouli, M.A., & Kalankesh, L.R. (2017). Removal of precursors and disinfection by-products (DBPs) by membrane filtration from water: A review. *J. Environ. Health Sci. Eng., 15*, 25.

6 Zularisam, A.W., Ismail, A.F., & Salim, R. (2006). Behaviours of natural organic matter in membrane filtration for surface water treatment-a review. *Desalination, 194*, 211–231.

7 Azimi, A., Azari, A., Rezakazemi, M., & Ansarpour, M. (2017). Removal of heavy metals from industrial wastewaters: A review. *ChemBioEng Rev., 4*, 37–59.

8 Yagub, M.T., Sen, T.K., Afroze, S., & Ang, H.M. (2014). Dye and its removal from aqueous solution by adsorption: A review. *Adv. Colloid Interface Sci., 209*, 172–184.

9 Mousset, E., & Doudrick, K. (2020). A review of electrochemical reduction processes to treat oxidized contaminants in water. *Curr. Opin. Electrochem, 22*, 221–227.

10 Arar, Ö., Yüksel, Ü., Kabay, N., & Yüksel, M. (2014). Various applications of electrodeionization (EDI) method for water treatment-A short review. *Desalination, 342*, 16–22.

11 Markhabayeva, Aiymkul, Abdullin, Khabibulla, Kalkozova, Zhanar, Nurbolat, Shyryn, & Nuraje, Nurxat. (2021). Effect of synthesis method parameters on the photocatalytic activity of tungsten oxide nanoplates. *AIP Advances, 11*, 095220.

12 Prikhodko, O.Yu., Aitzhanov, M.B., Gusseinov, N.R., Kalkozova, Zh.K., Dikhanbaev, K.K., Markhabayeva, A.A., Myrzabekova, M.M., Nemkayeva, R.R., & Mukhametkarimov, Ye.S. (2021). Photocatalytic activity of liquid-phase exfoliated gallium selenide flakes. *Chalcogenide Letters, 18*, 777-781.

13 Hyeonhan, L., Yusuf, M., Song, S., Park, S., & Park, K.H. (2021). Efficient photocatalytic degradation of dyes using photodeposited Ag nanoparticles on ZnO structures: simple morphological control of ZnO. RSC Adv., 11, 8709-8717.

14 Abdullin, Kh.A., Gabdullin, M.T., Gritsenko, L.V., Ismailov, D.V., Kalkozova, Zh.K., Kumekov, S.E., Mukash, Zh.O., Sazonov, A. Yu., & Terukov, E.I. (2016). Electrical, Optical, and Photoluminescence Properties of ZnO Films Subjected to Thermal Annealing and Treatment in Hydrogen Plasma. *J. Semiconductors, 50*(8), 1010-1014.

15 Katal, R., Masudy-Panah, S., Tanhaei, M., Farahani, M.H., & Jiangyong, H. (2020). A review on the synthesis of the various types of anatase TiO2 facets and their applications for Photocatalysis. *Chem. Eng. J., 384*, 123384.

16 Kedruk, Y.Y., Bobkov, A.A., Gritsenko, L.V., & Moshnikov, V.A. (2022). Investigation of the Properties of Zinc Oxide by the Method of impedance spectroscopy. *Glass Physics and Chemistry*, *48* (2). 123–129.

17 Adawiya, J.H., Allaa, A.J., & Ghalib, A.A. (2021). A review of Pure and Doped ZnO Nanostructure Production and its Optical Properties Using Pulsed Laser Deposition Technique. *Journal of Physics: Conference Series*, *1795*, 012015.

18 Ramírez, A.E., Montero-Muñoz, M., López, L.L., Ramos-Ibarra, J.E., Coaquira, J.A.H., Heinrichs, B., & Páez, C.A. (2021). Significantly enhancement of sunlight photocatalytic performance of ZnO by doping with transition metal oxides. *Scientific Reports*, *11*, 2804.

19 EL-Dafrawy Sh.M., Tarek, M., Samra, S., & Hassan, Sh.M. (2021). Synthesis, photocatalytic and antidiabetic properties of ZnO/ PVA nanoparticles. *Scientific Reports*, *11*, 11404.

20 Blažeka, D., Car, J., Klobučar, N., Jurov, A., Zavašnik, J., Jagodar, A., Kovačević, E., & Krstulović, N. (2020). Photodegradation of Methylene Blue and Rhodamine B Using Laser-Synthesized ZnO Nanoparticles. Materials, *13*, 4357.

21 Alberti, S., Basciu, I., Vocciante, M., & Ferretti, M. (2021). Experimental and Physico-Chemical Comparison of ZnO Nanoparticles' Activity for Photocatalytic Applications in Wastewater Treatment. *Catalysts*, *11*, 678.

22 Kedruk, Y.Y., Baigarinova, G.A., Gritsenko, L.V., Cicero G., & Abdullin Kh.A. (2022). Facile Low-Cost Synthesis of Highly Photocatalitycally Active Zinc Oxide Powders. *Frontiers in Materials*, *9*, 1-11.

23 Guaraldo, T.T., Wenk, J., & Mattia, D. (2021). Photocatalytic ZnO Foams for Micropollutant Degradation. *Adv. Sustainable Syst., 5*, 2000208.

24 Al-Kordy, H.M.H., Sabry, S.A., & Mabrouk, M.E.M. (2021). Statistical optimization of experimental parameters for extracellular synthesis of zinc oxide nanoparticles by a novel haloalaliphilic Alkalibacillus sp. W7. *Sci. Rep., 11*, 10924.

25 Balakumaran, M.D., Ramachandran, R., Balashanmugam, P., Mukeshkumar, D.J., & Kalaichelvan, P.T. (2016). Mycosynthesis of silver and gold nanoparticles: optimization, characterization and antimicrobial activity against human pathogens. *Microbiol. Res., 182*, 8–20.

26 Wibowo, A., Marsudi, M.A., Amal, M.I., Ananda, M.B., Stephanie, R., Ardy, H., & Diguna, L.J. (2020). ZnO nanostructured materials for emerging solar cell applications. *RSC Advances*, *10*, 42838-42859.

27 Kang, Y., Yu, F., Zhang, L., Wang, W., Chen, L., & Li, Y. (2021). Review of ZnO-based nanomaterials in gas sensors. *Solid State Ionics*, *360*, 115544.

28 Zakria, M., Huynh, T.T., Ling, F.C.C., Su, S.C., Phillips, M.R., & Ton-That, C. (2019). Highly Luminescent MgZnO/ZnO Multiple Quantum Wells for Photonics Devices. A*CS Appl. Nano Mater.*, *2*, 2574–2579.

29 Rahman, F. (2019). Zinc oxide light-emitting diodes: a review. *Optical Engineering*, *58*(1), 1010901.

30 Maraeva, E.V., Permiakov, N.V., Kedruk, Y.Y., Gritsenko, L.V., & Abdullin, Kh.A. (2020). Creating a virtual device for processing the results of sorption measurements in the study of zinc oxide nanorods. *Chimica Techno Acta*, *7* (4), 154-158.

31 Ualikhanov, R.E., Kedruk, Ye.Yu., Gritsenko, L.V., Cicero, G., & Abdullin, Kh.A. (2019). Fotokataliticheskie svoistva nanostrukturirovannogo oksida tsinka [Photocatalytic properties of nanostructured zinc oxide. *Vestnik Kazakhskogo natsionalnogo issledovatelskogo tekhnicheskogo universiteta — Bulletin of the Kazakh Natoinal Research Technical University*, *3* (133), 542–548 [in Russian].

32 Labuayai, S., Promarak, V., & Maensiri, S. (2009). Synthesis and optical properties of nanocrystalline ZnO powders prepared by a direct thermal decomposition route. *Appl Phys A., 94*, 755–761.

33 Rusdi, R., Rahman, A.A., Mohamed, N.S., Kamarudin, N., & Kamarulzaman, N. (2011). Preparation and band gap energies of ZnO nanotubes, nanorods and spherical nanostructures. *Powder Technol*, *210* (1), 8–22.

34 Azfar, A.K., Kasim, M.F., Lokman, I.M., Rafaie, H.A., & Mastuli, M.S. (2020). Comparative study on photocatalytic activity of transition metals (Ag and Ni)-doped ZnO nanomaterials synthesized via sol–gel method. *R. Soc. open sci., 7*, 191590.

35 Onga, Ch.B., Ngb, L.Y., & Mohammad, A.W. (2018). A review of ZnO nanoparticles as solar photocatalysts: Synthesis, mechanisms and applications. *Renewable and Sustainable Energy Reviews*, *81*, 536–551.

36 Mauro, A.D., Fragalà, M.E., Privitera, V., & Impellizzeri, G. (2017). ZnO for application in photocatalysis: From thin films to nanostructures. *Materials Science in Semiconductor Processing*. *69*, 44–51.

37 Godin, R., Hisatomi, T., Domen, K., & Durran, J.R. (2018). Understanding the visible-light photocatalytic activity of GaN: ZnO solid solution: the role of $Rh_{2-y}Cr_yO_3$ cocatalyst and charge carrier lifetimes over tens of seconds. *Chem. Sci*., *9*, 7546–7555.

DOI 10.31489/2023PH2/46-51

UDC: 535.215; 539.23; 535.3; 535.3; 538.9

T.E. Seisembekova[1], A.K. Aimukhanov[2], B.R. Ilyassov[3],
D. Valiev[4], A.K. Zeinidenov[5], A.M. Zhakhanova[6]

[1,2,5,6] Karaganda University of the name of academician E. A. Buketov, Scientific Center for Nanotechnology and Functional Nanomaterials, Karaganda, Kazakhstan;
[3]Astana IT University, Astana, Kazakhstan;
[4] Tomsk Polytechnic University, Lenin avenue, 30, Tomsk, Russian Federation
(E-mail: tosh_0809@mail.ru)

Effect of ZnO in various alcohols on photoelectric characteristics of OSC

The paper presents the results of a study of the effect of alcohols on the electron transport of the ETL layer of a ZnO polymer solar cell with an inverted structure. To obtain films, zinc acetate was dissolved under the same experimental conditions in isopropanol, butanol and ethanol. According to the SEM data, it was found that the use of various alcohol solvents in the synthesis of the film shows a change in the morphology of the surface. The observed changes in the interface of the surface of the films are associated with the formation of ZnO aggregates depending on the polarity used of the alcohols. It is shown that the optical width of the ZnO band gap also depends on alcohol solvents. It is shown that the aggregation of ZnO has an effect on the electron transport and efficiency of the polymer solar cell. The voltage characteristics of the solar cells FTO/ ZnO/P3HT: IC60MA/PEDOT: PSS/Ag were measured. It is shown that the smallest aggregation of ZnO is observed in Isopropanol, in which the organic cell showed the highest efficiency of converting solar energy into electrical energy. The polymer solar cell has been the efficiency 2.5 %. From the obtained ETL impedance measurement data, the ZnO based layer obtained in Ethanol has the lowest electron transport parameters. This is due to the high degree of aggregation of ZnO, as a result of which the resistance to increases of the interface ZnO/FTO. The solar cells based ZnO in Ethanol demonstrated an efficiency value of 0.9 % compared to ZnO in Butanol with an efficiency of 1.6 %.

Keywords: ZnO, Isopropanol, Ethanol, Butanol, surface morphology, thermal annealing, optical spectroscopy, impedance spectroscopy.

Introduction

Obtaining electrical energy from the sun is one of the ways that in the near future can provide a rapidly growing demand for clean energy. Among the currently existing various phototransverters, organic solar cells are of great interest. Currently, the efficiency of organic solar cells (OSC) already exceeds 15 % [1-3]. The photoactive OSC layer is a volumetric heterojunction in which electron and acceptor materials are mixed in the active layer, forming an interfacial region where excitons are separated. To minimize charge recombination at both interfaces and increase the efficiency of charge extraction, a volumetric heterojunction is placed between the electron transfer transport layer (ETL) and the hole transfer layer (HTL). The inverted structure is widely used in OSC due to the simple manufacturing technology, good stability and efficient phase separation [4].

The ETL layer based on metal oxides has attracted great attention due to its high transparency in the visible spectral region, as well as the possibility of changing energy levels and electrical properties by doping or chemical modification [5]. Among the known metal oxides used in OSC, ZnO [6], TiO2 [7], etc. can be distinguished. In inverted OSCs, the morphology and structure of ZnO have a strong influence on the efficiency of organic solar cells [8].

ZnO is a multifunctional semiconductor with a straight wide band gap (3.37 eV for ZnO wurtzite). ZnO has a fairly high exciton binding energy (60 MeV), which makes the semiconductor thermally and chemically stable [9]. However, the high reactivity in water leads to a rapid growth of ZnO crystallites, which makes it difficult to control the synthesis of nanometer-scale particles. Alcohol solvents are used to prevent the growth of ZnO nanoparticles [10]. It is known that the morphology of the surface of ZnO films depends on the length of the alkyl chain of alcohols [11].

In this work, the influence of alcohol solvents of different polarities on the morphology, optical and electrophysical characteristics of ZnO films was studied. The results of the study of the effect of ZnO films obtained in alcohols of different polarities on the efficiency of OSC are presented.

Experimental

To obtain compact layers of ZnO, the following materials were used: $Zn_5(OH)_8Cl_2$, Isopropanol, Ethanol, Butanol (pure 99.9 % Sigma Aldrich). At first the FTO covered glass substrates were rigorously cleaned [12]. The preparation of solutions was carried out in accordance with the method. For this $Zn_5(OH)_8Cl_2$ (weighted m =49.3 mg) was dissolved separately in volume (V= 0.5 ml) in Isopropanol, Ethanol, Butanol. After Monoethanolamine (Sigma Aldrich) was added to the obtained solutions after 20 minutes in an amount (V = 38 μl). Further, the solutions were mixed at a temperature of T = 60 °C for 2 hours, and then kept for 24 hours at room temperature.

At the next stage, the solutions were applied to the FTO surface by spin-coating at a speed of 4000 rpm. After the film was annealed in an air atmosphere at a temperature of 200 °C for 15 minutes, then annealed at a temperature of 450 °C for one hour. A photoactive layer of P3HT: IC60MA (pure 97 % Sigma Aldrich) at a concentration of 1:0.8 was applied to the surface of the resulting ZnO film by spin-coating. After that, the samples were annealed in an air atmosphere at a temperature of 140 °C for 10 minutes, then PEDOT: PSS was applied to the surface of the photoactive layer by spin-coating in volume (V=25 μl) after annealing in an air atmosphere at a temperature of 115 °C for 10 minutes, then to the surface of the film by thermal deposition silver electrode was sprayed on the CY-1700x-spc-2 installation (Zhengzhou CY Scientific Instruments Co., Ltd).

Microstructural characterization of the obtained samples was carried out using a scanning electron microscope MIRA 3 LMU(TESCAN). The absorption spectra of the studied samples were recorded using an AvaSpec-ULS2048CL-EVO spectrometer manufactured by Avantes, which registers absorption spectra in the range of 200-1100 nm and has an optical resolution of 0.04 nm. Measurements of the impedance spectra were carried out using in the impedance mode a potentiostat-galvanostat P45X. The VAC of photosensitive cells was determined by the Sol 3A Class AAA Solar Simulators (Newport) with the PV IV-1A IV Test Station.

Results and Discussion

Figure 1 shows SEM images of ZnO films obtained in isopropanol (a), butanol (b) and ethanol (c). It can be seen from the figures that the surface interfaces of the films differ. This is due to the influence of alcohol solvents such as isopropanol, butanol, and ethanol. So, in isopropanol, the grain sizes on the surface of the film are about 10 nm. Further, it can be seen that the ZnO grains obtained in butanol are less than 20 nm (Fig. 1b). At the same time, the coarse-grained structure of ZnO is obtained in ethanol with a size greater than 20 nm (Fig. 1c).

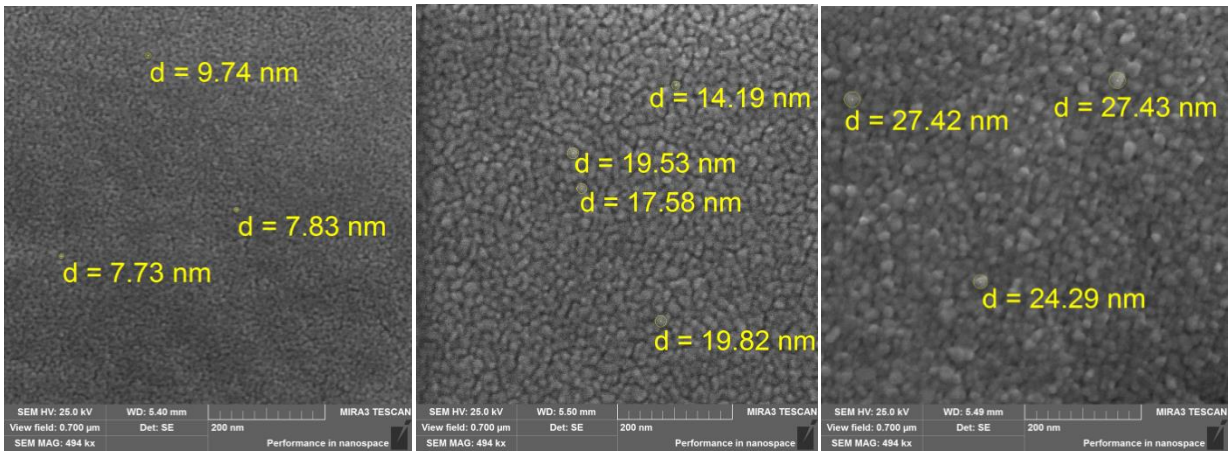

a) b) c)

Figure 1. SEM images of a) Isopropanol; b) Butanol; c) Ethanol

The influence of alcohol solvents of different polarities is associated with the aggregation of ZnO nanoparticles due to non-covalent interactions, such as hydrogen bonding, which provides a weaker electrostatic interaction in the film.

Figure 2 shows the absorption spectra of ZnO films obtained with different alcohols.The absorption spectrum is typical of the absorption spectrum of wide-band semiconductors.The edge of the fundamental

absorption band falls at 380 nm, which corresponds to the optical transition of the ZnO band gap. The figure shows the dependences of the ZnO band gap width depending on alcohol solvents. The graph shows that the aggregation of ZnO in the film leads to a decrease in the optical band gap from 3.2 eV to 2.8 eV. A decrease in the optical band gap leads to a decrease in the degree of crystallinity of ZnO.

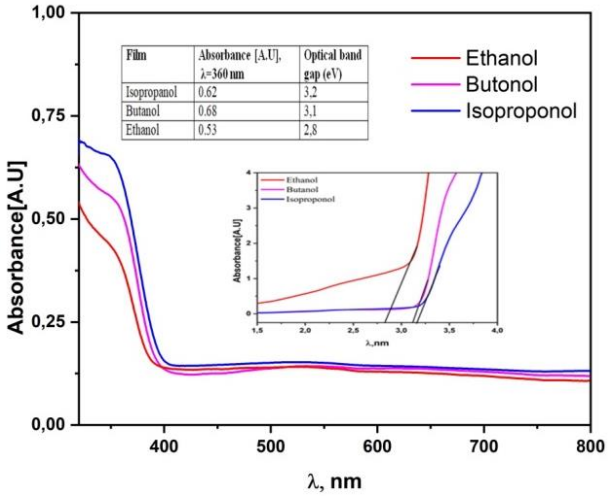

Figure 2. Absorption spectra and Tauc plots (the inset) of films

To determine the effect of alcohol solvents on the transport and recombination of charges in the ZnO of a polymer solar cell, an organic cell FTO/ZnO/P3HT: IC60MA/PEDOT: PSS/Ag was assembled. The voltage characteristics of ZnO in different alcohols are shown in Figure 3. Photovoltaic parameters of organic solar cells are presented in Table 1.

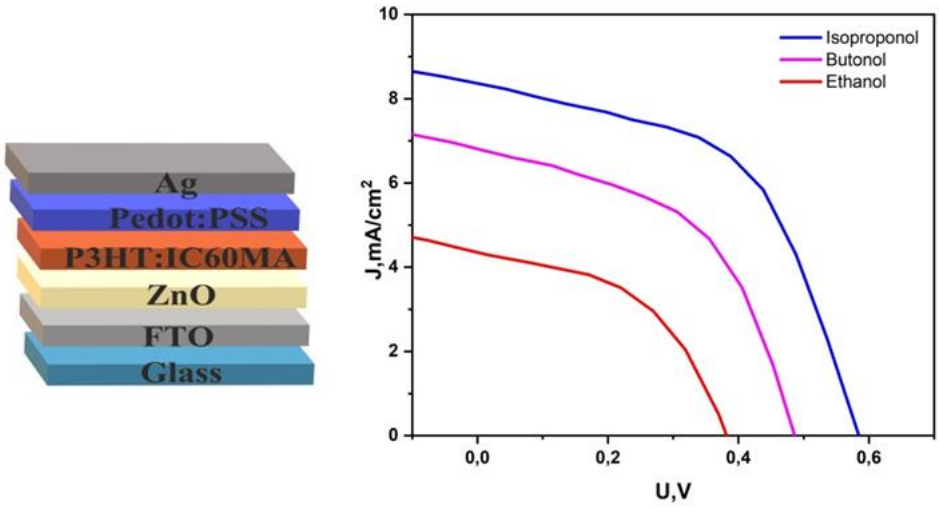

a) b)

Figure 3. a) the architecture of the inverted PSC; b) current – voltage characteristics of FTO/ZnO/P3HT: IC60MA/PEDOT: PSS/Ag devices

Data analysis showed that the values of short-circuit current densities vary depending on alcohol solvents, so for Isoproponol (J_{sc}) 8.6, Butanol (J_{sc}) 7.1 and Ethanol (J_{sc}) 4.7 mA/cm^2, respectively. The no-load voltage (U_{oc}) also depends on alcohol solvents (Table 1). The change in the values of the current density is associated with the process of aggregation of ZnO depending on alcohol solvents. The lowest aggregation of ZnO is observed in Isopropanol, in which the organic cell showed the highest efficiency of converting solar energy into electrical energy.

Table 1

Photovoltaic characteristics of organic solar cells

Sample	U_{oc} (V)	J_{sc}(mA/cm^2)	U_{max}(V)	J_{max}(mA/cm^2)	FF	PCE %
Isopropanol	0.58	8.6	0.40	6.33	0.50	2.5
Butanol	0.48	7.1	0.32	5.04	0.47	1.6
Ethanol	0.38	4.7	0.24	3.2	0.43	0.9

Studies of the mechanisms of transport and recombination of charge carriers of the electron transport layer of the ZnO film in different alcohols were carried out by the method of impedance spectroscopy. The impedance spectra of the ETL layer in Nyquist coordinates based on solid films are shown in Figure 4. Table 2 shows the electron transport parameters of the ETL layer calculated using the EIS-analyzer software package, where (R_w) is the equivalent resistance of the film; (R_{rec}) is the resistance characterizing the recombination of localized electrons with holes; (k_{eff}) is the effective recombination rate of charge carriers; (τ_{eff}) is the effective lifetime of charge carriers; (D_{eff}) is the diffusion coefficient.

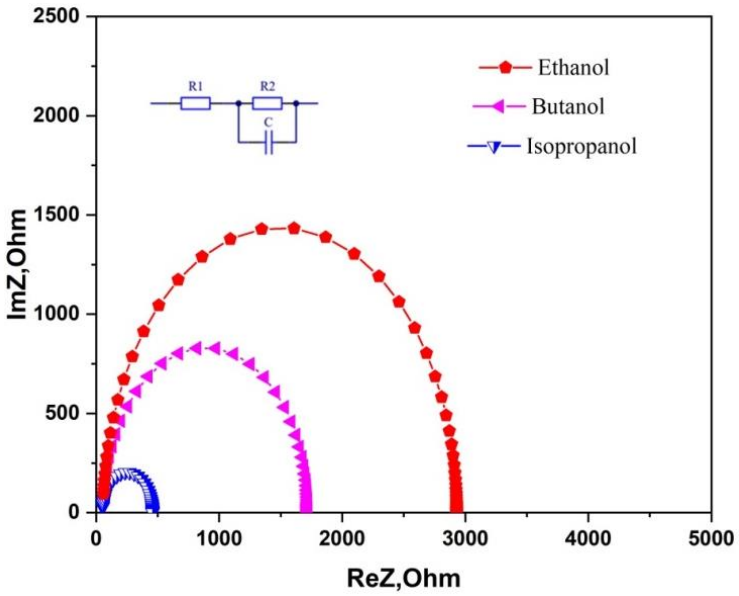

Figure 4. Impedance spectra of ZnO

From the obtained impedance measurement data, it follows that the ETL layer based on ZnO obtained in Ethanol has the lowest electron transport parameters. This is due to the high degree of aggregation of ZnO, as a result of which the resistance to increases interface of the ZnO/FTO.

In polymer solar cell with ZnO in Isoproponol, due to the low degree of aggregation, rapid electron transfer to the cathode (FTO) and a decrease in recombination of injected electrons at the boundary with the photoactive layer are observed, as a result, the photovoltaic characteristics of the polymer solar cell increase compared to other alcohols.

Table 2

The value of electrophysical parameters of films

Sample	R_1, (ohm)	R_2, (ohm)	R_2 / R_1	τ_{eff}, (ms)	k_{eff}, (s^{-1})	D_{eff}, ($см^2 \cdot с^{-1}$)
Isopropanol	51	406	7.9	10.2	807	$1.7 \cdot 10^{-7}$
Butanol	59	1662	28.1	5.1	1937	$1.5 \cdot 10^{-8}$
Ethanol	82	4020	49.0	4.2	2329	$3.3 \cdot 10^{-8}$

Conclusions

The paper presents the results of a study of the effect of different alcohols in the synthesis of ZnO films on the electron transport of a polymer solar cell. The analysis of experiments showed that depending on alcohols, there is a change in the morphology of ZnO, which in turn affects the efficiency of electron transport. It is established that the optical band gap of ZnO in isopropanol is 3.2 eV and in ethanol decreases to 2.8 eV. It is shown that changes in the morphology of the ZnO surface affect the parameters of the VAC polymer solar cell. So for Isopropanol (J_{sc} -8.6 mA/cm^2), Butanol (J_{sc} -7.1 mA/cm^2) and Ethanol (J_{sc} -4.7 mA/cm^2) respectively. ZnO based photocells in Isopropanol have shown the highest efficiency of converting light energy into electrical energy.

References

1 Lipomi, D.J. (2018). Focus on Its Strengths. *Organic Photovoltaics.* Joule. 2(2). 195–198. doi:10.1016/j.joule.2017.12.011

2 Park, S.H., Roy, A., Beaupré, S., Cho, S., Coates, N., Moon, J.S., & Heeger, A.J. (2009). Bulk heterojunction solar cells with internal quantum efficiency approaching 100%. *Nature Photonics, 3*(5), 297–302. doi:10.1038/nphoton.2009.69

3 Huang, Y.F., Inigo, A.R., Chang, C.C., Li, K.C., Liang, C.F., Chang, C.W., & Fann, W.S. (2008). Nanostructure-Dependent Vertical Charge Transport in MEH-PPV Films. *Advanced Functional Materials, 18*(22). doi:10.1002/adfm.200890094

4 Huang, Y.-F., Inigo, A.R., Chang, C.C., Li, K.C., Liang, C.F., Chang, C.W., & Fann, W.S. (2007). Nanostructure-Dependent Vertical Charge Transport in MEH-PPV Films. *Advanced Functional Materials, 17*(15), 2902–2910. doi:10.1002/adfm.200600825

5 Chen, L., Lei, Y., Zhang, Q., & Xiong, Z. (2015). Negative magnetoconductance effects in amorphous copper phthalocyanine thin film: trap-assisted bipolaron formation. *Journal of Materials Chemistry C, 3*(46), 12056–12060. doi:10.1039/c5tc01908g

6 Janssen, P., Cox, M., Wouters, S.H.W., Kemerink, M., Wienk, M.M., & Koopmans, B. (2013). Tuning organic magnetoresistance in polymer-fullerene blends by controlling spin reaction pathways. *Nature Communications, 4*(1). doi:10.1038/ncomms3286

7 Zhang, S., Qin, Y., Zhu, J., & Hou, J. (2018). Over 14% Efficiency in Polymer Solar Cells Enabled by a Chlorinated Polymer Donor. *Advanced Materials, 30*(20), 1800868. doi:10.1002/adma.201800868

8 Zheng, Z., Hu, Q., Zhang, S., Zhang, D., Wang, J., Xie, S., & Zhou, H. (2018). A Highly Efficient Non-Fullerene Organic Solar Cell with a Fill Factor over 0.80 Enabled by a Fine-Tuned Hole-Transporting Layer. *Advanced Materials*, 1801801. doi:10.1002/adma.201801801

9 Oprea, O. Andronescu, E., Ficai, D., Ficai, A., Oktar, F.N., & Yetmez, M. (2014). ZnO applications and challenges. *Curr. Or.g Chem., 18,* 192–203. doi:10.2174/1385272813176660143

10 Motelica, L. Ficai, D., Oprea, O.C., & Ficai, A. (2020). Andronescu E. Smart food packaging designed by nanotechnological and drug delivery approaches. *Coatings,* 10, 806. DOI:10.3390/coatings10090806

11 Spoiala A. (2021). Zinc oxide nanoparticles for water purification. *Materials, 14,* 4747. doi:10.3390/ma14164747

12 Zhang, H., Yao, J., Hou, J., Zhu, J. Zhang, W., Li, R. Yu, B. Gao, S. Zhang, & Hou J., Over, H. (2018). 14 % Efficiency in Organic Solar Cells Enabled by Chlorinated Nonfullerene Small-Molecule Acceptors. *Advanced Materials, 30*(28), 1800613. https://doi.org/10.1002/adma.201800613

13 Aimukhanov, A.K., Rozhkova, X.S., Zeinidenov, A.K., & Seisembekova, T.E. (2021). Influence of surface structure and morphology of PEDOT: PSS on its optical and electrophysical characteristics. *Bulletin of the University of Karagand*a. – *Physics, 3*(103). 93-100. doi:10.31489/2021Ph3/93-100

Т.Е. Сейсембекова, А.К. Аймуханов, Б.Р. Ильясов,
Д. Валиев, А.К. Зейниденов, А.М. Жаканова

Әр түрлі спирттердегі ZnO-нің OSC фотоэлектрлік сипаттамаларына әсері

Жұмыста инверттелген құрылымы бар ZnO полимерлі күн элементінің ETL қабатының электрон тасымалдауына спирттердің әсерін зерттеу нәтижелері берілген. Пленкаларды алу үшін мырыш ацетаты изопропанолда, бутанолда және этанолда бірдей тәжірибелік жағдайларда ерітілді. СЭМ мәліметтері бойынша пленка синтезінде әртүрлі спиртті еріткіштерді қолдану беттік морфологияның өзгеруіне әкелетіні анықталды. Пленка бетінің интерфейсінің өзгеруі қолданылатын спирттердің полярлығына және ZnO агрегаттарының пайда болуымен байланысты. ZnO тыйым салынған аймақтың оптикалық ені спирт еріткіштерінен тәуелді екендігі көрсетілген. ZnO агрегациясы электронды тасымалдауға және полимерлі күн элементінің тиімділігіне әсер ететіні дәлелденген. ZnO:P3HT:IC60MA/PEDOT:PSS/Ag күн ұяшықтарының вольтамперлік сипаттамалары өлшенді. Көрсетілген ең аз ZnO агрегациясы Isoproranol-да байқалады, онда органикалық ұяшық күн энергиясын электр энергиясына айналдырудың ең жоғары тиімділігін көрсетті. Полимерлі күн ұяшықтарының тиімділігі 2.5% құрады. Алынған импедансометрия мәліметтері көрсеткендей Ethanol-да ZnO негізіндегі алынған ETL қабат ең төменгі электр тасымалдау параметрлеріне ие. Бұл ZnO агрегациясының жоғары деңгейіне байланысты, нәтижесінде ZnO / FTO интерфейсінің кедергісі

артады. Ethanol-дағы ZnO негізіндегі күн элементтері 1,6% болатын ПӘК Butanol-дағы ZnO-мен салыстырғанда ПӘК мәні 0,9%-ға тең болатынын көрсетті.

Кілт сөздер: ZnO, изопропанол, этанол, бутанол, беттік морфология, термиялық күйдіру, оптикалық спектроскопия, импеданс спектроскопиясы.

Т.Е. Сейсембекова, А.К. Аймуханов, Б.Р. Ильясов,
Д. Валиев, А.К. Зейниденов, А.М. Жаканова

Влияние ZnO в различных спиртах на фотоэлектрические характеристики OSC

В статье представлены результаты исследования влияния спиртов на электронный транспорт ETL слоя ZnO полимерного солнечного элемента с инвертированной структурой. Для получения пленок ацетат цинка растворяли при одинаковых условиях эксперимента в изопропаноле, бутаноле и этаноле. По данным СЭМ, было установлено, что использование различных спиртовых растворителей при синтезе пленки ведет к изменению морфологии поверхности. Наблюдаемые изменения интерфейса поверхности пленок связаны с образованием агрегатов ZnO в зависимости от полярности используемых спиртов. Показано, что оптическая ширина запрещенной зоны ZnO также зависит от спиртовых растворителей, и агрегация ZnO оказывает влияние на электронный транспорт и эффективность полимерного солнечного элемента. Измерены вольтамперные характеристики солнечных ячеек ZnO:P3HT:IC60MA/PEDOT:PSS/Ag. Обнаружено, что наименьшая агрегация ZnO наблюдается в Isoproponol, в которой органическая ячейка показала наибольшую эффективность преобразования солнечной энергии в электрическую. КПД полимерного солнечного элемента составил 2,5 %. Из полученных данных импедансометрии ETL слой на основе ZnO, полученном в Ethanol, имеет самые низкие электротранспортные параметры. Это связано с высокой степенью агрегацией ZnO, в результате чего возрастает сопротивление интерфейса ZnO/FTO. Солнечные элементы на основе ZnO в Ethanol продемонстрировали значение КПД, равное 0,9 %, по сравнению с ZnO в Butanol (КПД 1,6 %).

Ключевые слова: ZnO, изопропанол, этанол, бутанол, морфология поверхности, термический отжиг, оптическая спектроскопия, спектроскопия импеданса.

DOI 10.31489/2023PH2/52-65

UDC 530.1;53.04

P.Yu. Tsyba, G.S. Altayeva, O.V. Razina*

L.N. Gumilyov Eurasian National University, Astana, Kazakhstan
*(*E-mail: olvikraz@mail.ru)*

Study of the scalar-fermionic model containing linear lagrangian fields of matter within the framework of minimal coupling

In this article, we study a model of the universe with the scalar field and the fermionic field interacting via a Yukawa-type potential. In the model, the component contributions of each of the fields are determined to the total density and pressure of dark energy. We have considered the solution of the cosmological model for the scale factor with two functional time dependences. The Yukawa-type field does not give its input to the general pressure. In the power law case, there is a significant contribution to the total increase in pressure, to the exponential — the scalar field. There are many cases when the universe makes a transition between successive epochs in various models of cosmological expansion. These regularities impose some restrictions on the profile of the scalar- fermionic field interaction and the general cosmological dynamics. Energy conditions were found to check the model under the study. In the studied model, the null energy condition, the strong energy condition, the dominant energy condition are fulfilled, and the weak energy condition, which is not mandatory, is not fulfilled. It is shown how it is possible to connect the cosmographic parameters — parameters of deceleration *q*, jerk *j* and snap *s* with the power low the scale factor. We investigated these restrictions using cosmological solutions with an evolving equation of state, such that a smooth transition between different epochs can always occur in the universe. The scalar-fermionic model under study describes the accelerated modes of expansion of the universe. The obtained solutions correspond to the results predicted by the theory and observational data.

Keywords: scalar field, fermionic field, Yukawa-type interaction, minimal coupling, energy condition, the cosmography.

Introduction

It is known that the universe is expanding with an acceleration, which is confirmed by the observational data. One of the simplest candidates for the description of the dark energy, which causes acceleration, is the cosmological constant Λ, introduced by Einstein in the theory of GR to describe the static universe. Space-time with a positive cosmological constant is known as the de Sitter space-time. Therefore, the universe can be described by the de Sitter geometry. The fermionic fields in cosmological models can be responsible for accelerated periods in the evolution of the universe. In most of these models, the fermionic field plays the role of inflation in the early universe and the role of dark energy in the later universe. These fermionic fields have been studied using several approaches, the results of which include numerical solutions, exact solutions, scenarios from anisotropy to isotropy, and cyclic cosmology [1-3]. The fermionic fields can be combined with other components, such as the canonical and non-canonical scalar fields. In particular, inflation and dark energy can be modeled in several ways. One subclass of these models considers this component as the tachyon field, and this idea goes back to the models of string theory. Compared to the usual canonical the scalar field, the resulting physics becomes richer as a whole, due to nonlinear effects. Depending on the initial conditions and interaction with other sources, these tachyons could contribute to the accelerated period of

the later universe and be considered as a contribution of the dark energy. They can be permanent even in the early universe, where they can be associated with the inflationary period. In works [4-13] the scalar and fermionic fields were considered responsible both for the inflationary period and for the modern accelerated expansion. This effect is recognized as a consequence of the dynamics of the model itself. The exotic nature of these components does not contradict the observational data, and an important point of discussion is their comparison with the canonical scalar field [14-18].

The work is structured as follows: we construct a model through an action, which represents the sum of the Lagrangian densities of gravitational, the scalar fields, the fermionic fields and Yukawa-type fields. The field equations of Dirac, Einstein, and Klein-Gordon are derived from the variation of the field action [19-21].

The dependence of the scale factor on time reflects the main events in the history of the universe. Moreover, it is the deceleration parameter that dictates the rate of the expansion of the Hubble sphere and determines the dynamic change in the number of observed galaxies: depending on the sign of the deceleration parameter, this number either increases (in the case of slow expansion), or we remain completely alone in space (if the expansion is accelerated).

When checking fermionic sources as responsible for the accelerated expansion of the universe, different regimes appear. In the scenario of the early universe, the fermionic field grows rapidly and the matter is created until it begins to dominate and as a result, the initial accelerated expansion slows down. When the universe enters the domain of matter dominance, then the fermionic field again dominates, which leads to an era of accelerated growth rates of the scale factor. In this case, the fermionic field is responsible for inflation in the early universe and dark energy for the later universe, without the need for a cosmological study of constant terms or a scalar field. In the later universe, energy again begins to dominate and there is a gradual transition to dark energy, the so-called fermionic energy period, in which the accelerated regime begins and continues into the modern era [22-33].

Methods

Let us consider the general action in the form

$$S = \int \sqrt{-g}d^4x\left\{\frac{R}{2} + \frac{1}{2}\partial^\mu\phi\partial_\mu\phi - V_1(\phi) + \frac{i}{2}\left[\bar{\psi}\Gamma^\mu D_\mu\psi - (D_\mu\bar{\psi})\Gamma^\mu\psi\right] - V_2(\bar{\psi}\psi) - \lambda\bar{\psi}\phi\psi\right\}. \quad (1)$$

Here the sources of gravity are: the density of the Lagrangian of the scalar field ϕ

$$L_b = \frac{1}{2}\partial^\mu\phi\partial_\mu\phi - V_1(\phi),$$

where $V_1(\phi)$ is the scalar field self-interaction potential.

The fermionic field with the potential of self-interaction $V_2(\bar{\psi}\psi)$

$$L_f = \frac{i}{2}\left[\bar{\psi}\Gamma^\mu D_\mu\psi - (D_\mu\bar{\psi})\Gamma^\mu\psi\right] - V_2(\bar{\psi}\psi),$$

where ψ and $\bar{\psi} = \psi^\dagger\gamma^0$ represent the spinor field and its adjoint, respectively.

The Lagrangian density corresponds to the Yukawa type interaction showing the relationship between the scalar and the fermionic fields

$$L_Y = -\lambda\bar{\psi}\phi\psi,$$

where λ is the coupling constant of the Yukawa potential.

From the variation of the action (1) on the spinor field ψ and its conjugate $\bar{\psi}$ follow the Dirac equations

$$i\Gamma^\mu D_\mu\psi - \frac{\partial V_2(\bar{\psi}\psi)}{\partial\bar{\psi}} - \lambda\phi\psi = 0,$$

$$iD_\mu\bar{\psi}\Gamma^\mu + \frac{\partial V_2(\bar{\psi}\psi)}{\partial\psi} + \lambda\bar{\psi}\phi = 0,$$

in addition, variation of action (1) with respect to the scalar field ϕ gives the Klein-Gordon equation for the scalar field, which has the form

$$\nabla_\mu \nabla^\mu \phi + V_1(\phi) + \lambda\bar{\psi}\psi = 0.$$

The Einstein equations are obtained by varying the action (1) with respect to the metric tensor

$$R_{\mu\nu} - \frac{1}{2} g_{\mu\nu} R = -T_{\mu\nu},$$

where $T_{\mu\nu}$ the energy-momentum tensor which is equal to the following expression

$$T^{\mu\nu} = \frac{i}{4}\left[\overline{\psi}\Gamma^\mu D^\nu \psi - D^\mu \overline{\psi}\Gamma^\nu \psi\right] + \partial^\mu \phi \partial^\nu \phi -$$

$$-g^{\mu\nu}\left[\frac{1}{2}\partial^\sigma \phi \partial_\sigma \phi - V_1(\phi) - \lambda\bar{\psi}\phi\psi + \frac{i}{2}(\bar{\psi}\Gamma^\lambda D_\lambda \psi - D_\lambda \bar{\psi}\Gamma^\lambda \psi) - V_2(\bar{\psi}\psi)\right].$$

In order to study the evolution of a homogeneous and isotropic spatially flat universe, we use the Friedmann-Robertson-Walker metric

$ds^2 = -dt^2 + a(t)^2(dx^2 + dy^2 + dz^2),$ (2)

where $a(t)$ is the scale factor of the universe. In this metric, the components of the tetrad are given by the formula as $e_0^\mu = \delta_0^\mu$ and $e_i^\mu = \delta_i^\mu / a(t)$, Dirac matrices and spin connectivity are equal

$$\Gamma^0 = \gamma^0,$$

$$\Gamma^0 = \frac{1}{a(t)}\gamma^i,$$

$$\Omega_0 = 0,$$

$$\Omega_i = \frac{1}{2}\dot{a}(t)\gamma^i\gamma_0.$$

Here, the dot means the time derivative, and in what follows we will use the bilinear function $u = \bar{\psi}\psi$ and let us introduce the notation $V_{2u} = \frac{dV_2}{du}$. Then the Lagrangian of the model under study (1) will take the form

$$L = -3a\dot{a}^2 + a^3\frac{1}{2}\dot{\phi}^2 - a^3 V_1(\phi) + a^3\frac{i}{2}(\bar{\psi}\gamma^0\dot{\psi} - \dot{\bar{\psi}}\gamma^0\psi) - a^3 V_2(u) - a^3\lambda u\phi. \quad (3)$$

From the Euler-Lagrange and energy-momentum tenzor, the complete system of equations of motion corresponding to the Lagrangian (3) is

$$3H^2 = \rho, \quad (4)$$

$$2\dot{H} + 3H^2 = -p, \quad (5)$$

$$\dot{\psi} + \frac{3}{2}H\psi + i\gamma^0 V_{2u}\psi + i\lambda\gamma^0\psi\phi = 0, \quad (6)$$

$$\dot{\bar{\psi}} + \frac{3}{2}H\bar{\psi} - i\gamma^0 V_{2u}\bar{\psi} - i\lambda\phi\bar{\psi}\gamma^0 = 0, \quad (7)$$

$$\ddot{\phi} + 3H\dot{\phi} + V_{1\phi} + \lambda u = 0, \quad (8)$$

where

$$\rho = \frac{\dot{\phi}^2}{2} + V_1(\phi) + V_2(u) + \lambda u\phi, \quad (9)$$

$$p = \frac{\dot{\phi}^2}{2} - V_1(\phi) + V_{2u}(u) - V_2(u). \quad (10)$$

For further calculations, we need an expression that follows from the definition of the bilinear function u and equations (6)-(7), valid for an arbitrary potential V

$$u = \frac{c}{a^3},$$

where c is the constant of integration.

Results

Example 1

The system of equations (4)-(10) can have the following solution in the form of an exponential function of the scale factor and the scalar field

$$a = a_0 e^{\alpha t}, \tag{11}$$

$$\phi = \phi_0 e^{-\gamma t},$$

where a_0,ϕ_0, α and γ are some constants and $\alpha > 0$, $\gamma > 0$. Then from the Klein-Gordon equation (8) the potential of the scalar field V_1 is equal

$$V_1 = -\frac{1}{2}\phi_0^2\gamma^2 e^{-2\gamma t} + \frac{3}{2}\alpha\phi_0^2\gamma e^{-2\gamma t} - \frac{\lambda\phi_0 c\gamma e^{-(3\alpha+\gamma)t}}{a_0^3(3\alpha+\gamma)} + V_{10},$$

where V_{10} is the constant of integration. From equations (8) and (9) we find the potential of the fermionic field V_2

$$V_2 = -3\alpha\phi_0\gamma\left(\frac{1}{2}\phi_0 e^{-2\gamma t} + \frac{\lambda c e^{-(3\alpha+\gamma)t}}{a_0^3(3\alpha+\gamma)}\right) + V_{20}.$$

The total energy density and pressure of the model under study from the Friedman equations (4) and (5) are

$$\rho = 3\alpha^2,$$

$$p = -3\alpha^2,$$

where the conditions $3\alpha^2 = V_{10} + V_{20}$ are satisfied for the constants.

The componentwise contributions of each of the fields to the total density (9), respectively, are equal to

$$\rho_b = \frac{\dot{\phi}^2}{2} + V_1(\phi) = \frac{3}{2}\alpha\phi_0^2\gamma e^{-2\gamma t} - \frac{\lambda\phi_0\gamma c e^{-(3\alpha+\gamma)t}}{a_0^3(3\alpha+\gamma)} + 3\alpha^2 - V_{20},$$

$$\rho_f = V_2(u) = -3\alpha\phi_0\gamma\left(\frac{1}{2}\phi_0 e^{-2\gamma t} + \frac{\lambda c e^{-(3\alpha+\gamma)t}}{a_0^3(3\alpha+\gamma)}\right) + V_{20},$$

$$\rho_Y = \lambda u\phi = \frac{\lambda c\phi_0}{a_0^3} e^{-(3\alpha+\gamma)t}.$$

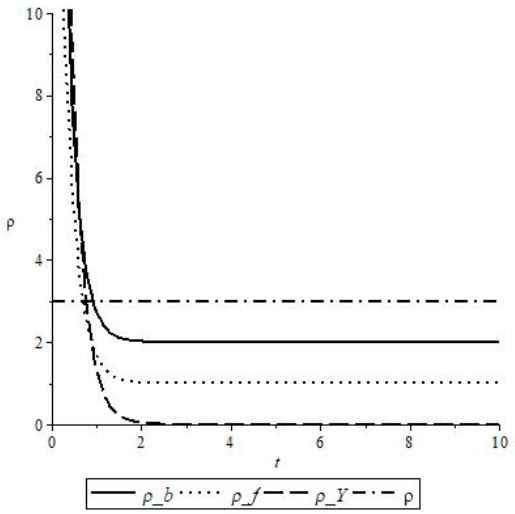

Figure 1. The energy density ρ and the componentwise contributions of the densities versus time t, at $\phi_0 = 4, c = 2, a_0 = 1, \alpha = 1, \gamma = 2, \lambda = 6, V_{20} = 1$.

Figure 1 shows the scalar field ρ_b (solid line), the fermionic field density ρ_f (dotted line), Yukawa type field density ρ_Y (dash line), the total dark energy density ρ (dash-dotted line). The figure shows that the componentwise contributions of the densities in the early epoch change with time, while the total density of dark energy remains constant.

The componentwise contributions of each of the fields to the total pressure (10) are respectively equal to

$$p_b = \frac{\dot{\phi}^2}{2} - V_1(\phi) = \phi_0^2\gamma^2 e^{-2\gamma t} - \frac{3}{2}\phi_0^2\gamma e^{-2\gamma t} + \frac{\lambda\phi_0\gamma c e^{-(3\alpha+\gamma)t}}{a_0^3(3\alpha+\gamma)} - 3\alpha^2 + V_{20},$$

$$p_f = V_{2u}(u) - V_2(u) - \phi_0^2\gamma^2 e^{-2\gamma t} - \frac{\lambda c\phi_0}{a_0^3}e^{-(3\alpha+\gamma)t} + 3\alpha\left[\frac{1}{2}\phi_0^2\gamma e^{-2\gamma t} + \frac{\lambda\phi_0\gamma c e^{-(3\alpha+\gamma)t}}{a_0^3(3\alpha+\gamma)}\right] - V_{20}.$$

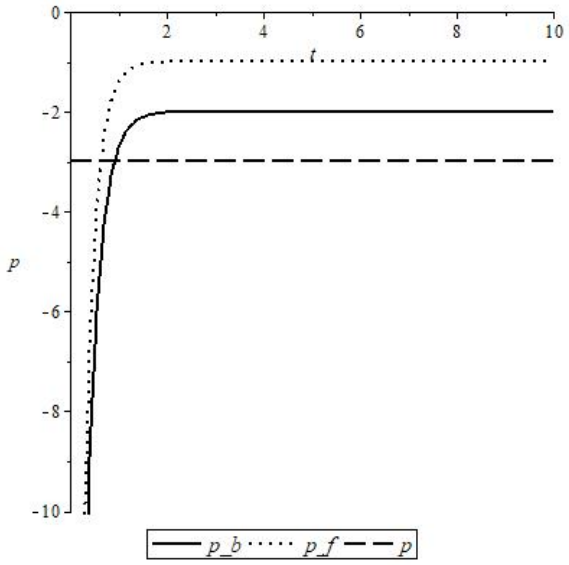

Figure 2. Total pressure p and componentwise contributions of the pressures versus time t, at $\phi_0 = 4, c = 2, a_0 = 1, \alpha = 1, \gamma = 2, \lambda = 6, V_{20} = 1$.

Figure 2 shows the scalar field pressure p_s (solid line), the fermionic field pressure p_f (dotted line), the total pressure p (dash line). The Yukawa-type field does not contribute to the total pressure. As seen from Figure 2, the scalar field has a greater effect on the total pressure.

The solution for the fermionic field will be sought in the form

$$\psi_k(t) = A_k(t)e^{iD_k(t)}, k = 0,1,2,3, \quad (12)$$

where $A_k(t)$ and $D_k(t)$ in the arbitrary functions of time.

Let us substitute the general form of the fermionic field function (12) into the Dirac equation (6), as a result we obtain

$$\psi_0(t) = A_{00}e^{-\frac{3}{2}\alpha t}\exp\left[i\left(\frac{\phi_0^2\gamma^2 a_0^3}{c}\frac{1}{3\alpha-2\gamma}e^{(3\alpha-2\gamma)t} + D_{00}\right)\right],$$

$$\psi_1(t) = A_{01}e^{-\frac{3}{2}\alpha t}\exp\left[i\left(\frac{\phi_0^2\gamma^2 a_0^3}{c}\frac{1}{3\alpha-2\gamma}e^{(3\alpha-2\gamma)t} + D_{01}\right)\right],$$

$$\psi_2(t) = A_{02}e^{-\frac{3}{2}\alpha t}\exp\left[i\left(-\frac{\phi_0^2\gamma^2 a_0^3}{c}\frac{1}{3\alpha-2\gamma}e^{(3\alpha-2\gamma)t} + D_{02}\right)\right],$$

$$\psi_3(t) = A_{03}e^{-\frac{3}{2}\alpha t}\exp\left[i\left(-\frac{\phi_0^2\gamma^2 a_0^3}{c}\frac{1}{3\alpha-2\gamma}e^{(3\alpha-2\gamma)t} + D_{03}\right)\right],$$

where A_{0k} and D_{0k} at $k = 0,1,2,3$ are the integration constants. Conjugated field $\bar{\psi} = \psi^\dagger\gamma^0$ respectively equal to

$$\bar{\psi}_0(t) = A_{00}e^{-\frac{3}{2}\alpha t}\exp\left[-i\left(\frac{\phi_0^2\gamma^2 a_0^3}{c}\frac{1}{3\alpha-2\gamma}e^{(3\alpha-2\gamma)t}+D_{00}\right)\right],$$
$$\bar{\psi}_1(t) = A_{01}e^{-\frac{3}{2}\alpha t}\exp\left[-i\left(\frac{\phi_0^2\gamma^2 a_0^3}{c}\frac{1}{3\alpha-2\gamma}e^{(3\alpha-2\gamma)t}+D_{01}\right)\right],$$

$$\bar{\psi}_2(t) = -A_{02}e^{-\frac{3}{2}\alpha t}\exp\left[-i\left(-\frac{\phi_0^2\gamma^2 a_0^3}{c}\frac{1}{3\alpha-2\gamma}e^{(3\alpha-2\gamma)t}+D_{02}\right)\right],$$
$$\bar{\psi}_3(t) = -A_{03}e^{-\frac{3}{2}\alpha t}\exp\left[-i\left(-\frac{\phi_0^2\gamma^2 a_0^3}{c}\frac{1}{3\alpha-2\gamma}e^{(3\alpha-2\gamma)t}+D_{03}\right)\right],$$

where the conditions for the constants are satisfied $\frac{c}{a_0^3} = A_{00}^2 + A_{01}^2 - A_{02}^2 - A_{03}^2$, the definition of a bilinear function that follows from $u = \bar{\psi}\psi = \frac{c}{a_0^3}$.

Example 2

The system of equations (4)-(10) can have the following solution in the form of the power low the scale factor and the scalar field

$$a = a_0 t^{\alpha}, \tag{13}$$

$$\phi = \phi_0 t^{\gamma},$$

where a_0,ϕ_0, α and γ are constants and $\alpha > 1$, $\gamma < 0$. Then from the Klein-Gordon equation (8) the potential of the scalar field V_1 is

$$V_1 = -\frac{1}{2}\phi_0^2\gamma^2 t^{2(\gamma-1)} - \frac{3\alpha\phi_0^2\gamma^2 t^{2(\gamma-1)}}{2(\gamma-1)} - \frac{\lambda\phi_0 c\gamma t^{(\gamma-3\alpha)}}{a_0^3(\gamma-3\alpha)} + V_{10},$$

where V_{10} is the integration constant. From equations (9) and (10) we find the potential of the fermionic field V_2

$$V_2 = 3\alpha\left(\frac{\phi_0^2\gamma^2 t^{2(\gamma-1)}}{2(\gamma-1)} + \frac{\alpha}{t^2} - \frac{\lambda\phi_0 c t^{\gamma-3\alpha}}{a_0^3(\gamma-3\alpha)}\right) + V_{20}.$$

The total energy density and pressure of the model under study from the Friedman equations (4) and (5) are

$$\rho = \frac{3\alpha^2}{t^2}, \tag{14}$$

$$p = \frac{\alpha}{t^2}(2-3\alpha),$$

where the conditions $V_{10} + V_{20} = 0$ are satisfied for the constants.

The componentwise contributions of each of the fields to the total density (14) are respectively equal to

$$\rho_b = \frac{\dot{\phi}^2}{2} + V_1(\phi) = -\frac{3\alpha\phi_0^2\gamma t^{2(\gamma-1)}}{2(\gamma-1)} - \frac{\lambda\phi_0\gamma c t^{(\gamma-3\alpha)}}{a_0^3(\gamma-3\alpha)} + V_{10},$$

$$\rho_f = V_2(u) = \frac{3\alpha\phi_0^2\gamma^2 t^{2(\gamma-1)}}{2(\gamma-1)} + \frac{3\alpha^2}{t^2} - \frac{3\alpha\lambda\phi_0 c t^{(\gamma-3\alpha)}}{a_0^3(\gamma-3\alpha)} - V_{10},$$

$$\rho_Y = \lambda u\phi = \frac{\lambda c\phi_0 t^{\gamma-3\alpha}}{a_0^3}.$$

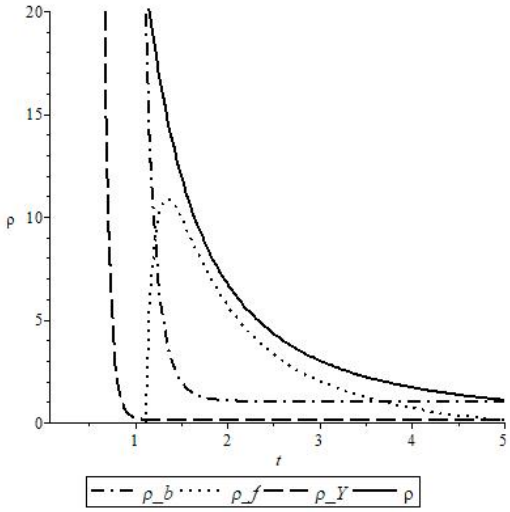

Figure 3. The energy density ρ and the componentwise contributions of the densities versus time t, at $V_{10} = 0, \phi_0 = 1, c = 1, a_0 = 2, \alpha = 3, \gamma = -2, \lambda = 0.5, a_0 = 2.$

Figure 3 shows the scalar field density ρ_b (dash-dotted line), the fermionic field density ρ_f (dotted line), Yukawa-type field density ρ_Y (dash line), the total dark energy density ρ (solid line).

The componentwise contributions of each of the fields to the total pressure (10) are respectively equal to

$$p_b = \frac{\dot{\phi}^2}{2} - V_1(\phi) = \phi_0^2\gamma^2 t^{2(\gamma-1)} + \frac{3\alpha\phi_0^2\gamma^2 t^{2(\gamma-1)}}{2(\gamma-1)} - \frac{\lambda\phi_0\gamma c t^{(\gamma-3\alpha)}}{a_0^3(\gamma-3\alpha)} - V_{10},$$

$$p_f = V_{2u}(u) - V_2(u) - \phi_0^2\gamma^2 t^{2(\gamma-1)} + \frac{2\alpha}{t^2} - \frac{\lambda\phi_0 t^\gamma c}{a_0^3 t^{3\alpha}} - \frac{3\alpha\phi_0^2\gamma^2 t^{2(\gamma-1)}}{2(\gamma-1)} - \frac{3\alpha^2}{t^2} + \frac{3\alpha\lambda\phi_0 c t^{(\gamma-3\alpha)}}{a_0^3(\gamma-3\alpha)} + V_{10}.$$

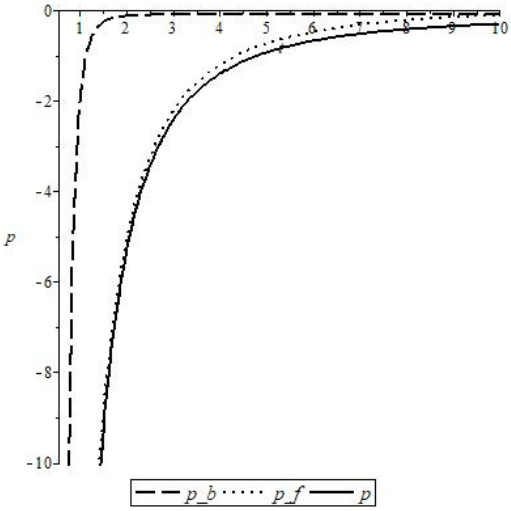

Figure 4. Total pressure p and componentwise contributions of the pressures versus time t, at $V_{10} = 0, \phi_0 = 1, c = 1, a_0 = 2, \alpha = 2, \gamma = -2, \lambda = 0.5.$

Figure 4 shows the scalar field pressure p_b (dash line), the fermionic field pressure p_f (dotted line), the total pressure p (solid line). In this case, the fermionic field contributes more to the total pressure.

The solution for the fermionic field will be sought in the form (12). We substitute the general form of the fermionic field function (12) into the Dirac equation (6), as a result, we obtain

$$\psi_0(t)=\frac{A_{00}}{t^{\frac{3}{2}\alpha}}\exp\left[i\left(\frac{\phi_0^2\gamma^2a_0^3t^{(3\alpha+2\gamma)}}{c(3\alpha+2\gamma)}-\frac{2\alpha a_0^3t^{3\alpha-1}}{c(3\alpha-1)}+D_{00}\right)\right],$$

$$\psi_1(t)=\frac{A_{01}}{t^{\frac{3}{2}\alpha}}\exp\left[i\left(\frac{\phi_0^2\gamma^2a_0^3t^{(3\alpha+2\gamma)}}{c(3\alpha+2\gamma)}-\frac{2\alpha a_0^3t^{3\alpha-1}}{c(3\alpha-1)}+D_{01}\right)\right],$$

$$\psi_2(t)=\frac{A_{02}}{t^{\frac{3}{2}\alpha}}\exp\left[i\left(-\frac{\phi_0^2\gamma^2a_0^3t^{(3\alpha+2\gamma)}}{c(3\alpha+2\gamma)}+\frac{2\alpha a_0^3t^{3\alpha-1}}{c(3\alpha-1)}+D_{02}\right)\right],$$

$$\psi_3(t)=\frac{A_{03}}{t^{\frac{3}{2}\alpha}}\exp\left[i\left(-\frac{\phi_0^2\gamma^2a_0^3t^{(3\alpha+2\gamma)}}{c(3\alpha+2\gamma)}+\frac{2\alpha a_0^3t^{3\alpha-1}}{c(3\alpha-1)}+D_{03}\right)\right],$$

where A_{0k} and D_{0k} at $k=0,1,2,3$ are the integration constants. Conjugated field $\bar{\psi}=\psi^{\dagger}\gamma^0$ respectively equal to

$$\bar{\psi}_0(t)=\frac{A_{00}}{t^{\frac{3}{2}\alpha}}\exp\left[-i\left(\frac{\phi_0^2\gamma^2a_0^3t^{(3\alpha+2\gamma)}}{c(3\alpha+2\gamma)}-\frac{2\alpha a_0^3t^{3\alpha-1}}{c(3\alpha-1)}+D_{00}\right)\right],$$

$$\bar{\psi}_1(t)=\frac{A_{01}}{t^{\frac{3}{2}\alpha}}\exp\left[-i\left(\frac{\phi_0^2\gamma^2a_0^3t^{(3\alpha+2\gamma)}}{c(3\alpha+2\gamma)}-\frac{2\alpha a_0^3t^{3\alpha-1}}{c(3\alpha-1)}+D_{01}\right)\right],$$

$$\bar{\psi}_2(t)=-\frac{A_{02}}{t^{\frac{3}{2}\alpha}}\exp\left[-i\left(-\frac{\phi_0^2\gamma^2a_0^3t^{(3\alpha+2\gamma)}}{c(3\alpha+2\gamma)}+\frac{2\alpha a_0^3t^{3\alpha-1}}{c(3\alpha-1)}+D_{02}\right)\right],$$

$$\bar{\psi}_3(t)=-\frac{A_{03}}{t^{\frac{3}{2}\alpha}}\exp\left[-i\left(-\frac{\phi_0^2\gamma^2a_0^3t^{(3\alpha+2\gamma)}}{c(3\alpha+2\gamma)}+\frac{2\alpha a_0^3t^{3\alpha-1}}{c(3\alpha-1)}+D_{03}\right)\right].$$

Cosmography

Cosmography makes it possible to test cosmological models that do not contradict the cosmological principle [33]. The components of dark energy introduced by us in the model change the equations of motion, but they do not affect the relationship between kinematic characteristics. Another approach to finding different models of dark energy is to use a pair of state determinants (j,s). It is known that the rate of expansion of the universe can be expressed through the scale factor, and the deceleration parameter q corresponds to the second derivative of the scale factor. The jerk parameter j corresponds to the fourth derivative of the scale factor, and the third snap parameter (s). Expansion of the scale factor in a Taylor series in the vicinity of the current moment of time t_0 leads to an expression that depends only on the metric (2) and is completely independent of the model [34].

$$a(t)=a_0+\dot{a}(t_0)+\frac{1}{2!}\ddot{a}(t_0)(t-t_0)^2+\frac{1}{3!}\dddot{a}(t_0)(t-t_0)^3+\frac{1}{4!}\ddot{a}(t_0)(t-t_0)^4, \quad (15)$$

where 0 means the current value of the quantity and terms above the fifth order have been omitted. The sign of j determines the change of the universe's dynamics, a positive value indicating the occurrence of a transition time during which the universe modifies its expansion. Moreover, the value of s is necessary to discriminate between an evolving dark energy term or a cosmological constant behaviour.

Let us represent relation (15) in the form

$$\frac{a(t)}{a(t_0)}=1+H_0(t-t_0)-\frac{q_0}{2}H_0^2(t-t_0)^2+\ldots,$$

where deceleration parameter

$$q(t) = -\frac{\ddot{a}(t)a(t)}{\dot{a}^2(t)} = -\frac{\ddot{a}(t)}{a(t)}\frac{1}{H^2(t)},$$

where a is the scale factor of the universe, and the dots denote derivatives with respect to proper time. The expansion of the universe is considered to be accelerated if $\ddot{a} > 0$, in which case the deceleration parameter will be negative.

For the most complete description of the kinematics of the cosmological expansion, it is useful to consider the expanded set of parameters. The function in terms of derivatives of the scale factor and their value at the power low the scale factor (13) is equal to:

Hubble parameter

$$H(t) = \frac{1}{a}\frac{da}{dt} = \frac{\alpha}{t},$$

Deceleration parameter

$$q(t) = -\frac{1}{a}\frac{d^2a}{dt^2}\left(\frac{1}{a}\frac{da}{dt}\right)^{-2} = -1 + \frac{1}{\alpha},$$

Jerk parameter

$$j(t) = \frac{1}{a}\frac{d^3a}{dt^3}\left(\frac{1}{a}\frac{da}{dt}\right)^{-3} = 1 - \frac{3}{\alpha} + \frac{2}{\alpha^2},$$

Snap parameter

$$s(t) = \frac{1}{a}\frac{d^4a}{dt^4}\left(\frac{1}{a}\frac{da}{dt}\right)^{-4} = 1 - \frac{6}{\alpha} + \frac{11}{\alpha^2} - \frac{6}{\alpha^3}.$$

The parameters of deceleration, jerk and snap are dimensionless. These parameters are used to study the dynamics of the later universe. The physical properties of the coefficients can be deduced in the form of the Hubble expansion. In particular, the sign of the parameter q indicates whether the Universe is accelerating or decelerating. The positive sign j defines a change in dynamics, indicating the emergence of a transitional time during which the universe modifies its expansion [35]. The meaning s is necessary to distinguish the evolutionary term of dark energy or the behavior of the cosmological constant. Using them, you can rewrite expression (15) as

$$a(t) = a_0\left[1 + H_0(t - t_0) - \frac{1}{2!}q_0H_0^2(t - t_0)^2 + \frac{1}{3!}j_0H_0^3(t - t_0)^3 + \frac{1}{4!}s_0H_0^4(t - t_0)^4\right].$$

Accelerated growth of the scale factor occurs at $q < 0$. Accelerated increase in the speed of expansion, $H > 0$, corresponds to $q < -1$.

Energy conditions

In the GR theory and modified theories of gravity, the distribution of mass, the momentum and the angular momentum must have values for any field described by the energy-momentum tensor or the matter tensor. However, Einstein's field equation does not impose restrictions on the types of states of matter or non-gravitational regions allowed in the space-time model. This is a strong point, since general relativity should be as independent as possible from any assumptions of non-gravitational physics. The weak point is that Einstein's equation allows for solutions based on properties that most cosmologists regard as non-physical, i.e. too unusual to correspond to anything in the real universe. The energy conditions are such criteria. They describe properties characteristic of all states of matter and all non-gravitational regions studied in physics. Many non-physical solutions of Einstein's equations can be excluded with the help of energy conditions. In cosmology, these four energy conditions are of great importance.

Null Energy Condition (NEC)

$$\rho + p \geq 0.$$

Weak Energy Condition (WEC)

$$\rho \geq 0, \rho + p \geq 0.$$

Strong Energy Condition (SEC)

$$\rho + 3p \geq 0, \rho + p \geq 0.$$

Dominant Energy Condition (DEC)

$$\rho \geq 0, -\rho \leq p \leq \rho.$$

For our model (13) the energy conditions will take the following form
NEC

$$\frac{2\alpha}{t^2} \geq 0.$$

WEC

$$\frac{3\alpha^2}{t^2} \geq 0, \quad \frac{2\alpha}{t^2} \geq 0.$$

SEC

$$\frac{6\alpha}{t^2}(1-\alpha) \geq 0, \quad \frac{2\alpha}{t^2} \geq 0.$$

DEC

$$\frac{3\alpha^2}{t^2} \geq 0, \quad -\frac{3\alpha^2}{t^2} \leq \frac{(2-3\alpha)\alpha}{t^2} \leq \frac{3\alpha^2}{t^2}.$$

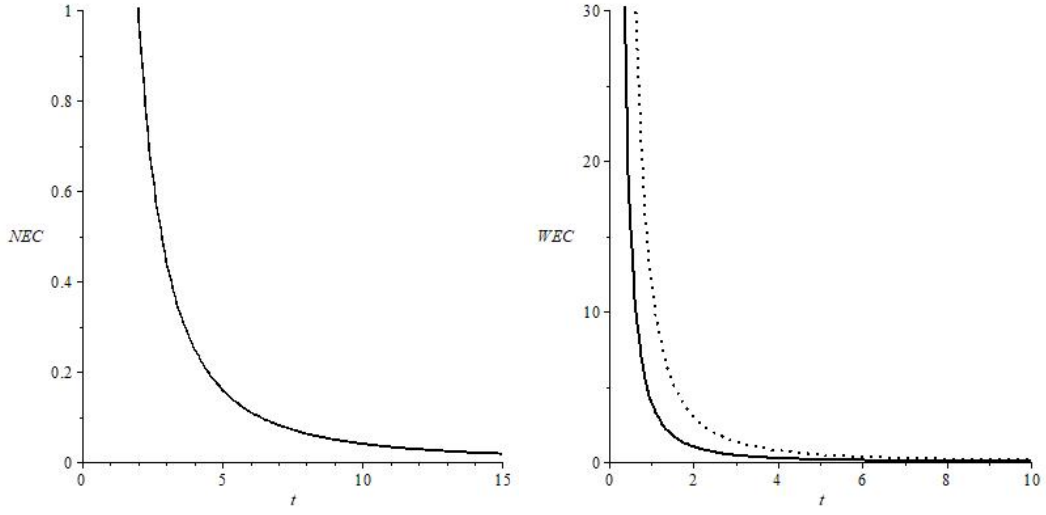

(a) Null energy Condition (5) (b) Strong energy Condition (5)

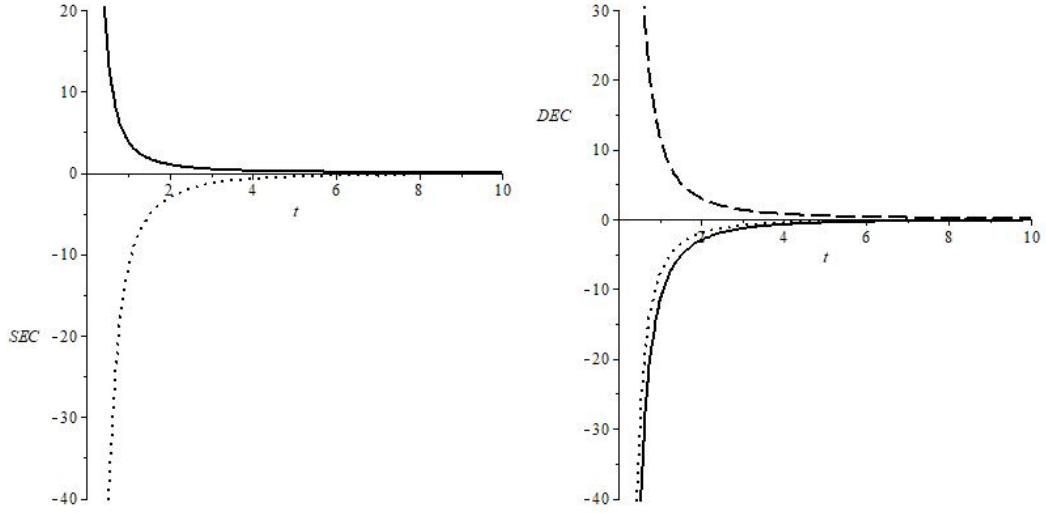

(c) Weak energy Condition (5) (d) Dominant energy Condition (5)
Figure 5. Energy Condition

NEC is shown in Figure 5(a) ($\rho + p$ is a solid line). WEC is shown in Figure 5(b) (ρ — solid line, $\rho + p$ — dotted line). SEC is shown in Figure 5(c) ($\rho + 3p$ — dotted line, $\rho + p$ — solid line). DEC is shown in Figure 5(d) (ρ — dashed line, ρ — solid line, p — dotted line). These conditions impose simple and model-independent constraints on the behavior of energy density and pressure. For our model, a null energy condition, a strong energy condition, a dominant energy condition, and a weak energy condition, which is not mandatory, are fulfilled.

Conclusion

In this work, we analyzed a cosmological model with two components, the scalar field and the fermionic field, interacting through a Yukawa-type potential. Cosmological solutions are obtained analytically for a given value of the exponential and power scale factor. We investigate a particular solution in which it was found that the Yukawa-type potential affects the density but does not contribute to the total pressure. These limitations were studied using cosmological solutions with evolving equations of state, such that a smooth transition between different epochs can always occur in the universe. We also considered some scalar-fermionic model that can describe a single of dark energy — dark matter. To describe the kinematics of the cosmological expansion, we found a wide set of parameters a small power scaling factor: the deceleration parameter q, the jerk parameter j, and the snap parameter s.

Acknowledgments

This *study was funded by the Science Committee of the Ministry of Education and Science of the Republic of Kazakhstan AP14869238.*

References

1 Ribas M.O Cosmological model with fermion and tachyon fields interacting via Yukawa-type potential / M.O. Ribas, F.P. Devecchu, G.M. Kremer / M.O. Ribas, F.P. Devecchu, G.M. Kremer // Modern Physics Letters A. — 2016. — Vol. 1. — No. 9. — P. 1650039.

2 Riess A.G. Observational Evidence from Supernovae for an Accelerating Universe and a Cosmological Constant / A.G. Riess., A.V. Filippenko, P. Challis, et al. // Astrophysical Journal. — 1998. — Vol. 116. — No. 3. — P. 1009.

3 Riess A.G. Type Ia supernova discoveries at z>1 from the Hubble Space Telescope: Evidence for past deceleration and constraints on dark energy evolution / A.G. Riess et al. // Astrophysical Journal. — 2004. — Vol. 607. — P. 665–687.

4 Ribas M.O. Fermionic cosmologies with Yukawa type interactions / M.O. Ribas, F.P. Devecchu, G.M. Kremer // Europhysics Letters Journal. — 2011. — Vol. 93. — No.2. — P.19002.

5 Nojiri S. The future evolution and finite-time singularities in F (R)-gravity unifying the inflation and cosmic acceleration / S. Nojiri, S.D. Odintsov // Physical Review D. — 2008. — Vol. 78. — P. 046006.

6 Nojiri S. Introduction to Modified Gravity and Gravitational Alternative for Dark Energy / S. Nojiri, S.D. Odintsov // International Journal of Geometric Methods in Modern Physics. — 2007. — Vol. 04. — No. 01. — P. 115–145.

7 Bamba K. Future of the universe in modified gravitational theories: Approaching to the finite-time future singularity / K. Bamba, S. Nojiri, S.D. Odintsov // Journal of Cosmology and Astroparticle Physics. — 2008. — Vol. 10. — P. 045.

8 Bamba K. Finite-time future singularities in modified Gauss-Bonnet and F (R, G) gravity and singularity avoidance / K. Bamba, S.D. Odintsov, L. Sebastiani, S. Zerbini // The European Physical Journal C. — 2010. — Vol. 67. — P. 295.

9 Padmanabhan T. Accelerated expansion of the universe driven by tachyonic matter / T. Padmanabhan // Physical Review D. — 2002. — Vol. 66. — P. 021301.

10 Abramo L.R.W. Cosmological dynamics of the tachyon with an inverse power-law potential / L.R.W. Abramo, F. Finelli // Physics Letters B. — 2003. — Vol. 575. — No. 3. — P. 165.

11 Calcagni G. Tachyon dark energy models: Dynamics and constraints / G. Calcagni, A.R. Liddle // Physical Review D. — 2006. — Vol. 74. — P. 043528.

12 Myrzakulov R. Cosmological solutions in F (T) gravity with the presence of spinor fields / R. Myrzakulov, D. Saez-Gomez, P. Tsyba // International Journal of Geometric Methods in Modern Physics. — 2015. — Vol. 12. — P. 1550023.

13 Yerzhanov K. g-Essence as the cosmic speed-up / K. Yerzhanov, K. Yesmakhanova, P. Tsyba, N. Myrzakulov, G. Nugmanova, R. Myrzakulov // Astrophysics and Space Science. — 2012. — Vol. 341, No. 2. — P. 681–688.

14 Avelino P. The politics of sustainability transitions / P. Avelino et al. // Journal of Environmental Policy and Planning. — 2016. — Vol. 8. — No. 2. — P.70.

15 Joyce A. Trodden M. Beyond the cosmological standard model / A. Joyce, B. Jain, J. Khoury // Physics Reports. — 2015. — Vol. 568. — No. 2. — P. 1–98.

16 Bamba K. Dark Energy Cosmology: The Equivalent Description via Different Theoretical Models and Cosmography Tests / K. Bamba, S. Capozziello, S. Nojiri, S. Odintsov // Astrophysics and Space Science. — 2012. — Vol. 342. — P. 155–228.

17 Copeland E.J. Dynamics of dark energy / E.J. Copeland, M. Sami, S. Tsujikawa // International Journal of Modern Physics D. — 2006. — Vol. 15. — No. 11. — P. 1753–1935.

18 Capozziello S. Classifying and avoiding singularities in the alternative gravity dark energy models / S. Capozziello, M. De Laurentis, S. Nojiri, S.D. Odintsov // Physical Review D. — 2009. — Vol. 79. — P. 559.

19 Ribas M.O. Fermions as sources of accelerated regimes in cosmology / M.O. Ribas, F.P. Devecchi, G.M. Kremer // Physical Review D. — 2005. — Vol. 72. — P. 3502.

20 Samojeden L.L. Fermions in Brans-Dicke cosmology / L.L. Samojeden, F.P. Devecchi, G.M. Kremer // Physical Review D. — 2010. — Vol. 81. — P. 7301.

21 Samojeden L.L. Accelerated expansion in bosonic and fermionic 2D cosmologies with quantum effects / L.L. Samojeden, G.M. Kremer, F P. Devecchi // Europhys. Letters. — 2009. — Vol. 87. — P.1.

22 Razina O. Cosmological Einstein-Maxwell model with g-essence / O. Razina, P. Tsyba, B. Meirbekov, R. Myrzakulov // International Journal of Modern Physics D. — 2019. — Vol. 28. – No. 10. — P. 1950126.

23 Razina O. Power solution of the f (R)-gravity with Maxwell term and g-essence / O. Razina, P. Tsyba, Z.M. Sagidullayeva // Bulletin of the university of Karaganda-Physics. — 2019. — Vol. 1. — No. 93. — P. 94–102.

24 Ribas M.O. Fermions in a Walecka-type cosmology / M.O. Ribas, P. Zambianchi, F.P. Devecchi, G.M. Kremer // Europhysics Letters. — 2012. — Vol. 97. — P. 5.

25 Kulnazarov I. G-essence with Yukawa Interactions / I. Kulnazarov, K. Yerzhanov, O. Razina, Sh. Myrzakul, P. Tsyba, R. Myrzakulov // The European Physical Journal C. — 2011. — Vol. 71. — No. 7. — P. 1698.

26 Tsyba P. Scenario of the evolution of the universe with equation of state of the Weierstrass type gas / P. Tsyba, O. Razina, Z. Barkova, S. Bekov, R. Myrzakulov // Journal of Physics: Conference Series. — 2019. — Vol. 1391. — P. 012162.

27 Razina O.V. Cosmological Yang-Mills model with k-essence / O.V. Razina, P.Yu. Tsyba, R. Myrzakulov, B. Meirbekov, Z. Shanina // Journal of Physics Conference Series. — 2019. — No. 1391(1). — P. 012164.

28 Altayeva G. Cosmography in the multifield cosmological model / G. Altayeva, O. Razina, P. Tsyba // Bulletin of the University of Karaganda-Physics. — 2022. — No. 2(106). — P. 37-48.

29 Myrzakulova S.A. Slow-roll inflation in the k-essence model with a periodic scalar field function / S.A. Myrzakulova, O.V. Razina, N.A. Myrzakulov, A.B. Altaybaeva // Recent Contributions to Physics. — 2022. — Vol. 81. — No. 2. — P. 19-27.

30 Rakhatov D.Z. Power-law solutions of the f(G) gravity model with electromagnetic and scalar field / D.Z. Rakhatov, P.Y. Tsyba, O.V. Razina // Recent Contributions to Physics. — 2022. — Vol. 80. — No. 1. — P. 12-21.

31 Razina O. G-essence cosmologies with scalar-fermion interactions / O. Razina, Y. Myrzakulov, N. Serikbayev, S. Myrzakul, G. Nugmanova, R. Myrzakulov // European Physical Journal Plus. — 2011. — Vol. 126. — No. 9. — P. 85.

32 Болотин Ю.Л. Расширяющаяся Вселенная: замедление или ускорение? / Ю.Л. Болотин, Д.А. Ерохин, О.А. Лемец // Успехи физических наук. — 2012. — Т. 55. — № 9. — С. 876–918.

33 Arjona R. Novel null tests for the spatial curvature and homogeneity of the Universe and their machine learning reconstructions / R. Arjona, S. Nesseris // Physical Review D. — 2021. — Vol. 103. — P. 063537.

34 Capozziello S. Cosmography of f (R) gravity / S. Capozziello, V.F. Cardone, V. Salzano // Physical Review D. — 2008. — Vol. 78. — P. 063504.

35 Capozziello S. Gravity Cosmography / S. Capozziello, R. D'Agostino, O. Luongo // General Relativity and Quantum Cosmology. — 2019. — Vol. 1. — No. 35. — P. 82.

П.Ю. Цыба, Г.С. Алтаева, О.В. Разина

Минималды өзара әсерлесуін қамтитын материя өрістерінің сызықты лагранжиандары бар скалярлық-фермиондық модельді зерттеу

Мақалада Юкава типті потенциал арқылы әрекеттесетін скалярлық және фермиондық өрістері бар Әлемнің моделі зерттелген. Зерттелетін модельде қараңғы энергияның жалпы тығыздығы мен қысымына өрістердің әрқайсысының құрамдас бөлігі бойынша үлестері анықталған. Космологиялық модель есептерін шешуде функционалды уақытқа тәуелді екі шешімі бар масштабты фактор қарастырылған. Юкава типті өріс жалпы қысымға өз үлесін қоспайды. Дәрежелік жағдайда фермиондық өріс, ал экспоненциалды — скалярлық өрісте толық қысымға көбірек үлес қосады. Көп жағдайларда, космологиялық ұлғаюдың әртүрлі модельдерінде Әлем кезекті дәуірлер арасында ауысуды жүзеге асырады. Бұл заңдылықтар скалярлық және фермиондық өріс әсерлесу профиліне және жалпы космологиялық динамикаға белгілі бір шектеулер қояды. Зерттелетін модельді тексеру үшін энергетикалық жағдай анықталды. Зерттелетін модельде нөлдік энергетикалық жағдай, күшті энергетикалық жағдай, үстемдік энергетикалық жағдай орындалады және міндетті емес әлсіз энергетикалық жағдай орындалмайды. Космографиялық параметрлердің — q баяулату параметрі, j серпілу параметрі және s басу параметрлерінің дәрежелік масштабты факторының мәнімен қалай байланыстыруға болатындығы көрсетілген. Бұл шектеулер космологиялық шешімдерді қолдана отырып, эволюционалдық күй теңдеуімен зерттелді, осылайша Әлемде әр түрлі дәуірлер арасында бірқалыпты ауысу болуы мүмкін. Зерт-

теліп отырған скалярлық-фермиондық модельдер Әлемнің үдемелі ұлғаю режимдерін сипаттайды. Алынған нәтиже бойынша шешімдер, бақылау деректер нәтижелерімен теориясына болжау сәйкес келеді.

Кілт сөздер: скалярлы өріс, фермиондық өріс, Юкава типті әсерлесу, минималды әсерлесу, энергетикалық жағдай, космография.

П.Ю. Цыба, Г.С. Алтаева, О.В. Разина

Исследование скалярно-фермионной модели, содержащей линейные лагранжианы полей материи, в рамках минимального взаимодействия

В статье исследована модель Вселенной со скалярными и фермионными полями, взаимодействующими через потенциал типа Юкавы. В данной модели определены покомпонентные вклады каждого из полей в полную плотность и давление темной энергии. Рассмотрено решение космологической модели для масштабного фактора с двумя функциональными зависимостями от времени. Поле типа Юкавы не дает своего вклада в общее давление. В степенном случае больший вклад в полное давление осуществляет фермионное поле, в экспоненциальном — скалярное. Существует множество случаев, когда Вселенная совершает переход между последующими эпохами в различных моделях космологического расширения. Эти закономерности накладывают некоторые ограничения на профиль скалярно-фермионного взаимодействия и на общую космологическую динамику. Для проверки исследуемой модели найдены энергетические условия. В указанной модели выполняется нулевое энергетическое условие, сильное энергетическое условие, доминирующее энергетическое условие и не осуществляется слабое энергетическое условие, которое необязательное. Показано, как можно связать космографические параметры — параметры замедления q, рывка j и щелчка s со степенным значением масштабного фактора. Авторами исследованы ограничения, с использованием космологических решений с эволюционирующим уравнением состояния, таким, что во Вселенной всегда может произойти плавный переход между разными эпохами. В исследуемой скалярно-фермионной модели описаны ускоренные режимы расширения Вселенной. Полученные решения соответствуют результатам, предсказанным теорией.

Ключевые слова: скалярное поле, фермионное поле, взаимодействие типа Юкавы, минимальное взаимодействие, энергетические условия, космография.

References

1 Ribas, M.O., Devecchu, F.P., & Kremer, G.M. (2016). Cosmological model with fermion and tachyon fields interacting via Yukawa-type potential. *Modern Physics Letters A, 1*(9) 1650039.

2 Riess, A.G., Filippenko, A.V., & Challis, P. et al. (1998). Observational evidence from supernovae for an Accelerating Universe and a Cosmological Constant. *Astrophysical Journal, 116*(3), 1009–1038.

3 Riess, A.G., Strolger, L.G., Tonry, J., et al. (2004). Type Ia supernova discoveries at z > 1 from the hubble space telescope: evidence for past deceleration and constraints on dark energy evolution. *Astrophysical Journal, 607*, 665–687.

4 Ribas, M.O., Devecchu, F.P., & Kremer, G.M. (2011). Fermionic cosmologies with Yukawa type interactions. *Europhysics Letters Journal, 93*(2), 19002.

5 Nojiri, S., & Odintsov, S.D. (2008). Future evolution and finite-time singularities in F (R) gravity unifying inflation and cosmic acceleration. *Physical Review D, 78*, 046006.

6 Nojiri, S., & Odintsov, S.D. (2007). Introduction to modified gravity and gravitational alternative for dark energy. *International Journal of Geometric Methods in Modern Physics, 4*(1), 115–145.

7 Bamba, K., Nojiri, S., & Odintsov, S.D. (2008). Future of the universe in modified gravitational theories: Approaching to the finite-time future singularity. *Journal of Cosmology and Astroparticle Physics, 10*, 045.

8 Bamba, K., Odintsov, S.D., Sebastiani, L., et al. (2010). Finite-time future singularities in modified Gauss-Bonnet and F(R, G) gravity and singularity avoidance. *The European Physical Journal C, 67*, 295–310.

9 Padmanabhan, T. (2002). Accelerated expansion of the universe driven by tachyonic matter. *Physical Review D, 66*, 021301.

10 Abramo, L.R.W., & Finelli, F. (2003). Cosmological dynamics of the tachyon with an inverse power-law potential. *Physics Letters B, 575*(3), 165.

11 Calcagni, G., & Liddle, A.R. (2006). Tachyon dark energy models: Dynamics and constraints. *Physical Review D, 74*, 043528.

12 Myrzakulov, R., Saez-Gomez, D., & Tsyba, P. (2015). Cosmological solutions in F (T) gravity with the presence of spinor fields. *International Journal of Geometric Methods in Modern Physics, 12*, 1550023.

13 Yerzhanov, K., Yesmakhanova, K., Tsyba, P., Myrzakulov, N., Nugmanova, G., & Myrzakulov, R. (2012). g-Essence as the cosmic speed-up. *Astrophysics and Space Science, 341*(2), 681–688.

14 Avelino, P. et al. (2016). The politics of sustainability transitions. *Journal of Environmental Policy and Planning, 8*(2), 70.

15 Joyce, A., Jain, B., Khoury, J., & Trodden, M. (2015). Beyond the cosmological standard model. *Physics Reports, 568*(2), 1–98.

16 Bamba, K., Capozziello, S., Nojiri, S., & Odintsov, S. (2012). Dark Energy Cosmology: The Equivalent Description via Different Theoretical Models and Cosmography Tests. *Astrophysics and Space Science, 342*, 155-228.

17 Copeland, E.J., Sami, M., & Tsujikawa, S. (2006). Dynamics of dark energy. *International Journal of Modern Physics D, 15*(11), 1753–1935.

18 Capozziello, S., De Laurentis, M., Nojiri, S., & Odintsov, S.D. (2009). Classifying and avoiding singularities in the alternative gravity dark energy models. *Physical Review D, 79*, 559.

19 Ribas, M.O., Devecchi, F.P., & Kremer, G.M. (2005). Fermions as sources of accelerated regimes in cosmology. *Physical Review D, 72*, 3502.

20 Samojeden, L.L., Devecchi, F.P., & Kremer, G.M. (2010). Fermions in Brans-Dicke cosmology. *Physical Review D, 81*, 7301.

21 Samojeden, L.L., Kremer, G.M., & Devecchi, F.P. (2009). Accelerated expansion in bosonic and fermionic 2D cosmologies with quantum effects. *Europhys. Letters, 87*, 1.

22 Razina, O., Tsyba, P., Meirbekov, B., & Myrzakulov, R. (2019). Cosmological Einstein-Maxwell model with g-essence. *International Journal of Modern Physics D, 28*(10), 1950126.

23 Razina, O., Tsyba, P., & Sagidullayeva, Z.M. (2019). Power solution of the f (R)-gravity with Maxwell term and g-essence. *Bulletin of the university of Karaganda-Physics, 1*(93), 94–102.

24 Ribas, M.O., Zambianchi, P., Devecchi, F.P., & Kremer, G.M. (2012). Fermions in a Walecka-type cosmology. *Europhysics Letters, 97*, 5.

25 Kulnazarov, I., Yerzhanov, K., Razina, O., Myrzakul, Sh., Tsyba, P., & Myrzakulov, R. (2011). G-essence with Yukawa Interactions. *The European Physical Journal C, 71*(7), 1698.

26 Tsyba, P., Razina, O., Barkova, Z., Bekov, S., & Myrzakulov, R. (2019). Scenario of the evolution of the universe with equation of state of the Weierstrass type gas. *Journal of Physics: Conference Series, 1391*, 012162.

27 Razina, O.V., Tsyba, Yu. P., Myrzakulov, R., Meirbekov, B., & Shanina, Z. (2019). Cosmological Yang-Mills model with k-essence. *Journal of Physics Conference Series, 1391*, 012164.

28 Altayeva, G., Razina, O., & Tsyba, P. (2022). Cosmography in the multifield cosmological model. *Bulletin of the University of Karaganda-Physics, 2*(106), 37-48.

29 Myrzakulova, S.A., Razina, O.V., Myrzakulov, N.A., & Altaybaeva, A.B. (2022). Slow-roll inflation in the k-essence model with a periodic scalar field function. *Recent Contributions to Physics, 81*(2), 19-27.

30 Rakhatov, D.Z., Tsyba, P.Y., & Razina, O.V. (2022). Power-law solutions of the f(G) gravity model with electromagnetic and scalar field. *Recent Contributions to Physics, 80*(1), 12-21.

31 Razino, O., Myrzakulov, Y., Serikbayev, N., Myrzakul, S., Nugmanova, G., & Myrzakulov, R. (2011). G-essence cosmologies with scalar-fermion interactions. *European Physical Journal Plus, 126*(9), 85.

32 Bolotin, Yu.L., Erokhin, D.A., & Lemets, O.A. (2012). Rasshiriaiushchaiasia Vselennaia: zamedlenie ili uskorenie? [Expanding Universe: slowdown or speedup?]. *Uspekhi fizicheskikh nauk — Advances in the physical sciences, 55* (9), 876–918 [in Russian].

33 Arjona, R., & Nesseris, S. (2021). Novel null tests for the spatial curvature and homogeneity of the Universe and their machine learning reconstructions. *Physical Review D, 103*, 063537.

34 Capozziello, S., Cardone, V.F., & Salzano, V. (2008). Cosmography of f (R) gravity. *Physical Review D, 78*, 063504.

35 Capozziello, S., D'Agostino, R., & Luongo, O. (2008). Gravity Cosmography. *General Relativity and Quantum Cosmology, 1*(35), 82.

DOI 10.31489/2023PH2/66-71

UDC: 538.9

E.R. Hasanov[1], Sh.G. Khalilova[2]

[1] *Baku State University, Baku, Azerbaijan Republic;*
[1,2] Institute of Physics, Baku, *Azerbaijan Republic*
(E_mail: shahlaganbarova@gmail.com)

Instability in multi-valley semiconductors in external electric and magnetic fields

It is theoretically proved that the excited wave in two-valley semiconductors is growing. It is indicated that the directions of external fields play an essential role for the appearance of growing waves in the sample. It is shown that oscillations can occur at certain values of the sample dimensions L_x, L_y, L_z Analytical formulas for the frequency of the growing waves are obtained. The interval of variation of the external electric field in a strong magnetic field $\mu H >> c$ has been determined. The paper takes into account that the time of transition from the lower valley to the upper valley differs from the time of transition from the upper valley to the lower valley. It means $\tau_{12} \neq \tau_{21}$ In the sample, the total concentration is constant, and therefore, $n_0 = n_a + n_b = const$. The changes in the corresponding concentrations are equal to each other and have the opposite sign, i.e. $n_a' = -n_b'$. It is taken into account that at critical values of the electric and magnetic fields and the corresponding concentrations they change as a monochromatic wave. And the change in these quantities differs little from their equilibrium value. For simplicity of mathematical calculations, the external electric and magnetic fields are directed in the same way, i.e. in x direction. Since the current oscillations in one direction (for example, along x) are studied in the experiment, the following equalities were taken into account $j_y' = 0, j_z' = 0$. In the vicinity of the critical field at the beginning of the current oscillation in the sample, the current oscillation frequency is $\varpi = \varpi_0 + i\varpi_1$, $\varpi_1 << \varpi_0$. In addition, the magnitude of the critical electric field, at which the current fluctuation changes depending on the magnetic field as follows $E_{kr} \sim \frac{1}{H_{external}^4}$.

Keywords: growth, oscillation, frequency, increment, valley, mobility, effective mass, Gunn's effect.

Introduction

In [1-5], current oscillations in semiconductors with one type of charge carriers and in semiconductors with two types of charge carriers were theoretically investigated. In these theoretical studies, analytical expressions were obtained for the vibration frequency and for the critical electric field at the onset of vibration inside the sample. It is known that fluctuations in the current in the Gunn effect occurs due to the transition of electrons from a low energy level to a higher energy level. Of course, after the transition of electrons from the lower energy level to the upper energy level, the number of charge carriers in the lower valley decreases, and in the upper valley their number increases. After the inelastic interaction of charge carriers, losing the energy received from the electric field, they return to the lower valley. The transition time from the lower valley to the upper valley τ_{12} differs from the time of the transition from the upper valley to the lower valley τ_{21}, i.e.

$$\tau_{12} \neq \tau_{21}. \quad (1)$$

Under the influence of external electric magnetic fields, current fluctuations in the circuit occur due to the presence of inequality (1). The effective mass of charge carriers m_a in the lower valley, and the effective mass of charge carriers m_b differ significantly

$$m_a << m_b \quad (2)$$

(in GaAs, $m_a = 0{,}072 m_0$, $m_b = 1{,}2 m_0$, m_0 is the mass of a free electron). In the Gunn effect [6], current oscillations begin at a critical value of the external electric field, approximately $2 \cdot 10^3 V/cm$ or $3 \cdot 10^3 V/cm$. In these critical values of the electric field, the inequality

$$eE_0L >> D\nabla n \quad (3)$$

(L is electron mean free path, e is elementary charge, D is diffusion coefficient, ∇n is electron concentration gradient). In force (3), during the transition from valley a to valley b, diffusion currents do not play the main role. In this theoretical work, we will investigate current oscillations in semiconductors of the GaAs type under the action of an external constant electric and magnetic fields, taking into account inequalities (1-3). Under the conditions of execution (1-3) and taking into account the direction of the external electric and magnetic fields, we will theoretically investigate the frequency of current oscillations in the above semiconductors and the critical value of the external electric field. We will investigate current oscillations in two-valley semiconductors at different directions of external electric and magnetic fields.

Basic equations of the problem

The electron concentration in GaAs is constant, therefore

$$n_0 = n_a + n_b = const$$
$$n'_a = -n'_b . \quad (4)$$

The equation of continuity in the valleys "a" and "b" is as follows:

$$\frac{\partial n'_a}{\partial t} + div\vec{j}'_a = \frac{n'_a}{\tau_{12}} \quad (5)$$
$$\frac{\partial n'_b}{\partial t} + div\vec{j}'_b = \frac{n'_b}{\tau_{21}} . \quad (6)$$

Taking into account (3) in the presence of external electric and magnetic fields, the expressions for the flux density in the valleys "a" and "b" have the form:

$$\vec{j}_a = \sigma_a\vec{E} + \sigma_{1a}\left[\vec{E}\vec{H}\right] + \sigma_{2a}\vec{H}\left[\vec{E}\vec{H}\right] \quad (7)$$
$$\vec{j}_b = \sigma_b\vec{E} + \sigma_{1b}\left[\vec{E}\vec{H}\right] + \sigma_{2b}\vec{H}\left[\vec{E}\vec{H}\right] . \quad (8)$$

Here $\sigma_{a,b} = en_{a,b}\mu_{a,b}$; $\sigma_{1a,b} = en_{a,b}\mu_{1a,b}$; $\sigma_{2a,b} = en_{a,b}\mu_{2a,b}$, $\mu_{a,b}, \mu_{1a,b}, \mu_{2a,b}$, corresponding to electron mobility

$$\frac{\partial H'}{\partial t} = -irot\vec{E}' \quad (9)$$

Theory

To determine the dispersion equation from (5, 6), taking into account (7-9), we will assume that all variable quantities change as monochromatic waves, i.e.

$$\left(E', H', n'_a, n'_b\right) \sim e^{i\left(\vec{k}\vec{r} - wt\right)} \quad [8]$$

($\vec{k}$ is wave vector, ω is vibration frequency within the sample)

$$\vec{E} = \vec{E}_0 + \vec{E}', n_a = n_a^0 + n'_a, n_b = n_b^0 + n'_b, \vec{H} = \vec{H}_0 + \vec{H}' . \quad (10)$$

The direction of the magnetic field $\vec{H}_0$ relative to the electric field $\vec{E}_0$ is essential for determining the dispersion equation. First, we obtain the dispersion equation from (5-6) with the orientation of the electric and magnetic fields by the following sample

$$\vec{E}_0 = \vec{i}E_0, \vec{H}_0 = \vec{i}H_0 \quad (11)$$

($\vec{i}$ is unit vector in x). On the basis of (11) from (7) it is easy to obtain:

$$\vec{j}'_a = \sigma_a^0\vec{E}' + \vec{i}\,2E'_x\left(\sigma_a^0\varphi_a + \sigma_{2a}^0\varphi_{2a}\right) + \vec{i}\,\frac{n'_a}{n_{a0}}E_0\left(\sigma_a^0 + \sigma_{2a}^0\right) + \vec{i}\,\sigma_{2a}^0E'_x + \frac{\sigma_{1a}^0cE_0}{\omega H_0}\left(E'_x\vec{k} - k_x\vec{E}'\right) + \frac{2\sigma_{2a}^0cE_0}{\omega H_0}\left[\vec{k}\vec{E}'\right] \quad (12)$$

$\vec{j}'_b$ has the form (12) only "a" must be replaced by "b". Writing down the components (12) ($\vec{j}'_{ax}, \vec{j}'_{ay}, \vec{j}'_{az}$) and from the condition $j'_{ay} = 0, j'_{az} = 0$ finds the components E'_y and E'_z then supplying the values E'_y and E'_z in j'_{ax} we find:

$$j'_{ax}=\left[\sigma^0_{2a}\left(1+2\varphi_{2a}\right)+2\varphi_a\sigma'_a-\frac{2\sigma_{2a}ck_zE_0}{\omega H_0}\cdot\frac{1}{\frac{\sigma^0_a\sigma^0_{1a}}{2\left(\delta^0_{2a}\right)^2}\cdot\frac{\omega H}{ck_yE_0}-2}-\frac{2\sigma^0_{2a}ck_yE_0}{\omega H_0}\left(\frac{2L_y}{L_x}+\frac{1}{u^2}\right)\right]E'_x+\frac{n'_a}{n_{a0}}\sigma^0_{2a}E_0 \quad (13)$$

j'_{bx} has the form (13) if "a" is replaced by "b". Supplying j'_{ax} and j'_{bx} in (14) taking into account (4)

$$divj'_{ax}=\frac{n'_a\left(1+i\omega\tau_{12}\right)}{\tau_{12}}$$
$$divj'_{bx}=\frac{n'_b\left(1+i\omega\tau_{21}\right)}{\tau_{21}} \quad (14)$$

We easily obtain the following dispersion equation

$$\left(\frac{i}{\tau_{21}}-\omega+\mu^0_{2a}k_xE_0\right)\sigma^0_{2a}\left[\Phi_a\left(\frac{L_y\omega^2}{2\pi\mu_aE_0}-2\omega\right)-\frac{4\pi cE_0}{H_0L_z}-\frac{8\pi cE_0}{L_yH_0}\cdot\frac{1}{u^2}\left(\frac{1}{4\pi}\cdot\frac{\omega L_y}{\mu_aE_0}-2\right)-\frac{8\pi cE_0}{H_0L_x}\left(\frac{1}{4\pi}\cdot\frac{L_y\omega}{\mu_aE_0}-2\right)\right]+$$
$$+\left(\frac{i}{\tau_{12}}+\mu^0_{2b}k_xE_0\right)\sigma^0_{2b}\left[\Phi_b\left(\frac{1}{4\pi}\frac{L_y\omega^2}{\mu_bE_0}-2\omega\right)-\frac{4\pi cE_0}{H_0L_z}-\frac{8\pi cE_0}{L_yH_0}\cdot\frac{1}{u^2}\left(\frac{1}{4\pi}\cdot\frac{\omega L_y}{\mu_bE_0}-2\right)-\frac{8\pi cE_0}{H_0L_x}\left(\frac{1}{4\pi}\cdot\frac{L_y\omega}{\mu_bE_0}-2\right)\right] \quad (15)$$

Here $\Phi_a=2\varphi_a+1+2\varphi_{2a}$, $\Phi_b=2\varphi_b+2\varphi_{2b}$.

From (15) it turns out:

$$\omega^3-\left[\frac{i}{\tau_{21}}+\mu^0_{2b}k_xE_0+\alpha_a\omega_a+\frac{m_a}{m_b}\frac{\omega_a}{\omega_b}\left(\frac{i}{\tau_{12}}+\mu^0_{2a}k_xE_0\right)\right]\omega^2+$$
$$+\left[\omega_a\left(\frac{i}{\tau_{21}}+\mu^0_{2b}k_xE_0\right)\alpha_a+\omega_x\omega_a+\alpha_b\omega_a\left(\frac{i}{\tau_{12}}+\mu^0_{2a}E_0k_x\right)\right]\omega- \quad (16)$$
$$-\omega_a\omega_x\left(\frac{i}{\tau_{21}}+\mu^0_{2b}E_0k_x\right)-\omega_x\omega_a\frac{m_a}{m_b}\left(\frac{i}{\tau_{12}}+\mu^0_{2a}k_xE_0\right)=0$$

Here $\omega_x=\frac{16\pi cE_0}{H_0L_x}$, $\alpha_a=2\Phi_a+\frac{2cL_y}{\mu_aH_0L_x}$, $\alpha_b=2\Phi_b+\frac{2cL_y}{\mu_bH_0L_x}$, $\omega_a=\frac{4\pi\mu^0_aE_0}{\Phi_aL_y}$.

Supplying in (16) $\omega=\omega_0+i\omega_1$, taking into account $\omega_1<<\omega_0$ (17), we obtain the following two equations for determining ω_0 and ω_1

$$\omega_0^3-\Omega_0\omega_0^2+2\Omega_1\omega_0\omega_1+\gamma_0^2\omega_0-\gamma_1^2\omega_1-\delta_0^3=0 \quad (17)$$
$$3\omega_0^2\omega_1-2\Omega_0\omega_0\omega_1-\Omega_1\omega_0^2+\gamma_0^2\omega_1+\gamma_1^2\omega_0-\delta_1^3=0 \quad (18)$$

Here $\Omega_0=\mu^0_{2b}E_0k_x$, $\Omega_1=\frac{m_a}{m_b}\cdot\frac{1}{\tau_{12}}$, $\gamma_0^2=\frac{64\pi^2}{\Phi_au}\cdot\frac{\left(\mu_aE_0\right)^2}{L_xL_y}$; $\gamma_1^2=\frac{8\pi}{\tau_{12}u}\cdot\frac{\mu_aE_0}{k_x}$; $\delta_0^3=\frac{32\pi^2}{u}\sigma^0_{2b}\frac{\mu^0_{2a}\mu_aE_0^2}{L_x^2}$,

$\delta_1^3=\frac{64\pi^2}{4}\frac{\left(\mu_aE_0\right)^2}{\Phi_aL_xL_y}\cdot\frac{2}{\tau_{12}}\cdot\frac{m_a}{m_b}$.

When obtaining dispersion equations (17-18), we assumed that

$$\tau_{21}=\tau_{12}\frac{m_b}{m_a},\ L_y=4L_z,\ L_x>>\frac{1}{2}\left(\frac{m_b}{m_a}\right)^2L_y.$$

Analysis of equation (17-18) shows that for

$$E_0 >> E_{кр},\ K_{кр} = \left(\frac{1}{\tau_{12}}\right)^2 \frac{L_x}{12\pi\sigma_{2b}^0\mu_{2a}^0} \quad (19)$$

$$\omega_0 = \frac{8\sigma_{2b}^0}{u}\frac{m_b}{m_a}\frac{\mu_a}{\mu_{2b}^0},\ \omega_1 = \frac{1}{3}\frac{m_b}{m_a}\cdot\frac{1}{\tau_{12}} \quad (20)$$

And the condition $\omega_0 >> \omega_1$ is met if

$$\tau_{12} >> \frac{1}{24en_{0b}\mu_a}\left(\frac{m_a}{m_b}\right)^2 \quad (21)$$

It can be seen from (20) that the frequency of the growing oscillations decreases with ω_1 an increase in the external magnetic field as $\omega \sim \frac{1}{H}$, and the critical field decreases as $E_{kr} \sim \frac{1}{H^4}$. Thus, with an external magnetic field, it is possible to obtain current oscillations in two-valley semiconductors at lower values of the external electric field. This result was obtained in our previous theoretical works [7]. If we evaluate the existing experimental values (19-20), then we can easily get approximate values

$$\omega_0 \sim 10^9\,Hz,\ \omega_1 \sim 2\cdot 10^7\,Hz,\ E_{kr} \sim 10^2\,V/cm,\ \tau_{21} \approx 6\tau_{12}.$$

Now we will choose the following orientation of the electric and magnetic fields

$$\vec{E}_0 = \vec{i}E_0,\ \vec{H}_0 = \vec{j}H_0 \quad (22)$$

With orientation (22), repeating calculations using equations (5.6) taking into account (4), we obtain the following dispersion equation

$$\omega^2 - \left[\omega_b + \omega_a\frac{\tilde{\sigma}_b}{\tilde{\sigma}_a} - \frac{\sigma_1^2+\sigma_2^2}{\tilde{\sigma}_a} + i\left(\frac{1}{\tau_{21}} + \frac{\tilde{\sigma}_b}{\tilde{\sigma}_a}\frac{1}{\tau_{12}}\right)\right]\omega - \frac{\sigma_1^2 u_{b_0} + \sigma_1^2 u_{a_0}}{\tilde{\sigma}_a} - \frac{i}{\tilde{\sigma}_a}\left(\frac{\sigma_1^2}{\tau_{21}} + \frac{\sigma_2^2}{\tau_{12}}\right) = 0 \quad (23)$$

Here

$$\sigma_1^2 = k_x\tilde{\sigma}_a u_{b_0},\ \sigma_2^2 = k_x\tilde{\sigma}_b u_{a_0},\ \tilde{\sigma}_a = \sigma_{a_0}(1+2\varphi_a);\ \tilde{\sigma}_b = \sigma_{b_0}(1+2\varphi_b);\ \varphi_a = \frac{d\ln\mu_a}{d\ln\left(E_0^2\right)};\ \varphi_b = \frac{d\ln\mu_b}{d\ln\left(E_0^2\right)}$$

From (23) is the electric field

$$E_0 = \frac{2\sigma_{a_0}\sigma_{b_0}(1+\varphi_a+\varphi_b)}{en_0\mu_{a_0}\mu_{b_0}k_x} = 2\varphi\frac{en_{b_0}}{k_x} \quad (24)$$

Supplying (24) to (23) with

$$\left(\frac{1}{\tau_{21}} + \frac{\tilde{\sigma}_b}{\tilde{\sigma}_a}\cdot\frac{1}{\tau_{12}}\right)^2 = 8\varphi en_{b_0}\frac{\sigma_1^2\mu_{b_0} + \sigma_2^2\mu_{a_0}}{\tilde{\sigma}_a} \quad (25)$$

We obtain the following expressions for the oscillation frequency in the above two-valley semiconductors

$$\omega_1 = \frac{1}{\sqrt{2}}\left(\frac{1}{\tau_{21}} + \frac{\tilde{\sigma}_b}{\tilde{\sigma}_a}\cdot\frac{1}{\tau_{12}}\right)\left[\frac{i}{2}\left(1+\sqrt{2}\right)\right],\ \omega_2 = -\frac{1}{\sqrt{2}}\left(\frac{1}{\tau_{21}} + \frac{\tilde{\sigma}_b}{\tilde{\sigma}_a}\cdot\frac{1}{\tau_{12}}\right)\left[\frac{i}{2}\left(1-\sqrt{2}\right)\right] \quad (26)$$

It can be seen from (26) that the excited wave with frequency $\omega_0 = \frac{1}{\sqrt{2}}\left(\frac{1}{\tau_{21}} + \frac{\tilde{\sigma}_b}{\tilde{\sigma}_a}\cdot\frac{1}{\tau_{12}}\right)$ and grows with the increment $\gamma = \frac{1}{\sqrt{2}}\left(\frac{1}{\tau_{21}} + \frac{\tilde{\sigma}_b}{\tilde{\sigma}_a}\cdot\frac{1}{\tau_{12}}\right)\frac{1+\sqrt{2}}{2}$.

A wave with a frequency ω_2 is damped. This means that when the magnetic field is directed perpendicular to the electric field, a wave is excited with a frequency that is very different from the case $\vec{E}_0 \perp \vec{H}_0$.

Conclusion

Two-valley semiconductors with valleys “a” and “b” effective masses of electrons are $m_a \ll m_b$. In an external constant electric and magnetic fields, we radiate energy at a high frequency, at certain values of the electric field. Magnetic field values are $\mu_{a_0} H_0 >> c$ and $\mu_{b_0} H_0 >> c$. These fluctuations occur in the sample with certain values L_x, L_y, L_z. $H_0 \perp E_0$, the oscillation is excited with a different frequency and in a different value of the external electric field. Rough estimates of the electric field and vibration frequency within the existing experiments are quite satisfactory.

Reference

1 Hasanov, E.R., Islamzade, A.V., & Hasanov, H.Sh. (2016). Thermomagnetic Waves In Anisotropic Conductors. *International Journal On Technical And Physical Problems Of Engineering, l,* 50-54.

2 Hasanov, E.R., & Mustafayeva, I.I.(2017). Non-linear fluctuations of concentration of charge carriers and an electric field in semiconductors. *13th International Conference on “Technical and Physical Problems of Electrical Engineering”, 38*, 39-43.

3 Hasanov, E.R., & Aliev, F.F. (2018). Nonlinear Oscillation Task for the Concentration of Field Carriers in Semiconductors with Deep Traps. *IOSR Journal of Applied Physics, l0*, 36-42.

4 Hasanov, E.R., Khalilova, Sh.G., Mansurova, E.O., & Tabatabaei, N.M. (2020). Unstable thermomagnetic waves in anisotropic medium of electronic type of charge carriers. *International Journal on “Technical and Physical Problems of Engineering” (IJTPE) Turkey, 12,* 49-52.

5 Hasanov, E.R., Khalilova, Sh.G., Tagiyeva, Z.A., Hajiyeva, V.M., & Ahadova, S.S. (2021). Excitation of thermomagnetic and recombination waves in impurity with two types of current carriers. *International Journal on “Technical and Physical Problems of Engineering”(IJTPE), 13,* 57-61.

6 Gunn, J.B. (1964). “Current instabilities and potential distribution in GaAs and InP. Plasma Effects in Solids, Paris. 199-207.

7 Hasanov, E.R., Khalilova, Sh.G., Mammadova, G.M., & Mansurova, E.O. (2021). Excitation of unstable waves in impurity semiconductors with two types of charge carriers in external electric and weak magnetic fields. *International Journal on “Technical and Physical Problems of Engineering” (IJTPE), 13,* 94-97.

8 Mammadova, G.M. (2022).The frequency of current fluctuations in two-valley semiconductors in an external electric and strong magnetic ($\mu h > c$) fields. *Bulletin of the University of Karaganda-Physics, 4*, 65-72.

Э.Р. Гасанов, Ш.Г. Халилова

Сыртқы электр және магнит өрістеріндегі көпжақты жартылай өткізгіштердегі тұрақсыздық

Екіжақты жартылай өткізгіштердегі қозған толқын біртіндеп артатыны теориялық түрде дәлелденді. Сыртқы өрістердің бағыттары үлгідегі артып келе жатқан толқындардың пайда болуы үшін маңызды рөл атқаратыны көрсетілген. Тербелістер үлгі өлшемдерінің белгілі бір мәндерінде L_x, L_y, L_z болуы мүмкін екендігі дәлелденген. Артып келе жатқан толқындардың жиілігі үшін аналитикалық формулалар алынды. Күшті магнит өрісі бар $\mu H >> c$ сыртқы электр өрісінің өзгеру аралығы анықталды. Жұмыста төменгі аймақтан жоғарғы аймаққа өту уақыты жоғарғы аймақтан төменгі аймаққа өту уақытынан өзгеше екендігі ескерілген. Бұл дегеніміз $\tau_{12} \neq \tau_{21}$. Үлгіде жалпы концентрация тұрақты, сондықтан $n_0 = n_a + n_b = const$. Тиісті концентрациялардың өзгеруі бір-біріне тең және қарама-қарсы таңбаға ие, яғни $n_a' = -n_b'$. Электр және магнит өрістерінің критикалық мәндерінде және тиісті концентрацияларда монохроматты толқын ретінде өзгеретіні ескерілді. Және бұл шамалардың өзгеруі олардың тепе-теңдік мәнінен аз ерекшеленеді. Математикалық есептеулердің қарапайымдылығы үшін сыртқы электр және магнит өрістері бір бағытта, яғни x бойынша бағытталған. Экспериментте токтың тербелістері бір бағытта (мысалы, x бойынша) зерттелгендіктен, келесі теңдіктер $j_y' = 0, j_z' = 0$ болатыны ескерілді. Үлгідегі бастапқы ток тербелісінің критикалық өрісінің айналасында ток тербелісінің жиілігі $\varpi = \varpi_0 + i\varpi_1, \varpi_1 << \varpi_0$. Сонымен қатар, критикалық электр өрісінің шамасы, токтың тербелісі магнит өрісіне байланысты келесідей өзгереді $E_{kr} \sim \frac{1}{H_{external}^4}$.

Кілт сөздер: арту, тербеліс, жиілік, өсу, жақты, қозғалыс, тиімді масса, Ганн эффектісі.

Э.Р. Гасанов, Ш.Г. Халилова

Неустойчивость в многодолинных полупроводниках во внешнем электрическом и магнитном полях

Теоретическим образом доказано, что возбуждаемая волна в двухдолинных полупроводниках является нарастающей. Указано, что направления внешних полей играют существенную роль для появления нарастающих волн в образце. Показано, что колебания могут происходить при определенных значениях размеров образца L_x, L_y, L_z. Получены аналитические формулы для частоты нарастающих волн. Определен интервал изменения внешнего электрического поля при сильном магнитном поле $\mu H >> c$. В статье учтено, что время перехода из нижней долины в верхнюю отличается от времени перехода из верхней долины в нижнюю. Это означает $\tau_{12} \neq \tau_{21}$. В образце общая концентрация постоянна, поэтому $n_0 = n_a + n_b = const$. Изменения соответствующих концентраций равны друг другу и имеют противоположный знак, то есть $n'_a = -n'_b$ Учтено, что при критических значениях электрического и магнитного полей соответствующие концентрации меняются как монохроматические волны. Изменение этих величин мало отличается от их равновесного значения. Для простоты математических вычислений внешнее электрическое и магнитное поля направлены в одном направлении, то есть по направлению *x*. Поскольку в эксперименте исследованы колебания тока в одном направлении (например, вдоль *x*), учитывались следующие равенства: $j'_y = 0, j'_z = 0$. В окрестности критического поля в начале колебания тока в образце, частота колебания тока $\varpi = \varpi_0 + i\varpi_1$, $\varpi_1 << \varpi_0$. Кроме того, величина критического электрического поля, при котором колебание тока изменяется в зависимости от магнитного поля, выглядит следующим образом: $E_{kr} \sim \frac{1}{H^4_{external}}$.

Ключевые слова: нарастание, колебание, частота, приращение, долина, подвижность, эффективная масса, эффект Ганна.

DOI 10.31489/2023PH2/72-78

УДК 538.915

T.M. Inerbaev[1] , Zh.Ye. Zakiyeva[2*], F.U. Abuova[3], A.U. Abuova[4],
S.A. Nurkenov[5], G.A. Kaptagay[6]

[1,2,3,4,5] L.N. Gumilyov Eurasian National University, Astana, Kazakhstan;
[5] Astana International University, Astana, Kazakhstan;
[6] Kazakh National Women's Teacher Training University, Almaty, Kazakhstan
([*]E-mail for contacts: zhadyrazakiyeva@gmail.com)

DFT studies of $BaTiO_3$

The structure of stable phases is investigated using first-principle calculations based on the functionals: LDA, GGA and newly developed general-purpose heavily constrained and appropriately normalized meta-GGA-functional (SCAN). The purpose of this study is to theoretically study the atomic displacements and band gap of the cubic, tetragonal, orthorhombic, rhombohedral perovskite phases for the comparison LDA, GGA-PBE and meta-GGA functionals using the density functional theory method. The obtained data of the density of states (DOS) showed that the values of the band gap energies are underestimated, and the DOS values show that the upper part (valence band) mainly consists of O 2*p* orbitals, the lower part (conduction band) consists of Ti 3*d* orbitals. The rhombohedral phase has a mixed composition of Ti states in the conduction band with a greater degree of $3d_{z2}$ than $3d_{xy}$. The values of the energies of the band gap (E_{gap}) and the density of states show reasonable agreement with experimental and theoretical data. The LDA functional and, to a lesser extent, the GGA - PBE functional can also provide fairly accurate information about atomic displacements in these crystals. The values calculated by the SCAN functional do not differ much from the GGA and LDA functionals.

Keywords: perovskite, unit cell, density of states, distortion of atoms, band gap, first-principle calculations, density functional theory, plane waves, space group.

Introduction

Barium titanate - perovskite was discovered half a century ago, but due to its unique crystal structures, physical and chemical properties, the material still attracts a lot of attention of researchers. In addition, barium titanate has a high dielectric constant, and their excellent piezoelectric and ferroelectric properties are also known. Over the past decade, it has become one of the important materials with excellent dielectric, ferroelectric and piezoelectric properties, due to which this type of material has great capabilities, which allows them to be used in the production of electronic devices. It is one of the most thoroughly studied cubic perovskites, and has paraelectric properties at high temperatures and has a simple cubic perovskite structure. Most of the ABO_3 type perovskites have the same stable phases at different temperatures.

Perovskites are complex oxides, mainly of the composition ABO_3, where A is a divalent metal, and B is a tetravalent (transition) metal. Perovskite is the object of scientific research in connection with promising electrical, magnetic, photoelectric and redox properties [1-4] for energy production (SOFC – solid oxide fuel cell technology) [5]. Perovskites can exist in various phace modifications, which generally exhibit different properties. The number of phase modifications depends on the specific combination of A and B cations [1, 6]. Many perovskites, specifically, demonstrate the presence of other phases. The highly symmetrical cubic phase of the *Pm-3m* crystal is also stable at high temperatures and demonstrates a series of three phase transitions with decreasing temperature: tetragonal *I4/mcm* at 393 K, orthorhombic *Amm2* at 278 K and rhombohedral *R3m* at 183 K, as shown in Figure 1.

Over the past 20 years, several first principles calculations have been carried out, in which more attention was paid to the structural and electronic properties of the four phases [7-10]. The theoretical study of this perovskite still requires detailed analysis, since it does not show the same result compared to experimental data and still remains an object research. Experimental data [11] showed band gap widths of about 3.7 eV for the cubic phase and 3.9 eV for the tetragonal phase. In general, density functional theory (DFT) will be applied with a combination of different approximations to describe the structure of the perovskite band gap. The method is distinguished for describing the wave function and allows us to determine the energy state of the system, which includes the stationary Schrodinger equation. In this paper, the width of the forbidden zone with three different functionals is calculated: LDA, GGA and meta-GGA.

Since phases other than the cubic phase have an internal degree of freedom, some of them must be optimized. Thus, DFT calculations are carried out with high accuracy to precisely obtain ferroelectric phases. Minimization is not required for a cubic structure. The tetragonal structure was optimized by changing the coordinates of the ions, since the symmetry (distortion in the z direction) allows optimization in a fixed c/a ratio, while maintaining a fixed volume. Then, using the optimized coordinates of the ion particles, the relation (maybe the ratio) c/a was optimized at a constant volume. Thus, the relation $Ti\left(1/2,1/2,1/2+\Delta z_{Ti}\right)$, $O_1\left(1/2,1/2,\Delta z_{O_1}\right)$, $O_2\left(1/2,0,1/2+\Delta z_{O_2}\right)$ it has been optimized while minimizing. The lattice parameters were also optimized in the orthorhombic phase: a, b, c and $Ti\left(1/2,0,1/2+\Delta z_{Ti}\right)$ $O1\left(0,0,1/2+\Delta z_{O1}\right)$ $O2\left(1/2,1/4+\Delta y_{O2,}\,1/4+\Delta z_{O2}\right)$. Lattice parameter a $\left(a=b=c\right)$, angle α $\left(\alpha=\beta=\gamma\right)\Delta$ $Ti\left(1/2+\Delta x,1/2+\Delta x_{Ti,}\,1/2+\Delta x_{Ti}\right)$ $O\left(1/2+\Delta x_O,1/2+\Delta x_{O,}\,0+\Delta z_O\right)$ were optimized values for the rhombohedral phase. The atomic positions are shown in Table 1.

Calculation methods

Calculations of the electronic structure were carried out by the density functional method in the basis of plane waves, as implemented in the VASP program code [12, 13]. The method of projection attached waves (projector augmented wave – PAW) was used [14]. LDA [15, 16], GGA with PBE [17], and SCAN [18] meta GGA [19, 20] were used for comparative analysis. The cutting energy of plane waves in all calculations was 520 eV. The partition of the inverse space was chosen using the Monhorst–Pack scheme in the form of an 8×6×6 grid for the orthorhombic phase, 8×8×8 for the tetragonal and rhombohedral phase. Levels were considered as valence states.

Results and discussion

The coordinates of the location of the atoms of the unit cell *BaTiO3*, tetragonal, orthorhombic, and rhombohedral, cubic phase are given in Table 1.

Table 1

Coordinates of the arrangement of atoms in the unit cell $BaTiO_3$.

Cubic phase *(Pm3m)* SG-221	Tetragonal phase *(P4/mmm)* SG-99	Orthorhombic phase *(Amm2)* SG-38	Rhombohedral phase *(R3m)* SG-160	Ref.
Ba:1a (0,0,0)	Ba:1a(0,0,0)	Ba: 2a (0,0,0)	Ba:1a (0,0,0)	[8]
$Ti:1b\left(1/2;1/2;1/2\right)$	$Ti:1b\left(1/2,1/2,1/2+\Delta z_{Ti}\right)$	$Ti:2b\left(1/2,0,1/2+\Delta z_{Ti}\right)$	$Ti:1a\left(1/2+\Delta x,1/2+\Delta x_{Ti,}\,1/2+\Delta x_{Ti}\right)$	[8]
$O:3c\left(1/2;1/2;0\right)$	$O_1:1b\left(1/2,1/2,\Delta z_{O_1}\right)$	$O1:2a\left(0,0,1/2+\Delta z_{O1}\right)$	$O:3b\left(1/2+\Delta x_O,1/2+\Delta x_{O,}\,0+\Delta z_O\right)$	[8]
—	$O_2:2c\left(1/2,0,1/2+\Delta z_{O_2}\right)$	$O2:4e\left(1/2,1/4+\Delta y_{O2,}\,1/4+\Delta z_{O2}\right)$	—	[8]

The atom Ba is located in the position (0,0,0), $Ti\left(1/2,1/2,1/2+\Delta z_{Ti}\right)$ and $O_2\left(1/2,0,1/2+\Delta z_{O_2}\right)$ are distortions of Ti and O atoms in a tetragonal structure. In an orthorhombic structure $Ti\left(1/2,0,1/2+\Delta z_{Ti}\right)$ $O1\left(0,0,1/2+\Delta z_{O1}\right)$ and $O2\left(1/2,1/4+\Delta y_{O2,}\,1/4+\Delta z_{O2}\right)$ are distortions of Ti and O atoms. In a rhombohedral structure $Ti\left(1/2+\Delta x,1/2+\Delta x_{Ti,}\,1/2+\Delta x_{Ti}\right)$ and $O\left(1/2+\Delta x_O,1/2+\Delta x_{O,}\Delta z_O\right)$ are distortions of Ti and O atoms [8].

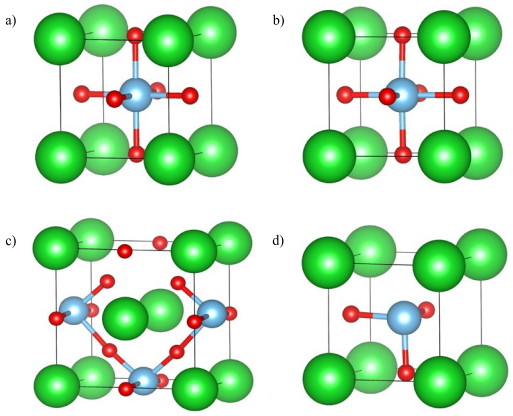

Figure 1. Unit cells *BaTiO3* in cubic, tetragonal, orthorhombic and rhombohedral phases

Table 2

Calculated volumetric properties of the unit cell $BaTiO_3$ tetragonal, orthorhombic and rhombohedral phases

Our results				Other theoretical data [7]		Experimental data	Ref.
	LDA	SCAN	PBE	LDA	PBE		
Cubic phase							
a, Å	3,95206	4,03462	4,03661	3,922	4,008	4,03558	[8]
bandgap E_g *(eV)*	1,08	1,09	1,08	1,93	1,87	3,2	[7]
Tetragonal phase							
a, Å	3,937	4,011	4,008	3,911	3,967	3,997	[8]
c, Å	4,031	4,157	4,188	3,967	4,232	4,0314	[8]
Δz_{Ti}	0,0203	0,0169	0,0182	0,0154	0,0335	0,0203	[8]
Δz_{O1}	-0,0258	-0,0392	-0,0409	–0,0210	–0,0431	-0,0258	[8]
Δz_{O2}	-0,0123	-0,0227	-0,0238	–0,0138	–0,0183	-0,0123	[8]
bandgap E_g *(eV)*	2	2,4	2	1,95	1,95	3,4	[7]
Orthorhombic phase							
a, Å	3,934	3,997	3,9954	3,911	3,955	3,9828	[8]
b, Å	5,6269	5,7843	5,7989	5,566	5,778	5,6745	[8]
c, Å	5,6411	5,8239	5,8397	5,576	5,836	5,6916	[8]
Δz_{Ti}	0,0122	0,0157	0,0158	0,0102	0,0253	0,0170	[8]
Δz_{O1}	-0,0140	-0,0197	-0,0205	–0,0109	–0,0173	-0,0110	[8]
Δy_{O2}	0,0043	0,0073	0,0071	–0,0010	– 0,0113	0,0061	[8]
Δz_{O2}	-0,0156	-0,0231	-0,0228	–0,0155	–0,0300	-0,0157	[8]
bandgap E_g *(eV)*	2,1	2,2	2,5	2,121	2,563	-	
Rhombohedral phase							
a, Å	3,9659	4,0702	4,0739	3,931	4,053	4,0036	[8]
α, deg	89,9039	89,7579	89,7568	89,92	89,65	89,840	[8]
Δx_{Ti}	-0,0099	-0,0143	-0,0138	–0,0073	–0,0190	-0,0120	[8]
Δx_O	0,0097	0,0142	0,0142	0,0101	0,0129	0,0116	[8]
Δz_O	0,0152	0,0244	0,0233	0,0144	0,0248	0,0195	[8]
bandgap E_g *(eV)*	2,2	2,2	2,5	2,234	2,796	-	

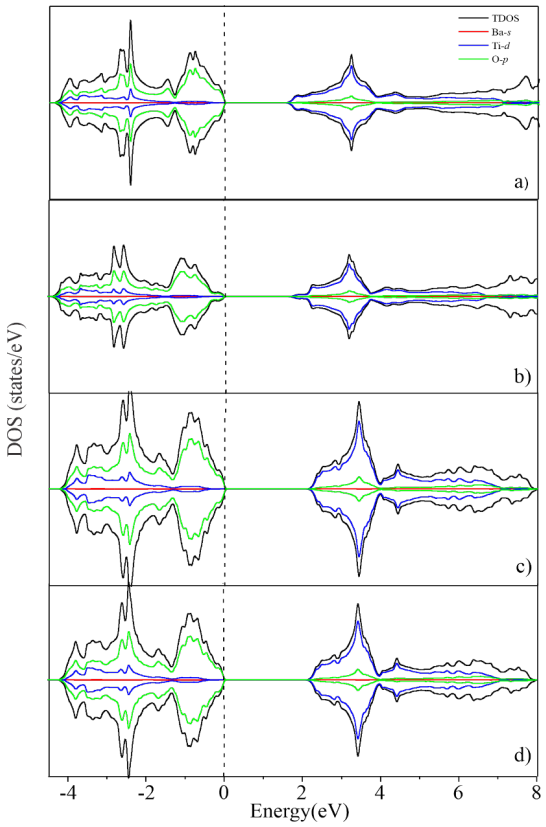

Figure 2. GGA density of states for the phase $BaTiO_3$ (a) cubic, (b) tetragonal, (c) orthorhombic, (d) rhombohedral

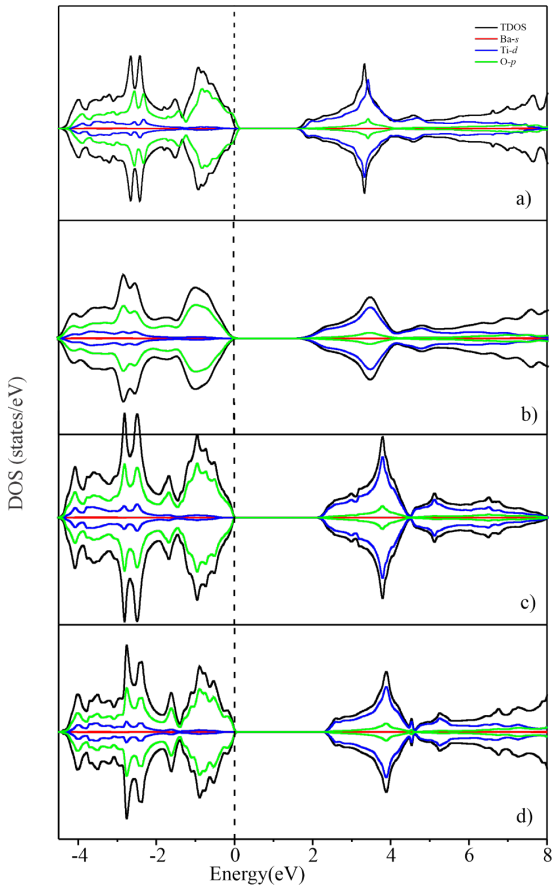

Figure 3. SCAN density of states for the phase $BaTiO_3$ (a) cubic, (b) tetragonal, (c) orthorhombic, (d) rhombohedral

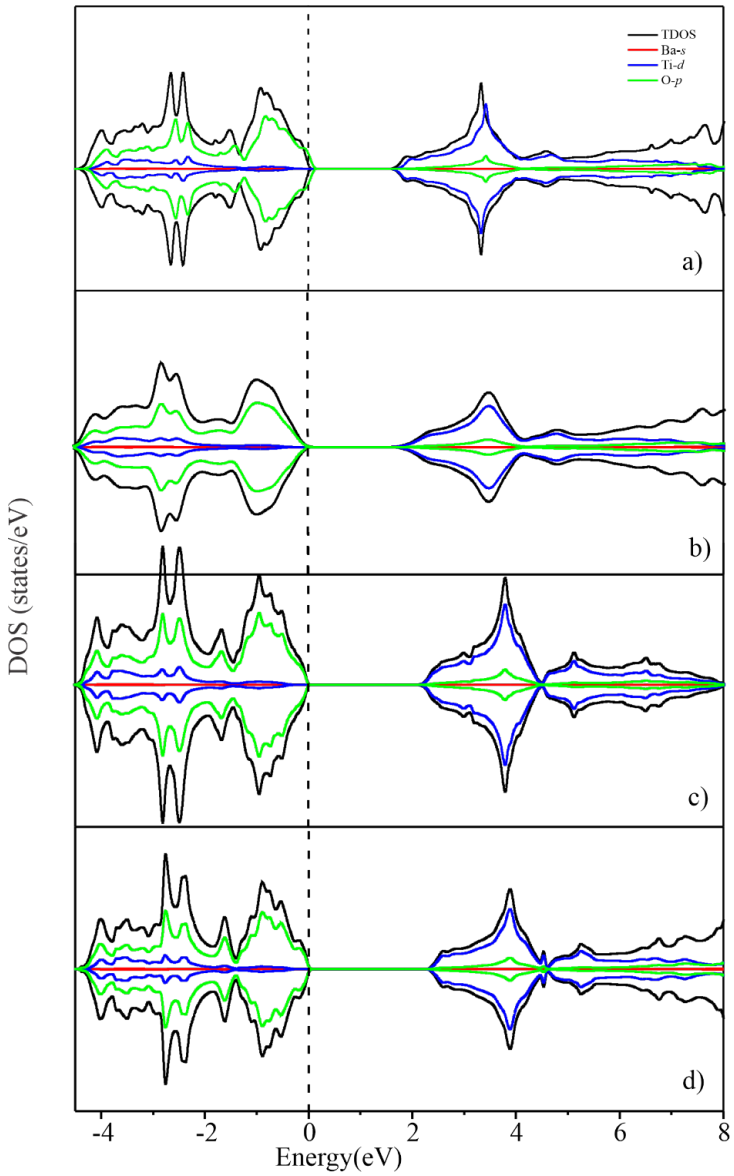

Figure 4. LDA density of states for the (a) cubic, (b) tetragonal, (c) orthorhombic, (d) rhombohedral phase of $BaTiO_3$

Based on the first-principle calculations, the calculation of the BTO was carried out using the GGA - PBE, LDA, SCAN functionality for four modification of the perovskite structure. The obtained calculated values were compared with the experimental results. The lattice parameters *a, b, c* and the band gap are given in Table 2, the sequence of the arrangement of atoms are given in Table 1. For the rhombohedral phase, the angle of the lattice a is also shown. As can be seen from Table 2, the calculation using the PBE functional makes it possible to more accurately predict the cubic properties of BTO compared to other functionals [7]. When calculating with the PBE functional, one can see the correspondence between the experimental results' values of the lattice constant. The three ferroelectric phases of the BTO, as shown in the theoretical work [7], are calculated by the same DFT method. In these works, the structural properties of ferroelectric phases are considered. Table 2 shows a comparison of the results obtained with other theoretical values calculated with different functionals [7] and using experimental data for the crystals under study. LDA calculations [7] coincide with experimental data for BTO. On the other hand, as expected, the LDA and PBE functions significantly underestimate the band gap width. It can be seen that all DFT calculations do not estimate the band gap width, as shown in Figure 2. One of the shortcomings of the density functional theory method is inaccurate prediction of the free or excited state of semiconductor systems and dielectrics [10]. The calculated values by the SCAN functional do not differ much from the previous two functionals.

The band gap width is closely related to the difference in energy level between the valence band (VB) and the conduction band, which can be caused by structural distortions in the material.

Zone structures of the BTO using the functionals: PBE, LDA and SCAN for the four phases of BTO indicate that the energy of the band gap of the cubic structure is equal to: *Pm3m* 1.08 eV (LDA) and 1.09 eV (SCAN), 1.08 eV (PBE), tetragonal structure *P4/mmm* 2 *e*V (LDA) and 2.4 *e*V (SCAN), 2 *e*V (PBE), orthorhombic structure *Amm2* 2.1 *e*V (LDA) and 2.2 *e*V (SCAN), 2.5 *e*V (PBE), and rhombohedral structure *R3m* 2.2 *e*V (LDA) and 2.2 *e*V (SCAN), 2.5 *e*V (PBE). Analyses of band structures and density of states (DOS) using the PBE, LDA and SCAN functionals for the four phases of BTO showed that the values of the forbidden zones are underestimated. A general analysis of DOS projected onto atoms and orbitals is presented in Figures 2-4. An analysis of the density of DOS states shows that the upper part (valence band) mainly consists of O 2*p* orbitals. The lower part (conduction band) mainly comes from Ti 3*d* orbitals in all phases.

The conduction band for the tetragonal phase using the PBE, LDA and SCAN functionals consists of Ti 3*d* states, as well as the orthorhombic phase. The rhombohedral phase has a mixed composition of Ti states in the conduction band with a greater degree of $3d_{z2}$ than $3d_{xy}$. The projected state densities (PDOS) on atoms and orbitals are shown in Figure 2-4. The values of the band gap energy (E_{gap}) calculated using the PBE, LDA and SCAN functionals, as well as available theoretical and experimental data are shown in Table 2. The calculated values show reasonable agreement with previous theoretical results.

Conclusion

In this paper, the structure of stable phases is investigated using first-principle calculations based on the functionals: LDA, GGA- PBE and meta-GGA. When analyzing the electronic structures, the energies of the band gap were determined for the cubic structure: *Pm3m* 1.08 *e*V (LDA) and 1.09 *e*V (SCAN), 1.08 *e*V (PBE), for the tetragonal structure: *P4/mmm* 2 *e*V (LDA) and 2.4 *e*V (SCAN), 2 *e*V (PBE) for the orthorhombic structure: *Amm2* 2.1 *e*V (LDA) and 2.2 *e*V (SCAN), 2.5 *e*V (PBE) and for rhombohedral structure: *R3m* 2.2 *e*V (LDA) and 2.2 *e*V (SCAN), 2.5 *e*V (PBE). The data obtained for the density of states (DOS) showed that the upper part (valence band) mainly consists of O 2*p* orbitals, and the lower part (conduction band) comes from Ti 3*d* orbitals. The rhombohedral phase has a mixed composition of Ti states in the conduction band with a greater degree of $3d_{z2}$ than $3d_{xy}$. The values of the energies of the band gap (E_{gap}) and the density of states present reasonable agreement with experimental and theoretical data. The deviation in the theoretical calculations of the lattice parameters carried out in [7] using the LDA and PBE functionals in comparison with the results of the experimental study is 3 %. The deviation of calculations with our theoretical calculations using the LDA and PBE functionals was approximately the same as the authors [7], while the calculation with the Scan functional showed 0.02 % compared to the experimental result.

Acknowledgements

The work was carried out with the financial support of the Ministry of Science and Higher Education of the Republic of Kazakhstan, grant IRN AR14869492 "Development of nanocrystalline metal oxide catalysts for hydrogen production".

References

1 Steele, C.H., & Heinzel, A. (2001). Materials for fuel-cell technologies. *Nature, 414,* 345-352.

2 Abuova, A.U., Mastrikov, Y.A., & Kotomin, E.A. (2019). First-Principles Modeling of Oxygen Adsorption on Ag-Doped $LaMnO_3$ (001) Surface. *J. Electron. Mater*, *49,* 1421–1434.

3 Abuova, A.U., Mastrikov, Yu.A., Kotomin, E.A., Kawazoe, Y., Inerbaev, T.M., & Akilbekov, A.T. (2015). First principles modeling of Ag adsorption on the $LaMnO_3$ (001) surfaces. *Solid State Ionics,* 273*, 46-50.*

4 Abuova, A.U., Akilbekov, A.T., Abuova, F.U., & Inerbaev, T.M. (2015). Modelling of structural and electronic properties surface (001) $LaMnO_3$ perovskite structure. *Condensed matter physics, 77,* 4-8.

5 Kuterbekov, K.A., Nurkenov, S.A., Rabotkin, S.V., Ionov, I.V., & Solovyev, A.A. (2021). Anode-supported solid oxide fuel cells with multilayer LSC/CGO/LSC cathode. *Fuel Cells*, *21,* 408-412.

6 Woodward, P.M. (1997). Octahedral tilting in perovskites. II Structure stabilizing forces. *Acta crystallographica, 53,* 44.

7 Huai, Y.Z., Zhao, Y.Z., Ying, Q.Zh., Qing, L., & Yan, Ch. (2016). First-Principles Study of Lattice Dynamics, Structural Phase Transition, and Thermodynamic Properties of Barium Titanate. *Chemistry Physical,* 71*, 759-768*.

8 Kwei, G.H., Lawson, A.C., Billinge, S.J.L., & Cbeong, S.W. (1993). Structures of the Ferroelectric Phases of Barium Titanate. *J. Phys. Chem*., *97,* 2368-2377.

9 Evarestov, R.A., & Bandura, A.V. (2012). First principles calculations on the four phases of $BaTiO_3$. *Journal of computational chemistry, 33,* 1123-1130.

10 Holm, B., Ahuja, R., Yourdshabyan, Y., Johanson, B., & Lundqvist, B.I. (1999). *Phys. Rev*., *59,* 12777.

11 Sanna, S.C. (2011). Barium titanate ground and excited-state properties from first-principles calculations. *American Physical Society, 83,* 054112.

12 Kresse, G., & Furthmüller, J. (1996). Efficiency of ab-initio total energy calculations for metals and semiconductors using a plane-wave basis set. *Comput. Mater. Sci*., *6,* 15-50.

13 Kresse, G., & Furthmüller, J. (1996). Efficient iterative schemes for ab initio total-energy calculations using a plane-wave basis set. *Phys. Rev., 54,* 11169.

14 Blöchl, P.E. (1994). Projector augmented−wave method. *Phys. Rev., 24,* 17953-17979.

15 Hohenberg, P., & Kohn, W. (1964). *Phys. Rev., 136,* 864.

16 Kohn, W., & Sham, L.J. (1965). *Phys. Rev*., *140,* 1133.

17 Perdew, J.P., Burke, K., & Ernzerhof, M. (1996). *Phys.Rev*., *77,* 3865-3868.

18 Sun, J., Remsing, R.C., Zhang, Y.Z., Sun, A., Ruzsinszky, H., Peng, Z., Yang, A., Paul, U., Waghmare, X., Wu, Klein, M.L., & Perdew, J.P. (2016). *Nat. Chem*., *8,* 831-836.

19 Sun, J., Xiao, B., Fang, Y., Haunschild, R., Hao, P., Ruzsinszky, A., Csonka, G.I., Scuseria, G.E., & Perdew, J.P. (2013). *Phys. Rev., 111,* 106401.

20 Inerbaev, T.M., Matsuoka, T., & Kawazoe, Y. (2022). Optical band gap energy values in wurtzite $In_xGa_{1-x}N$. *Bulletin of the university of Karaganda-Physics*, 105*, 107-116.*

Т.М. Инербаев, Ж.Е. Зәкиева, Ф.У. Абуова, А.У. Абуова, С.А. Нуркенов, Г.А. Каптагай

$BaTiO_3$ бойынша DFT зерттеулері

Тұрақты фазалардың құрылымы функционалдық функцияларға негізделген алғашқыпринципті есептеулердің көмегімен зерттелген: LDA, GGA және жақында әзірленген әмбебап қатты шектелген және сәйкесінше нормаланған мета-GGA функционалы (SCAN). Бұл жұмыстың мақсаты тығыздық функционалы теориясы әдісін қолдана отырып, LDA, GGA-PBE және мета-GGA функционалдарын салыстыру үшін кубтық, тетрагональды, орторомбты, ромбоэдрлік перовскит фазаларының кристалдағы атом координаттарының өзгерісі мен рұқсат етілмеген аумақты теориялық тұрғыдан зерттеу. Алынған күйлердің тығыздығы (DOS) деректері тыйым салынған аймақта энергия мәнінің төмендегенін; ал DOS мәндерінің жоғарғы бөлігі (валенттік аумақ) негізінен O 2*p*-орбитальдарынан, төменгі бөлігі (өткізгіштік аумақ) Ti 3*d* орбитальдарынан тұратынын көрсетті. Ромбоэдрлік фазада $3d_{xy}$-ге қарағанда $3d_{z2}$ үлкен дәрежелі өткізгіштік аумағында Ti күйлерінің аралас құрамы бар. Рұқсат етілмеген аумақ (E_{gap}) және күйлердің тығыздығы эксперименттік және теориялық мәліметтермен сәйкестігін көрсетеді. LDA функционалдығы және аз дәрежеде GGA-PBE функционалдығы да осы кристалдардағы атомдық орын ауыстырулар туралы жеткілікті дәл ақпарат бере алады. SCAN функциясынан есептелген мәндер GGA және LDA функцияларынан аз ерекшеленеді.

Кілт сөздер: перовскит, қарапайым ұяшықтар, күйлердің тығыздығы, атомдардың ығысуы, тыйым салынған аймақ, алғашқыпринципті есептеулер, тығыздық функционалының теориясы, жазық толқындар, кеңістіктік топ.

Т.М. Инербаев, Ж.Е. Закиева, Ф.У. Абуова, А.У. Абуова, С.А. Нуркенов, Г.А. Каптагай

DFT исследования $BaTiO_3$

Структура стабильных фаз исследована с помощью первопринципных расчетов на основе функционалов: LDA, GGA и недавно разработанного универсального сильно ограниченного и соответствующим образом нормализованного мета-GGA-функционала (SCAN). Целью данной работы является теоретическое исследование атомных смещений и ширины запрещенной зоны кубической, тетрагональной, орторомбической, ромбоэдрической фаз перовскита для сравнения функционалов LDA, GGA-PBE и мета-GGA с использованием метода теории функционала плотности. Полученные данные плотности состояний (DOS) показали, что значения энергии запрещенной зоны занижены, а значения DOS указывают, что верхняя часть (валентная зона), в основном, состоит из O 2*p*-орбиталей, нижняя часть (зона проводимости) — из 3*d*-орбиталей Ti. Ромбоэдрическая фаза имеет смешанный состав состояний Ti в зоне проводимости с большей степенью $3d_{z2}$, чем $3d_{xy}$. Значения энергий запрещенной зоны (E_{gap}) и плотности состояний показывают разумное согласие с экспериментальными и теоретическими данными. Функционал LDA и, в меньшей степени, функционал GGA–PBE также могут дать достаточно точную информацию о смещениях атомов в этих кристаллах. Значения, рассчитанные по функционалу SCAN, мало чем отличаются от функционалов GGA и LDA.

Ключевые слова: перовскит, элементарная ячейка, плотность состояний, искажение атомов, запрещенная зона, первопринципные расчеты, теория функционала плотности, плоские волны, пространственная группа.

DOI 10.31489/2023PH2/79-92

UDC 678.076

D. Yeskermessov[*1], Y. Tabiyeva[2], Z. Aringozhina[3], M. Booth[4], A. Tussupbekova[5], S. Pazylbek[6].

[1,2,3]*East Kazakhstan Technical University, Ust-Kamenogorsk, Kazakhstan;*
[1,2,3,4]*University of Lincoln, School of Mathematics and Physics, Lincoln, United Kingdom;*
[5] *Karaganda University of the name of academician E.A. Buketov, Karaganda, Kazakhstan;*
[6]*Tashenov University, Shymkent, Kazakhstan*
([*]E-mail: dyeskermessov@ektu.kz)

The current state of electrospinning technology and its prospects for the future

With the development of nanotechnology and modern research methods, the use of biodegradable polymer materials in various sectors of human life is of interest not only to the scientific world community, but also is a way to solve one of the global problems related to resource conservation and environmental protection. Polyvinyl alcohol-based materials have been widely used in various fields due to their biological and physical properties, such as biocompatibility, biodegradability, antimicrobial ability, non-toxicity and the ability to easily form a film. One of the methods of obtaining polymer films that exist today is electrospinning, the advantages of which are the relative simplicity of the technological process and the possibility of obtaining continuous nanofibers from both synthetic and natural polymers. In this work, the influence of various process parameters on the formation of nanofiber mats from a biodegradable synthetic polymer by electrospinning was studied. The technology of wet spinning, melt spinning and dry spinning is discussed. A number of experimental studies have been carried out to identify optimal modes of obtaining nanofibers from polyvinyl alcohol with the most homogeneous structure without the formation of defects.

Keywords: electrospinning, technological parameters, nanofibers, polyvinyl alcohol (PVOH), nonwoven mats, SEM, nanofiber diameter, biodegradable polymer material.

Introduction

Over the past few decades, nanomaterials research has been one of the most popular topics in the field of nanotechnology. To date, nanomaterials have found their potential application in various fields of research and industry due to their unique properties. Petroleum-based polymers are widely used in the production of various polymer products for various commercial, machine-building and promising purposes. However, the depletion of natural resources and the increasing demand for polymer-based materials raises questions about the further production of synthetic polymers. Moreover, most of the petroleum-based polymers used are not biodegradable and are stored in the environment as non-degradable waste. To solve these issues, many studies have been directed at the production of biodegradable polymers from renewable resources [1] and the development of technologies for the production of nanostructured polymer fibers, one of which is electrospinning.

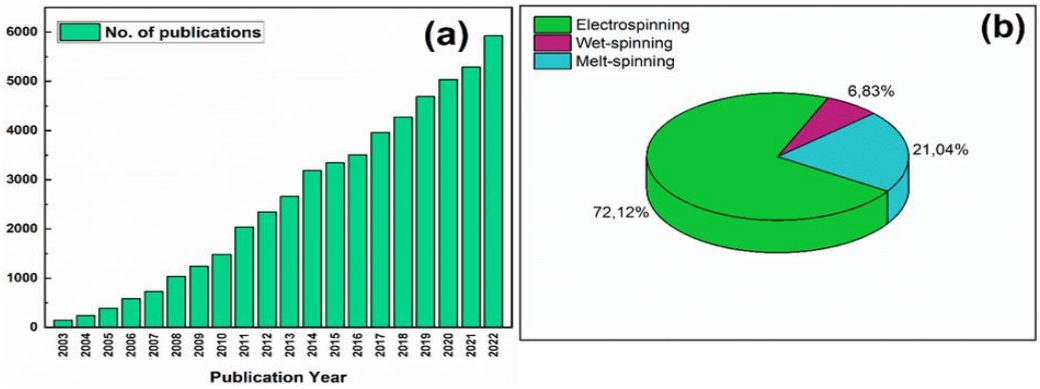

Figure 1. (a) Comparison of the annual number of scientific publications in the field of electrospinning over the past two decades and (b) the ratio of publications in the main areas of electrical engineering (the analysis of these publications was carried out using a single database of peer-reviewed scientific literature SCOPUS with the term "Electrospinning" as of February 15, 2023)

Due to the relative simplicity of the technological process that makes it possible to obtain multifunctional polymer mats from nanofibers, this technology is attracting increasing attention from the world scientific community, as evidenced by the increasing number of scientific publications in this field over the past two decades (Fig. 1).

Spinning is a technology for making fibers by pulling and twisting natural or synthetic materials, which is classified depending on the type of fiber as mechanical and chemical spinning. Mechanical spinning is a multi-step process in which fibers are physically twisted into yarn. Namely, rotary, annular, frictional or self-twisting rotation [2]. The production of threads from artificial fibers is also possible using chemical spinning. This is achieved by squeezing a viscous polymer solution through a die. There are three main types of production processes for the formation of synthetic fibers, namely wet spinning, melt spinning and dry spinning [3]. The wet spinning process is when the solidification of the dissolved polymer occurs after diffusion in the counterflow between the spinning solution and the coagulation bath. In this process, a very viscous polymer solution is squeezed out through small holes of a die immersed in a liquid bath. A diagram of the wet spinning process is shown in Figure 2. The technological analysis of the wet spinning process is much more complicated than dry spinning. Polymer solidification occurs as a result of diffusion exchange between freshly prepared fluid filaments and this bath. During this coagulation process, one or more components of the bath diffuse into the thread, and the solvent diffuses out of it.

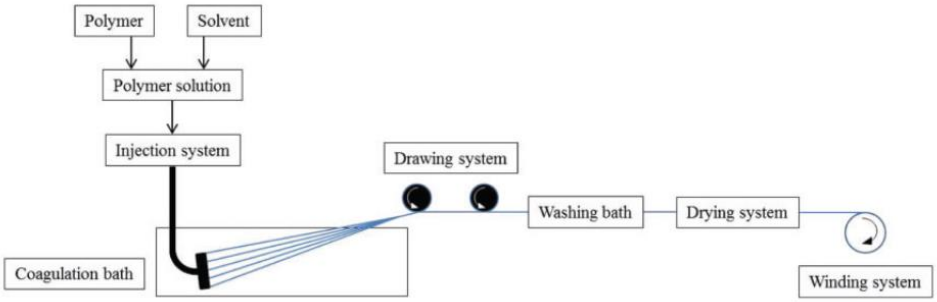

Figure 2: Diagram of the wet spinning process [4]

In melt spinning, phase transformations occur due to solidification of the molten mass. This type of spinning is the most economical process for the production of polymer fibers on an industrial scale [5]. The comparative ease of processing is an important advantage of melt molding. However, this method has some disadvantages, such as fiber rupture, non-uniform thread thickness, fiber fineness limit and die clogging (diagram of the process see in Figure 3).

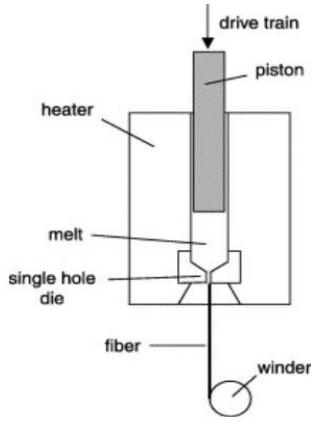

Figure 3. Diagram of the melt spinning process [6]

During dry spinning, the solvent contained in the spinning solution evaporates after the formation of a nanofiber mat, which leads to its drying. In the process of dry spinning, the fiber structure is formed by

squeezing the polymer solution through a thin nozzle and subsequent evaporation of the solvent (diagram of the process see in Figure 4).

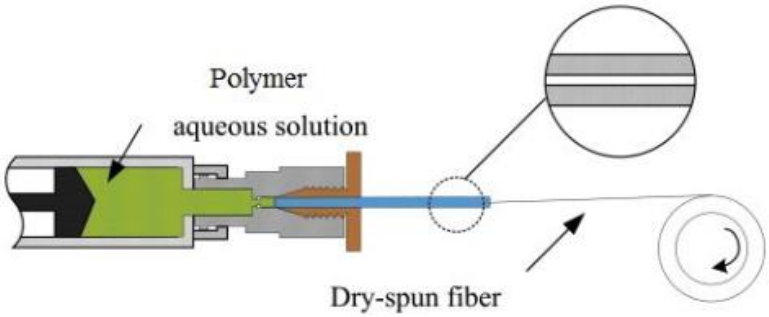

Figure 4. Diagram of the dry spinning process [7]

Electrospinning is a dry spinning method in which the solvent evaporates under high voltage [8]. This method makes it possible to produce ultrathin fibers for various polymers of submicron or nanometer size.

The principle of electrospinning is based on the deformation of a charged polymer in response to a strong applied electric field. The polymer solution is fed (e.g. by gravity) to a nozzle opposite an electrode. In the absence of an electric field the polymer solution surface forms a meniscus at the nozzle outlet. In an electric field, however, the meniscus deforms into a so-called Taylor cone and, if the field is strong enough, the electrostatic forces can overcome the surface tension and a jet is formed. The acceleration of this jet towards the electrode causes the thinning of the jet, and the evaporation of the solvent as the jet is accelerated towards the electrode leads to solid fibre formation at atmospheric pressure and ambient temperature [9].

Thus, the purpose of this work is to obtain nanofibers by dry electrospinning and to study the effect of voltage, the distance from the collector to the nozzle, and the formation time in the production of polymer fibers.

Experimental

This study was conducted at the laboratory of Lincoln University, Isaac Newton Building, UK. At the Electrospinz Nanofibre Engineering installation, nanofibers were obtained by electrospinning in an atmospheric environment on the surface of substrates (material: deltalab laboratory glass with dimensions of 26 x 76 mm^2) at room temperature of 20 °C and humidity of 33 % (Fig. 6). Evaporable material poly vinyl alcohol "PVOH" with added antiomicrobial preservatives (concentration: 8wt % PVOH Solution; 0.1wt % Sodium Benzoate; 0.1wt % Porassium Sorbate) is an environmentally friendly biodegradable synthetic polymer, which is widely studied due to its high film-forming and physical properties, as well as its high hydrophilicity, manufacturability, biocompatibility and chemical resistance [10-14]. Figure 5 shows a schematic molecular formula PVOH $(C_2H_4O)_X$.

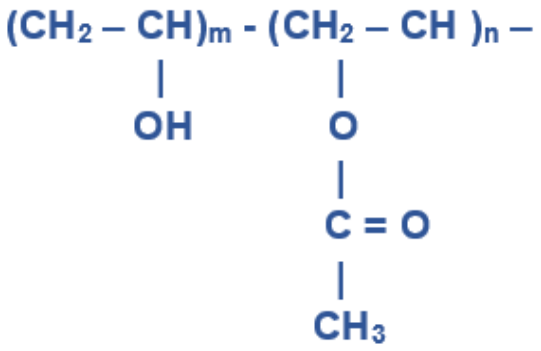

Figure 5. General structure of PVOH

During the electrospinning process, the applied electrostatic forces overcome the surface tension of the liquid, so the electrified liquid forms a jet from the tip of the capillary to the grounded filter on which the nanofiber material is formed. The appearance and scheme of the installation for electric spinning are shown

in Figures 6 and 7. The flow rate was controlled by gravity, depending on the height of the filled polymer in the container.

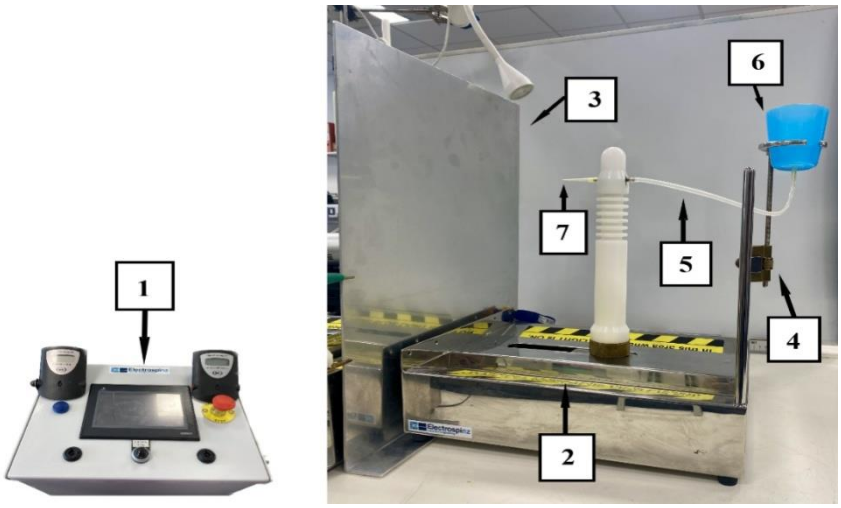

1 — High voltage and Control box, 2 — Spinning platform, 3 — Target plane, 4 — Constant head system, 5 — Hose, 6 — Header tank, 7– Nozzle.
Figure 6. Appearance of the installation “ELECTROSPINZ NANOFIBRE ENGINEERING”

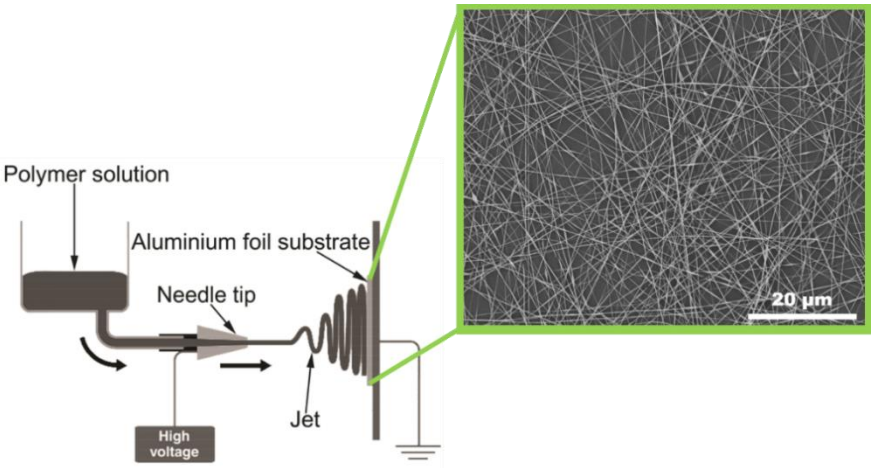

Figure 7. Installation diagram for electrospinning [15]

To provide conductive surfaces, nanofibers assembled on a collector (aluminum foil) by electrospinning were sprayed with a thin layer of gold on an “Emitech K550X” magnetron sputtering unit (Fig. 8) with an “Edwards RV8” vacuum pump, an argon pressure regulator. When using magnetron technology, the deposition process is quite “cold” and minimizes thermal damage to soft polymer materials.

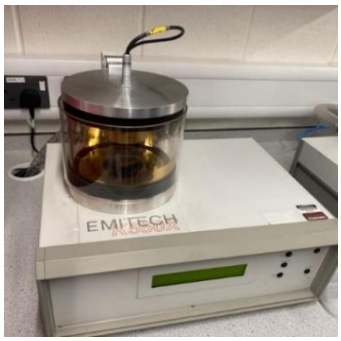

Figure 8. Appearance of the “Emitech K550X” installation

The morphology and size of PVOH nanofibers were observed and analyzed using a scanning electron microscope (SEM) “JeolNeoscope JCM 5000” at high vacuum with accelerating voltages of 10 and 15 kV, depending on the required magnification.

Results and Discussion

Some of the first results of the study obtained by the authors of this work were obtained of nanofibers by the electrospinning method are presented. Variables such as the applied electrical voltage, the duration of the process and the change in the distance from the collector to the needle were investigated. Their relationship with the microstructure of the obtained new fibers is briefly described below. Table 1 lists the process parameters used in the study for electrospinning at various voltages, the results of which are shown in Figure 9.

Table 1

Technological parameters of the electrospinning process

№	Voltage, ± 0.1 kV	Electrospinning time, ± 0.1 min	Distance, ± 2 mm
Sample 1	12.0	5.0	140
Sample 2	15.0	5.0	140
Sample 3	18.0	5.0	140
Sample 4	21.0	5.0	140
Sample 5	24.0	5.0	140
Sample 6	27.0	5.0	140
Sample 7	30.0	5.0	140

The applied voltage is an important factor in the process of electrospinning, since it controls the electric field strength between the tip of the nozzle and the collector and therefore the acceleration rate of the polymer jet. In principle, the higher the acceleration, the more stretching that occurs, leading to thinner fibres. However, this higher acceleration also means shorter flight duration between the nozzle and electrode, which may lead to thicker than expected fibres at high electrospinning voltages. It is not clear which of these factors is the more important in general, and results may differ depending on other process parameters.

The nanofiber diameter is measured by software-nano measurer using Start JCM-5000 open source image analysis software to determine the size and average diameter of nanofibers obtained by electrospun. Based on images obtained using a scanning electron microscope at constant magnification x8000 and a voltage of 10 kV, the diameters of 30 randomly selected PVOH nanofibers at each electrospinning voltage (12.0, 15.0, 18.0, 21.0, 24.0, 27.0 and 30.0 kV) were measured, and the average value calculated. The results are shown in Table 2 and shown in Figure 10.

Table 2

Average diameter of the PVOHfiber, depending on the voltage between the nozzle and the collector

Electrospinning voltage, ± 0.1 kV	12.0	15.0	18.0	21.0	24.0	27.0	30.0
Average diameter of the PVOH nanofiber (± 5 nm)	120	133	193	174	182	190	205

It was found that when a voltage is applied above the critical, charged jets are ejected from the Taylor cone. Indeed, when an electric field is applied to a drop of polymer solution at the tip of the nozzle, the surface of the drop is charged, and the electric force exceeds the surface tension force; as a result, an electrically charged jet is formed. A higher voltage increases the electrostatic repulsion force of the charged jet, which ensures relative uniformity of the diameters of electroformed polymer nanofibers [16].

However, after a certain value of the applied voltage, drops of liquid polymer appeared at the end of the nozzle, which subsequently caused the formation of defects in the form of beads or drops over the entire surface of the nanofibers shown in Figure 11.

Thus, for PVOH (8 wt %) polymer, the SEM study showed the importance of the applied voltage of 21 kV, the relative uniformity of the diameter of the electrospinning polymer nanofibers (Fig. 9).

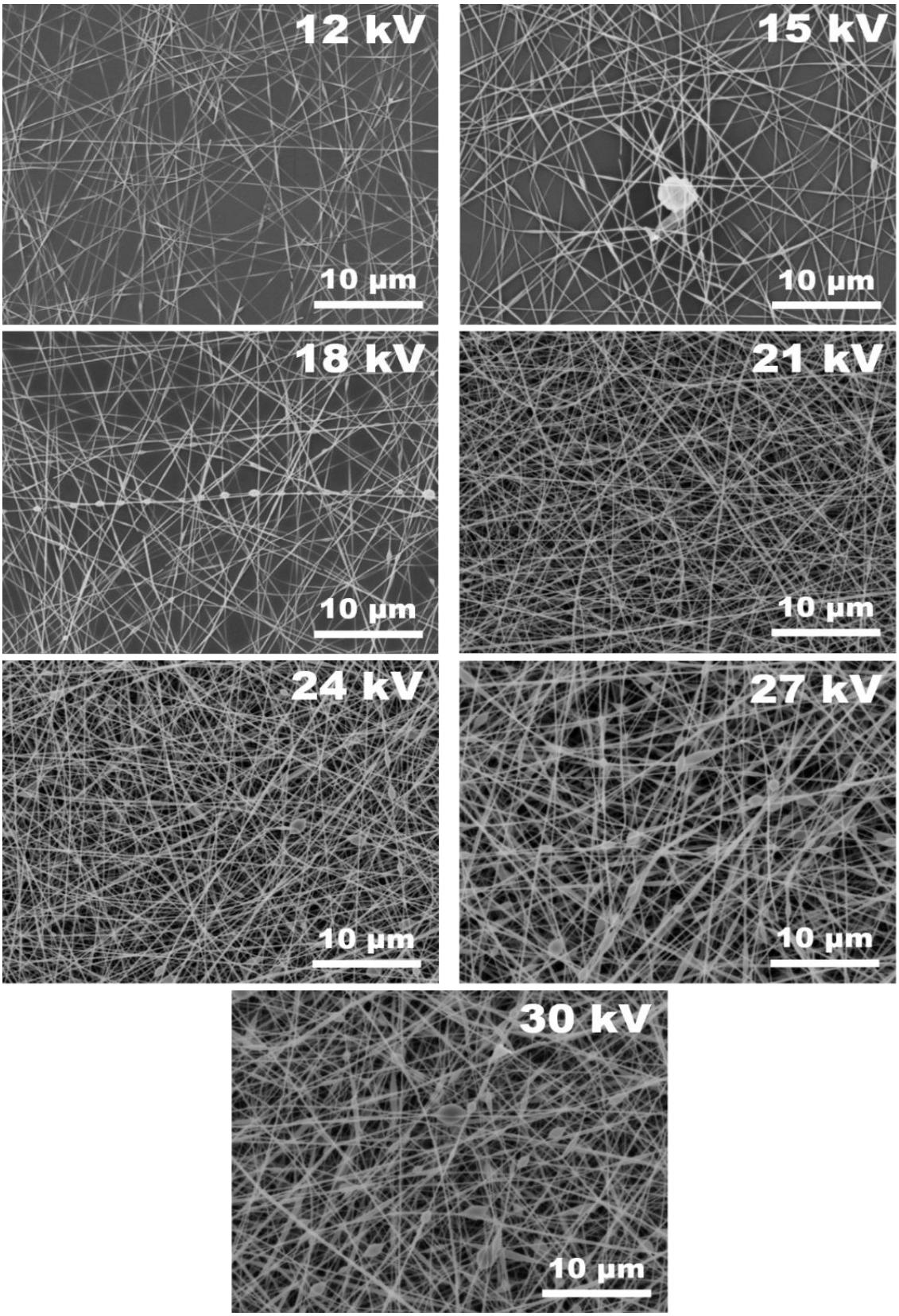

Figure 9. SEM image of the surface of the obtained nanofibers at different electrospinning voltage values

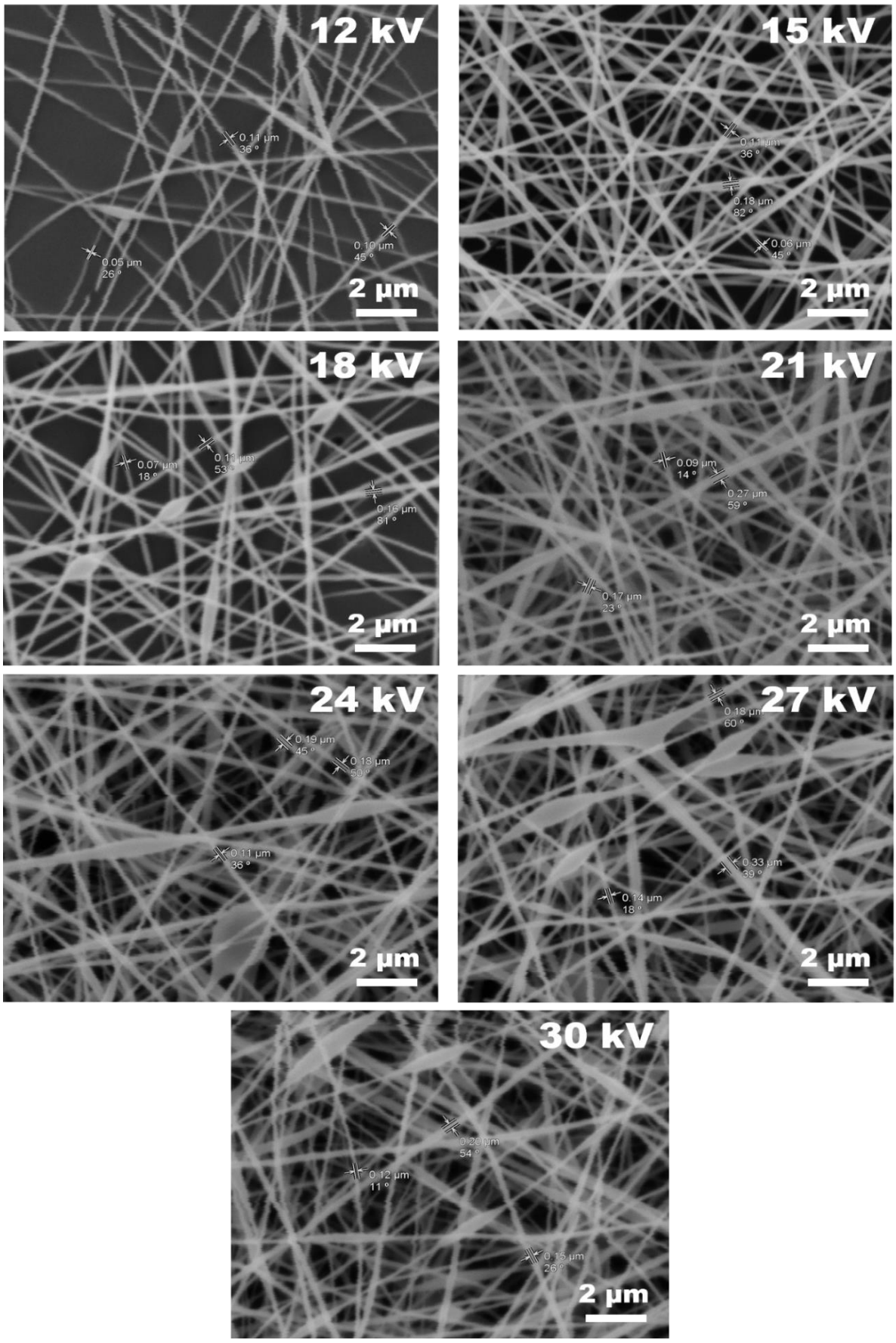

Figure 10. SEM images of PVOH nanofibers

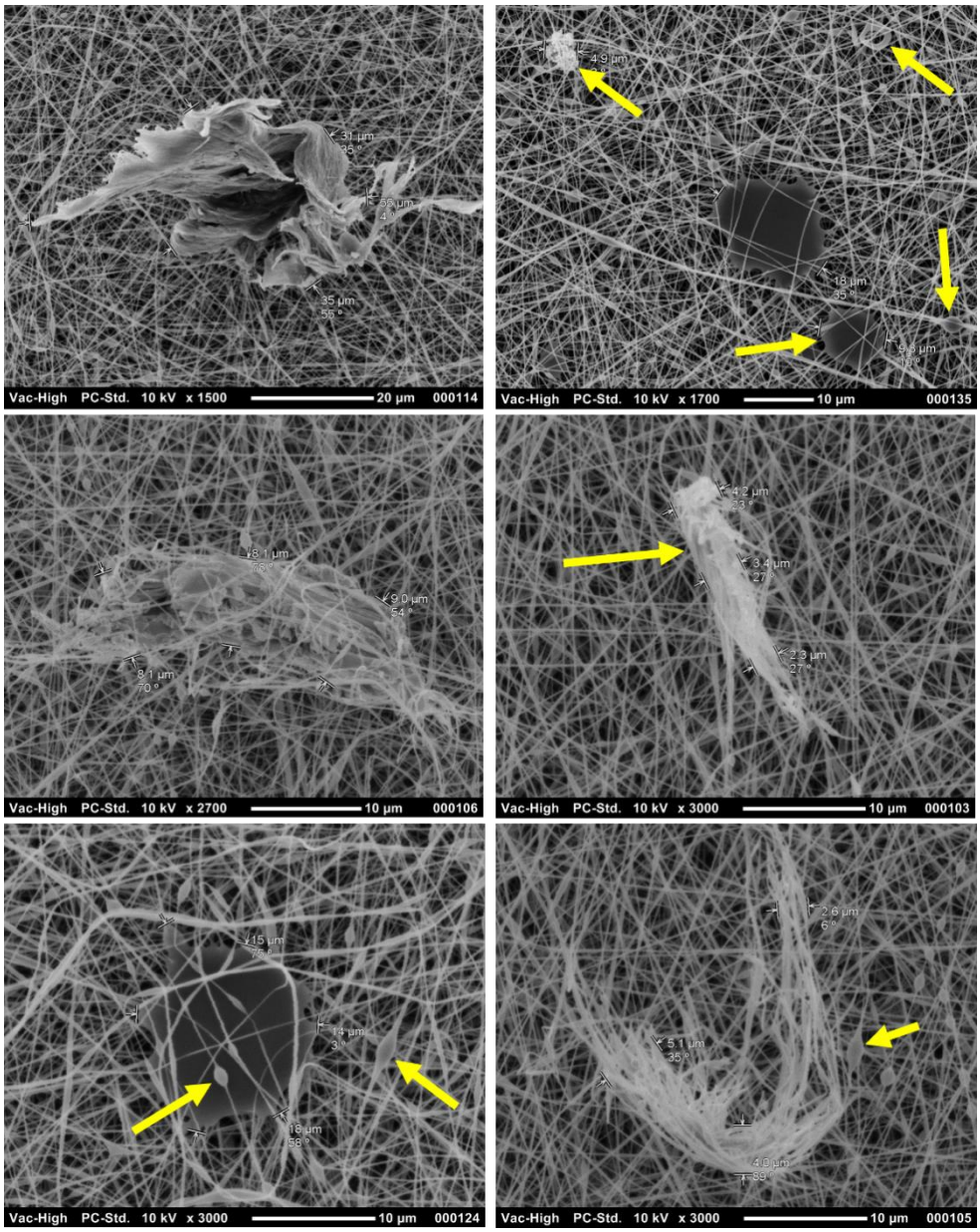

Figure 11. SEM image of defects on the surface of nanofibers at high electrospinning voltage values

The dependence of the nanofiber formation process on the deposition time, the parameters of which are presented in Table 3, was investigated. A decrease in the rate of electrospinning over time was observed, since the deposited fibre acted as an insulator allowing charge to accumulate on the target, leading to a charge screening effect between the target electrode and nozzle. The structure and thickness of the obtained fibres with varying deposition time is shown in Figure 12.

Table 3

The mode of formation of nanofibers with variable values of the duration of the process

№	Voltage, ± 0.1 kV	Electrospinning time, ± 0.1 min	Distance, ± 2 mm
Sample 1	21.0	3.0	140
Sample 2	21.0	6.0	140
Sample 3	21.0	9.0	140
Sample 4	21.0	12.0	140
Sample 5	21.0	15.0	140

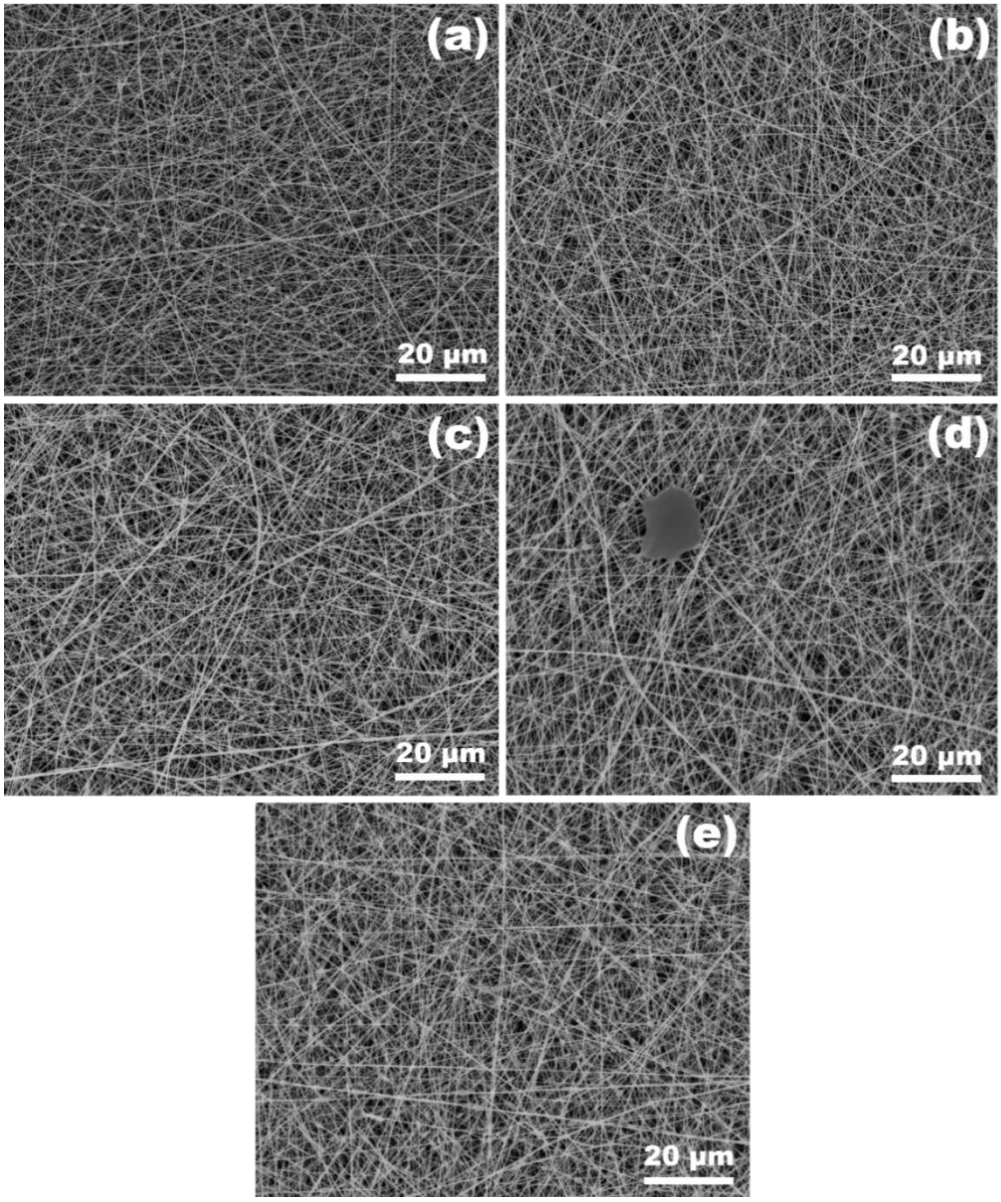

a) 3 min; b) 6 min; c) 9 min; d) 12 min; e) 15min.
Figure 12. SEM image of the surface of PVOH nanofibers

A study was conducted to identify the dependence of the nanofiber formation process on the distance between the needle tip and the collector, the values of which are presented in Table 4.

Table 4

Values of the distance between the nozzle tip and the collector during electrofspinning

№	**Voltage, ± 0.1 kV**	**Electrospinning time, ± 0.1 min**	**Average distance, ± 2 mm**
Sample 1	21.0	3.0	80
Sample 2	21.0	3.0	100
Sample 3	21.0	3.0	120
Sample 4	21.0	3.0	140
Sample 5	21.0	3.0	160

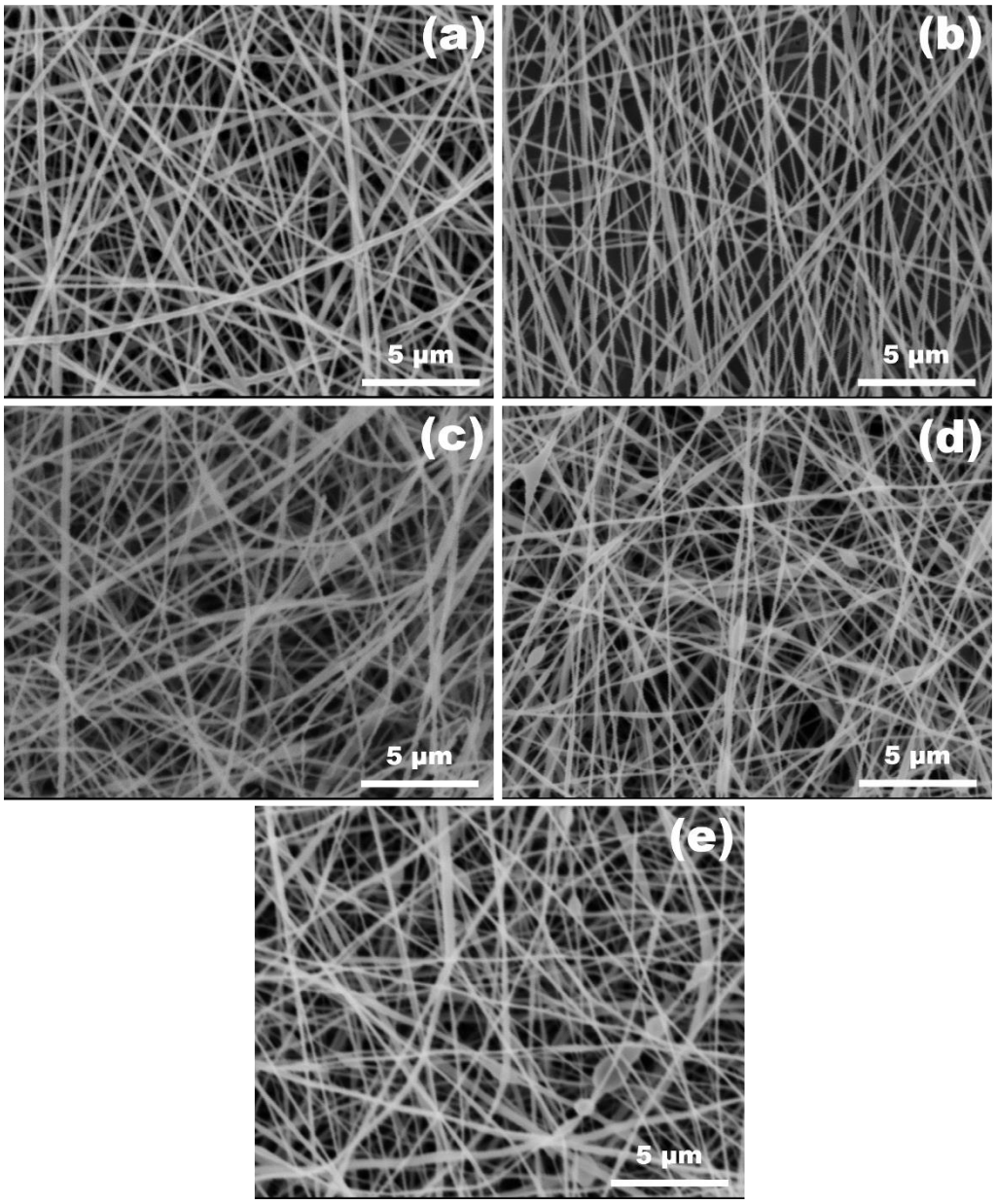

a) 80 mm; b) 100 mm; c)120 mm; d) 140 mm; e) 160 mm.
Figure 13. SEM image of the surface of PVOH nanofibers

Figure 13 shows that when the distance between the collector and the nozzle was 80 mm, the distribution of fibers was loose and heterogeneous. At a distance of 100-140 mm, the fibers were located closer to each other, and the pores between the fibers were relatively small. When the distance was 160 mm, the fibers were located just as close to each other, but defects in the form of beads formed over the entire surface.

Thus, reducing the distance between the electrodes to a certain value leads to a decrease in the diameter of the nanofibers. The difference in the distance between the tip of the nozzle and the collector has a direct effect on the electric field strength. The smaller the distance between the collector and the nozzle, the greater the electric field strength. As a result, the acceleration and elongation of the jet increase during the electric spinning process, and the diameter of the electric-spun polymer nanofibers decreases. In order to determine the thermal stability of the obtained nanofiber mats, annealing was carried out, the conditions of which are shown in Table 5. To minimize the ingress of various impurities on the surface of nanofibers during heating, a high-vacuum installation “NanoPVD-S10A” was used.

After the annealing, no significant changes in the fiber samples were observed (Fig. 14), which are associated with insufficient temperature for melting and a short duration of exposure time. To determine the melting point of T_3, a number of experimental work is required at the “identiPol QA2” installation. Matrices

of nanofibers were obtained at various voltages listed in Table 1. The paper presents the results of one of the experiments performed at an applied voltage of 12 kV (Table 5).

Table 5

Annealing conditions of nanofiber samples obtained by electroforming

№	Voltage, ± 0.1 kV	Electrospinning time, ± 0.1 min	Distance, ± 2 mm	Heat, ± 1 °C	Time to heat, ± 0.1 min
Sample 1	12.0	5.0	140	90	30.0
Sample 2	12.0	5.0	140	100	30.0
Sample 3	12.0	5.0	140	110	30.0
Sample 4	12.0	5.0	140	120	30.0

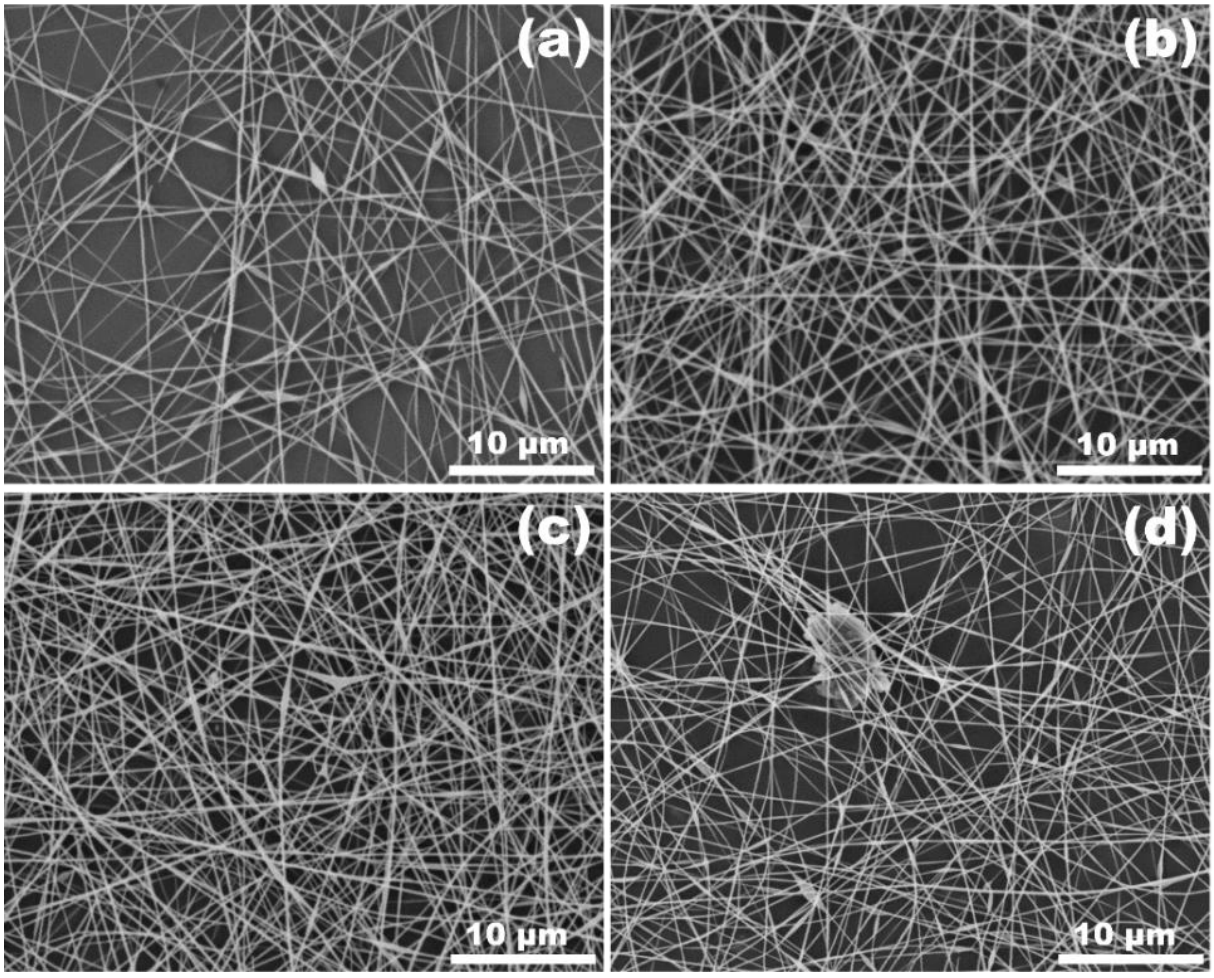

a) 90 °C; b) 100 °C; c) 110 °C; d) 120 °C.
Figure 14. SEM image of the surface of PVOH nanofibers after exposure to vacuum PVD 30 min

Manufacture of electrospun polymer materials for tissue engineering frameworks [17], wound dressings [18], drug shells [19] and other areas of biomedicine, the use of electroformed polymer nanofibers as a medium for filtration of solid particles from air, water or any target liquid at different filtration levels [20], for the absorption of toxic gases from industrial exhaust gases or for separating water from oil [21] as well as the use (Fig. 15) of electroformed nanofiber materials in separators [22], electrodes for lithium-ion batteries and supercapacitors, sensitized solar cells, electrolytes [23], nanogenerators [24] for energy conversion and storage show a high demand for these materials.

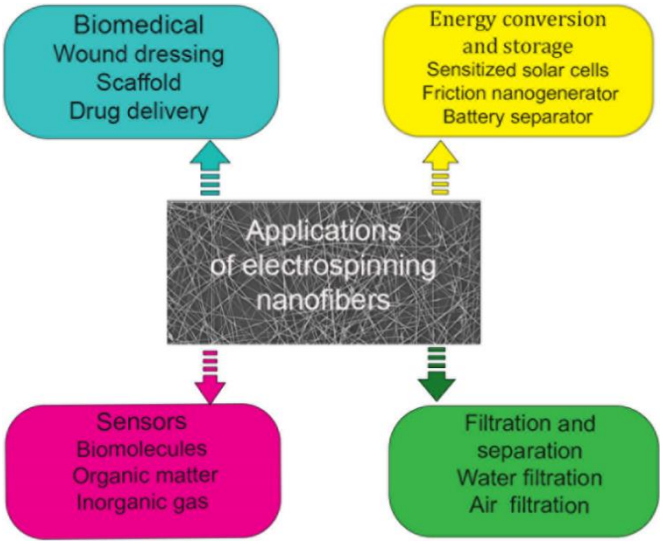

Figure 15. Potential applications of electroformed polymer nanofibers

Polymer nanofibers obtained by electrospinning provide unlimited possibilities for the formation of substrates and materials with different properties, controlled by different additional materials depending on the field of application. Showing high practical significance and having an undiscovered potential that is of interest to the world scientific community, electrospun polymer materials are one of the valuable achievements in the field of nanotechnology.

Conclusions

In this paper, the main processes for the formation of synthetic fibers such as wet spinning, melt spinning and dry spinning were discussed.

The investigated polymer fibers were obtained by dry electrospinning from a solution of PVOH polymer. The effect of the electrospinning voltage, the deposition time and the distance from the collector to the nozzle were all investigated using an Electrospinz electrospinning machine.

It was found that the small diameter of nanofibers is determined by the optimal combination of the applied voltage level and the distance from the tip of the nozzle to the collector.

The parameters of the electrospinning process required to obtain uniform defect-free nanofibers with a diameter from 120 to 174 nm were as follows: the distance between the nozzle and the collector was 140 mm and the voltage between the needle and the collector was 12-21 kV.

The above process parameters of electrospinning, are not independent of the concentration and type of polymer solution used. The effect of these additional details on the formation of nanofibers will be considered in the future.

References

1 Nofar, M., Sacligil, D., Carreau, P.J., Kamal, M.R. & Heuzey, M.C. (2019). Poly (lactic acid) blends: Processing, properties and applications. *International Journal of Biological Macromolecules*, *125*, 307–360.DOI:10.1016/j.ijbiomac.2018.12.002

2 Sun, J., Guo, J., Qian, Y., Guan, F., Zhang, Y., He, J. & Feng, Sh. (2022). Humidity-Responsive Guar Gum Fibers by Wet Spinning. *Langmuir*, *38* (49), 15327-15339. DOI:10.1021/acs.langmuir.2c02552

3 Sagdoldina, Zh., Rakhadilov, B., Akatan, K., Kowalewski, P., & Karabekova, D. (2020). The impact of non-vacuum electron beam treatment on the structure and properties of ultra-high molecular weight polyethylene. *Bulletin of the University of Karaganda - Physics,1*(97): DOI 10.31489/2020Ph1/35-41

4 Weisser, P., Barbier, G., Richard, C. & Drean, J.-Y. (2016). Characterization of the coagulation process: wet-spinning tool development and void fraction evaluation. *Textile Research Journal*, *86*(11):1210-1219. DOI:10.1177/0040517514551469

5 Wente, V.A. (1956). Superfine Thermoplastic Fibers. *Industrial & Engineering Chemistry*, *48*, 1342-1346. DOI:10.1021/IE50560A034

6 Pötschke, P., Brünig, H., Janke, A., Fischer, D., & Jehnichen, D. (2005). Orientation of Multiwalled Carbon Nanotubes in Composites with Polycarbonate by Melt Spinning. *Polymer*, *46*, 10355 — 10363.doi.org/10.1016/j.polymer.2005.07.106

7 Wei, W., Zhang, Y., Zhao, Y., Luo, J., Shao, H. & Hu, X. (2011). Bio-Inspired Capillary Dry Spinning of Regenerated Silk Fibroin Aqueous Solution. *Materials Science and Engineering*, *31*, 1602-1608. doi.org/10.1016/j.msec.2011.07.013

8 Sorkhabi, T.S., Samberan, M.F., Ostrowski, K.A., Zajdel, P., Stempkowska, A., & Gawenda, T. (2022). Electrospinning of Poly (Acrylamide), Poly (Acrylic Acid) and Poly (Vinyl Alcohol) Nanofibers: Characterization and Optimization Study on the Effect of Different Parameters on Mean Diameter Using Taguchi Design of Experiment Method. *Materials*, *15*, 5876. doi.org/10.3390/ma15175876

9 Haider, A., Haider, S. & Kang, I.-K. (2018). A comprehensive review summarizing the effect of electrospinning parameters and potential applications of nanofibers in biomedical and biotechnology. *Arabian Journal of Chemistry*, *11*, 1165–1188. doi.org/10.1016/j.arabjc.2015.11.015

10 Jung, Y.H., Kim, H.Y., Lee, D.R. & Park, S.Y. (2005). Characterization of PVOH Nonwoven Mats Prepared from Surfactant-Polymer System via Electrospinning. *Macromolecular Research*, *13*(5), 385-390. DOI:10.1007/BF03218470

11 Aslam, M., Kalyar, M.A. & Raza, Z.A. (2018). Polyvinyl alcohol: a review of research status and use of polyvinyl alcohol based nanocomposites. *Polymer Engineering and Science*, *58*, 2119–2132. doi.org/10.1002/pen.24855

12 Zhang, J., Huang, Y., Wu, H., Geng, S., & Wang, F. (2021). Corrosion protection properties of an environmentally friendly polyvinyl alcohol coating reinforced by a heating treatment and lignin nanocellulose. *Progress in Organic Coatings*, *155*, 106224. doi.org/10.1016/j.porgcoat.2021.106224

13 Hou, Q. & Wang, X. The effect of PVA foaming characteristics on foam forming. (2017). *Cellulose*, *24*, 4939–4948. doi.org/10.1007/s10570-017-1452-1

14 Jain, N., Singh, V. & Chauhan, S. (2018). A review on mechanical and water absorption properties of polyvinyl alcohol based composites/films. *Journal of the Mechanical Behavior of Materials*, *26*(5-6):213-222. doi.org/10.1515/jmbm-2017-0027

15 Ero-Phillips, O., Jenkins, M., & Stamboulis, A. (2012). Tailoring Crystallinity of Electrospun Plla Fibres by Control of Electrospinning Parameters. *Polymers*, *4*, 1331-1348. DOI:10.3390/polym4031331

16 Coronas, M., Holade, Y. & Cornu, D. (2022). Review of the Electrospinning Process and the Electro-Conversion of 5-Hydroxymethylfurfural (HMF) into Added-Value Chemicals. *Materials*, *15*, 4336. Doi: doi.org/10.3390/ma15124336

17 Zhao, X., Yuan, S.L., Choo, C.K.C., Wan, T.S., Charlotte, Liwen H., Kee, W.Ng., Lay, P.T. & Joachim, S.C.L. (2015). Calcium phosphate coated Keratin–PCL scaffolds for potential bone tissue regeneration. *Materials Science and Engineering*, *49*, 746–753. doi.org/10.1016/j.msec.2015.01.084

18 Yanfang, W., Pengfei, Li., Ping, X., Jueting, L., Jiang, Y., & Jian, S. (2016). Electrospun polyurethane/keratin/ AgNPbiocomposite mats for biocompatible and antibacterial wound dressings. *Journal of Materials Chemistry: B*, *4*, 635–648.doi.org/10.1039/C5TB02358K

19 Kenawy, E., Abdel-Hay, F., El-Newehy, M. & Wnek, G. (2009). Processing of polymer nanofibers through electrospinning as drug delivery systems. *Materials Chemistry and Physics*, *113*(1), 296–302. doi.org/10.1016/j.matchemphys.2008.07.081

20 Qayum, A., Wei, J., Li, Q., Chen, D., Jiao, X. & Xia, Y. (2019). Efficient decontamination of multicomponent wastewater by hydrophilic electrospun PAN/AgBr/Ag fibrous membrane. *Chemical Engineering Journal*, *361*, 1225–1263. doi.org/10.1016/j.cej.2018.12.161

21 Ge, J., Zong, D., Jin, Q., Yu, J., & Ding, B. (2018). Biomimetic and superwettable nanofibrous skins for highly efficient separation of oil-in-water emulsions. *Advanced Functional Materials*, *28*(10), 1705051(1-10). doi.org/10.1002/adfm.201705051

22 Yuriar-Arredondo, K., Armstrong, M., Shan, B., Zeng, W., Xu, W., Jiang, H., & Mu, B. (2018). Nanofiber based Matrimidorganogel membranes for battery separator. *Journal of Membrane Science*, *546*, 158–164. doi.org/10.1016/j.memsci.2017.10.004

23 Bandara, T., Weerasinghe, A., Dissanayake, M., Senadeera, G., Furlani, M., Albinsson, I., & Mellander, B. (2018). Characterization of poly (vinylidene fluoride-cohexafluoropropylene) (PVdF-HFP) nanofiber membrane based quasi solid electrolytes and their application in a dye sensitized solar cell. *Electrochimica Acta*, *266*, 276–283. doi.org/10.1016/j.electacta.2018.02.025

24 Yang, W., Chen, J., Zhu, G., Wen, X., Bai, P., Su, Y., Lin, Y., & Wang, Z. (2013). Harvesting vibration energy by a triple-cantilever based triboelectric nanogenerator. *Nano Research*, *6*(12), 880–886. DOI: 10.1007/s12274-013-0364-0

Д. Ескермесов, Е. Табиева, З. Аринғожина, М. Буз, А. Тусупбекова, С. Пазылбек

Электрспиннинг технологиясының қазіргі жағдайы және оның болашағы

Нанотехнологиялар мен зерттеудің заманауи әдістерінің дамуымен биологиялық ыдырайтын полимерлі материалдарды адамзат өмірінің әртүрлі салаларында қолдану ғылыми әлемдік қауымдастықтың қызығушылығын тудырып қана қоймайды, сонымен қатар ресурстарды үнемдеу мен қоршаған ортаны қорғауға байланысты жаһандық мәселелердің бірін шешуге жол болып табылады. Поливинил спирті негізіндегі материалдар биоүйлесімділік, биологиялық ыдырау қабілеті, микробқақарсы қабілеті, уытсыз үлдірді оңай түзу қабілеті сияқты биологиялық және физикалық қасиеттеріне байланысты әртүрлі салаларда кеңінен қолданылады. Полимерлі үлдірлерді алудың қазіргі кездегі әдістерінің бірі — электроспининг, оның артықшылығы технологиялық процестің салыстырмалы қарапайымдылығы мен синтетикалық және табиғи полимерлерден үздіксіз наноталшықтарды алу мүмкіндігі болып табылады. Бұл жұмыста биологиялық ыдырайтын синтетикалық полимерден электроспиннинг әдісімен наноталшықты төсеніштердің түзілуіне технологиялық үрдіс параметрлерінің әсері зерттелді. Ылғал-

ды спиннинг, балқыма спиннинг және құрғақ спиннинг технологиясы талқыланған. Поливинил спиртінен құрылымы біртекті, ақаусыз наноталшықтарды алудың оңтайлы режимдерін анықтау үшін бірқатар тәжірибелік зерттеулер жүргізілді.

Кілт сөздер: электрспиннинг, технологиялық параметрлер, наноталшықтар, поливинил спирті (PVOH), тоқылмаған төсеніштер, СЭМ, наноталшық диаметрі, биологиялық ыдырайтын полимер материалы.

Д. Ескермесов, Е. Табиева, З. Аринғожина, М. Буз, А. Тусупбекова, С. Пазылбек

Современное состояние технологии электроспиннинга и ее перспективы

С развитием нанотехнологий и современных методов исследования применение биоразлагаемых полимерных материалов в разных отраслях жизнедеятельности человечества вызывает интерес не только научного мирового сообщества, но и является путем к решению одной из глобальных проблем, связанных с ресурсосбережением и охраной окружающей среды. Материалы на основе поливинилового спирта получили широкое применение в различных областях благодаря своим биологическим и физическим свойствам, таким как биосовместимость, способность к биологическому разложению, антимикробная способность, нетоксичность и способность легко образовывать пленку. Одним из методов получения полимерных пленок существующих на сегодняшний день является электроспиннинг, преимуществом которого является относительная простота технологического процесса и возможность получения непрерывных нановолокон как из синтетических, так и натуральных полимеров. В статье было изучено влияние переменных характеристик технологических параметров процесса на формирование нановолоконных матов из биоразлагаемого синтетического полимера методом электроспиннинга. Обсуждены технологии мокрого прядения, прядения из расплава и сухого прядения. Проведен ряд экспериментальных исследований для выявления оптимальных режимов получения нановолокон из поливинилового спирта с наиболее однородной структурой без образования дефектов.

Ключевые слова: электроспиннинг, технологические параметры, нановолокна, поливиниловый спирт, нетканые матрицы, СЭМ, диаметр нановолокон, биоразлагаемый полимерный материал.

DOI 10.31489/2023PH2/93-99

UDC 621.314: 621.926.9: 537.528

A.K. Khassenov*, D.Zh. Karabekova, B.R. Nussupbekov, G.A. Bulkairova, A.S. Kudussov, G.K. Alpyssova, M.M. Bolatbekova

Karaganda University of the name of academician E.A. Buketov, Karaganda, Kazakhstan
*(*E-mail:* ayanbergen@mail.ru*)*

Investigation of the influences of pulsed electrical discharges on the grinding of quartz raw materials

The article considers a method for obtaining raw materials — quartz powder, used to increase the resistance of building materials to adverse natural facts (wind, rain, etc.). When obtaining raw materials necessary for construction from quartz mineral, it is pre-crushed to the desired size. New methods and technologies are proposed to improve the processes of grinding solid materials. One of these methods is the electric pulse method. This method is designed for grinding solid materials with the formation of pulsed electrical discharges in a liquid volume. When processing natural ores by the electric pulse method, the resulting products are not contaminated with metal in the working chamber. The paper analyzes the granulometric composition of quartz powder and determines the degree of grinding of raw materials depending on the parameters of electrical pulse discharges. The investigations on the processing of raw materials were carried out at various parameters of the number of pulse discharges and discharge voltage. In experiments, quartz fractions with a diameter of 10 mm were crushed by the electric pulse method and a product with a diameter of 0.4-1 mm was obtained. Since quartz is crushed in a liquid medium, the amount of water consumed was studied to obtain the necessary granulometric composition of raw materials. The dependences of the degree of quartz grinding on the number of pulse discharges and the discharge voltage are obtained. The results of grinding the material by pulsed electrical discharges allow us to evaluate the main parameters of the process implemented in the electro-pulse method of destruction of solid material.

Keywords: electrohydraulic effect, discharge voltage, quartz powder, electric pulse, degree of grinding, number of pulse discharges.

Introduction

Most quartz concentrates are obtained from natural quartz after its processing. The main types of natural quartz raw materials are: Rock crystal, quartzite, quartz sands [1]. The use of quartz sand, based in many industries, has a number of distinctive features that distinguish it from other materials. By its structure, this material is crushed quartz, which is formed in a natural environment or extracted after special processing. The following sizes of quartz sand fraction are assigned: fine-less than 0.1 mm; fine fraction-0.1-0.8 mm; the average fraction is 0.8-1.6 mm; the large fraction is 1.6-6.0 mm. The first two types of quartz sand are added to the composition of various building materials: putty, gypsum, mortar, abrasives, paint. Water purification of medium fraction is used, and is also added to mixtures for construction, finishing and decorative plasters, self-leveling floors [2-4]. Large quartz sand is used in the production of paving slabs, concrete blocks, as well as in the creation of landscape design. Various mechanical methods and mills (vibrating, cone, ball) are widely used in the enrichment and grinding of natural ores. Mechanical mills have the following disadvantages: a more complex and expensive design, more complex maintenance, the need for precise alignment of the rotors, wear of grinding bodies and contamination of raw materials with these wear products [5-7]. The solution of problems arising during the processing of quartz raw materials can be implemented using non-traditional grinding methods that do not introduce additional pollutants into the finished product. Since one of these methods is the electric pulse method of grinding natural minerals [8-10], the scientific work carried out works on grinding quartz raw materials in a liquid medium under the action of pulse discharges.

The experimental setup consists of a power supply and a working channel for grinding natural minerals [11, 12]. Electric pulse devices, unlike mechanical crushers, have no moving parts, are made of ordinary structural steel, and their body practically does not wear out. During operation, these devices do not emit dust, occupy relatively small production areas and allow grinding, mixing and flotation of materials. The process of electric pulse crushing is easy to automate, since the maintenance of electric pulse crushers does not require a large number of highly skilled workers. Under the influence of electrical impulses on a solid, process water was used as a pressure conductor, since it is the most accessible, economical and envi-

ronmentally friendly environment. The proposed method of ore crushing is based on the use of the energy of a pulsed shock wave resulting from a spark electric discharge in a liquid. As the experiments show, this method of crushing is efficient, economical, environmentally friendly, easily integrated into any technological chain. The essence und distinctive feature of the proposed technology is that ore processing using the pressure energy released during electrohydraulic action makes it possible to obtain a quickly crushed and purified from impurities dispersed product of a given size, which can then be used directly for subsequent enrichment [13-15].

Experimental

The object of the investigations was a quartz mineral from the Aktas deposit (Fig. 1). The initial diameter of the raw material fraction was 10 mm. For each experiment, the mass of the quartz mineral was constant (100 g). The granulometric composition of the crushed material was determined using standard sieves calibrated in accordance with GOST R 51568-99. The mass of the feedstock and the resulting product was determined using laboratory scales (maximum load — 1200 g; discreteness 0.1 g).

a) b) c)

Figure 1. Quartz: a) large piece; b) raw materials with a fraction diameter of 13-17 mm, c) quartz powder obtained by electric pulse method, fraction diameter 0.4 mm

In experimental investigations, the discharge voltage was changed to an interval of 18-24 kV and a quartz mineral was crushed at a discharge amount of 300-1500, a capacitor capacity of 0.5 μF (Tables 1-4). In experimental investigations, the degree of grinding of raw materials (K) was determined.

Table 1

Granulometric composition of the quartz mineral at a discharge voltage of 18 kV and a capacitor capacity of 0.4 μF

d, mm	N=300	N=600	N=900	N=1200	N=1500
	K, %				
d<0,4	-	-	3	4,8	3,6
d<0,7	0	2,4	8,9	6,5	18,2
d<1	66,3	57,6	47,7	63,2	49
d>1	33,7	40	40,4	25,5	29,2

Table 2

Granulometric composition of the quartz mineral at a discharge voltage of 20 kV and a capacitor capacity of 0.4 μF

d, mm	N=300	N=600	N=900	N=1200	N=1500
	K, %				
d<0,4	-	3,2	5,6	7,4	6,2
d<0,7	4,2	7,5	4,4	12	15,3
d<1	47	64,7	45,9	47,5	72,5
d>1	48,8	24,6	44,1	33,1	6

Table 3

Granulometric composition of the quartz mineral at a discharge voltage of 22 kV and a capacitor capacity of 0.4 μF

d, mm	N=300	N=600	N=900	N=1200	N=1500
	K, %				
d<0,4	2,1	5,6	8,9	13,3	10,9
d<0,7	4,3	3,1	13,6	11,2	22,6
d<1	45,7	30,8	46,2	29,7	43,7
d>1	47,9	60,5	31,3	45,8	22,8

Table 4

Granulometric composition of the quartz mineral at a discharge voltage of 24 kV and a capacitor capacity of 0.4 μF

d, mm	N=300	N=600	N=900	N=1200	N=1500
	K, %				
d<0,4	2,8	3,2	6,7	10,5	14
d<0,7	5	6,4	12,5	18,7	24
d<1	54,2	42	54,3	49,7	41,1
d>1	37,3	47,5	25	19,3	18,7

It can be seen from the above results that quartz powder with a diameter of less than 1 mm is intensively extracted with an increase in the number of pulse discharges from 900 to 1500. But it is established that these indicators are achieved only at the breakdown voltage of the air medium in the intervals of the converter in the range of 22-24 kV.

In subsequent studies, the dependence of the processed product on the amount of process water was considered, since the work on grinding raw materials is carried out in a liquid medium. For this purpose, work was carried out on the treatment of various levels of liquid (process water) in the working channel. The experiments were carried out with the same volume of water (V_{water}) as the volume of processed raw materials ($V_{raw\ materials}$) in the working channel — $V_{raw\ materials} = V_{water}$, with an increase in the volume of water by 1.5-5 times ($1.5V_{water}$ — $5V_{water}$) (Fig. 2 a, b, c).

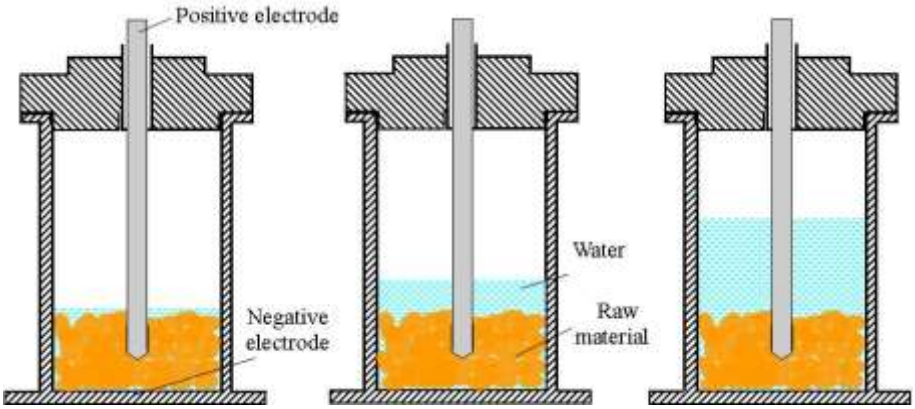

a) $V_{raw\ materials} = V_{water}$ b) $V_{raw\ materials} = 1{,}5V_{water}$ c) $V_{raw\ materials} = 5V_{water}$

Figure 2. Working channel

A metal cylindrical bowl was used as a working cell and performed the function of working electrodes in it — a metal rod (positive electrode) attached to the lid of the working cell and an inner tray of a metal

cylindrical bowl (negative electrode). Experimental investigations were carried out with the following parameters of the electric pulse unit (Fig. 3 a, b, c):

- number of pulse discharges (N) — 1000-1500;
- breakdown voltage of the air space in the intervals of the converter — 22-28 kV;
- the capacity of the energy storage capacitor — C = 0.5 μF.

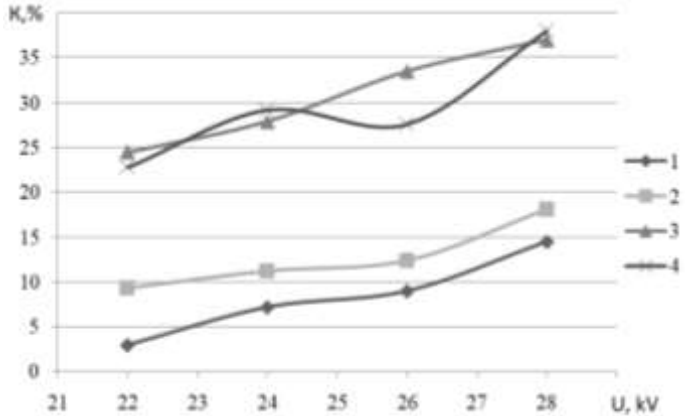

a) N=1000; C=0,5 μF

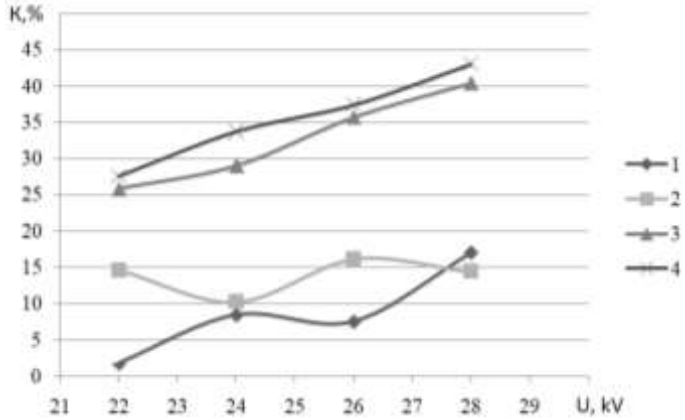

b) N=1500; C=0,5 μF

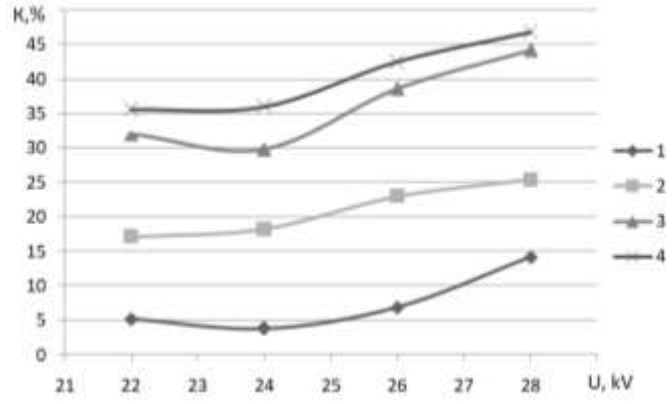

c) N=2000; C=0,5 μF

Figure 3. The dependence of the degree of grinding of a quartz mineral on the amount of water: 1 — $V_{raw\ materials} = V_{water}$; 2 — $V_{raw\ materials} = 1{,}5V_{water}$; 3 — $V_{raw\ materials} = 3V_{water}$; 4 — $V_{raw\ materials} = 5V_{water}$

The dependence shown in the figures is the results after grinding the quartz mineral with a diameter of the initial fraction of 13-17 mm (the diameter of the resulting product is below 1 mm). It can be seen from the results that with an increase in the volume of water by 3-5 times compared to the volume of processed

raw materials ($3V_{water}$ — $5V_{water}$), the degree of grinding of the product increases. With an increase in the amount of water from the specified level, the output of the finished product changed at about the same level.

Conclusions

In the scientific work, the influence of electric pulse discharges on quartz mineral was considered, raw materials were obtained that are widely used in construction — quartz powder. Since the processing of raw materials is carried out in a liquid medium, the dependence of the quantity of finished products on the amount of liquid is investigated. From the results obtained, the amount of liquid required for intensive grinding of quartz mineral was determined. The experimental data can be used in obtaining the production of granulometric composition from natural ores by the electric pulse method.

This research is funded by the Science Committee of the Ministry of Science and Higher Education of the Republic of Kazakhstan (Grant AP14870607)

References

1 Гадиятов В.Г. К проблеме использования кварцевого песка для получения особо чистого кварца / В.Г. Гадиятов, Д.А. Киях, С.А. Жидкова // Вестн. Воронеж. гос. ун-та. Сер. Геология. — 2010. — № 2. — С. 324–327.

2 Осовская И.И. Полимерные материалы / И.И. Осовская. — СПб.: Высш. шк. технол. и энерг. СПб. гос. ун-та промышл. технол. и дизайна, 2017. — 89 с.

3 Фракционированный кварцевый песок. — [Электронный ресурс]. — Режим доступа: https://binom-c.ru/raboty/vidy-kvarcevogo-peska.html

4 Florea M.V.A. Properties of various size fractions of crushed concrete related to process conditions and re-use / M.V.A. Florea, H.J.H. Brouwers // Cement and Concrete Research. — 2013. — № 52. — P. 11-21.

5 Еренков О.Ю. Оборудование механических процессов в химической технологии / О.Ю. Еренков, А.П. Богачев. — Хабаровск: Тихоокеан. гос. ун-т, 2014. — 80 с.

6 Пузыревская И.А. Обогащение полезных ископаемых / И.А. Пузыревская. — Благовещенск: Амур. гос. ун-т, 2014. — 96 с.

7 Постникова И.В. Струйные мельницы / И.В. Постникова, В.Н. Блиничев, Я. Кравчик // Современные наукоемкие технологии. Региональное приложение. — 2015. — № 2 (42). — С. 144–151.

8 Зиновьев Н.Т. Энергетические и размерные характеристики электроимпульсного разрушения кварцитов / Н.Т. Зиновьев, В.И. Курец, Г.П. Филатов, А.Ю. Юшков // Изв. высш. учеб. завед. Физика. — 2011. — № 1/2. — С. 277–283.

9 Корженевский С.Р. Выбор режимов электрогидравлического селективного дробления кварцевой руды / С.Р. Корженевский, В.А. Бессонова, А.А. Комарский, В.А. Мотовилов, А.С. Чепусов // Физико-технические проблемы разработки полезных ископаемых. — 2016. — № 3. — С. 70–74.

10 Chornyi V. Investigation of particle size distribution of grinded amber by electropulse discharges in a liquid medium / V.Chornyi, Y. Kharchenko, T. Mysiura, N. Popova, V. Zavialov // ARCHIVE OF MECHANICAL ENGINEERING. — 2021. — 68(3). — P. 337-348.

11 Nussupbekov B.R. Coal pulverization by electric pulse method for water-coal fuel / B.R. Nussupbekov, A.K. Khassenov, D.Zh. Karabekova, U.B. Nussupbekov, M. Stoev, M.M. Bolatbekova // Bulletin of the university of Karaganda — Physics. — 2019. — № 4(96). — P. 80-84.

12 Kurytnik I.P. Investigation of a crushing and grinding unit of an electropulse installation / I.P. Kurytnik, B.R. Nussupbekov, A.K. Khassenov, D.Zh. Karabekova, A.Sh. Kazhikenova // Archives of Foundry Engineering. — 2018. — Vol. 18(1). — P. 61-64.

13 Юткин Л.А. Электрогидравлический эффект и его применение в промышленности / Л.А. Юткин. — Л., 1986. — 253 с.

14 Курец В.И. Электроразрядные технологии обработки и разрушения материалов / В.И. Курец, М.А. Соловьев, А.И. Жучков, А.В. Барская. — Томск: Том. политехн. ун-т, 2012. — 272 с.

15 Kurytnik I.P. Development of a grinding device for producing coal powder-raw materials of coal-water fuel / I.P. Kurytnik, A.K. Khassenov, D.Z. Karabekova, U.B. Nussupbekov, B.R. Nussupbekov, M. Bolatbekova // Archive of Mechanical Engineering. — 2022. — 69(2). — P. 259-268.

А.К. Хасенов, Д.Ж. Карабекова, Б.Р. Нусупбеков, Г.А. Булкаирова,
А.С. Кудусов, Г.К. Алпысова, М.М. Болатбекова

Кварц шикізатының ұнтақталуына импульсті электр разрядтарының әсерін зерттеу

Мақалада құрылыстық материалдардың табиғаттың қолайсыз факторларына (жел, жаңбыр және т.б.) төзімділігін арттыру мақсатында пайдаланылатын шикізат — кварц ұнтағын алу тәсілі қарастырылған. Кварц минералынан құрылысқа қажетті шикізатты алуда ол алдыменен керекті мөлшерге дейін ұнтақталады. Қатты материалдарды ұнтақтау процестерін жетілдіруде жаңа әдістер мен технологиялар ұсынылуда. Осындай әдістердің бірі — электроимпульсті әдіс. Аталмыш әдіс сұйықтық көлемінде импульсті электр разрядттарын қалыптастыра отырып, қатты материалдарды ұнтақтауға арналған. Электримпульсті әдіспен табиғи кедерді өңдеу кезінде алынатын өнім жұмыс камерасындағы металмен ластанбайды. Жұмыста кварц ұнтағының гранулометрлік құрамы талданып, электроимпульсті разрядтардың параметрлеріне тәуелді шикізаттың ұнтақталу дәрежесі анықталды. Шикізатты өңдеу зерттеулері импульсті разрядтар санының және разряд кернеуінің әртүрлі параметрлерінде орындалды. Тәжірибелерде электроимпульсті әдіспен фракция диаметрі 10 мм кварц кесектері ұнтақталып, диаметрі 0,4-1 мм ұнтақ алынды. Кварц сұйық ортада ұнтақталатындықтан, шикізаттың қажетті грануламетрлік құрамын алу үшін тұтынылатын су мөлшері зерттелді. Кварцтың ұнтақталу дәрежесінің импульсі разрядтар санына, разряд кернеуіне тәуелділіктері алынды. Материалды импульсті электр разрядтарымен ұнтақтау нәтижелері қатты материалды бұзуға арналған электроимпульсті әдісте іске асатын процестің негізгі көрсеткіштерін бағалауға мүмкіндік береді.

Кілт сөздер: электрогидравликалық эффект, разряд кернеуі, кварц ұнтағы, электроимпульс, ұнтақталу дәрежесі, импульсті разрядтар саны.

А.К. Хасенов, Д.Ж. Карабекова, Б.Р. Нусупбеков, Г.А. Булкаирова, А.С. Кудусов,
Г.К. Алпысова, М.М. Болатбекова

Исследование влияния импульсных электрических разрядов на измельчение кварцевого сырья

В статье рассмотрен способ получения сырья — кварцевого порошка, используемого с целью повышения устойчивости строительных материалов к неблагоприятным фактам природы (ветер, дождь и др.). При получении сырья, необходимого для строительства из кварцевого минерала, его предварительно измельчают до нужного размера. В совершенствовании процессов измельчения твердых материалов предложены новые методы и технологии. Одним из таких является электроимпульсный метод. Данный способ предназначен для измельчения твердых материалов с образованием импульсных электрических разрядов в объеме жидкости. При переработке природных руд электроимпульсным методом получаемая продукция не загрязняется металлом в рабочей камере. Авторами проанализирован гранулометрический состав кварцевого порошка и определена степень измельчения сырья в зависимости от параметров электрических импульсных разрядов. Исследования переработки сырья проводились при различных параметрах количества импульсных разрядов и напряжения разряда. В опытах кварц диаметром фракции 10 мм измельчался электроимпульсным методом и был получен продукт диаметром 0,4–1 мм. Поскольку кварц измельчался в жидкой среде, было изучено количество расходуемой воды для получения необходимого гранулометрического состава сырья. Получены зависимости степени измельчения кварца от количества импульсных разрядов и напряжения разряда. Результаты измельчения материала импульсными электрическими разрядами позволяют оценить основные параметры процесса, реализуемого в электроимпульсном методе разрушения твердого материала.

Ключевые слова: электрогидравлический эффект, напряжение разряда, кварцевый порошок, электроимпульс, степень помола, количество импульсных разрядов.

References

1 Gadiiatov, V.G., Kiiakh, D.A., & Zhidkova, S.A. (2010). K probleme ispolzovaniia kvartsevogo peska dlia polucheniia osobo chistogo kvartsa [On the problem of using quartz sand to obtain highly pure quartz]. *Vestnik Voronezhskogo gosudarstvennogo universiteta. Seriia Geologiia — Bulletin of Voronezh State University, series: geology*, *2*, 324–327 [in Russian].

2 Osovskaia, I.I. (2017). Polimernye materialy [Polymeric materials]. Saint-Petersburg: Vysshaia shkola tekhnologii i energetiki Sankt-Peterburgskogo gosudarstvennogo universiteta promyshlennoi tekhnologii i dizaina [in Russian].

3 Fraktsionirovannyi kvartsevyi pesok [Graded quartz sand]. Retrieved from: https://binom-c.ru/raboty/vidy-kvarcevogo-peska.html [in Russian].

4 Florea, M.V.A., & Brouwers, H.J.H. (2013). Properties of various size fractions of crushed concrete related to process conditions and re-use. *Cement and Concrete Research, 52*, 11-21.

5 Erenkov, O.Yu., & Bogachev, A.P. (2014). Oborudovanie mekhanicheskikh protsessov v khimicheskoi tekhnologii [Equipment for mechanical processes in chemical technology]. Khabarovsk: Tikhookeanskii gosudarstvennyi universitet [in Russian].

6 Puzyrevskaia, I.A. (2014). Obogashchenie poleznykh iskopaemykh [Enrichment of minerals]. Blagoveshchensk: Amurskii gosudarstvennyi universitet [in Russian].

7 Postnikova, I.V., Blinichev, V.N., & Kravchik, Ya. (2015). Struinye melnitsy [Jet mills]. *Sovremennye naukoemkie tekhnologii. Regionalnoe prilozhenie — Modern science-intensive technologies. Regional application*, 2(42), 144–151 [in Russian].

8 Zinovev, N.T., Kurets, V.I., Filatov, G.P., & Iushkov, A.Yu. (2011). Energeticheskie i razmernye kharakteristiki elektroimpulsnogo razrusheniia kvartsitov [Energy and dimensional characteristics of electropulse destruction of quartzites]. *Izvestiia vysshikh uchebnykh zavedenii. Fizika — News of higher educational institutions. Physics*, *1/2*, 277–283 [in Russian].

9 Korzhenevskii, S.R., Bessonova, V.A., Komarskii, A.A., Motovilov, V.A., & Chepusov, A.S. (2016). Vybor rezhimov elektrogidravlicheskogo selektivnogo drobleniia kvartsevoi rudy [Choice of modes of electrohydraulic selective crushing of quartz ore]. *Fiziko-tekhnicheskie problemy razrabotki poleznykh iskopaemykh — Physical and technical problems of mining*, *3*, 70–74 [in Russian].

10 Chornyi, V., Kharchenko, Y., Mysiura, T., Popova, N., & Zavialov, V. (2021). Investigation of particle size distribution of grinded amber by electropulse discharges in a liquid medium. *ARCHIVE OF MECHANICAL ENGINE, 68*(3), 337-348.

11 Nussupbekov, B.R., Khassenov, A.K., Karabekova, D.Zh., Nussupbekov, U.B., Stoev, M., & Bolatbekova, M.M. (2019). Coal pulverization by electric pulse method for water-coal fuel. *Bulletin of the university of Karaganda-Physics, 4* (96), 80-84.

12 Kurytnik, I.P., Nussupbekov, B.R., Khassenov, A.K., Karabekova, D.Zh., & Kazhikenova, A.Sh. (2018). Investigation of a crushing and grinding unit of an electropulse installation. *Archives of Foundry Engineering, 18*(1), 61-64.

13 Yutkin, L.A. (1986). Elektrogidravlicheskii effekt i ego primeneniie v promyshlennosti [Electrohydraulic effect and its application in industry]. Leningrad: Mashinostroenie [in Russian].

14 Kurets, V.I., Solovev, M.A., Zhuchkov, A.I., & Barskaia, A.V. (2012). Elektrorazriadnye tekhnologii obrabotki i razrusheniia materialov [Electrodischarge technologies for processing and destruction of materials]. Tomsk: Tomskii politekhnicheskii universitet [in Russian].

15 Kurytnik, I.P., Khassenov, A.K., Karabekova, D.Z., Nussupbekov, U.B., Nussupbekov, B.R., & Bolatbekova, M. (2022). Development of a grinding device for producing coal powder-raw materials of coal-water fuel. *Archive of Mechanical Engineering*, *69*(2), 259–268.

АВТОРЛАР ТУРАЛЫ МӘЛІМЕТТЕР
СВЕДЕНИЯ ОБ АВТОРАХ
INFORMATION ABOUT AUTHORS

Abdullin, Kh.A. – Doctor of physics and mathematics, Professor, al-Farabi Kazakh National University, Almaty, Kazakhstan.

Abuova, A.U. – Ph.D., Acting associate professor of the Department of Technical Physics, L.N. Gumilyov Eurasian National University, K. Munaitpasov St. 13, Astana, Kazakhstan.

Abuova, F.U. – Ph.D, Acting professor of Nuclear Physics, New Materials and Technologies, L.N Gumilyov Eurasian National University, K. Munaytpasov St. 13, Astana, Kazakhstan.

Aimukhanov, A.K. – Candidate of Physical and Mathematical Sciences, Associate professor, Professor of the Department of Radiophysics and Electronics, Leading Researcher, Karaganda University of the name of academician E. A. Buketov, Scientific Center for Nanotechnology and Functional Nanomaterials, Karaganda, Kazakhstan; ORCID-0000-0002-4384-5164. Scopus Author ID-35321945000

Aitzhanov, M.B. – PhD student, Solid State Physics and Nonlinear Physics Department, al-Farabi Kazakh National University, Almaty, Kazakhstan.

Alexeev, A.M. – Candidate of physical and mathematical sciences, Kazan Federal University, Kazan, Russia. Researcher ID – A-8526-2012, ORCID ID – 0000-0002-2800-6047

Alpyssova, G.K. – PhD, Karaganda University of the name of academician E.A. Buketov, Kazakhstan, E-mail: gulnur-0909@mail.ru

Altayeva, G.S. – 2 course PhD student, Department of General and Theoretical Physics, L. N. Gumilyov Eurasian National University, Astana, Kazakhstan, Tel: +7 7057815355, E-mail: altayeva_gg@mail.ru

Aringozhina, Z.Y. – Master of technical sciences, Lecturer at the Department of Physics, East Kazakhstan Technical University, Ust-Kamenogorsk, Kazakhstan, E-mail: *zaringozhina@ektu.kz* Academic visitor: University of Lincoln, Lincoln, UK, E-mail: *zaringozhina@lincoln.ac.uk*

Baizhan, D.R. – Senior researcher of scientific research center "Surface engineering and tribology", Sarsen Amanzholov East Kazakhstan University, Ust-Kamenogorsk, Kazakhstan, E-mail: daryn.baizhan@mail.ru

Berdimuratov, N.E. – Senior researcher of scientific research center "Surface engineering and tribology", Sarsen Amanzholov East Kazakhstan University, Ust-Kamenogorsk, Kazakhstan, E-mail: nurbol.ber@gmail.com

Bolatbekova, M.M. – Teacher, Karaganda University of the name of academician E.A. Buketov, Kazakhstan, E-mail: ya.reneit@yandex.kz

Booth, M. – PhD, Senior lecturer at the School of Maths and Physics, University of Lincoln, Lincoln, UK, E-mail: *mbooth@lincoln.ac.uk*

Buitkenov, D.B. – PhD, Leading researcher of scientific research center "Surface engineering and tribology", Sarsen Amanzholov East Kazakhstan University, Ust-Kamenogorsk, Kazakhstan, E-mail: buitkenovd@mail.ru

Bulkairova, G.A. – 2st year doctoral student, Karaganda University of the name of academician E.A. Buketov, Kazakhstan; e-mail: gulden2111@mail.ru

Gert, S.S. – Master degree in metallurgy at D. Serikbayev East Kazakhstan Technical University, Ust-Kamenogorsk, Kazakhstan, E-mail: gert_sergej@mail.ru

Gritsenko, L.V. (contact person) – PhD in Nanomaterials and Nanotechnology, Professor, General Physics Department, Satbayev University, Almaty, Kazakhstan, E-mail: gritsenko_lv@mail.ru.

Hasanov, E.R. – Candidate of physical and mathematical sciences, Baku State University, Associate professor of Solid State Physics Department, Leader of Department of Encyclopedia and Terminology. Baku, Azerbaijan, E-mail: egasanov065@gmail.com

Ilyassov, B. R. – PhD, Associate professor, Astana IT University, Astana, Kazakhstan, Author ID в Scopus-56669724700; Researcher ID Web of Science - C-1411-2015; ORCID ID - 0000-0003-4563-2004; Researcher ID in Publons - C-1411-2015

Inerbaev, T.M. – Candidate of physical-mathematical speciality, Acting associate professor of the Department of Technical Physics, L.N. Gumilyov Eurasian National University, K. Munaitpasov St. 13, Astana, Kazakhstan.

Kaptagay, G.A. – Ph.D, Acting associate professor of the Department of Technical Physics, Kazakh National Women's Teacher Training University, Aiteke bi St. 99, Almaty, Kazakhstan.

Karabekova, D.Zh. – PhD, Assistant professor, Karaganda University of the name of academician E.A. Buketov, Kazakhstan, E-mail: karabekova71@mail.ru

Kedruk, Y.Y. – PhD, Senior Lecturer, General Physics Department, Satbayev University, Almaty, Kazakhstan.

Khalilova, Sh. G. (contact person) – Candidate of physical sciences. Senior researcher of Department of Encyclopedia and Terminology. Baku, Azerbaijan, E-mail: shahlaganbarova@gmail.com

Khassenov, A.K. – PhD, Assistant professor, Karaganda University of the name of academician E.A. Buketov, Kazakhstan, E-mail: ayanbergen@mail.ru

Kudussov, A.S. – Candidate of physical and mathematical sciences, Assistant professor, Karaganda University of the name of academician E.A. Buketov, Kazakhstan; e-mail: akudusov@mail.ru

Magazov, N.M. (contact person) – Junior researcher of research center "Surface Engineering and Tribology" at Sarsen Amanzholov East Kazakhstan University, Ust-Kamenogorsk, Kazakhstan, E-mail: magazovn@gmail.com

Mustafina, K.K. – Master of Technical Sciences, Tutor, General Physics Department, Satbayev University, Almaty, Kazakhstan.

Nabioldina, A.B. – Master degree student of Sarsen Amanzholov East Kazakhstan University, Ust-Kamenogorsk, Kazakhstan

Nurkenov, S.A. – Ph.D., Astana International University, Astana, Kazakhstan, K. Munaitpasov St. 13, Astana, Kazakhstan.

Nussupbekov, B.R. – Candidate of technical sciences, Full professor of the Department of Engineering Thermophysics named after prof. Zh.S. Akylbayev, Karaganda University of the name of academician E. A. Buketov, E-mail: bek_nr1963@mail.ru

Omarbekova, G.I. – 3rd year PhD student, Researcher, Karaganda University of the name of academician E. A. Buketov, Scientific Center for Nanotechnology and Functional Nanomaterials, Karaganda, Kazakhstan; ORCID ID – 0000-0002-0755-6832, E-mail: gulnur_130983@mail.ru

Pavlov, A.V. – Technical Director of KAZ CERAMICS LLP, Ust-Kamenogorsk, Kazakhstan, E-mail: alexandr_pavlov_1988@mail.ru

Pazylbek, S. – PhD, Associate professor at the Department of Mathematics and Informatics, Tashenov University, Shymkent, Kazakhstan, E-mail: *pazylbek.sapargali@yandex.kz*

Rakhadilov, B.K. – PhD, Associate professor, Sarsen Amanzholov East Kazakhstan University, Director of "PlasmaScience" LLP, Ust-Kamenogorsk, Kazakhstan, E-mail: rakhadilovb@mail.ru

Razina, O.V. – PhD, Associate professor, Department of General and Theoretical Physics, L.N. Gumilyov Eurasian National University, Astana, Kazakhstan, Tel: +7 7014915691, E-mail: olvikraz@mail.ru

Sagdoldina, Zh.B. – PhD, Associate professor, Leading researcher of scientific research center "Surface engineering and tribology", Sarsen Amanzholov East Kazakhstan University, Ust-Kamenogorsk, Kazakhstan, E-mail: sagdoldina@mail.ru

Seisembekova, T.E. – 3rd year PhD student, Researcher, Karaganda University of the name of academician E. A. Buketov, Scientific Center for Nanotechnology and Functional Nanomaterials, Karaganda, Kazakhstan; ORCID ID-0000-0002-1497-0759, E-mail: tosh_0809@mail.ru

Tabiyeva, Y.Y. – PhD, Senior lecturer at the Department of Physics, East Kazakhstan Technical University, Ust-Kamenogorsk, Kazakhstan, E-mail: *etabieva@ektu.kz* Academic visitor: University of Lincoln, Lincoln, UK. e-mail: *ytabiyeva@lincoln.ac.uk*

Tolubayeva, D.B. – PhD student, Karaganda Industrial University, Temirtau, Kazakhstan.

Tsyba, P.Yu. – PhD, Associate professor, Department of General and Theoretical Physics, L.N. Gumilyov Eurasian National University, Astana, Kazakhstan, Tel: +7 7017787567, E-mail: pyotrtsyba@gmail.com

Turar, Zh.S. – Engineer of research center "Surface Engineering and Tribology" at Sarsen Amanzholov East Kazakhstan University, Ust-Kamenogorsk, Kazakhstan, E-mail: tuurar2021@mail.ru

Tussupbekova, A.K. – PhD, Associate professor at the Department of Radiophysics and Electronics, Karaganda University of the name of academician E.A. Buketov, Karaganda, Kazakhstan, E-mail: *aintus_070482@mail.ru*

Valiev, D.T. – Candidate of physical and mathematical sciences, Tomsk Polytechnic University, Tomsk, Russia, ORCID ID – 0000-0001-6880-7642

Yeskermessov, D.K. (contact person) – PhD, Associate professor at the Department of Physics, East Kazakhstan Technical University, Ust-Kamenogorsk, Kazakhstan. E-mail: *dyeskermessov@ektu.kz* Academic visitor: University of Lincoln, Lincoln, UK, E-mail: *dyeskermessov@lincoln.ac.uk*

Zakiyeva, Zh.Ye. – 3 d year doctoral student "Technical Physics", L.N. Gumilyov Eurasian National University, K. Munaitpasov St. 13, Astana, Kazakhstan.

Zeinidenov, A.K. – PhD, Associate Professor, Dean of the Physical-Technical Faculty, Leading Researcher, Karaganda University of the name of academician E. A. Buketov, Scientific Center for Nanotechnology and Functional Nanomaterials, Karaganda, Kazakhstan; ORCID-0000-0001-9780-5072. Scopus Author ID-56386144000

Zhakhanova, A.M. – Junior Researcher, Karaganda University of the name of academician E. A. Buketov, Scientific Center for Nanotechnology and Functional Nanomaterials, Karaganda, Kazakhstan; ORCID ID - 0000-0002-3863-2682

Zhaparova, M.S. – Senior lecturer of the Department of Physics, Sarsen Amanzholov East Kazakhstan University, Ust-Kamenogorsk, Kazakhstan

Zhilkashinova, A.M. – PhD, Senior researcher of National Labaratory of Collective Use at Sarsen Amanzholov East Kazakhstan University, E-mail: almira_1981@mail.ru